1-1-2014

Neutron Multiplicity in Atmospheric Neutrino Events at the Sudbury Neutrino Observatory

Richard Bonventre
University of Pennsylvania, rbonv@hep.upenn.edu

Neutron Multiplicity in Atmospheric Neutrino Events at the Sudbury Neutrino Observatory

Abstract
This thesis describes the results of two separate analyses. Part I is the description of the first analysis which uses the newest measurements of neutrino mixing to study various non-standard models of neutrino interactions through their impact on solar neutrinos. These models can be motivated by the fact that solar neutrino experiments have yet to see directly the transition region between matter-enhanced and vacuum oscillations. The transition region is particularly sensitive to models of non-standard neutrino interactions and propagation. I examine several such non-standard models which predict a lower-energy transition region. I find that while several models provide a better fit to the solar neutrino data set, large experimental uncertainties lead to a low statistical significance.

Part II describes the second analysis, where I look at neutron followers of contained atmospheric neutrino events in the SNO data set. These kinds of events are difficult backgrounds for nucleon decay measurements, and understanding the neutron follower multiplicity will allow for better rejection. It can also help improve measurements of the neutrino mass hierarchy and neutrino-nuclear cross sections. I find that the dependence of the average multiplicity on the visible energy agrees well with the predictions of simulations except for an unexplained deficit between 100 MeV and 600 MeV and an excess above 4 GeV. I determined the ability to distinguish neutrino and antineutrino events using the multiplicity by fitting for the double ratio $R \equiv (\overline{\nu}/\nu)_{\text{data}} / (\overline{\nu}/{\nu})_{\text{MC}})$. I find $R = 0.93^{+0.91}_{-0.63}$ for a fit to a single multiplicity distribution per phase, and $R < 1.00$ for a fit to separate distributions for single electron ring, single muon ring, and multi-ring events. I also look at the agreement with a meson-exchange current cross section model developed to explain anomalous cross sections measured by MiniBooNE. Fitting for the strength of the MEC contribution as a fraction of the quasielastic charged-current cross section, I find an upper limit of $\sigma_{MEC}/\sigma_{QECC} < 0.17$ for a fit to combined distributions and $\sigma_{MEC}/\sigma_{QECC} < 0.04$ for a fit to separate distributions for ring count and type.

Degree Type
Dissertation

Degree Name
Doctor of Philosophy (PhD)

Graduate Group
Physics & Astronomy

First Advisor
Joshua R. Klein

Subject Categories
Elementary Particles and Fields and String Theory

NEUTRON MULTIPLICITY IN ATMOSPHERIC NEUTRINO EVENTS AT THE SUDBURY NEUTRINO OBSERVATORY

Richard J. Bonventre

A DISSERTATION

in

Physics and Astronomy

Presented to the Faculties of the University of Pennsylvania

in Partial Fulfillment of the Requirements for the Degree of Doctor of Philosophy

2014

Supervisor of Dissertation

_____

Joshua R. Klein
Professor of Physics

Graduate Group Chairperson

_____

Marija Drndic
Professor of Physics

Dissertation Committee
Eugene W. Beier, Professor of Physics
Elliot Lipeles, Associate Professor of Physics
I. Joseph Kroll, Professor of Physics
Justin Khoury, Associate Professor of Physics

To my parents, my brothers, and my wife.

Acknowledgments

This thesis and my graduate student career were built on the support and guidance of many people. I would first like to thank my advisor, Josh Klein, who really shaped my experience of what graduate school is and what research should be. It was clear from the beginning that Josh believed that ensuring the success of his students should be one of his top priorities. He was always a helpful and encouraging presence in the office, and was always patient with me, no matter how many times I refused to label the axes on my plots.

It has been a pleasure to work with Gene Beier and Bill Heintzelman, who have been an invaluable source of knowledge and expertise. Without Gene's help with SNOMAN this thesis would have been impossible.

I would like to thank the rest of the XL3 development crew. Tim Shokair was there to share frustrations with Cadence, and as the senior student showed me that it was possible to graduate some day. Rob Knapik provided unending enthusiam into every project we worked on. Rick Van Berg and Godwin Mayers were essential sources of electronics help and general detector wisdom. Without the work of Noel

Gagnon, Cam Beaudoin, and Mike Schwendener at site, SNO+ would never be functional.

I was fortunate to have the opportunity to work with Stan Seibert and Gabriel Orebi Gann. Together, I believe the two of them know everything there is to know about science, and I hope that I was able to absorb a little bit of it by pestering them with questions about my analysis. I would like to thank Tony LaTorre and Olivia Wasalski for the incredible amount of work they put in to developing the foundation for the first part of this thesis.

I would like to thank Andy Mastbaum for being my partner in crime for the majority of my time at Penn. There was nothing better than to come up with a bad idea, walk over to Andy's desk to talk it over, and refine it into a truly terrible idea. On occasion good ideas would work their way out as well. I'd also like to thank the rest of the Penn group: Jeff Secrest, Sean Grullon, Ian Coulter, Nuno Barros, Tom Caldwell, Eric Marzec, and Rehan Deen for their friendship and support.

I have to thank Byron Dieterle for being incredibly generous with his time to mentor a complete stranger, and introducing me to the world of neutrino physics, and Michael Vineyard for providing me with all the opportunities and support I needed to make it to graduate school.

I would like to thank my family, who have given me all the emotional support one could ask for. My parents and my brothers always believed in me, and gave me the confidence to keep going when things were uncertain. Finally, I would like

to thank my wife Olga, who somehow has put up with me throughout the whole process.

ABSTRACT

NEUTRON MULTIPLICITY IN ATMOSPHERIC NEUTRINO EVENTS AT THE SUDBURY NEUTRINO OBSERVATORY

Richard J. Bonventre

Joshua Klein

This thesis describes the results of two separate analyses. Part I is the description of the first analysis which uses the newest measurements of neutrino mixing to study various non-standard models of neutrino interactions through their impact on solar neutrinos. These models can be motivated by the fact that solar neutrino experiments have yet to see directly the transition region between matter-enhanced and vacuum oscillations. The transition region is particularly sensitive to models of non-standard neutrino interactions and propagation. I examine several such non-standard models which predict a lower-energy transition region. I find that while several models provide a better fit to the solar neutrino data set, large experimental uncertainties lead to a low statistical significance.

Part II describes the second analysis, where I look at neutron followers of contained atmospheric neutrino events in the SNO data set. These kinds of events are difficult backgrounds for nucleon decay measurements, and understanding the neutron follower multiplicity will allow for better rejection. It can also help improve measurements of the neutrino mass hierarchy and neutrino-nuclear cross sections.

I find that the dependence of the average multiplicity on the visible energy agrees well with the predictions of simulations except for an unexplained deficit between 100 MeV and 600 MeV and an excess above 4 GeV. I determined the ability to distinguish neutrino and antineutrino events using the multiplicity by fitting for the double ratio $R \equiv (\overline{\nu}/\nu)_{\rm data}/(\overline{\nu}/\nu)_{\rm MC})$. I find $R = 0.93^{+0.91}_{-0.63}$ for a fit to a single multiplicity distribution per phase, and $R < 1.00$ for a fit to separate distributions for single electron ring, single muon ring, and multi-ring events. I also look at the agreement with a meson-exchange current cross section model developed to explain anomalous cross sections measured by MiniBooNE. Fitting for the strength of the MEC contribution as a fraction of the quasielastic charged-current cross section, I find an upper limit of $\sigma_{MEC}/\sigma_{QECC} < 0.17$ for a fit to combined distributions and $\sigma_{MEC}/\sigma_{QECC} < 0.04$ for a fit to separate distributions for ring count and type.

Contents

List of Tables

List of Figures

Part I

Nonstandard Models, Solar Neutrinos, and large θ_{13}

Chapter 1

Introduction

The neutrino is a fundamental particle that interacts only via the weak force and gravity. Its existence was first proposed in 1930 by Wolfgang Pauli as a solution to the apparent violation of energy conservation in beta decays [12]. Due to the weakness of its interactions, it remained undetectable for several decades. The initial observation in 1956 by Cowan and Reines required the use of the enormous neutrino flux from a nuclear reactor [13]. However this same weakness makes neutrinos a unique probe of previously unreachable physics. As they leave the Sun without interacting, they can be used to study fusion in the Sun's core. It was through attempts to do exactly this that new and unexpected properties of the neutrino were discovered.

Originally only massless left-handed neutrinos were included in the standard model, since a right handed neutrino would be a completely noninteracting singlet state. Three generations of neutrinos were included, corresponding to the three charged leptons. However the measurements of solar neutrinos proved that they underwent lepton flavor oscillations, which required a nonzero mass. Neutrino oscillations have been studied using a variety of detection methods and using sources

ranging from fusion in the Sun, cosmic ray interactions in the atmosphere, to fission in nuclear reactors. Each source gives a different view of the oscillations and allows for complimentary constraints on the theoretical model. As the measurements get more precise and the model gets better constrained, it becomes possible to go further and look for small deviations from the expected oscillations as a sign of new physics.

1.1 Neutrino Oscillations

In matrix form the neutrino mass term can be written

$$\mathbf{L} = \begin{pmatrix} \overline{\nu}_{eR} & \overline{\nu}_{\mu R} & \overline{\nu}_{\tau R} \end{pmatrix} \begin{pmatrix} m_{ee} & m_{e\mu} & m_{e\tau} \\ m_{\mu e} & m_{\mu\mu} & m_{\mu\tau} \\ m_{\tau e} & m_{\tau\mu} & m_{\tau\tau} \end{pmatrix} \begin{pmatrix} \nu_{eL} \\ \nu_{\mu L} \\ \nu_{\tau L} \end{pmatrix} + h.c. \tag{1.1}$$

$$= \begin{pmatrix} \overline{\nu}_{eR} & \overline{\nu}_{\mu R} & \overline{\nu}_{\tau R} \end{pmatrix} U \begin{pmatrix} m_1 & 0 & 0 \\ 0 & m_2 & 0 \\ 0 & 0 & m_3 \end{pmatrix} U^{\dagger} \begin{pmatrix} \nu_{eL} \\ \nu_{\mu L} \\ \nu_{\tau L} \end{pmatrix} + h.c. \tag{1.2}$$

where U diagonalizes the mass matrix. U is called the Pontecorvo-Maki-Nakagava-Sakata or PMNS matrix, and transforms the neutrino lepton flavor eigenstates to mass eigenstates. We thus have that

$$|\hat{\nu}_\alpha\rangle = U^*_{\alpha i} |\hat{\nu}_i\rangle \tag{1.3}$$

for lepton flavor α and mass state i. The PMNS matrix can be decomposed into the three possible rotations between pairs of neutrino states and can thus be parameterized by three mixing angles θ_{12},θ_{23}, θ_{13}, and a single complex phase δ (in

the case of Majorana neutrinos there exist two additional phases). Broken up into these rotations it can be written as

$$\begin{aligned}
\mathbf{U} &= U_{\theta_{23}} U_{\theta_{13}} U_{\theta 12} && (1.4)\\
&= \begin{pmatrix} 1 & 0 & 0 \\ 0 & \cos\theta_{23} & \sin\theta_{23} \\ 0 & -\sin\theta_{23} & \cos\theta_{23} \end{pmatrix} \times \begin{pmatrix} \cos\theta_{13} & 0 & \sin\theta_{13} e^{-i\delta} \\ 0 & 1 & 0 \\ -\sin\theta_{13} e^{i\delta} & 0 & \cos\theta_{13} \end{pmatrix} && (1.5)\\
&\quad \times \begin{pmatrix} \cos\theta_{12} & \sin\theta_{12} & 0 \\ -\sin\theta_{12} & \cos\theta_{12} & 0 \\ 0 & 0 & 1 \end{pmatrix}. && (1.6)
\end{aligned}$$

In many situations, to first order the oscillations can be considered to be between only two flavors. In this two flavor case, we have just one mixing angle θ and

$$\mathbf{U} = \begin{pmatrix} \cos\theta & \sin\theta \\ -\sin\theta & \cos\theta \end{pmatrix} \tag{1.7}$$

We can find the time evolution of our neutrino states by solving the Schödinger equation,

$$\begin{aligned}
i\hbar \frac{\partial}{\partial t} \vec{\nu}(t) &= \mathbf{H}\vec{\nu}(t), && (1.8)\\
i\hbar c \frac{\partial}{\partial r} |\nu_i(r)\rangle &= (E + \frac{m_i^2}{2E}) |\nu_i(r)\rangle , && (1.9)
\end{aligned}$$

where in the second line we assume the neutrinos are highly relativistic. Since the

mass states are eigenstates of the Hamiltonian, we get a plane wave solution

$$|\nu_\alpha(r)\rangle = \sum_i U^*_{\alpha i} e^{-i(E+m_i^2/2E)r} \, |\hat{\nu}_i\rangle \, . \tag{1.10}$$

Then transforming back from mass to flavor eigenstates at a later point we can find the probability that we will have changed flavors. The probability that a neutrino that starts out in one flavor eigenstate is measured at a later point in that same flavor is called the survival probability, given by

$$P_{\nu_\alpha \to \nu_\beta}(r) = |\, \langle \hat{\nu}_\beta | \nu_\alpha(r) \rangle \,|^2 = \sum_{ij} U^*_{\alpha i} U_{\beta i} U_{\alpha j} U^*_{\beta i} e^{-i(\Delta m^2_{ij})/2E)r}. \tag{1.11}$$

For our two flavor case this simplifies to

$$P_{\nu_e \to \nu_e}(r) = 1 - \sin^2 2\theta \sin^2 \frac{\Delta m^2}{4E} r \tag{1.12}$$

Wolfenstein predicted that oscillations could be modified by the presence of matter [14]. Matter can cause the neutrino flavors to undergo different amounts of coherent scattering, causing an effect analogous to that of an index of refraction. In normal matter, neutrinos will be interacting with electrons, protons, and neutrons. All flavors of neutrinos can undergo neutral current interactions with electrons and nucleons. On the other hand, only the electron flavor neutrino can undergo charged-current coherent scattering with the electrons. These interactions produce additional potential terms in the Hamiltonian. Since the neutral-current potential is the same for all flavors, it adds a term proportional to the identity matrix, creating only a constant phase change that does not affect oscillations. The charged-current potential for the electron neutrino is very small, but Mikheyev

and Smirnov subsequently demonstrated that in matter of varying density—such as that of the Sun—when added to standard oscillations it can lead to resonant flavor conversion [15]. The change in oscillations due to this charged-current forward scattering in matter is called the MSW effect.

The effective potential from charged-current scattering on the electron neutrino is given by

$$V_{cc} = \sqrt{(}2)G_F n_e \tag{1.13}$$

where G_F is the Fermi constant and n_e is the number density of electrons in the medium the neutrinos are traveling through. Then in the flavor basis, we can write

$$i\hbar c\frac{\partial}{\partial r}\vec{\nu}_f = \frac{1}{2E}\left(U\mathbf{M}^2U^\dagger + \mathbf{A}\right)\vec{\nu}_f \tag{1.14}$$

where

$$\mathbf{M} = \begin{pmatrix} m1 & 0 & 0 \\ 0 & m2 & 0 \\ 0 & 0 & m3 \end{pmatrix} \tag{1.15}$$

is the vacuum Hamiltonian consisting of just the vacuum mass eigenstates, and

$$\mathbf{A} = 2E\mathbf{V} = 2E\begin{pmatrix} \sqrt{2}G_f n_e & 0 & 0 \\ 0 & 0 & 0 \\ 0 & 0 & 0 \end{pmatrix}. \tag{1.16}$$

If we are interested only in electron flavor survival probabilities, we can always define a new basis to rotate out any dependence on θ_{23}: $\vec{\nu}_z = U^\dagger_{\theta_{13}}U^\dagger_{\theta_{23}}\vec{\nu}_f$. Then

$$i\hbar c\frac{\partial}{\partial r}\vec{\nu}_z = \frac{1}{2E}\left(U_{\theta_{12}}\mathbf{M}^2U^\dagger_{\theta_{12}} + U^\dagger_{\theta_{13}}U^\dagger_{\theta_{23}}\mathbf{A}U_{\theta_{23}}U_{\theta_{13}}\right)\vec{\nu}_z \tag{1.17}$$

The Hamiltonian in this basis is now

$$\mathbf{H} = \frac{1}{2E}\begin{pmatrix} Ac_{13}^2 + \Delta m_{12}^2 s_{12}^2 & \Delta m_{12}^2 s_{12}c_{12} & Ac_{13}s_{13}e^{-i\delta} \\ \Delta m_{12}^2 s_{12}c_{12} & c_{12}^2\Delta m_{12}^2 & 0 \\ Ac_{13}s_{13}e^{i\delta} & 0 & As_{13}^2 + \Delta m_{31}^2 \end{pmatrix} \tag{1.18}$$

If $\theta_{13} \ll 1$ and A s small compared to Δm_{31}^2, then the oscillations effectively decouple into a single neutrino and two oscillating neutrinos. Then

$$\mathbf{H} \approx \frac{1}{4E}\begin{pmatrix} 2A\cos^2\theta_{13} + \Delta m_{12}^2(1-\cos 2\theta_{12}) & \Delta m_{12}^2 \sin 2\theta_{12} & 0 \\ \Delta m_{12}^2 \sin 2\theta_{12} & \Delta m_{12}^2(1+\cos 2\theta_{12}) & 0 \\ 0 & 0 & 2\Delta m_{31}^2 \end{pmatrix} \tag{1.19}$$

and one can diagonalize the Hamiltonian using the matrix

$$U_{m,2} = \begin{pmatrix} \cos\theta_m & \sin\theta_m & 0 \\ -\sin\theta_m & \cos\theta_m & 0 \\ 0 & 0 & 1 \end{pmatrix} \tag{1.20}$$

$$\sin 2\theta_m = \frac{\Delta m_{12}^2 \sin 2\theta_{12}}{\Delta M_m^2} \tag{1.21}$$

$$\cos 2\theta_m = \frac{\Delta m_{12}^2 \cos 2\theta_{12} - A\cos^2\theta_{13}}{\Delta M_m^2}. \tag{1.22}$$

The eigenvalues of the Hamiltonian are now

$$\Delta m_{m1}^2 = \frac{1}{4E}\left(\Delta m_{12}^2 + \cos^2\theta_{13}A - \Delta M_m^2\right) \tag{1.23}$$

$$\Delta m_{m2}^2 = \frac{1}{4E}\left(\Delta m_{12}^2 + \cos^2\theta_{13}A + \Delta M_m^2\right) \tag{1.24}$$

$$\Delta m_{m3}^2 = \frac{1}{2E}\Delta m_{13}^2 \tag{1.25}$$

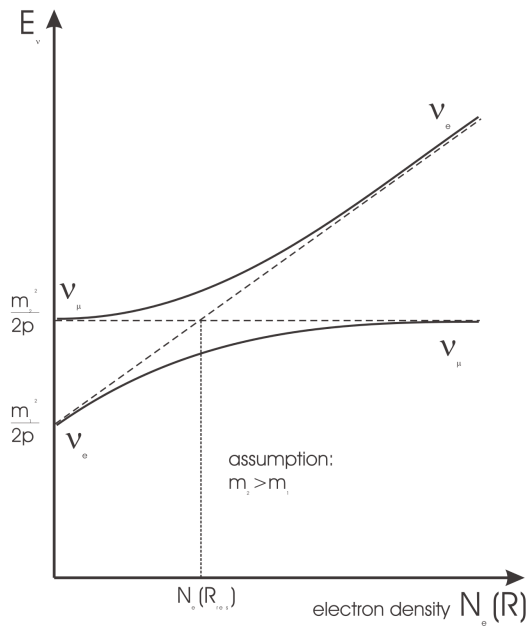

Figure 1.1: Mass eigenstates in matter as a function of electron density. Figure from [1].

where

$$\Delta M_m^2 = \sqrt{(\Delta m_{12}^2)^2 + A^2 \cos^4\theta_{13} - 2A\cos^2\theta_{13}\Delta m_{12}^2 \cos 2\theta_{12}}. \tag{1.26}$$

We can see then that

$$\tan 2\theta_m = \frac{\Delta m_{12}^2 \sin 2\theta_{12}}{\Delta m_{12}^2 \cos 2\theta_{12} - A\cos^2\theta_{13}} \tag{1.27}$$

so there is a resonance at $A\cos^2\theta_{13} = \Delta m^2 \cos 2\theta_{12}$, where our effective mixing angle can become maximal regardless of how small the vacuum mixing angle is. Figure 1.1 shows the eigenvalues as a function of the electron density. One can see that at the resonance Δm_{m1}^2 approaches Δm_{m2}^2.

Defining $\vec{\nu}_m = U^\dagger_{m,2}\vec{\nu}_z = U^\dagger_{m,2}U^\dagger_{\theta_{13}}U^\dagger_{\theta_{23}}\vec{\nu}_f \equiv U^\dagger_{m,3}\vec{\nu}_f$, we have

$$
\begin{aligned}
i\hbar c\frac{\partial}{\partial r}\vec{\nu}_m &= i\hbar c\frac{\partial}{\partial r}U^\dagger_{m,3}\vec{\nu}_f && (1.28)\\
&= U^\dagger_{m,3}\left(i\hbar c\frac{\partial}{\partial r}\vec{\nu}_f\right) + i\hbar c\left(\frac{\partial U^\dagger_{m,3}}{\partial r}\right)\vec{\nu}_f && (1.29)\\
&= \frac{1}{4E}\begin{pmatrix}\Delta m^2_{m1} & 0 & 0\\ 0 & \Delta m^2_{m2} & 0\\ 0 & 0 & \Delta m^2_{m3}\end{pmatrix}\vec{\nu}_m && (1.30)\\
&\quad + i\hbar c\left(\frac{\partial U^\dagger_{m,2}}{\partial r}\right)U^\dagger_{\theta_{13}}U^\dagger_{\theta_{23}}\left(U_{\theta_{23}}U_{\theta_{13}}U_{m,2}\vec{\nu}_m\right) && (1.31)\\
&= \frac{1}{4E}\begin{pmatrix}\Delta m^2_{m1} & -4Ei\hbar c\frac{\partial\theta_m}{\partial r} & 0\\ 4Ei\hbar c\frac{\partial\theta_m}{\partial r} & \Delta m^2_{m2} & 0\\ 0 & 0 & \Delta m^2_{m3}\end{pmatrix}\vec{\nu}_m. && (1.32)
\end{aligned}
$$

Then the two off diagonal terms act to create transitions between ν_{m1} and ν_{m2}. If these terms are always small, then the evolution is 'adiabatic', and the probability of transitions is negligible. We can quantify this condition by comparing the rate of change of the mixing angle with the oscillation length in matter, $\lambda_m = 4\pi E\hbar c/\Delta M^2_m$:

$$\frac{1}{\lambda_m \partial\theta_m/\partial r} \equiv \gamma \gg 1 \qquad (1.33)$$

When this condition holds, the matter states evolve independently and the only effect of the propagation is a phase:

$$\frac{\partial}{\partial r}\left|\nu_{i,m}(r)\right\rangle \approx \frac{\Delta m^2_{mi}}{4Ei\hbar c}\left|\nu_{i,m}(r)\right\rangle \qquad (1.34)$$

where $|\hat{\nu}_{i,m}(r)\rangle$ is the ith eigenstate of the matter Hamiltonian at position r, so

$$\langle\hat{\nu}_{i,m}(r)|\nu(r)\rangle = \exp\left(\frac{-i}{4E\hbar c}\int_{r_0}^{r}\Delta m^2_{mi}(r')dr'\right)\langle\hat{\nu}_{i,m}(r_0)|\nu(r_0)\rangle\,. \tag{1.35}$$

Then if the neutrino is created in an electron flavor state,

$$\vec{\nu}_m(r_0) = U^{\dagger}_{m,3}\begin{pmatrix}1\\0\\0\end{pmatrix} \tag{1.36}$$

$$= \begin{pmatrix}\cos\theta_{13}\cos\theta_m(r_0)\\ \cos\theta_{13}\sin\theta_m(r_0)\\ \sin\theta_{13}e^{-i\delta}\end{pmatrix}, \tag{1.37}$$

and using that

$$\langle\hat{\nu}_e\,|\,\nu(r)\rangle = \sum_i \langle\hat{\nu}_e\,|\,\hat{\nu}_{i,m}(r)\rangle\,\langle\hat{\nu}_{i,m}(r)\,|\,\nu(r)\rangle \tag{1.38}$$

$$= \left[U_{m,3}\vec{\nu}_m(r)\right]_e \tag{1.39}$$

$$= \cos\theta_{13}\cos\theta_m(r)\,\langle\hat{\nu}_{1,m}(r)\,|\,\nu(r)\rangle \tag{1.40}$$

$$+ \cos\theta_{13}\sin\theta_m(r)\,\langle\hat{\nu}_2(r,m)\,|\,\nu(r)\rangle + \sin\theta_{13}e^{i\delta}\,\langle\hat{\nu}_{3,m}(r)\,|\,\nu(r)\rangle \tag{1.41}$$

we get

$$P_{\nu_e\to\nu_e}(r) = |\langle\hat{\nu}_e \,|\, \nu_e(r)\rangle|^2 = |\sum_i \langle\hat{\nu}_e \,|\, \hat{\nu}_{i,m}(r)\rangle \langle\hat{\nu}_{i,m}(r) \,|\, \nu_e(r)\rangle|^2 \tag{1.42}$$

$$= |c_{13}^2 c_m(r)c_m(r_0) + c_{13}^2 s_m(r)s_m(r_0) e^{\frac{-i}{4E\hbar c}\int_{r_0}^{r}\Delta M_m^2(r')dr'} \tag{1.43}$$

$$+ s_{13}^2 e^{\frac{-i}{4E\hbar c}\int_{r_0}^{r}\Delta m_{m3}^2(r')dr'}|^2 \tag{1.44}$$

$$= s_{13}^4 + c_{13}^4\left[c_m^2(r)c_m^2(r_0) + s_m^2(r)s_m^2(r_0) + 2s_m(r)c_m(r)s_m(r_0)c_m(r_0)\cos\phi_1\right]$$

$$+ 2s_{13}^2 c_{13}^2 c_m(r)c_m(r_0)\cos\phi_2 + 2s_{13}^2 c_{13}^2 s_m(r)s_m(r_0)\cos(\phi_2-\phi_1) \tag{1.45}$$

where $\phi_{1,2}$ are the integrated phase factors. If we assume that the phase oscillations are averaged out, then the cosine of these phases goes to zero and we get

$$P_{\nu_e\to\nu_e}(r) \approx \sum_i |\langle\hat{\nu}_e \,|\, \hat{\nu}_{i,m}(r)\rangle \langle\hat{\nu}_{i,m}(r_0) \,|\, \hat{\nu}_e\rangle|^2 \tag{1.46}$$

$$= \sum_i P_{ie}(r)P_{ei}(r_0) \tag{1.47}$$

$$= s_{13}^4 + c_{13}^4\left[\frac{1}{2} + \frac{1}{2}\cos 2\theta_m(r)\cos 2\theta_m(r_0)\right] \tag{1.48}$$

$$= s_{13}^4 + c_{13}^4 P^{2\nu}_{\nu_e\to\nu_e}|_{A\to Ac_{13}^2} \tag{1.49}$$

To correct for any non-adiabatic region of propagation, consider in the two flavor system the probability P_j, called the 'jump probability', to change from one mass eigenstate to the other at the resonance point of maximum non-adiabaticity, r_{res}.

Then

$$\left\langle \hat{\nu}'_{1,m}(r) \,\middle|\, \nu(r) \right\rangle = \left[\langle \hat{\nu}_{1,m}(r_{res}) \,|\, \nu(r_{res}) \rangle \, (1 - P_j) + \langle \hat{\nu}_{2,m}(r_{res}) \,|\, \nu(r_{res}) \rangle \, (P_j) \right] \quad (1.50)$$

$$x \exp\left(\frac{-i}{4E\hbar c} \int_{r_{res}}^{r} \Delta m^2_{m1}(r') dr' \right) \quad (1.51)$$

$$\left\langle \hat{\nu}'_{2,m}(r) \,\middle|\, \nu(r) \right\rangle = \left[\langle \hat{\nu}_{2,m}(r_{res}) \,|\, \nu(r_{res}) \rangle \, (1 - P_j) + \langle \hat{\nu}_{1,m}(r_{res}) \,|\, \nu(r_{res}) \rangle \, (P_j) \right] \quad (1.52)$$

$$\exp\left(\frac{-i}{4E\hbar c} \int_{r_{res}}^{r} \Delta m^2_{m2}(r') dr' \right) \quad (1.53)$$

and

$$P_{\nu_e \to \nu_e}(r) \approx s^4_{13} + c^4_{13} \left[\frac{1}{2} + \left(\frac{1}{2} - P_j \right) \cos 2\theta_m(r) \cos 2\theta_m(r_0) \right]. \quad (1.54)$$

The jump probability itself in general can only be found through numerical integration, but analytic forms can be found for particular density profiles. For example, if the density is exponential so that $A \propto \exp(-r/r_0)$,

$$P_j = \frac{\exp(-2\pi r_0 \frac{\Delta m^2}{2E} \sin^2 \theta_{12}) - \exp(-2\pi r_0 \frac{\Delta m^2}{2E})}{1 - \exp(-2\pi r_0 \frac{\Delta m^2}{2E})} \quad (1.55)$$

We also see that with these approximations our full three flavor survival probability in vacuum is given by

$$P_{\nu_e \to \nu_e}(r) \approx s^4_{13} + c^4_{13} \left[1 - \frac{1}{2} \sin^2 2\theta_{12} \right]. \quad (1.56)$$

1.2 Solar Neutrinos

Neutrinos are produced not only in beta decay, but also by nuclear fusion and fission reactions. The Sun, being powered by fusion, is the most powerful source

of neutrinos available. Since neutrinos only interact via the weak force, even those produced deep in the core of the Sun usually travel straight out without interacting. Therefore, neutrinos give us the ability to probe the regions of the Sun where fusion occurs. In addition, the Sun gives us the ability to study neutrinos that have traveled a large distance including through different matter densities.

1.2.1 Solar Model

The Sun is powered by two main series of fusion reactions that convert hydrogen into helium. The pp chain, shown in Figure 1.2, starts with hydrogen, while the CNO cycle uses carbon, nitrogen, and oxygen to drive the reaction. Neutrinos are created at various steps in these chain. Each step produces neutrinos with a different energy distribution. These distributions are shown in Figure 1.3, labeled by the parent particles in the interaction.

The standard solar model (SSM) is a model of the Sun based on simple assumptions about its evolution and constrained by its age, mass, radius, and luminosity. It predicts the Sun's current composition, fusion rates and locations, and thus neutrino production. Many variations of the solar model have been developed. In this thesis I will use models calculated with the updated nuclear fusion cross sections (SFII) [10].

Helioseismological measurements of sound speeds matched the predictions of the SSM well. However, updated calculations changed the predicted solar metallicity, and models using these new metallicities no longer agreed. It will hopefully be possible to determine the correct metallicity by measuring neutrino fluxes. The solar neutrino flux predictions for models using the newer low metallicity (SFII-GS98) and older high metallicity (SFII-AGSS09) calculations are given in Table

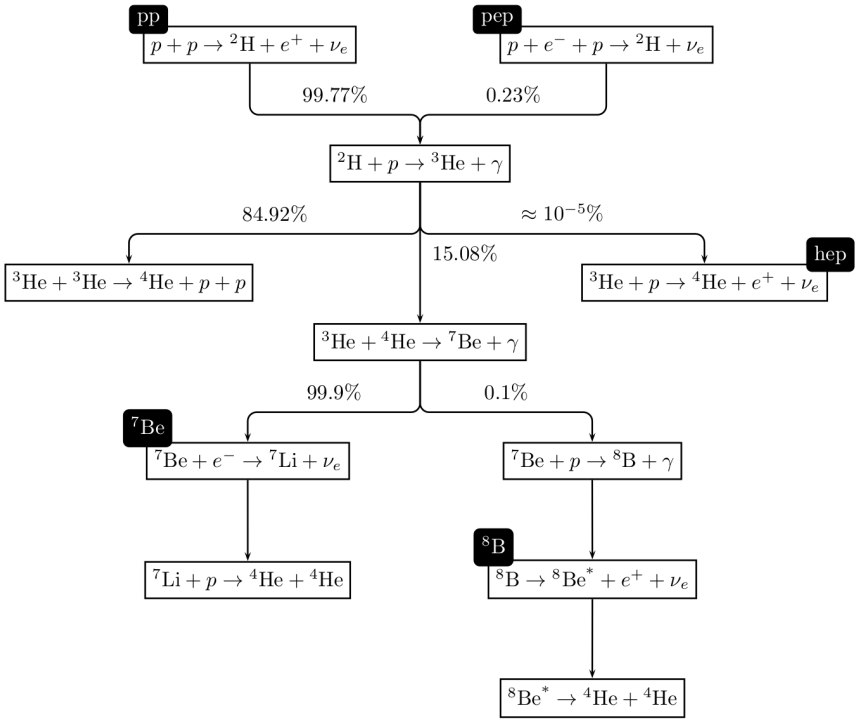

Figure 1.2: Nuclear reactions forming the solar pp chain. Figure from [2].

	SFII-GS98	SFII-AGSS09
pp (x10^{10})	$5.98(1 \pm 0.006)$	$6.03(1 \pm 0.006)$
pep (x10^{8})	$1.44(1 \pm 0.012)$	$1.47(1 \pm 0.012)$
hep (x10^{3})	$8.04(1 \pm 0.30)$	$8.31(1 \pm 0.30)$
^{7}Be (x10^{9})	$5.00(1 \pm 0.07)$	$4.56(1 \pm 0.07)$
^{8}B (x10^{6})	$5.58(1 \pm 0.14)$	$4.59(1 \pm 0.14)$
^{13}N (x10^{8})	$2.96(1 \pm 0.14)$	$2.17(1 \pm 0.14)$
^{15}O (x10^{8})	$2.23(1 \pm 0.15)$	$1.56(1 \pm 0.15)$
^{17}F (x10^{6})	$5.52(1 \pm 0.17)$	$3.40(1 \pm 0.16)$

Table 1.1: Neutrino flux predictions for solar models using SFII cross sections and either the GS98 or AGSS09 metallicities [10].

1.1. Current measurements of the ^{8}B flux are still compatible with both model.

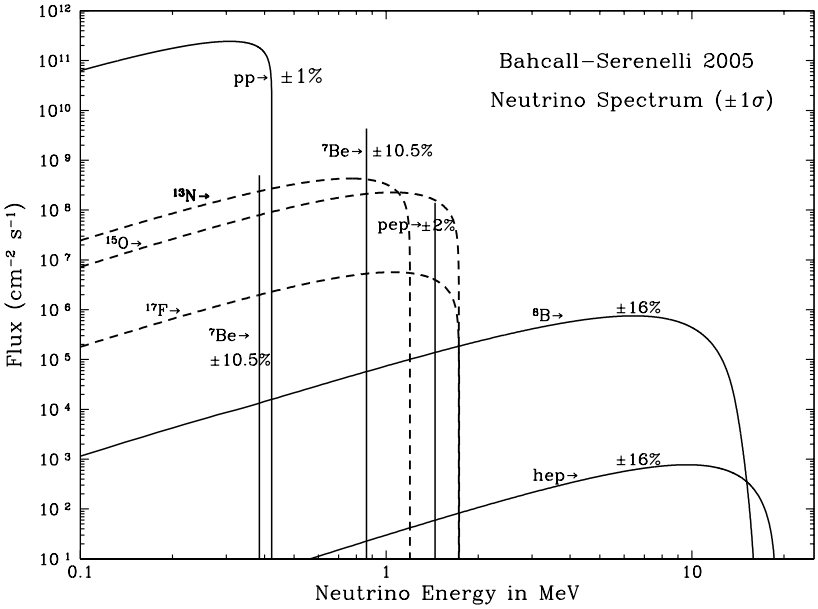

Figure 1.3: Solar neutrino energy spectrum [3].

1.2.2 Solar Neutrino Problem

The solar neutrino problem first became apparent in 1968 when Ray Davis made the first measurements of these neutrinos. He measured the event rate of these neutrinos using a chlorine detector in the Homestake mine [16]. By this time there were already predictions from solar models for the neutrino flux. The results of the Homestake experiment showed an event rate about one third of what was expected. At this point it was unclear whether the solar model or the experiment was to blame. In the following decades many experiments using various detection techniques were built in order to solve the solar neutrino problem. All agreed that the neutrino flux was lower than what the model predicted, although they did not agree on how much lower it was.

Among the many theorized solutions to the solar neutrino problem was neutrino

flavor oscillation. It was not immediately favored as the quark sector suggested that small mixing was the rule, and even maximal mixing could not give more than a factor of two suppression, not enough to explain the Homestake results. As described earlier, the MSW effect gave a means to greatly enhance the oscillation, making it a much more plausible answer.

The solar neutrino problem was finally solved by the Sudbury Neutrino Observatory (SNO) experiment. SNO was able to make independent measurements of the ν_e flux and the combined flux of all flavors, showing that the combined flux matched the SSM predictions while the ν_e alone did not.

1.2.3 MSW LMA oscillations

The combined results from solar and reactor neutrino experiments settled on a region of the mixing parameter space called the large mixing angle (LMA) solution, named after the nearly maximal θ_{12}. This solution came as a surprise due to the much smaller mixing seen in the quark sector.

For solar neutrinos, the LMA solution and the MSW effect combined with the high electron density of the Sun gives rise to three distinct oscillation regimes. As shown in Equation 1.16, the matter potential scales with energy. Thus the oscillation of low energy neutrinos is barely influenced at all by the MSW effect, and these neutrinos undergo standard vacuum oscillations. We see from Equation 1.12 that after averaging over the phase we get an energy independent survival probability,

$$P_{\nu_e \to \nu_e} = 1 - \frac{1}{2}\sin^2 2\theta_{12}. \tag{1.57}$$

At energies of several MeV or higher, we are in the matter dominated regime. Here the matter potential A is large enough that $\theta_m \to \frac{\pi}{2}$ and as shown in Equation

1.37 this means that the electron neutrino produced in our fusion reactions starts out as a $\nu_{2,m}$. If the electron density changes slowly enough that we cross the resonance adiabatically, or if we never cross the resonance, the neutrino will stay in this mass state even as this mass state changes with the varying matter density. Eventually we get a pure vacuum ν_2 state leaving the Sun. This is practically the only way to create a pure mass state neutrino. Thus in this regime the survival probability is just the projection of ν_2 onto ν_e,

$$P_{\nu_e \to \nu_e} = \cos^2 2\theta_{12}, \tag{1.58}$$

again independent of the neutrino energy.

These two regimes explain the differing results that the various solar experiments saw—which regime they saw was dependent on their detector's energy threshold. Between the two regimes is a transition region where the survival probability changes. This transition region is sensitive to new physics, but unfortunately is the most difficult to measure.

1.2.4 Day / Night Effect

The solar neutrino survival probability can also be affected by the time of day. At night the neutrinos have to travel through the earth to reach the detector, and so the earth's matter can impact the oscillations. In general, to take into account this effect for a survival probability calculation one would have to simultaneously integrate over all production locations in the Sun and all possible paths through the earth and calculate the propagation of each possible neutrino path the full distance to the detector. In practice, since neutrinos are produced throughout a large region

of the Sun greater in size than the typical oscillation lengths, they reach the Earth as an incoherent sum of mass eigenstates. This allows us to separate the integrals and calculate the survival probability from the Sun separate from the matter effect from the Earth.

We follow the procedure described in Ref. [17] for calculating the day-night effect. We know the daytime survival probability $P_{ie}(r)$ is just the projection of the ith mass state onto ν_e in vacuum (assuming that the change in the mass eigenstates due to the matter density at the detector is negligible), so

$$P^D_{\nu_e\to\nu_e} = \sum_i |P^\odot_{ei} P^{(0)}_{ie}|^2 \tag{1.59}$$

$$= s^4_{13} + c^4_{13}\left[\frac{1}{2} + \left(\frac{1}{2} - P_j\right)\cos 2\theta_m \cos 2\theta_{12}\right] \tag{1.60}$$

where $P^\odot$ is the probability in the sun and $P^{(0)}$ is the probability in vacuum. Then we can write the nighttime survival probability similarly as

$$P^N_{\nu_e\to\nu_e} = \sum_i |P^\odot_{ei} P^\oplus_{ie}|^2 \tag{1.61}$$

where now $P^\oplus$ is the probability that a neutrino arriving at the Earth in the ith mass eigenstate will be found in the detector as a ν_e after traveling through the Earth. Then

$$P^N - P^D = \sum_i P^\odot_{ei}(P^\oplus_{ie} - P^{(0)}_{ie}) \tag{1.62}$$

$$= (P^\odot_{e2} - P^\odot_{e1})(P^\oplus_{2e} - P^{(0)}_{2e}) \tag{1.63}$$

$$= - c^2_{13}\cos 2\theta_m(r_0)(P^\oplus_{2e} - P^{(0)}_{2e}) \tag{1.64}$$

where in the second line we have used unitarity and the fact that $P_{3e}^{\oplus} = P_{3e}^{(0)}$.

Suppose in our matter basis we define the evolution matrix $S(r, r_0)$ so that $\vec{\nu}_m(r) = S\vec{\nu}_m(r_0)$. Since the third eigenstate is decoupled, we can write

$$S(r, r_0) = \begin{pmatrix} \alpha(r, r_0) & \beta(r, r_0) & 0 \\ -\beta^*(r, r_0) & \alpha^*(r, r_0) & 0 \\ 0 & 0 & \exp\left(\frac{-i}{4E\hbar c}\int_{r_0}^{r} \Delta m^2_{m3}(r')dr'\right) \end{pmatrix} \tag{1.65}$$

with $|\alpha|^2 + |\beta|^2 = 1$. Then in terms of these variables, $P_{2e}^{\oplus} = c_{13}^2|s_{12}\alpha + c_{12}\beta|^2$, so

$$P_{2e}^{\oplus} - P_{2e}^{(0)} = c_{13}^2 \left[\cos 2\theta_{12}|\beta|^2 + \sin 2\theta_{12} Re(\alpha^*\beta)\right] \tag{1.66}$$

This factor can be estimated by considering the Earth's potential as a perturbation. We can get an analytic solution as shown by Akhmedov in [17] for a two slab approximation of the earth, where we assume the Earth is two regions of constant matter density—one for the higher density core, and one for the crust. To first order in the Earth potentials,

$$\begin{aligned} P_{2e}^{\oplus} - P_{2e}^{(0)} &= c_{13}^4 \sin^2 2\theta_{12} \frac{2E}{\Delta m^2_{21}} \left[V_1 \sin \frac{\Delta m^2_{21}}{4E}(2L_1 + L_2) \right. && (1.67) \\ &\quad \left. + (V_2 - V_1) \sin \frac{\Delta m^2_{21}}{4E} L_2 \right] \sin \frac{\Delta m^2_{21}}{4E}(2L_1 + L_2), && (1.68) \end{aligned}$$

where L_1 and L_2 are the distances traveled in the crust and core, respectively, and V_1 and V_2 are the corresponding matter potentials.

1.3 Reactor Neutrinos

Antineutrinos are produced in fission reactions, making nuclear power plants a neutrino source on a controllable baseline. The energy of the antineutrinos produced is the same scale as that of solar neutrinos (a few MeV). Without the large electron density of the Sun, the MSW effect is very small. For reactor experiments, the three flavor survival probability is approximately given by

$$\begin{aligned} P_{\nu_e \to \nu_e}(L/E) &= 1 - \sin^2 2\theta_{13} \sin^2 (1.267 \Delta m^2_{31} L/E) && (1.69) \\ &\quad - \cos^4 \theta_{13} \sin^2 2\theta_{12} \sin^2 (1.267 \Delta m^2_{21} L/E). && (1.70) \end{aligned}$$

At a distance of hundreds of kilometers, reactor antineutrinos are sensitive to the same mixing parameters as solar neutrinos. With the majority of the flux to any detector coming from a single location, the phase of the oscillation is not averaged over. This makes reactor experiments much more sensitive to the Δm^2 parameter which affects the oscillation wavelength. At much shorter baselines the first term becomes dominant, and so the scale of the oscillation peak gives a handle on θ_{13}

Reactor antineutrinos are detected via the inverse beta decay reaction,

$$p + \nu_e \to n + e^+. \tag{1.71}$$

Scintillation detectors are used so that the positron and the neutron capture can both be detected and their coincidence can be used to reject backgrounds.

1.4 Measurements of the Solar Mixing Parameters

1.4.1 Homestake

The solar neutrino flux was first measured using a 650 ton tank of C_2Cl_4 located in the Homestake Mine 1478 meters underground. It looked for the capture of neutrinos on chlorine through the inverse beta decay reaction

$$^{37}\mathrm{Cl} + \nu_e \rightarrow ^{37}\mathrm{Ar} + e^-. \tag{1.72}$$

The Homestake experiment did not make realtime measurements of neutrino events. Instead, periodically the Argon produced was extracted chemically and the amount of the ^{37}Ar isotope was measured. This allowed a measurement of the integrated solar neutrino event rate, and thus the neutrino flux. The inverse beta decay interaction has a threshold of 814 keV, which made this experiment sensitive to all solar neutrinos besides the low energy pp, and mostly sensitive to the high energy ^{8}B. The measured event rate was $2.56 \pm 0.16 \pm 0.16$ SNU, or 10^{-36} neutrino captures per target per second, while the rate predicted by a typical solar model was 9.3 ± 1.3 SNU [18]. This was the beginning of the solar neutrino problem.

1.4.2 Gallium Experiments

One problem with the Homestake experiment was that the relatively high energy threshold meant that the large majority of its signal came from ^{8}B. The ^{8}B flux is very sensitive to the solar temperature, making it possible to explain the results with a simple change to the SSM instead of neutrino oscillations. To resolve

this ambiguity, several similar experiments were conducted using gallium instead of chlorine. The interaction on gallium,

$$^{71}Ga + \nu_e \rightarrow ^{71} Ge + e- \tag{1.73}$$

has an energy threshold of only 233 keV. This makes gallium experiments sensitive to the pp neutrinos, which have a much higher flux and a very small theoretical uncertainty, since their flux is tied directly to the solar luminosity. The combined results of three experiments (SAGE, GALLEX, GNO) gave a rate of 66.1 ± 3.1 SNU, while a typical solar model predicted 128 ± 8 SNU [19]. This result matched neither the theory nor the results of the Homestake experiment.

1.4.3 Super-Kamiokande

Super-Kamiokande is a water Cherenkov detector located 1000 meters underground in Kamioka, Japan. It contains 50 kilotons of water instrumented by 11,146 photomultiplier tubes (PMTs). This experiment can see solar neutrinos through elastic scattering of electrons,

$$\nu + e^- \rightarrow \nu + e^-. \tag{1.74}$$

This interaction occurs for all three flavors of neutrinos, although with unequal cross sections. As in the MSW effect, electron neutrinos can interact through an exchange of either a W or a Z, while the other two flavors can only interact via Z exchange. The outgoing electron produces a cone of Cherenkov radiation pointing in the direction of its motion, which is detected by the PMTs, allowing a determination of the electron's energy and direction. The electron's direction is strongly correlated with the incident neutrino direction, allowing for a confirmation of the

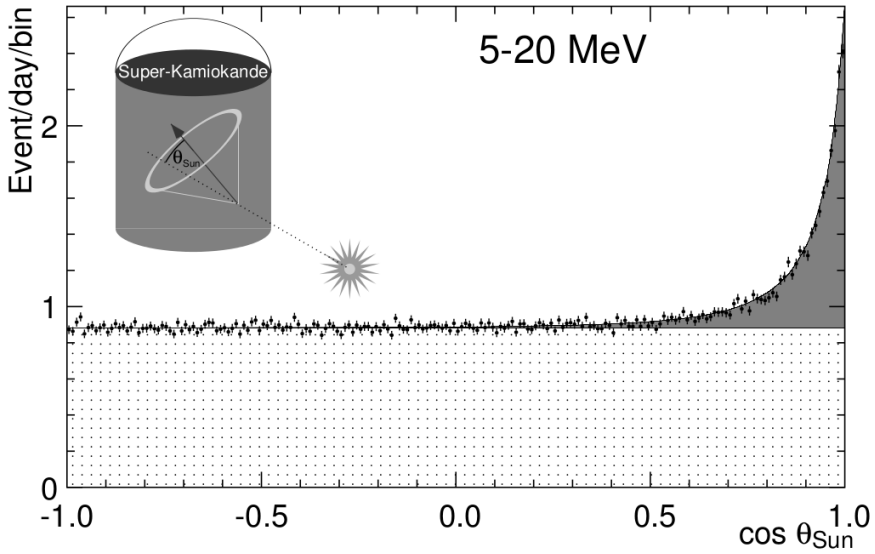

Figure 1.4: Angular distribution of solar neutrino candidate events in SK-I relative to the Sun [4].

source of neutrinos. The angular distribution of events is shown in Fig. 1.4. On the other hand, high background rates force water Cherenkov experiments like Super-Kamiokande to have a much higher energy threshold than the radiochemical experiments. This makes water Cherenkov experiments primarily sensitive to the high energy ^{8}B neutrinos.

The Super Kamiokande experiment ran in several phases. The first phase (SK-I) ran from 1996 to 2001 with an energy threshold of 5 MeV. An accident in 2001 destroyed 6777 PMTs, and the second phase (SK-II) ran from 2002 to 2005 with roughly half the original number of PMTs and a higher threshold of 7 MeV. After the second phase, the majority of the destroyed PMTs were replaced, and SK-III ran from 2005 to 2008, again with a lower energy threshold. Finally starting in 2008, the fourth phase (SK-IV) began, with upgraded data acquisition electronics. This allowed for triggerless readout of all events for 500μs following high energy

events in order to see 2.2 MeV neutron capture gammas.

The solar neutrino fluxes measured by the first three phases were $2.32 \pm 0.02 \pm 0.08$, $2.38 \pm 0.05^{+0.16}_{-0.15}$, and $2.32 \pm 0.04 \pm 0.05 \times 10^6 \mathrm{cm}^{-2}\mathrm{s}^{-1}$, again lower than that predicted by solar models [4, 20, 21].

1.4.4 Borexino

Unlike Super-Kamiokande, Borexino uses a liquid scintillator target in order to have a much lower energy threshold. Scintillation produces much more light than Cherenkov radiation, and liquid scintillator can be made very pure. On the other hand, the scintillation light does not preserve any directional information. The Borexino detector contains 300 tons of pseudocumene surrounded by 2212 8" PMTs. It also detects solar neutrinos through elastic scattering off electrons, but its lower energy threshold makes it sensitive to neutrinos from all the reactions in the fusion chains. Borexino has measured the ^{7}Be flux to be $(3.10 \pm 0.15) \times 10^9 \mathrm{cm}^{-2}\mathrm{s}^{-1}$, the pep flux as $(1.6 \pm 0.3) \times 10^8 \mathrm{cm}^{-2}\mathrm{s}^{-1}$, and set an upper limit on the CNO flux of $7.7 \times 10^8 \mathrm{cm}^{-2}\mathrm{s}^{-1}$ [22, 23].

1.4.5 KamLAND

KamLAND is a 1 kiloton liquid scintillator detector located next to the Super-Kamiokande experiment. This detector was designed to be sensitive to antineutrinos produced from the numerous nuclear reactors in Japan, with an average baseline of 180 km. Antineutrinos are detected via the inverse beta decay interaction

$$p + \overline{\nu}_e \rightarrow n + e^+. \tag{1.75}$$

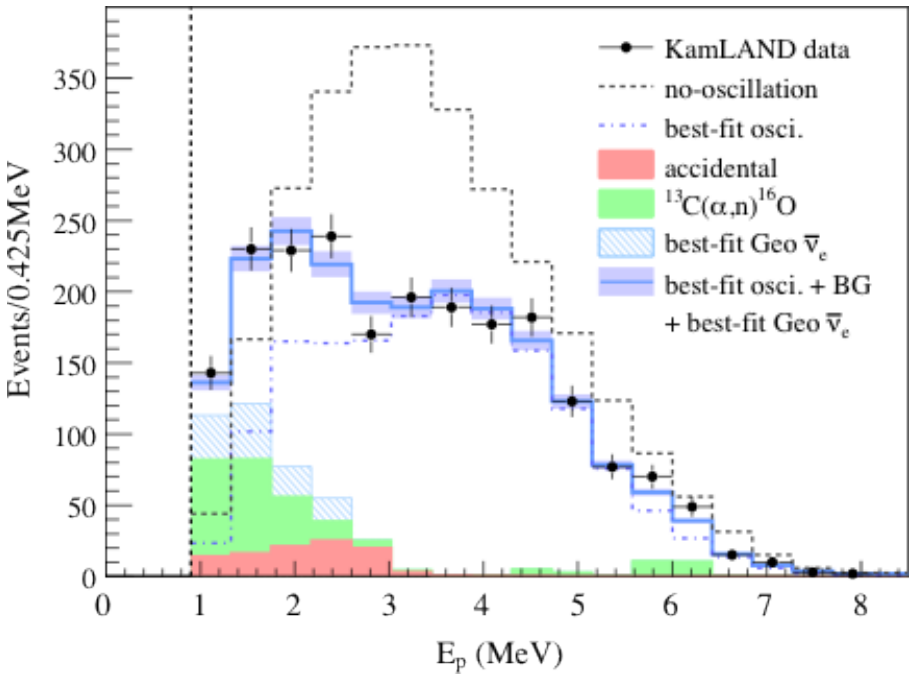

Figure 1.5: Prompt event energy distribution in KamLAND compared to no-oscillation and best fit oscillation predictions [5].

The positron annihilates, producing the prompt signal. The positron energy is highly correlated with the antineutrino energy, allowing for a precise determination of L/E. Afterwards, the neutron captures on hydrogen producing a delayed 2.2 MeV gamma signal. This coincidence allows for a high level of background rejection.

As shown in Equation 1.70, at this baseline KamLAND is sensitive to the solar mixing parameters θ_{12} and Δm^2_{12}, with a slight sensitivity to θ_{13}. Fig. 1.5 shows KamLAND's best fit energy spectrum, which has clear spectral distortion and gives them a good handle on the mass difference. For a three flavor analysis they found $\Delta m^2_{12} = 7.49^{+0.20}_{-0.20} \times 10^{-5}\text{eV}^2$, $\tan^2\theta_{12} = 0.436^{+0.102}_{-0.081}$ and $\sin^2\theta_{13} = 0.032^{+0.037}_{-0.037}$ [5].

1.4.6 SNO

The SNO experiment was designed to definitively measure the solar neutrino flux and solve the solar neutrino problem. It was a 1 kiloton water Cherenkov experiment, but was unique in that it had a heavy water target. This allowed it to detect solar neutrinos through three complimentary reactions:

$$\text{ES:} \quad \nu_x + e^- \rightarrow \nu_x + e^- \tag{1.76}$$

$$\text{CC:} \quad \nu_e + d \rightarrow p + p + e^- \tag{1.77}$$

$$\text{NC:} \quad \nu_x + d \rightarrow p + n + \nu_x. \tag{1.78}$$

As mentioned earlier, the elastic scattering interaction is mostly sensitive to electron neutrinos but has some contribution from the other flavors. On the other hand, the charged-current interaction on deuterium is only sensitive to electron neutrinos, and the neutral-current interaction is equally sensitive to all three flavors. This means that a measurement of the neutral-current event rate will be a measurement of the total solar neutrino flux independent of oscillations, and the ratio of charged-current to neutral-current event rates gives proof of oscillation.

From the neutral-current event rate SNO measured the ^{8}B flux to be $(5.140^{+0.160+0.132}_{-0.158-0.117}) \times 10^6 \text{cm}^{-2}\text{s}^{-1}$. A three flavor fit to the SNO results combined with all other solar experiments plus KamLAND found $\Delta m^2_{12} = (7.46^{+0.20}_{-0.19}) \times 10^{-5}\text{eV}^2$, $\tan^2\theta_{12} = 0.443^{+0.033}_{-0.026}$, and $\sin^2\theta_{13} = (2.5^{+1.8}_{-1.4}) \times 10^{-2}$.

1.4.7 Short Baseline Experiments

The combination of solar neutrino experiments and KamLAND gave strong constraints on both θ_{12} and Δm^2_{12}. On the other hand, these experiments only gave an

upper limit on θ_{13}. Several short baseline reactor neutrino experiments were built to look for a nonzero value of this angle.

These experiments sit at short baselines where the first term in Equation 1.70 is dominant, and so the scale of the oscillation peak gives a handle on θ_{13}. They then look for very small differences between the flux right at the reactor to that a short baseline away, using a ratio between measurements made at a near detector and a far detector. The detectors are designed to be identical so that systematic uncertainties cancel when taking this ratio. Like KamLAND, they use liquid scintillator to look for inverse beta decay interactions.

The Daya Bay experiment in China consists of three experimental halls with a total of six detectors. Two of the halls hold the near detectors at 470 m and 576 m from two different nuclear power stations, and the third is located at 1648 m. Each detector contains a 20 ton inner volume of Gadolinium-doped liquid scintillator surrounded by 192 PMTs. Daya Bay found θ_{13} to be nonzero with a significance of 7.7 sigma, and measured $\sin^2 2\theta_{13} = 0.089 \pm 0.010 \pm 0.005$ [24].

The RENO experiment consists of two identical detectors, one located at 294 m and one at 1393 m from the Yonggwang Nuclear Power Plant in Korea. Each detector contains 16 tons of Gd-doped liquid scintillator surrounded by 354 PMTs. It also saw a deficit in its far detector and measured $\sin^2 2\theta_{13} = 0.113 \pm 0.013 \pm 0.019$ with a rate only analysis [25].

Chapter 2

Nonstandard Models of Neutrino Interactions

[*This chapter reprinted from Phys. Rev. D 88, 053010 (2013), copyright 2013 by the American Physical Society.*]

With the addition of recent precision measurements of θ_{13} by short-baseline experiments [24,25], the model of neutrino mixing is nearly complete. In total, this description of neutrino flavor mixing adds seven new parameters to the standard model. Only two remain unmeasured: the sign of the mass difference between the first and third mass eigenstates, and the value of the CP-violating phase δ. The current knowledge of the parameters is expected to be enough to describe a large fraction of possible neutrino transformation measurements very accurately. Much of the trust in the model comes from the fact that it mirrors the quark mixing, which has been studied carefully for many decades. Yet until we test all of the predictions of the mixing model, we do not know whether it is in fact a complete

description of neutrinos.

It is difficult to make a broad precision measurement program with neutrino oscillations due to the difficulty in detecting neutrinos as well as the fact that the model makes few predictions other than oscillations themselves. In vacuum, experiments can measure oscillation behavior very precisely, but any measured deviation in the transformation probability from the prediction must first be interpreted as a change in the mixing parameters, rather than new physics. A search for new physics thus relies primarily on looking for deviations from the L/E behavior that mass-difference-driven oscillations must have. Such searches can be sensitive to interesting new physics scenarios such as transformation to sterile neutrinos [26–28], or neutrino decay [29, 30].

The situation is dramatically different once neutrino passage through matter is considered. The weakness of neutrino interactions allows coherent processes - including those from new interactions or more exotic physics - to affect flavor transformation in a measurable way. Indeed, even in Wolfenstein's [14] seminal paper, he considers primarily the effects of flavor-changing neutral currents (FCNC) as a driver of neutrino flavor transformation in matter. Mikheyev and Smirnov [15] subsequently demonstrated that 'standard' oscillations in matter of varying density—such as that of the Sun—can lead to resonant flavor conversion. This implied that even tiny effects may be observable. MSW flavor transformation is an explicit prediction of the Standard Model and the model of neutrino oscillations. It states that given measured mixing parameters, which can be provided independently from solar neutrino measurements, and density profiles of the Sun and the Earth, the phenomenology of the MSW effect is exactly specified. Yet any interaction with matter that distinguishes neutrino states, even interactions weaker than the weak

interaction itself, can spoil the agreement with MSW predictions. That precision measurements using solar neutrinos are possible has been demonstrated very clearly by the observed hints of non-zero θ_{13} that came out of comparing solar neutrino measurements with those of the KamLAND reactor experiment [31]. The precision of this comparison rivaled that of the measurements by the dedicated Double CHOOZ [32] experiment.

While many future experiments [33–35] are planned to terrestrially observe matter-enhanced oscillations, and thus look for non-standard effects, to date the only large observed matter enhancement is for solar neutrinos. Fig. 2.1 shows the predictions of the survival probability for solar neutrinos, spanning the energy regime from the lowest-energy *pp* neutrinos to the highest-energy *hep* neutrinos. It shows both the prediction for the mixing parameters as measured by KamLAND alone [5] and one with all solar data included, using the best-fit large-mixing angle (LMA) parameters. As has been pointed out by many authors [36, 37], the predicted survival probability has three regimes. At high energies the effects of matter are pronounced, and thus the suppression of ν_es exceeds the average value of $1-1/2\sin^2 2\theta$ expected for just vacuum oscillations. At low energies vacuum effects are dominant, thus the survival probability matches the vacuum value. Between about 1 MeV and 4 MeV there is a transition region between the low- and high-energy regimes, where the survival probability decreases from the vacuum average to the matter-dominated value. It is in this transition region where non-standard effects would be most pronounced, as they interfere with the expectations from standard MSW transformation. As Nature would have it, probing this region is particularly difficult. Water Cherenkov experiments have poor energy resolution and hence difficulty getting below thresholds of 4 MeV, whereas scintillation exper-

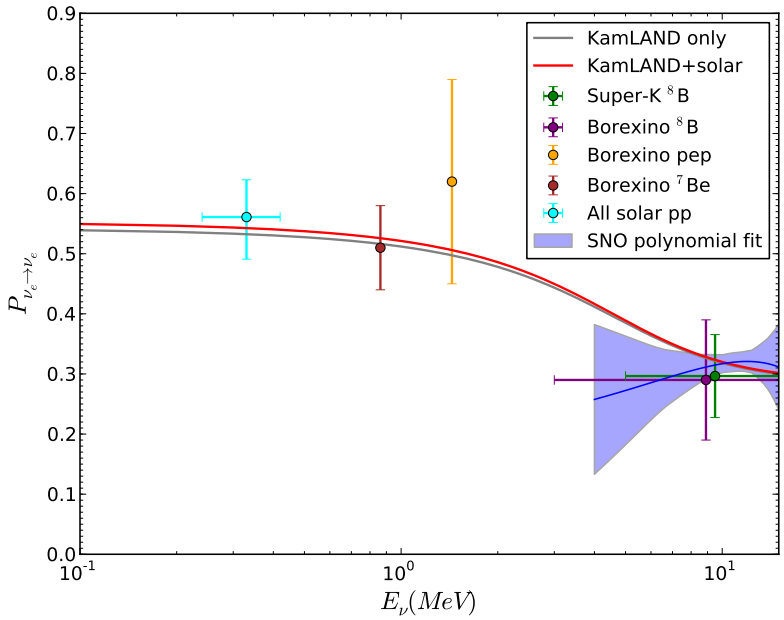

Figure 2.1: MSW prediction for $P_{\nu_e \to \nu_e}$ for the three-flavor KamLAND best fit parameters and the combined solar best fit parameters. Note that the *pep* uncertainties are not Gaussian and the value is only $\sim 2\sigma$ from zero. Data points for Borexino and S-K ^{8}B represent the survival probability averaged over the measured energy range.

iments are typically either small or restricted to observing neutrinos through the elastic scattering of electrons, whose differential cross section is maximally broad.

Many authors [38–46] have put forth non-standard models and performed fits to the solar neutrino data set. Prior to the recent θ_{13} measurements, Palazzo [41] showed that non-standard interaction models provide a somewhat better fit to the solar neutrino data than does the standard MSW flavor transformation. The reason non-standard effects are preferred is the frustratingly persistent flatness of the high-energy solar ν_e survival probability, as measured by experiments observing ^{8}B neutrinos. Figs. 2.2 and 2.3 show the ^{8}B measurements from the Sudbury Neutrino Observatory (SNO), Borexino, and the Super-Kamiokande (S-K) experiments, with

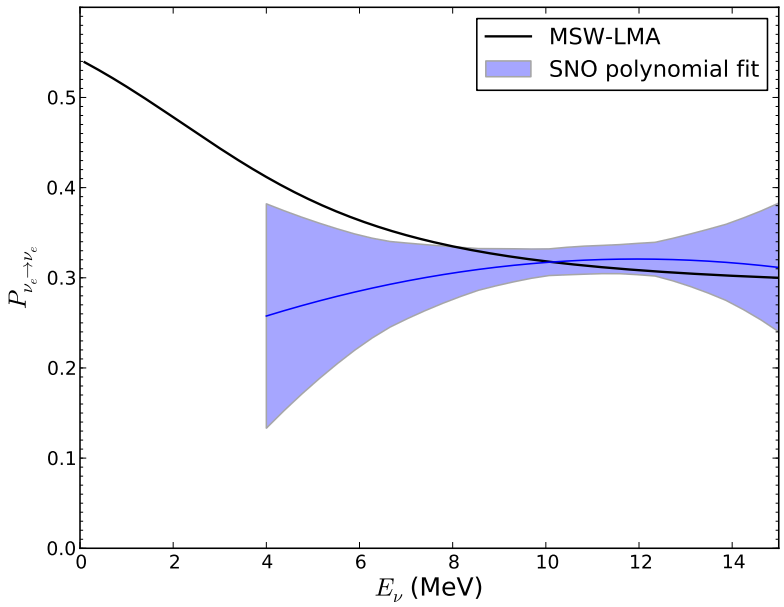

Figure 2.2: KamLAND's combined best fit MSW-LMA prediction versus SNO extracted ^8B survival probability. The band represents the RMS spread at any given energy, i.e., not including energy correlations.

the expectation from large-mixing angle MSW effect superimposed. We see that while the data is consistent with MSW, no experiment sees clear evidence of the expected rise due to the matter / vacuum transition region. The three experiments appear to differ in their comparison to the model: SNO fits the prediction best at high energies rather than low, while S-K is the reverse. In other words, SNO's data appears to be flatter than predicted by MSW due to the fact that at low energies the survival probability fit is lower than the MSW curve, while S-K's data appears to be flatter because the high energy event rate is higher than predicted by MSW, but in all cases the end result is that the data appears flatter than expected. The Borexino experiment's uncertainties are clearly too large to make a meaningful comparison with their data alone.

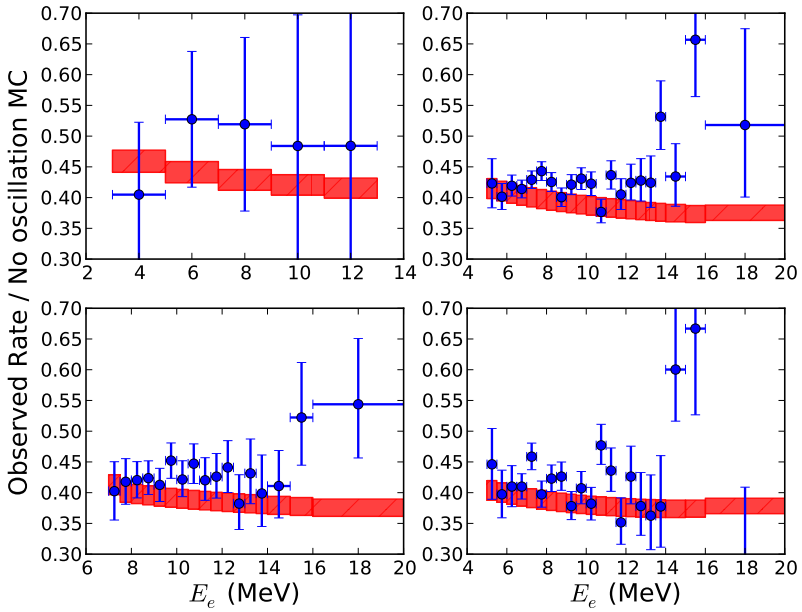

Figure 2.3: Top left: Borexino, top right: S-K I, bottom left: S-K II, bottom right: S-K III. Event rates binned in measured electron energy with each bin scaled by Monte Carlo predictions assuming GS98SF2 fluxes, versus the same ratio for the expected rates assuming KamLAND's combined best fit LMA parameters and SNO's NC ^8B flux prediction. Error bars on the data points represent statistical and energy uncorrelated systematic uncertainties combined in quadrature. Detector response parameters have been fixed at their reported value; the width of the band does not include the effect of correlated systematic uncertainties. The best fit oscillation prediction band width represents the uncertainty on the ^{8}B flux. Note that I have suppressed the zero for these figures to better illustrate the comparison between data and model.

In this analysis I performed fits to the global solar neutrino data sets, including constraints on θ_{13} and the most recent measurements by the SNO collaboration [47]. My interest is in reasonably generic non-standard models, especially those with the ability to flatten the ^{8}B survival probability. For this analysis I have chosen three types of models: non standard contributions to forward scattering as described in [38], mass varying neutrinos [42], and long-range leptonic forces [46].

2.1 Non-Standard Forward Scattering

As suggested by Friedland in [38], one can generically parameterize these non-standard contributions with an effective low-energy four-fermion operator

$$\mathcal{L} = -2\sqrt{2}G_F(\bar{\nu}_\alpha\gamma_\rho\nu_\beta)(\epsilon^{f\tilde{f}P}_{\alpha\beta}\bar{f}_P\gamma^\rho\tilde{f}_P) + h.c., \tag{2.1}$$

where P=L,R, and $\epsilon^{f\tilde{f}P}_{\alpha\beta}$ denotes the strength of the non-standard interaction between neutrinos of flavors α and β and the P handed components of fermions f and $\tilde{f}$. Only vector components where $f = \tilde{f}$ of the non-standard interaction can affect the neutrino propagation, so we let $\epsilon^f_{\alpha\beta} \equiv \epsilon^{ffL}_{\alpha\beta} + \epsilon^{ffR}_{\alpha\beta}$. One can define $\epsilon_{\alpha\beta} = \sum_{f=u,d,e}\epsilon^f_{\alpha\beta}n_f/n_e$. Then the matter part of the generic three flavor NSI oscillation Hamiltonian can be written as

$$\mathcal{H} = \sqrt{2}G_F n_e \begin{pmatrix} 1+\epsilon_{ee} & \epsilon^*_{e\mu} & \epsilon^*_{e\tau} \\ \epsilon_{e\mu} & \epsilon_{\mu\mu} & \epsilon^*_{\mu\tau} \\ \epsilon_{e\tau} & \epsilon_{\mu\tau} & \epsilon_{\tau\tau} \end{pmatrix}. \tag{2.2}$$

As in our standard survival probability calculation, we assume the third flavor decouples and that the non-standard contribution to the potential is much smaller

than $\Delta m^2_{31}/E$. Then the effective two flavor Hamiltonian is

$$\begin{aligned}\mathbf{H}^{2\nu} = & \frac{\Delta m^2_{21}}{4E}\begin{pmatrix} -\cos 2\theta_{12} & \sin 2\theta_{12} \\ \sin 2\theta_{12} & \cos 2\theta_{12}\end{pmatrix} \\ & +\sqrt{2}G_f n_e \begin{pmatrix} \cos^2\theta_{13} & \epsilon_1^* \\ \epsilon_1 & \epsilon_2\end{pmatrix} \end{aligned} \tag{2.3}$$

where

$$\begin{aligned}\epsilon_1 &= c_{13}(\epsilon_{e\mu}c_{23} - \epsilon_{e\tau}s_{23}) \\ &\quad -s_{13}[\epsilon_{\mu\tau}s^2_{23} - \epsilon^*_{\mu\tau}c^2_{23} + (\epsilon_{\mu\mu} - \epsilon_{\tau\tau})c_{23}s_{23}], \end{aligned} \tag{2.4}$$

$$\begin{aligned}\epsilon_2 &= \epsilon_{\mu\mu}c^2_{23} - (\epsilon_{\mu\tau} + \epsilon^*_{\mu\tau})s_{23}c_{23} + \epsilon_{\tau\tau}s^2_{23} \\ &\quad +c^2_{13}\epsilon_{ee} + s_{13}[(e^{-i\delta}\epsilon_{e\mu} + e^{i\delta}\epsilon^*_{e\mu})s_{23}c_{13} \\ &\quad +(e^{-i\delta}\epsilon_{e\tau} + e^{i\delta}\epsilon^*_{e\tau})c_{13}c_{23}] \\ &\quad -s^2_{13}[\epsilon_{\mu\mu}s^2_{23} + (\epsilon_{\mu\tau} + \epsilon^*_{\mu\tau})s_{23}c_{23} + \epsilon_{\tau\tau}c^2_{23}]. \end{aligned} \tag{2.5}$$

I follow the example of Ref. [38] to calculate a modified mixing angle in matter as well as a jump probability to get a predicted survival probability. Due to the small density of the Earth compared to the Sun, no significant non-standard effect on terrestrial experiments is expected [41], and so any constraints on mixing parameters from reactor experiments remain the same.

This model adds up to three new parameters to the survival probability: $Re[\epsilon_1]$, $Im[\epsilon_1]$, and ϵ_2. Fig. 2.4 shows the effect of each one on the shape of the survival probability.

Current constraints on the strength of these vertices come from accelerator ex-

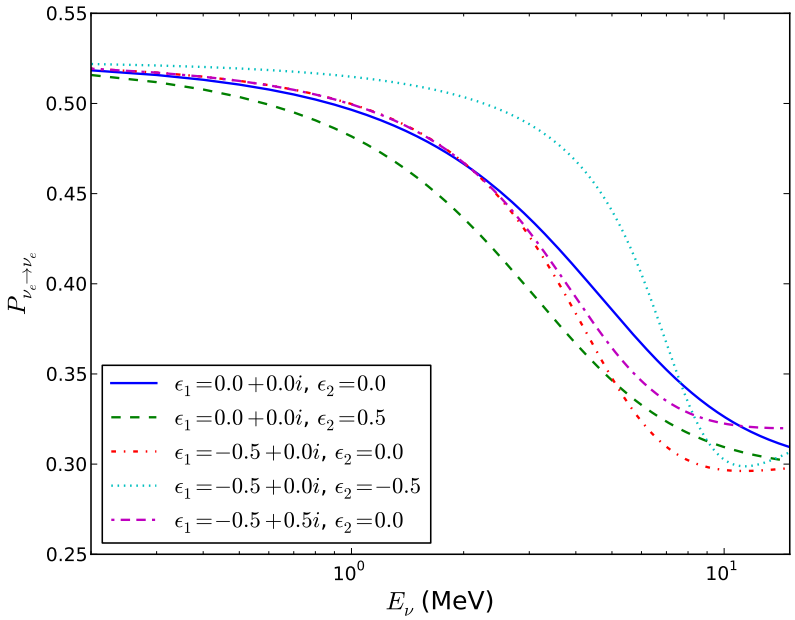

Figure 2.4: Survival probabilities for a range of the NSI parameters ϵ_1, ϵ_2

periments like NuTeV and CHARM, atmospheric neutrino and charged lepton experiments like LEP, and by limits on the charged lepton operators. The parameters $\epsilon_{e\mu}, \epsilon_{\mu\mu}$ are well constrained ($\lesssim 10^{-2} - 10^{-3}$), and analysis of atmospheric neutrino data has shown $\epsilon_{\mu\tau} \lesssim 10^{-2}$ [45]. However there remain vertices that can still be quite large, for example, $|\epsilon^f_{e\tau,ee}| \lesssim 0.5$, or $|\epsilon^{dR}_{tt}| < 6$.

By letting all the muon vertices go to zero, we get

$$\epsilon_1 = -c_{13}s_{23}\epsilon_{e\tau} + s_{13}c_{23}s_{23}\epsilon_{\tau\tau}, \tag{2.6}$$

$$\epsilon_2 = s^2_{23}\epsilon_{\tau\tau} + c^2_{13}\epsilon_{ee} + s_{13}c_{13}c_{23}(e^{-i\delta}\epsilon_{e\tau} + e^{i\delta}\epsilon^*_{e\tau}) - s^2_{13}c^2_{23}\epsilon_{\tau\tau}. \tag{2.7}$$

The effect of these non-standard parameters on the survival probability as a function

of energy is shown in Fig. 2.4.

Prior to the recent θ_{13} measurements, in Ref. [41] a two flavor fit to solar neutrino data with the addition of flavor changing couplings to the down quark was performed. It was found that the best fit to both the solar data alone as well as the solar data combined with the reactor results from KamLAND occurred at a nonzero value of the nonstandard coupling. A value of $\epsilon = 0$ was disfavored at 1.9 σ.

2.2 Mass Varying Neutrinos

2.2.1 Neutrino Density Effects

In Ref. [42] it was proposed that neutrinos are coupled to dark energy in a way that their energy densities track each other. This model was made to resolve the coincidence of the energy density of dark energy and matter being similar today even though their ratio scales as $\sim 1/(\text{scale factor})^3$. In general this implies so-called 'Mass Varying Neutrinos' (MaVaNs), where the neutrino mass becomes a function of the neutrino density. If the neutrino couples to a scalar field, then following Ref. [43] at low energy we can write an effective Lagrangian in a model independent way

$$\begin{aligned}\mathbf{L}(m_i) = \sum_i \Big[& m_i \overline{\nu}_i^c \nu_i + m_i n_i^{C\nu B} \\ & + \int \frac{d^3k}{(2\pi)^3} \sqrt{k^2 + m_i^2} f_i(k) + V_0(m_i) \Big] . \end{aligned} \tag{2.8}$$

Here $n_i^{C\nu B} = 112$ cm^{-3} is the number density of non-relativistic relic neutrinos of each type and $f_i(k)$ is the occupation number for momentum k of non-relic neutrinos

in our medium (in this case a function of the neutrino production profile in the Sun). Then we can parameterize the scalar potential $V_0(m_i) \propto f(m_i/\mu)$ where μ is some arbitrary mass scale. The observed equation of state for dark energy implies that the potential must be flat, while minimizing the total potential implies it must decrease with increasing neutrino mass. Various forms for the scalar potential have been suggested, for example, $\log(\mu/m_i)$ or $(m_i/\mu)^{-\alpha}$. For either of these forms, minimizing the effective potential implies that

$$m_i(r) \approx m_{i,0} - |U_{e,i}|^2 A(r) m_{i,0}^2, \tag{2.9}$$

where $m_{i,0}$ is the vacuum mass of ν_i and

$$A(r) = \frac{1}{n^{C\nu B}} \int \frac{d^3k}{(2\pi)^3} \frac{1}{\sqrt{k^2 + m_i^2}} f_e(k, r). \tag{2.10}$$

Here we have used the fact that $f_i(k, r) = |U_{e,i}|^2 f_e(k, r)$ [43].

Then before MSW matter effects, we have

$$\begin{aligned} \Delta m^2_{21,eff}(r) &= m_2^2(r) - m_1^2(r) \\ &\approx \Delta m^2_{21,0} \left[1 - 3 s^2_{12} c^2_{13} A(r) m_{1,0}\right] \\ &\quad + 2 c^2_{13} A(r) \left[c^2_{12} - s^2_{12}\right] m^3_{1,0}, \end{aligned} \tag{2.11}$$

and we can solve for the survival probability by substituting this effective mass squared difference into the survival probability calculations for normal MSW oscillations. Then given a particular distribution of neutrinos, our effective mass squared difference becomes a function of the vacuum neutrino mass $m_{1,0}$. The survival probability for various values of the vacuum mass is shown in Fig. 2.5. Again the effect

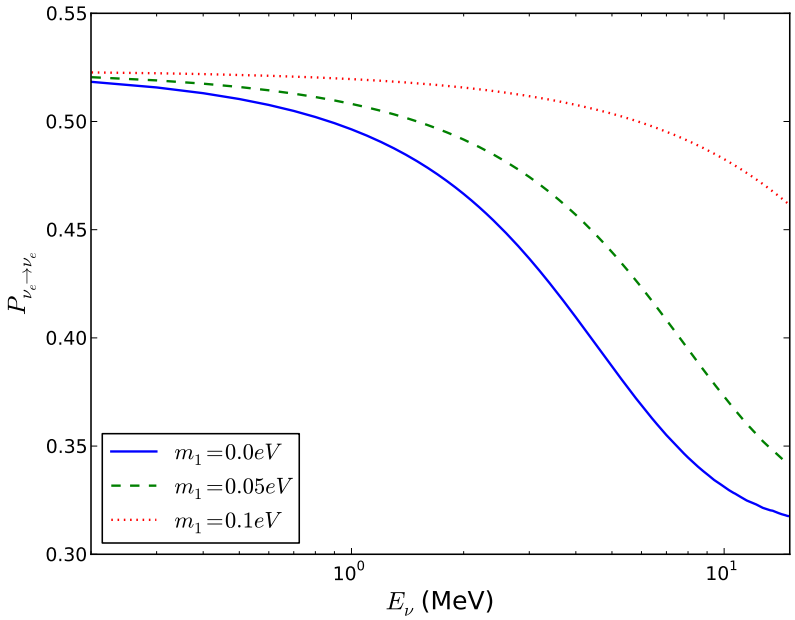

Figure 2.5: Survival probabilities for the neutrino density dependent MaVaN model at several values of $m_{1,0}$

on terrestrial experiments due to geoneutrinos and reactor antineutrinos is expected to be negligible [43], and will not modify the constraints on mixing parameters from KamLAND, RENO, or Daya Bay.

A previous two-flavor oscillation analysis of solar data and KamLAND found a 3σ upper limit of $m_{1,0} < 0.009$ eV, with no improvement in the fit to the data over MSW-LMA [43].

2.2.2 Fermion Density Effects

In addition to the effect described above, it is possible for this scalar field to couple to visible matter. Ref. [44] parameterizes this model by adding a light scalar field ϕ of mass m_ϕ, which is weakly coupled to neutrinos and fermions;

$$\begin{aligned}
\mathbf{L} &= \sum_i \overline{\nu}_i(i\partial\!\!\!/ - m_{i,0})\nu_i + \sum_f \overline{f}(i\partial\!\!\!/ - m_{f,0})f \\
&\quad + \frac{1}{2}\phi(\partial^2 - m_\phi^2)\phi + \sum_{ij} \lambda^{ij}\overline{\nu}_i\nu_j\phi \\
&\quad + \sum_f \lambda^f \overline{f} f \phi. \qquad (2.12)
\end{aligned}$$

Then the elements of the mass matrix become

$$\begin{aligned}
m_{ij}(r) &= m_{i,0}\delta_{ij} - M_{ij}(r), \\
M_{ij}(r) &= \frac{\lambda^{ij}}{m_\phi^2}\left(\sum_f \lambda^f n_f(r)\right. \\
&\quad \left. + \sum_i \lambda^{ii} \int \frac{d^3k}{(2\pi)^3} \frac{M_{ii}}{\sqrt{k^2 + M_{ii}^2}} f_i(k,r)\right). \qquad (2.13)
\end{aligned}$$

We will only consider the added effect of the coupling to fermionic matter by letting $m_{1,0} \sim 0$, such that

$$M_{ij}(r) = \frac{\lambda^{ij}}{m_\phi^2}\sum_f \lambda^f n_f(r). \qquad (2.14)$$

Assuming that effect of this coupling is small compared to $m_{3,0}$, we can decouple the third neutrino state. Then diagonalizing the 1-2 sector for the mass eigenstates in matter gives

$$\cos 2\theta_{12}^m(r_0) = \frac{2\Delta m_{21}^2(r)\cos 2\theta_{12} - A(r)}{\Delta m_m^2} \qquad (2.15)$$

where

$$\begin{aligned}\Delta m_m^2 &= \big((\Delta m_{21}^2(r))^2 + 4M_3^4(r) \\ &\quad -2A(r)\Delta m_{21}^2(r)\cos 2\theta_{12} + A^2\big)^{\frac{1}{2}}, \qquad (2.16)\\ \Delta m_{21}^2(r) &= (m_{2,0} - M_2(r))^2 - (m_{1,0} - M_1(r))^2, \qquad (2.17)\end{aligned}$$

and $M_{1,2,3}$ are linear combinations of the M_{ij}s, and can be parameterized as

$$M_i(r) = \alpha_i \rho(r) \qquad (2.18)$$

for matter density $\rho(r)$. Then we can substitute the mixing angle in matter from Eq. 2.15 into our standard oscillation equations to get a survival probability as a function of our parameters α_i. The survival probability for various values of the parameters α_i is shown in Fig. 2.6.

To interpret the KamLAND constraints on mixing parameters within the context of this model, we replace θ_{12} with θ_{12}^m and Δm_{21}^2 with Δm_m^2 as defined above except with $A \to -A$ and $\rho \sim 3\text{gr/cm}^3$ for the density of the Earth's crust.

Current limits for the effective Yukawa coupling of any scalar with $m_\phi \gtrsim 10^{-11}\text{eV}$ to nucleons from tests of the inverse square law are $|\lambda^N| \lesssim 10^{-21}$ [22]. A previous two-flavor oscillation analysis of solar data plus KamLAND [44] found 90% confidence level bounds of

$$\begin{aligned}-2.2\times 10^{-5} \leq \quad \alpha_2/\text{eV} &\leq 1.4\times 10^{-4}, \qquad (2.19)\\ |\alpha_3|/\text{eV} &\leq 2.3\times 10^{-5} \text{ for } \alpha_3^2 > 0, \qquad (2.20)\\ |\alpha_3|/\text{eV} &\leq 3.4\times 10^{-5} \text{ for } \alpha_3^2 < 0. \qquad (2.21)\end{aligned}$$

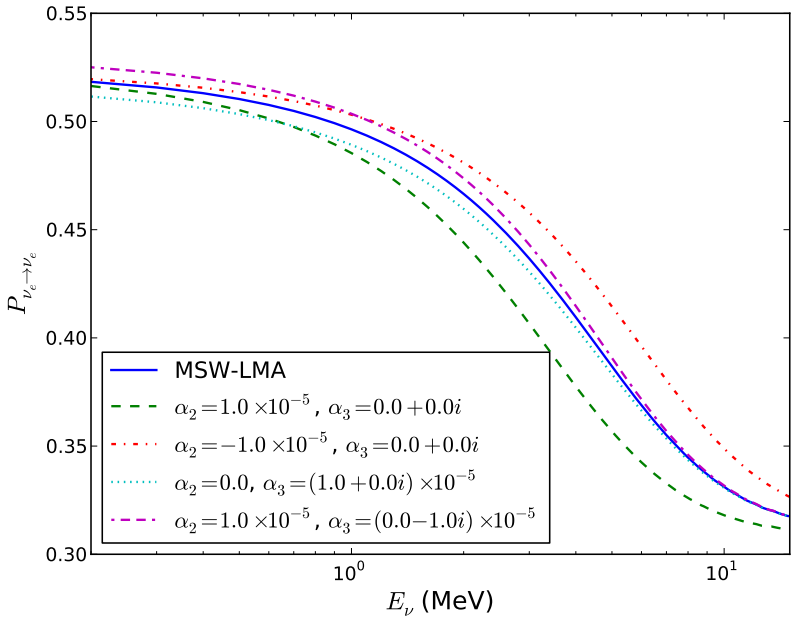

Figure 2.6: Survival probabilities for the fermion density dependent MaVaN model at several values of α_2, α_3

2.3 Long-Range Leptonic Forces

We consider another group of generic non-standard interactions characterized by a new long-range force coupling to lepton flavor number. Since lepton flavor number is not conserved, such a force is likely to have a finite range. In general if the range is long enough, we follow Ref. [46] and write the effect of the force at some point in the Sun in terms of a function

$$W(r) = \frac{2\pi\lambda}{r} \int_0^{R_{sun}} dr' r' n_e(r') \left(e^{-|r'-r|/\lambda} - e^{-(r'+r)/\lambda} \right), \tag{2.22}$$

where λ is the range of the force. Long range forces of this kind can be probed by studying experimental tests of the equivalence principle; this sort of analysis was

used to get a bound on a vector long-range force's dimensionless coupling constant $k_V < 10^{-49}$ [48]. More recently Gonzalez-Garcia et al [46] performed a two flavor oscillation analysis of solar data to find 3σ bounds for scalar, vector, and tensor forces of infinite range that couple to electron number of

$$k_S(e) \leq 5.0 \times 10^{-45} \ (m_1 = 0\text{eV}), \tag{2.23}$$

$$k_S(e) \leq 1.5 \times 10^{-46} \ (m_1 = 0.1\text{eV}), \tag{2.24}$$

$$k_V(e) \leq 2.5 \times 10^{-53}, \tag{2.25}$$

$$k_T(e) \leq 1.7 \times 10^{-60}\text{eV}^{-1}. \tag{2.26}$$

For these models we expect the effect on terrestrial experiments to be small due to the short baseline and small electron density so constraints from reactor experiments will remain the same.

2.3.1 Scalar Interaction

In the case where the new long-range force is a scalar coupling, we see a similar situation to the MaVaN. We now have a light scalar that only couples to neutrinos and electrons, which one can parameterize in terms of the function W(r). The new term in the Lagrangian for the neutrinos is

$$\mathbf{L} = -g_0 \phi \bar{\nu} \nu \tag{2.27}$$

and so the kinetic part of the Hamiltonian gains a term

$$\mathbf{M}' = U_{12}^{\dagger} U_{13}^{\dagger} U_{23}^{\dagger} \begin{pmatrix} -M_s(r) & 0 & 0 \\ 0 & 0 & 0 \\ 0 & 0 & 0 \end{pmatrix} U_{23} U_{13} U_{12}, \tag{2.28}$$

where $M_s(r) = k_s(e)W(r)$ and $k_s(e) = \frac{g_0^2}{4\pi}$. After decoupling the third flavor and diagonalizing the mass matrix for the remaining two we get the matter mixing angle in the adiabatic limit of

$$\sin 2\theta_{12}^m(r_0) = \frac{\sin 2\theta_{12}\Delta m_s^2}{\Delta m_s'^2} \tag{2.29}$$

where

$$\begin{aligned} \Delta m_s^2 &= \Delta m_{12}^2 - M_s(r_0)\Delta m_{12} c_{13}^2, & (2.30) \\ (\Delta m_s'^2)^2 &= \big[\Delta m_s^2 \cos 2\theta_{12} - 2E_\nu V(r_0) c_{13}^2 \\ &\quad - M_s^2(r_0)c_{13}^2 + M_s(r_0)(m_1 + m_2)\big]^2 \\ &\quad + \sin 2\theta_{12}\Delta m_s^2. & (2.31) \end{aligned}$$

The survival probability for various values of the range and coupling strength is shown in Fig. 2.7.

2.3.2 Vector Interaction

If the force is mediated by a vector boson A_α, then

$$\mathbf{L} = -g_1 A_\alpha \overline{\nu}\gamma^\alpha \nu \tag{2.32}$$

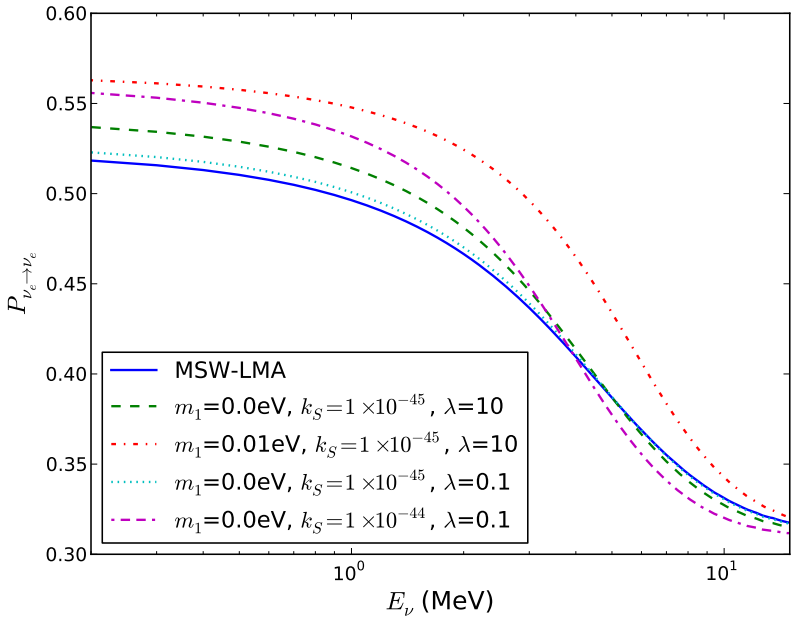

Figure 2.7: Survival probabilities for a long-range scalar interaction at various values of the range and strength of the coupling and the neutrino mass scale.

and the potential $V(r) = V_{MSW} + k_V W(r)$ where $k_V = \frac{g_1^2}{4\pi}$. We can solve for the survival probability using the standard MSW oscillation equations, substituting in the above for the MSW potential.

The survival probability for various values of the range and coupling strength is shown in Fig. 2.8.

2.3.3 Tensor Interaction

If the force is mediated by a tensor field with spin 2, $\chi_{\alpha\beta}$, then

$$\mathbf{L} = -\frac{g_2}{2}\chi_{\alpha\beta}\left(\overline{\nu}\gamma^\alpha i\partial^\beta\nu - i\partial^\alpha\overline{\nu}\gamma^\beta\nu\right). \tag{2.33}$$

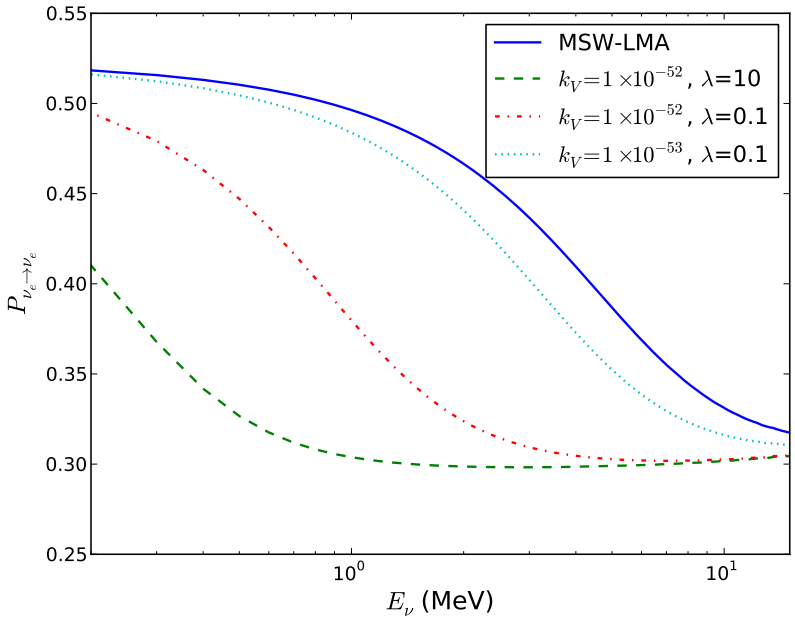

Figure 2.8: Survival probabilities for a long-range vector interaction at various values of the range and strength of the coupling.

Now the potential is $V(r) = V_{MSW} + E_\nu k_T W(r)$, where $k_T = m_e \frac{g_2^2}{4\pi}$. Again we can use the standard MSW oscillation equations substituting in this new potential.

The survival probability for various values of the range and coupling strength is shown in Fig. 2.9.

2.4 Nonstandard Solar Model

We also want a way to check that any improvement in the fit achieved by replacing MSW with a non-standard model cannot be easily reproduced by modifying solar model parameters. In addition, we want to see that we are sensitive to the transition region independent of exact knowledge of the Sun — that is, that small changes in the parameters of the solar model do not create changes in the transition region on

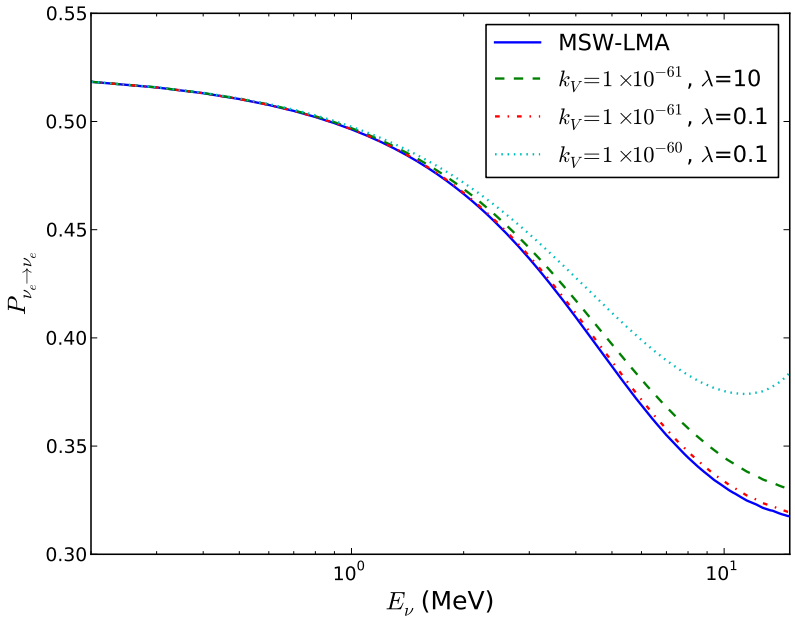

Figure 2.9: Survival probabilities for a long-range tensor interaction at various values of the range and strength of the coupling.

the order of the small effects expected from non-standard models. To this end, in addition to comparing fits using both the high metallicity and low metallicity solar models, I use the fact that in the adiabatic approximation, there are only two inputs from the solar model that affect the survival probability. They are the absolute flux constraints, and the convolution of the density profile with the neutrino production profiles. I can effectively remove many of our assumptions about the solar model from our fit by removing the absolute flux constraints entirely, and for the other two sets of parameters, distorting the density profile linearly, so that

$$n'_e(r) = (1 + \delta_0 + \alpha r) n_e(r) \tag{2.34}$$

for some change in the core density δ_0, where α is determined by δ_0 and the constraint that the total mass remains the same. A recent study has shown that a change in the central density is plausible, and was able to create a model with the central density increased by over 10% using stellar evolution software [49].

I can get a reasonable constraint on the uncertainty of the solar density profile by comparing the predictions of standard solar models to helioseismological measurements of the sound profile, which differ by around 1% [50, 51].

Chapter 3

Data Sets and Approach

The solar neutrino data sets used include the weighted average of the results of the gallium experiments (SAGE, GALLEX, and GNO) given in Ref. [19], and separately the results of the Chlorine experiment [18]. These experiments provide integral measurements of several solar neutrino fluxes. For the 'realtime' experiments, which measure exclusive fluxes, I include the most recent SNO results [7] for ^{8}B, the measurements of S-K I [4], S-K II [20], and S-K III [21] (which are also ^{8}B), and the measurements of Borexino for ^{7}Be [22], ^{8}B [52], and *pep* [23].

The modelling of the various experiments' results was developed primarily by Anthony LaTorre and Olivia Wasalski. They follow the standard approach taken by other authors, except for the handling of the SNO results, for which explicit energy-dependent survival probabilities are provided. For all data sets other than SNO the expected number of events either in a given energy bin or as an integral flux is predicted. To achieve this the neutrino energy spectrum is convolved with its interaction cross section on a given target, and the outgoing electron energy is convolved with the detector's response. For a given oscillation hypothesis, this integral includes the energy dependence of the survival probability. Because of the depen-

dence on the production region within the Sun survival probabilities are calculated separately for each solar neutrino source. The Super-Kamiokande collaboration has provided bin-by-bin "no-oscillation" spectra that include their full Monte Carlo detector model. Therefore for a given oscillation hypothesis the output is scaled by the ratio of oscillation to no-oscillation calculated using the analytic Gaussian response they have provided.

Interaction cross sections for the Chlorine experiment are taken from Bahcall [53], including the estimated theoretical uncertainties. For the Gallium experiments, we assume zero strength for capture to the first two excited states of ^{71}Ge, as given in Appendix C of Ref. [19] of the SAGE collaboration. The remaining cross section has uncertainties that are highly asymmetric for certain energies. We follow Bahcall's suggestion [54] and take a conservative approach that treats uncertainties for energies above 2 MeV and uncertainties below 2 MeV as being correlated with each group but not with each other. To handle the asymmetric nature of the uncertainties, we use a bifurcated Gaussian. For the elastic scattering cross section of electrons, which applies to Borexino and Super-Kamiokande, we use the cross section that includes radiative and electroweak corrections as given by Bahcall [55].

All experimental uncertainties are considered to be independent, with the exception of the three S-K measurements for which the normalization uncertainties are treated as being correlated across the three data sets. We have marginalized over systematic uncertainties for each experiment.

In my fits to data I float the mixing parameters, but constrain them by known terrestrial measurements. For the dominant θ_{12} and Δm^2_{21} parameters I use constraints from KamLAND [5], and constrain θ_{13} by the results of the Daya Bay [24] and RENO [25] collaborations. The KamLAND constraint is taken directly from

the $\Delta\chi^2$ map from [5], while the Daya Bay and RENO constraints are implemented by assuming their stated uncertainty in θ_{13} represents the width of a Gaussian $\Delta\chi^2$ distribution.

The survival probability calculation is an analytical approximation to a full three-flavor numerical integration of the wave equation. A large part of the implementation was also developed by Anthony LaTorre. It is assumed in all cases that $\Delta m^2_{31}/E$ is much larger than $\Delta m^2_{21}/E$ or any matter potential so the third flavor decouples and propagates independently of the other two. In addition, we assume adiabatic propagation in the Sun corrected by a two-flavor jump probability calculated at the resonance of maximal adiabaticity violation [56] (the results agree well with numerical calculations). We integrate over production location in the Sun for high metallicity model GS98SF2 [57] and low metallicity model AGSS09SF2 [58], using neutrino production and solar density distributions from each [10]. I extended the calculation to include the day-night effect using the procedure described in Ref. [17], modeling the Earth as two spherical shells of constant density. I used a parameterized average annual solar exposure as described in Ref. [59]. I also implemented the calculations of the survival probability for the nonstandard models as described above.

For Chlorine, Gallium, and Borexino, the reproduction of their data is checked by comparing their no-oscillation flux predictions to our calculations. Borexino only gives a prediction for their integral measurement, but as mentioned earlier S-K provides binned no-oscillation predictions, allowing our calculations to be checked more carefully. The binned predictions differ from our calculations by around a few percent per bin, which assumed to be due to unreported differences between the Gaussian detector response given in Ref. [21] and their full detector Monte Carlo.

After scaling the binned data by these differences, the integral flux predictions match within one percent.

For the results of the SNO collaboration, we can conveniently use the ν_e survival probability directly. To test a given oscillation hypothesis against the SNO survival probability, I use the prescription described in Refs. [31] and [7]. The survival probability is projected onto the detected ^{8}B spectrum, and the quadratic form used by the SNO collaboration is extracted. In this way, the comparison comes down to a test of just six parameters: three for the day survival probability,

$$\begin{aligned} P_{ee}^{day}(E_\nu &= c_0 + c_1(E_\nu[\mathrm{MeV}] - 10) \\ &\quad + c_2(E_\nu[\mathrm{MeV}] - 10)^2, \end{aligned} \tag{3.1}$$

two for the day-night asymmetry,

$$A_{ee}(E_\nu = a_0 + a_1(E_\nu[\mathrm{MeV}] - 10), \tag{3.2}$$

and one for the ^{8}B flux scale.

I used the models described in Chapter 2 to calculate survival probabilities, including the dominant standard MSW-LMA oscillation. I perform a maximum likelihood fit to the data, floating the standard mixing parameters $(\theta_{12}, \Delta m^2_{21}, \theta_{13})$ and various non-standard parameters for each model as well as the flux scaling for each neutrino production reaction and a systematic parameter for the shape of the ^{8}B spectrum [53]. Where I reference χ^2 I mean $-2\log\mathcal{L}$. I constrain the values of the known mixing parameters to the values measured by the KamLAND collaboration [5] for the (1,2) sector, and the measurements of KamLAND, Daya Bay, and RENO for θ_{13}. The flux for each neutrino production reaction is constrained by the

standard solar model values and uncertainties, although for ^{8}B the main constraint instead comes from SNO's NC measurement. The allowed range for the mixing parameters in my fit is set by the range of values covered in KamLAND's $\Delta\chi^2$ map. This limits Δm^2_{21} to the range 6.8×10^{-5} to 8.4×10^{-5} eV^2, $\tan^2\theta_{12}$ to between 0.1 to 1.0, and $\sin^2\theta_{13}$ to between 0.0 and 0.18.

For the fit to the nonstandard solar model I do not constrain the density change since I am also using it as a proxy for any change in the production profile. Additionally, although I cannot use the flux constraints from the solar model in this fit since they are no longer valid once we change the density, I constrain the sum of the fluxes using the luminosity of the Sun [60] and constrain the ratio of the *pp* to *pep* fluxes since the nuclear matrix elements are the same [61].

Chapter 4

Results and Discussion

4.1 Large Mixing Angle MSW

The best fit point for standard MSW-LMA is found at $\Delta m^2_{21} = 7.462 \times 10^{-5}$ eV$^2, \sin^2\theta_{12} = 0.301, \sin^2\theta_{13} = 0.0242$, with a ^{8}B flux of 5.31×10^6 cm^{-2}s^{-1}. The fit compared to the data sets of SNO, Borexino, and S-K is shown in Figs. 4.1-4.5. Although in general for the analyses in this chapter I marginalize over S-K's systematic uncertainties, it is important to note how they affect the goodness of the fit. To show this effect, I plot the observed rate in S-K against the predicted rate calculated from our best fit mixing parameters in two ways: first fixing the energy scale, energy resolution, and efficiency to the values reported by S-K, and second using values for these parameters obtained by floating them in our fit. In both cases the width of the band does not include any of the systematic uncertainties associated with these parameters since they are energy dependent and so cannot be captured in a single plot. I find the best fit with the energy scale at $+1.1\sigma$, the energy resolution at -1.0σ and the overall efficiency at $+0.6\sigma$. The efficiency systematic uncertainty increases the average predicted ratio while the other two each bend up

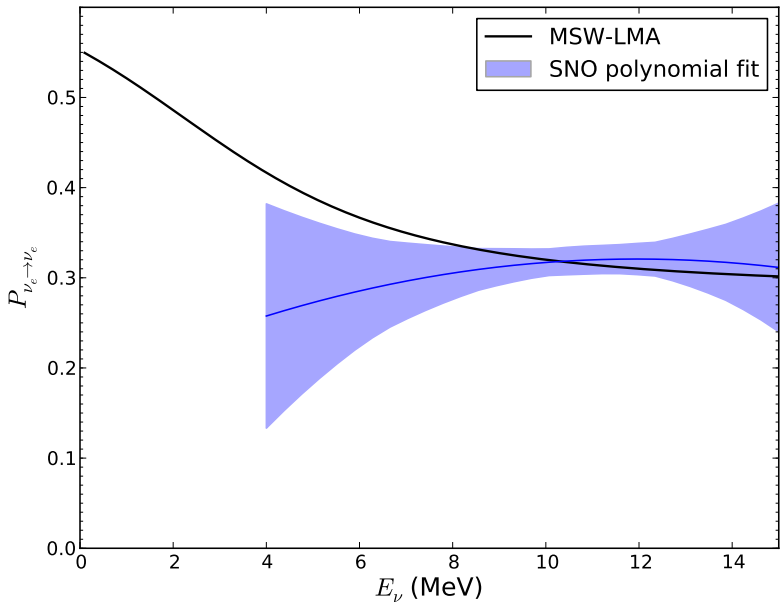

Figure 4.1: Our best fit MSW-LMA prediction versus SNO extracted ^8B survival probability. The band represents the RMS spread at any given energy, i.e., not including energy correlations.

the high energy end of the spectrum. In other words, while the LMA prediction appears to be a poor fit to the high-energy region of the S-K data, the allowed variation from S-K's systematic uncertainties can explain the difference if they are moved roughly 1σ from their central values. Better constraints on the S-K detector response parameters might therefore lead to a more significant disagreement with the LMA model.

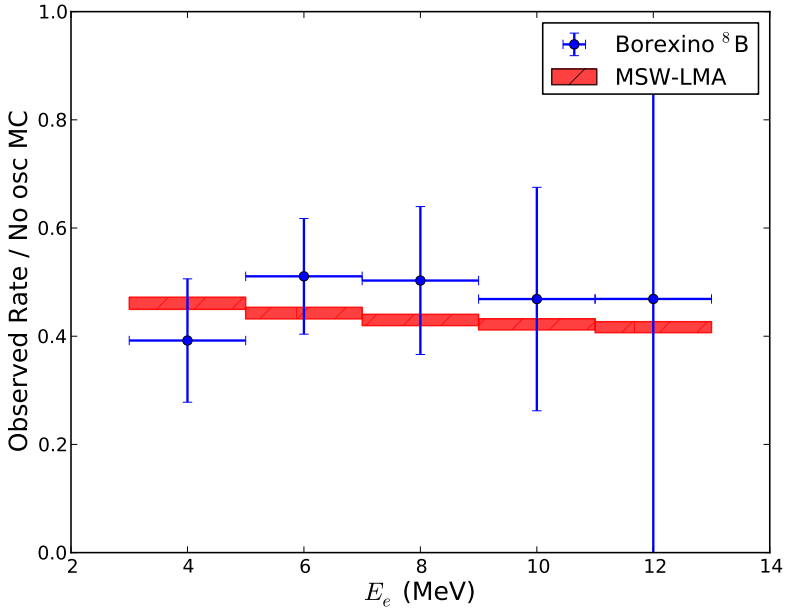

Figure 4.2: Borexino event rate binned in measured electron energy with each bin scaled by Monte Carlo predictions assuming GS98SF2 fluxes, versus the same ratio for the expected rates assuming our best fit LMA parameters and fluxes. Error bars on the data points represent statistical uncertainties only. The best fit oscillation prediction band width represents the uncertainty on the ^{8}B flux.

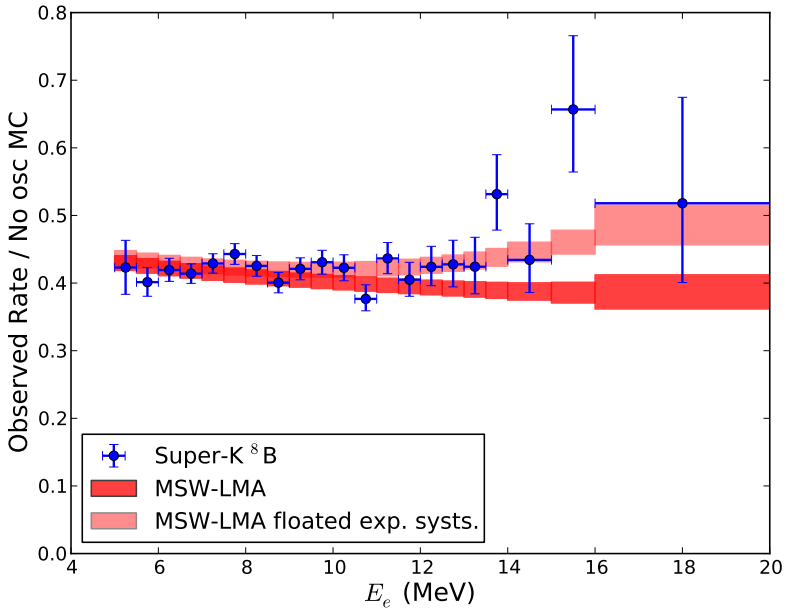

Figure 4.3: S-K I event rates binned in measured electron energy with each bin scaled by Monte Carlo predictions assuming GS98SF2 fluxes, versus the same ratio for the expected rates assuming our combined best fit LMA parameters and fluxes. Error bars on the data points represent statistical and energy uncorrelated systematic uncertainties combined in quadrature. The two bands show the effect of the correlated systematic uncertainties: for the dark band, detector response parameters have been fixed at their reported values, while for the light they have been floated in the fit. The best fit oscillation prediction band width represents the uncertainty on the ^{8}B flux.

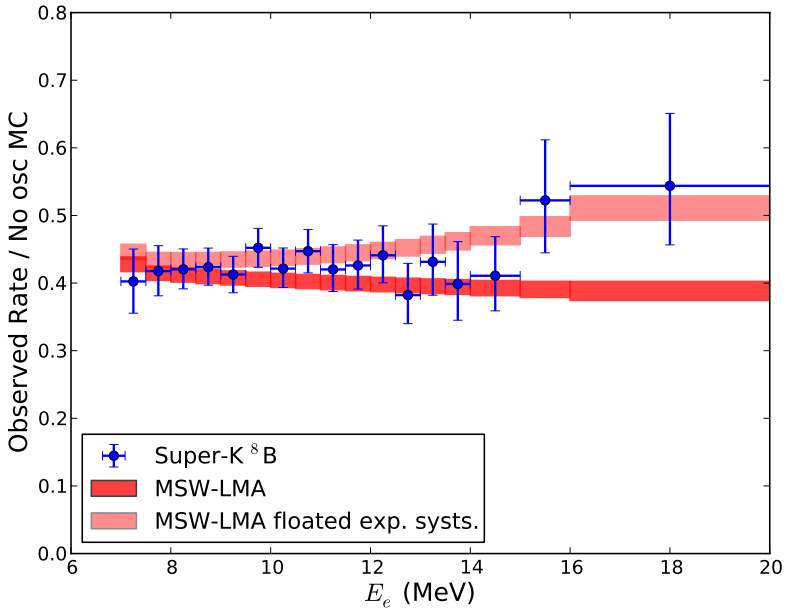

Figure 4.4: S-K II event rates binned in measured electron energy with each bin scaled by Monte Carlo predictions assuming GS98SF2 fluxes, versus the same ratio for the expected rates assuming our combined best fit LMA parameters and fluxes. Error bars on the data points represent statistical and energy uncorrelated systematic uncertainties combined in quadrature. The two bands show the effect of the correlated systematic uncertainties: for the dark band, detector response parameters have been fixed at their reported values, while for the light they have been floated in the fit. The best fit oscillation prediction band width represents the uncertainty on the ^{8}B flux.

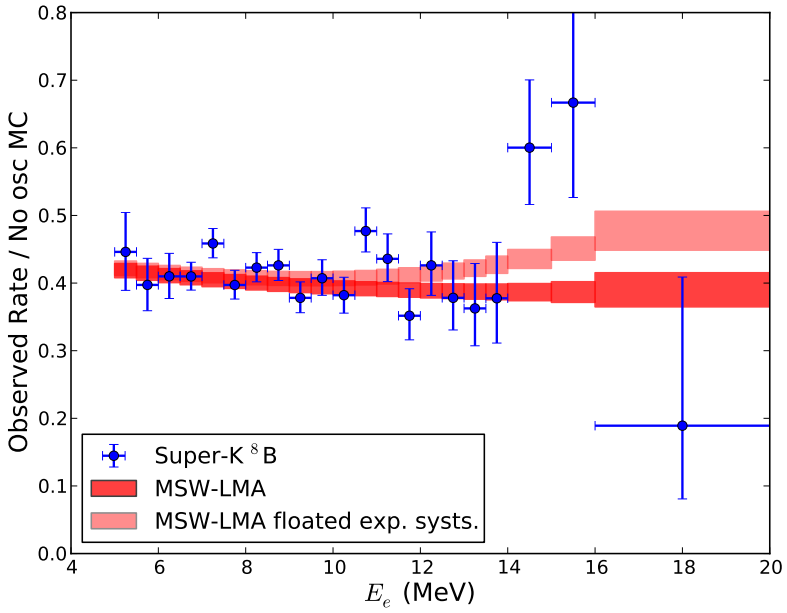

Figure 4.5: S-K III event rates binned in measured electron energy with each bin scaled by Monte Carlo predictions assuming GS98SF2 fluxes, versus the same ratio for the expected rates assuming our combined best fit LMA parameters and fluxes. Error bars on the data points represent statistical and energy uncorrelated systematic uncertainties combined in quadrature. The two bands show the effect of the correlated systematic uncertainties: for the dark band, detector response parameters have been fixed at their reported values, while for the light they have been floated in the fit. The best fit oscillation prediction band width represents the uncertainty on the ^{8}B flux.

4.2 Non-Standard Forward Scattering

I formulate my results for this section to be comparable to Palazzo [41], so $\epsilon^e_{\alpha\beta} = \epsilon^u_{\alpha\beta} = 0$. For a more general case to first order n_f/n_e can be considered constant in the Sun, thus any combination of $\epsilon^{e,u,d}$'s would just be a scaling of our results.

First I consider only real ϵ_1 with $\epsilon_2 = 0$. Including the most up-to-date solar results and the most recent KamLAND results as a constraint, letting θ_{12} and Δm^2_{12} float and fixing $\theta_{13} = 0$, I get a best fit of $\epsilon_1 = -0.137^{+0.070}_{-0.071}$, shown in Fig. 4.6, which well matches results from Palazzo. After letting θ_{13} float and adding in the constraint from RENO and Daya Bay, the significance becomes smaller, with a best fit value of $\epsilon_1 = -0.145^{+0.118}_{-0.109}$, shown in Figs. 4.7 and 4.8. The best fit survival probability compared to MSW-LMA and to data considered in this analysis is shown in Fig. 4.11.

I also consider the case of complex ϵ_1. Here the best fit is found at $\epsilon_1 = -0.146 + 0.031i$. The fit results are shown in Fig. 4.9 and the best fit survival probability in Fig. 4.12. For both ϵ_1 and ϵ_2 nonzero, we find the best fit point at $\epsilon_1 = 0.014, \epsilon_2 = 0.683$. The fit contours are shown in Fig. 4.10, and the best fit survival probability is shown in Fig. 4.13. In both cases the additional free parameter allows a slightly better fit, but the standard MSW-LMA is within the 68% confidence interval for two degrees of freedom. Once both ϵ_1 and ϵ_2 are allowed to be nonzero, there is no further improvement in the fit if we again let ϵ_1 be complex.

For all of these scenarios, the best fit values for the non-standard parameters ϵ_1 and ϵ_2 are well within the current experimental bounds. At the same time, they represent relatively substantial effects, considering that at $\epsilon_{\alpha\beta} = 1$ the non-standard interaction has the same strength as the MSW potential, as shown in Eq. 2.2.

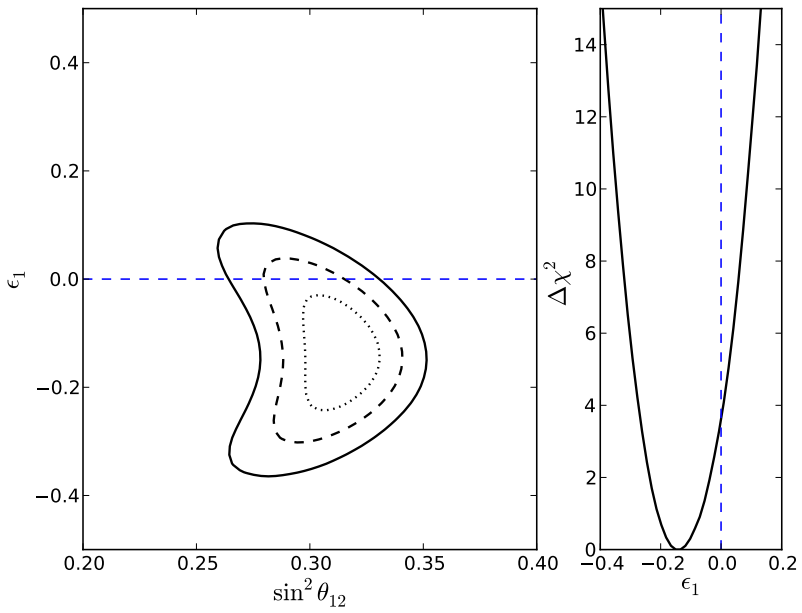

Figure 4.6: Left: Two flavor contours with $\epsilon_2 = 0$ and real ϵ_1. Contours are shown for 68%, 95%, and 99.73% confidence levels for 2 d.o.f., where the χ^2 has been minimized with respect to all undisplayed parameters. Right: $\Delta\chi^2$ as a function of ϵ_1.

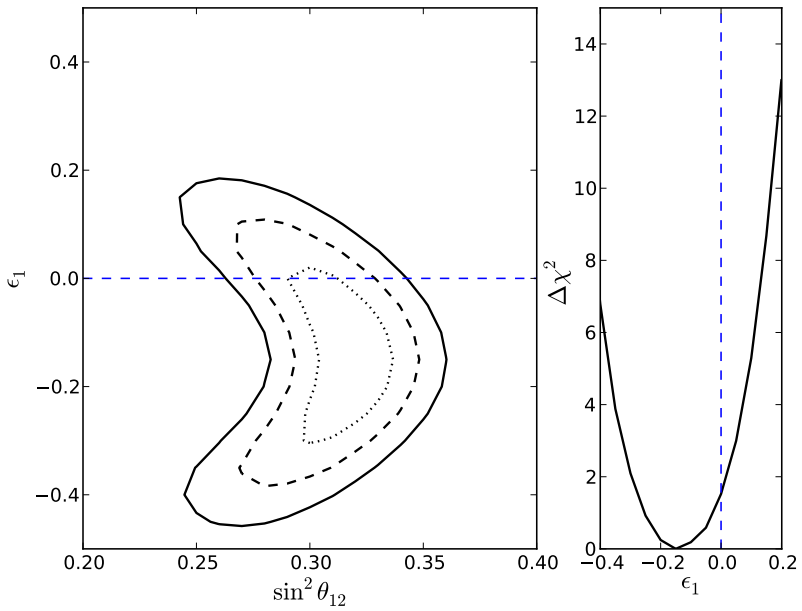

Figure 4.7: Left: Three flavor contours including constraints from RENO and Daya Bay. Contours are shown for 68%, 95%, and 99.73% confidence levels for 2 d.o.f., where the χ^2 has been minimized with respect to all undisplayed parameters. Right: $\Delta\chi^2$ as a function of ϵ_1.

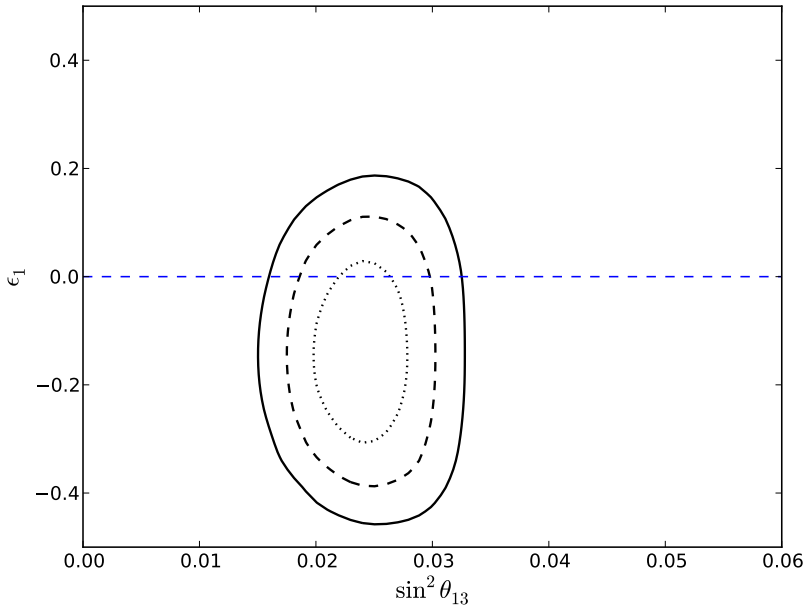

Figure 4.8: Three flavor contours including constraints from RENO and Daya Bay for ϵ_1 and θ_{13}. Contours are shown for 68%, 95%, and 99.73% confidence levels for 2 d.o.f., where the χ^2 has been minimized with respect to all undisplayed parameters.

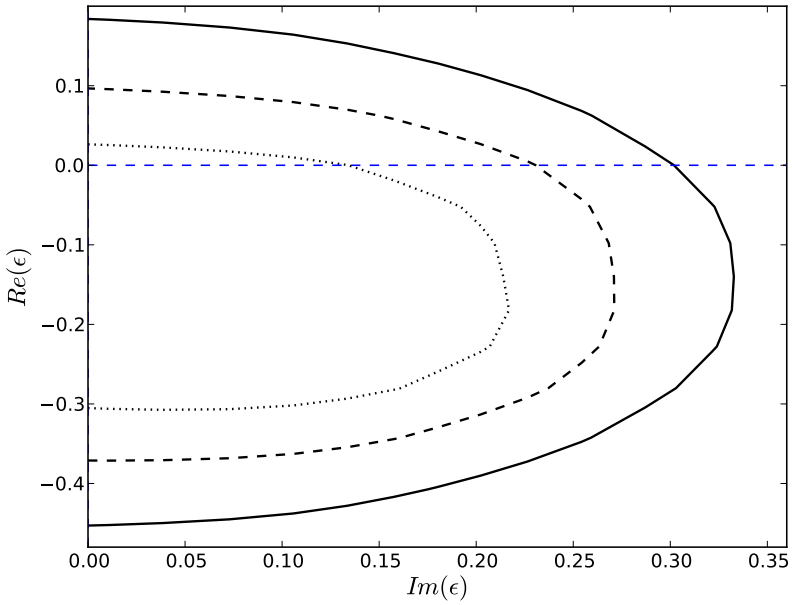

Figure 4.9: Results for NSI fit with $\epsilon_2 = 0$ but complex ϵ_1. Contours are shown for 68%, 95%, and 99.73% confidence levels (2 d.o.f.), where the χ^2 has been minimized with respect to all undisplayed parameters.

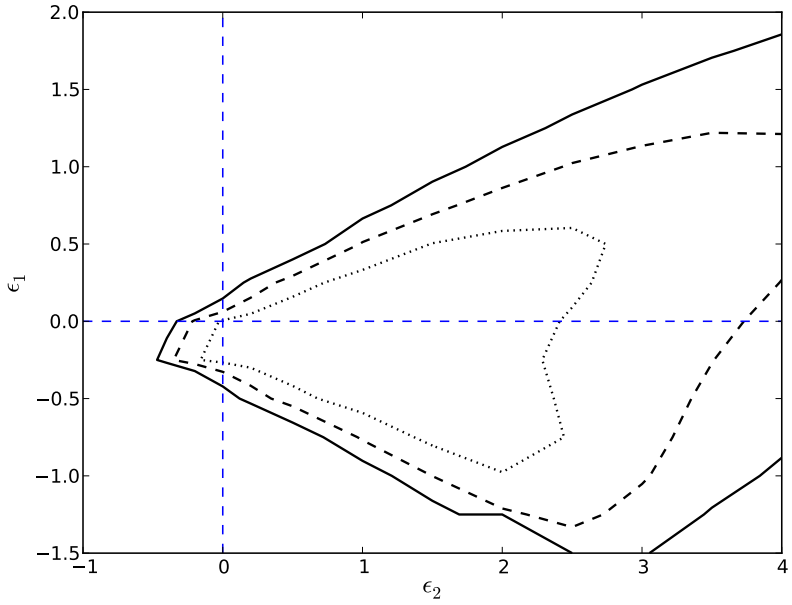

Figure 4.10: Results for NSI fit with real ϵ_1. Contours are shown for 68%, 95%, and 99.73% confidence levels (2 d.o.f.), where the χ^2 has been minimized with respect to all undisplayed parameters.

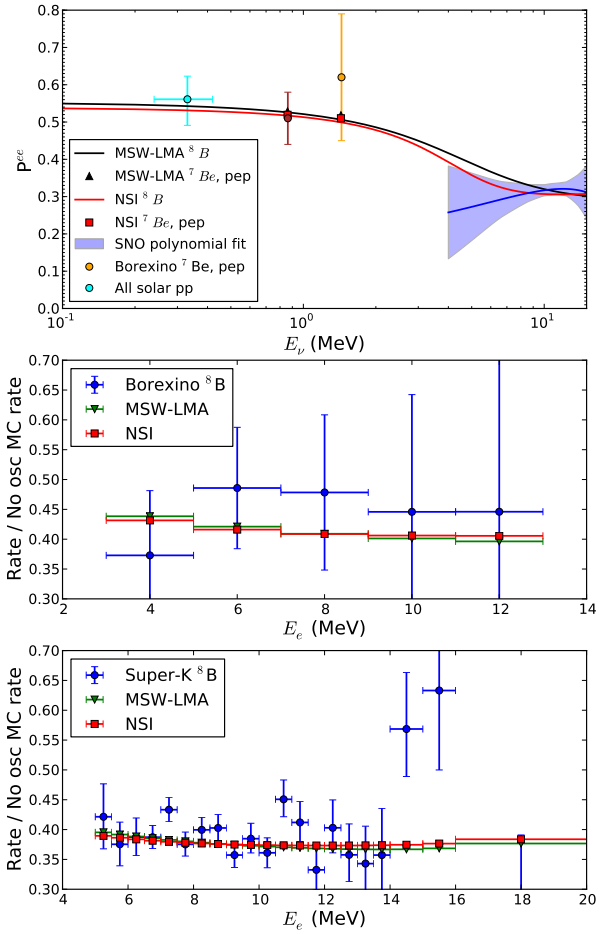

Figure 4.11: Three flavor best fit NSI survival probability compared to MSW-LMA at $\epsilon_1 = -0.145$, $\Delta m^2_{21} = 7.481 \times 10^{-5}\text{eV}^2, \sin^2\theta_{12} = 0.320, \sin^2\theta_{13} = 0.0238$. The top plot shows the survival probability as a function of incident neutrino energy. The middle shows the best fit's predicted event rate in Borexino for each of Borexino's measured electron energy bins scaled by the GS98SF2 flux no-oscillation prediction compared to Borexino's data, and the bottom shows the same for S-K III's energy bins and data.

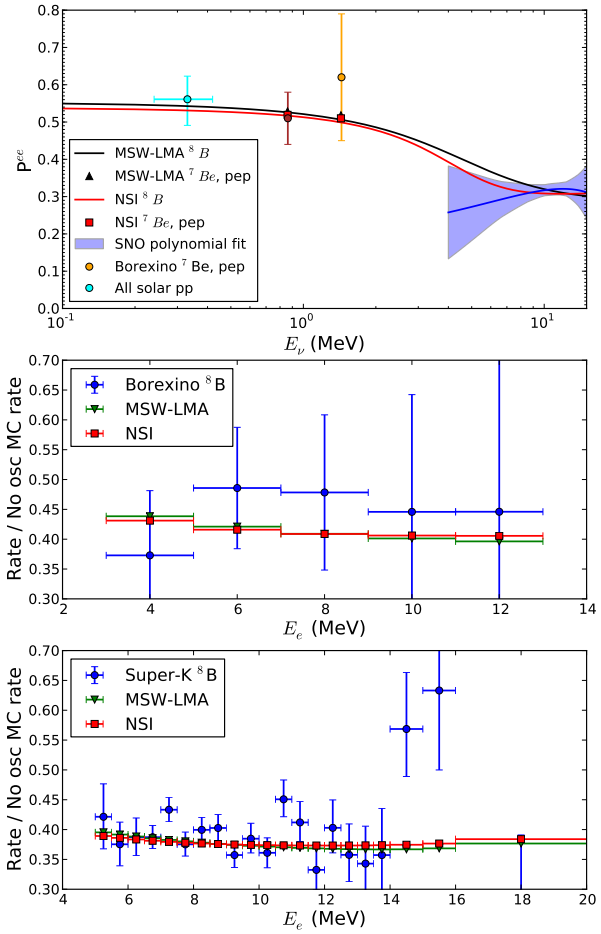

Figure 4.12: Best fit for NSI fit with $\epsilon_2 = 0$ but complex ϵ_1 at $\epsilon_1 = -0.146 + 0.31i$, $\Delta m^2_{21} = 7.472 \times 10^{-5}\text{eV}^2, \sin^2\theta_{12} = 0.320, \sin^2\theta_{13} = 0.0238$. The top plot shows the survival probability as a function of incident neutrino energy. The middle shows the best fit's predicted event rate in Borexino for each of Borexino's measured electron energy bins scaled by the GS98SF2 flux no-oscillation prediction compared to Borexino's data, and the bottom shows the same for S-K III's energy bins and data.

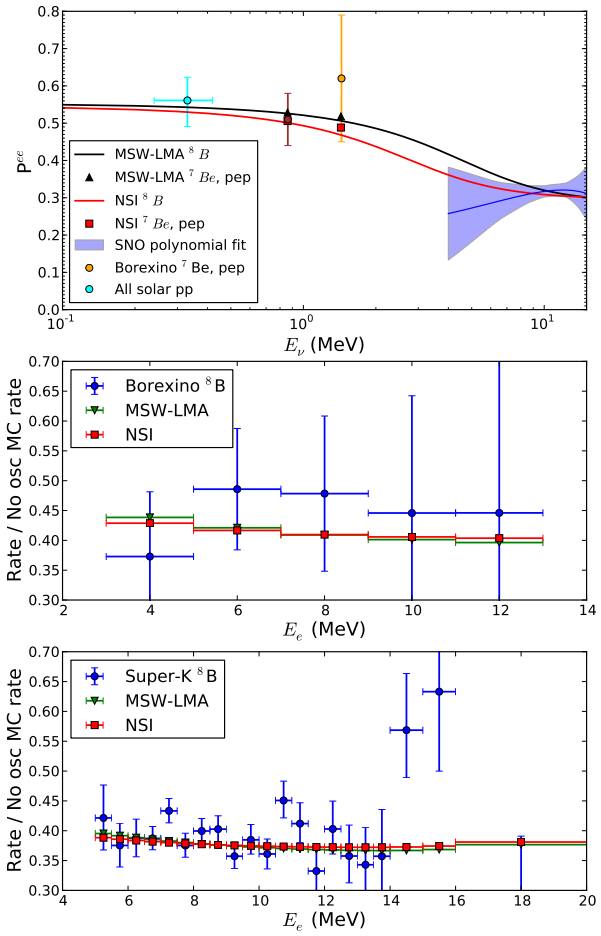

Figure 4.13: Best fit for NSI fit with real ϵ_1 at $\epsilon_1 = 0.014, \epsilon_2 = 0.683$, $\Delta m^2_{21} = 7.487 \times 10^{-5}\text{eV}^2, \sin^2\theta_{12} = 0.310, \sin^2\theta_{13} = 0.0238$. The top plot shows the survival probability as a function of incident neutrino energy. The middle shows the best fit's predicted event rate in Borexino for each of Borexino's measured electron energy bins scaled by the GS98SF2 flux no-oscillation prediction compared to Borexino's data, and the bottom shows the same for S-K III's energy bins and data.

4.3 Mass Varying Neutrinos

4.3.1 Neutrino Density Effects

After fitting for $m_{1,0}$ letting all mixing parameters float, I find that the best fit point is at $m_{1,0} = 0$, where this model's predictions become identical to MSW-LMA. Our fit results, as shown in Fig. 4.14, give a 90% confidence level upper limit on the neutrino mass scale of $m_{1,0} < 0.033$eV within this model. My results do not agree with the previous limit in [43], who found a limit an order of magnitude smaller. I cannot explain the difference, although they use older data sets for each experiment. For the inverted hierarchy we expect $m_{1,0} \gtrsim \sqrt{\Delta m^2_{atm}} \sim 0.05$ eV, so within the context of this model, the inverted hierarchy would be rejected.

4.3.2 Fermion Density Effects

For simplification I let $m_{1,0} = \alpha_1 = 0$, so I fit for $\alpha_2, Re[\alpha_3], Im[\alpha_3]$. Results for $\alpha_2 > 0$, $\alpha_3^2 < 0$ are shown in Fig. 4.15. In this case my best fit is at $\alpha_2 = 6.30 \times 10^{-5}$, $\alpha_3 = i2.00 \times 10^{-5}$, shown in Fig. 4.16, although the 2σ contour includes the origin. Note that although the ^{8}B survival probability in Fig. 4.16 seems to be far from the Borexino *pep* point, in this scenario the *pep* survival probability is actually significantly different than ^{8}B's at the same energy, making it more consistent with the data than it would appear. Minimizing over all other variables gives the bounds at 90% confidence for 1 d.o.f. of

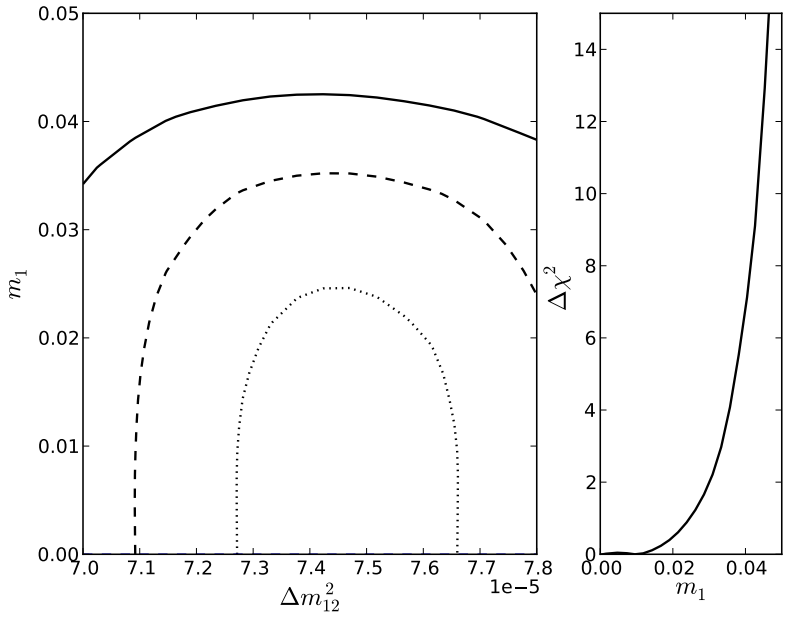

Figure 4.14: Results for MaVaN model with neutrino mass coupled to neutrino density. Left: Contours are shown for 68%, 95%, and 99.73% confidence levels for 2 d.o.f., where the χ^2 has been minimized with respect to all undisplayed parameters. Right: $\Delta\chi^2$ as a function of $m_{1,0}$.

$$1.12 \times 10^{-6} \leq \quad \alpha_2/\text{eV} \quad \leq 1.38 \times 10^{-4}, \tag{4.1}$$

$$|\alpha_3|/\text{eV} \quad \leq 2.15 \times 10^{-5} \text{ for } \alpha_3^2 > 0, \tag{4.2}$$

$$|\alpha_3|/\text{eV} \quad \leq 2.48 \times 10^{-5} \text{ for } \alpha_3^2 < 0. \tag{4.3}$$

Then from Eq. 2.14, we can use our limits on the parameters to get a combined limit on the couplings of $|\lambda^{ij}\lambda^N|/m_\phi^2 \leq 2.9 \times 10^{-14}\text{eV}^{-2}$ [44].

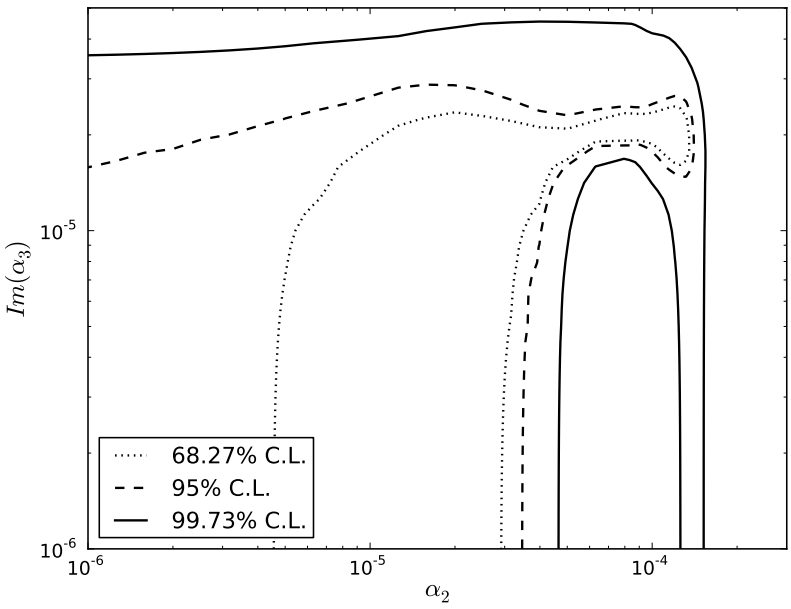

Figure 4.15: Results for MaVaN model with neutrino mass coupled to fermion density with $\alpha_2 > 0$ and $\alpha_3^2 < 0$. Contours are shown for 68%, 95%, and 99.73% confidence levels (2 d.o.f.), where the χ^2 has been minimized with respect to all undisplayed parameters.

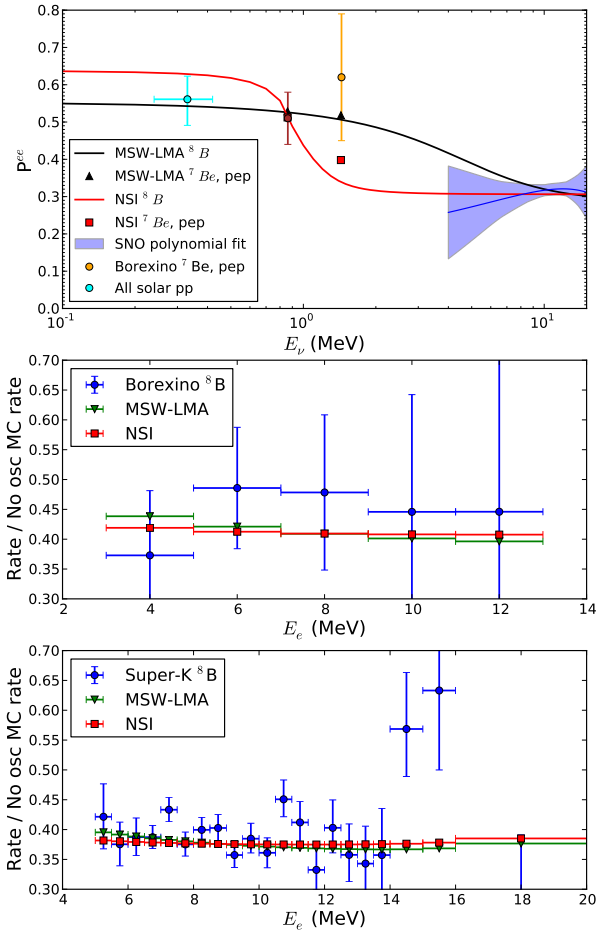

Figure 4.16: Best fit for fermion density dependent MaVaN at $\alpha_2 = 6.30\times10^{-5}, \alpha_3 = i2.00 \times 10^{-5}$, $\Delta m^2_{21} = 7.840 \times 10^{-5}\text{eV}^2, \sin^2\theta_{12} = 0.321, \sin^2\theta_{13} = 0.0239$. The top plot shows the survival probability as a function of incident neutrino energy. The middle shows the best fit's predicted event rate in Borexino for each of Borexino's measured electron energy bins scaled by the GS98SF2 flux no-oscillation prediction compared to Borexino's data, and the bottom shows the same for S-K III's energy bins and data.

4.4 Long-Range Leptonic Forces

For the scalar long-range leptonic force, I find that after again fixing $m_{1,0} = 0$, the best fit is at $k_S = 6.73 \times 10^{-45}$, $\lambda = 1.56 R_\odot$. Since $\lambda = 1/m_S$, this point represents a force mediated by a scalar particle with mass $m_S = 9.1 \times 10^{-17}$eV and a coupling strength $g_0 = 2.91 \times 10^{-22}$. The best fit survival probability is shown in Fig. 4.18. Like the MaVaN case, the *pep* survival probability is higher than ^{8}B's at the same energy. For the long-range vector force, I find the best fit at $k_V = 3.26 \times 10^{-54}, \lambda = 16.97 R_\odot$, shown in Fig. 4.19. For the tensor long-range force, there is no improvement of the fit to the data and the best fit remains at MSW-LMA.

In all three cases, standard MSW-LMA is within the 1σ contour, but the constraint on the coupling strength gets stronger as λ increases. The contours for the scalar case are shown in Fig. 4.17. At $\lambda = \infty$, we can set upper limits on the coupling strengths at 90% confidence level for 1 d.o.f. of

$$k_S(e) \leq 6.31 \times 10^{-45} \text{ with } m_1 = 0\text{eV}, \tag{4.4}$$

$$k_V(e) \leq 1.23 \times 10^{-53}, \tag{4.5}$$

$$k_T(e) \leq 1.31 \times 10^{-61}\text{eV}^{-1}. \tag{4.6}$$

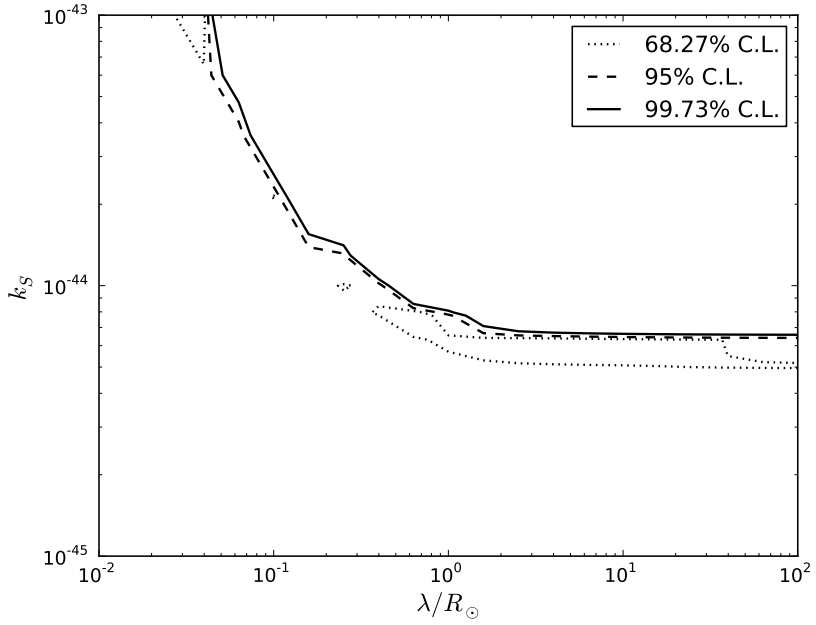

Figure 4.17: Results for a model with a scalar long-range force and $m_{1,0} = 0$. Contours are shown for 68%, 95%, and 99.73% confidence levels (2 d.o.f.), where the χ^2 has been minimized with respect to all undisplayed parameters.

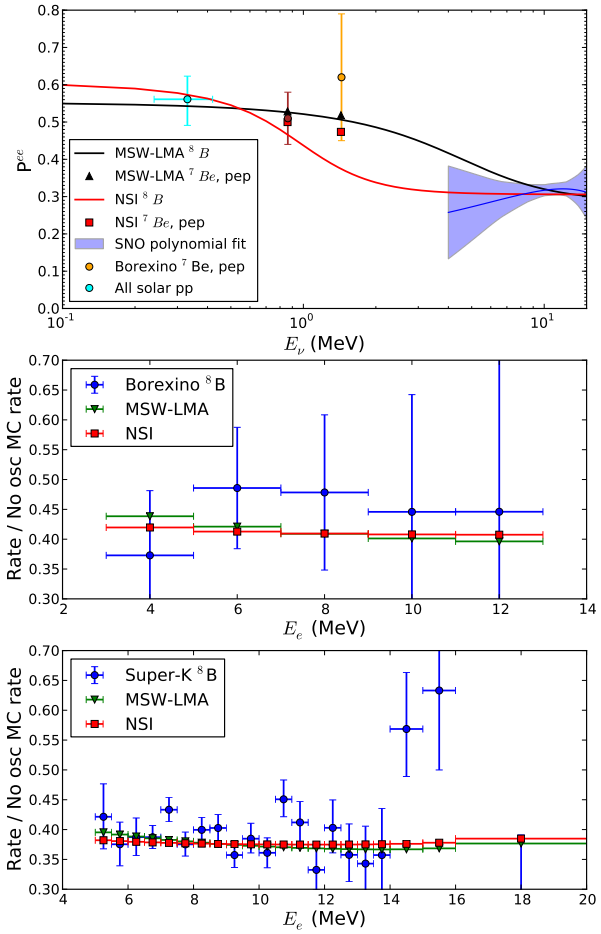

Figure 4.18: Best fit for scalar long-range force at $m_{1,0} = 0$, $\lambda = 1.56 R_\odot$, $k_S = 6.73 \times 10^{-45}$, $\Delta m^2_{21} = 7.484 \times 10^{-5}\text{eV}^2, \sin^2\theta_{12} = 0.320, \sin^2\theta_{13} = 0.0239$. The top plot shows the survival probability as a function of incident neutrino energy. The middle shows the best fit's predicted event rate in Borexino for each of Borexino's measured electron energy bins scaled by the GS98SF2 flux no-oscillation prediction compared to Borexino's data, and the bottom shows the same for S-K III's energy bins and data.

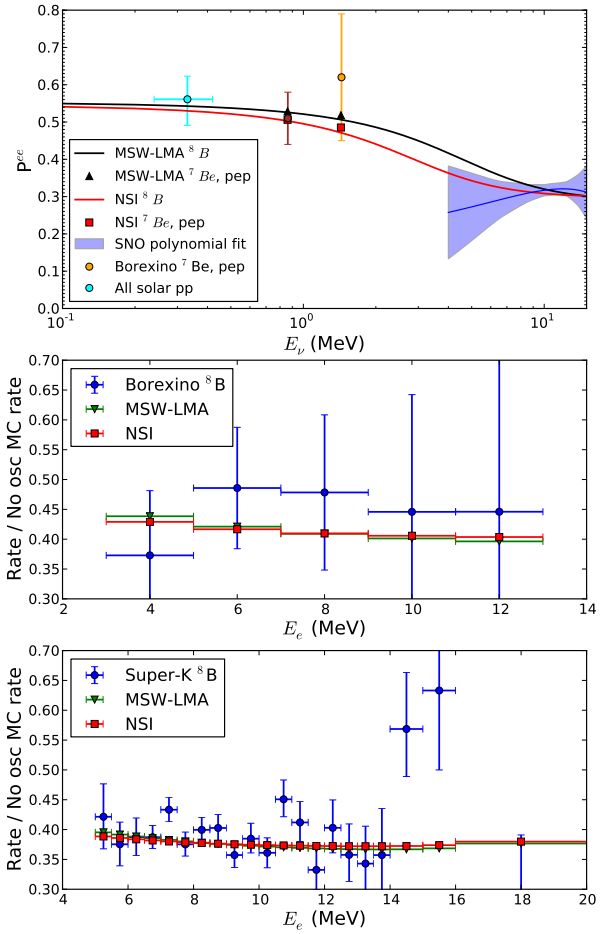

Figure 4.19: Best fit for vector long-range force at $\lambda = 16.97 R_\odot$, $k_V = 3.26 \times 10^{-54}$, $\Delta m^2_{21} = 7.487 \times 10^{-5}\text{eV}^2, \sin^2\theta_{12} = 0.311, \sin^2\theta_{13} = 0.0238$. The top plot shows the survival probability as a function of incident neutrino energy. The middle shows the best fit's predicted event rate in Borexino for each of Borexino's measured electron energy bins scaled by the GS98SF2 flux no-oscillation prediction compared to Borexino's data, and the bottom shows the same for S-K III's energy bins and data.

4.5 Non-Standard Solar Model

I find that using the low metallicity (AGSS09SF2) solar model's flux constraints and solar distributions does not give noticeably different results, and in general worsened the fits for any model.

As described in Section 3, I look at the effect of changing the density of the solar core to see whether we are susceptible to mistaking a small difference in the expected solar model for a non-standard interaction. Fig. 4.20 shows the survival probability with the core density increased by various amounts. It is clear that within the range suggested by helioseismological measurements of about 1%, the change in the ^{8}B upturn is not large enough to mimic any of the non-standard models. Fitting for the central density while keeping the rest of the fit the same, I find that the improvement in the fit for a change of up to 1% is marginal, and we don't reach a minimum until an implausible increase in the solar core density of around 90%. Since any change in the central density would change the core temperature and thus also the expected fluxes, I fit again allowing the density to float and replacing the flux constraints from the solar model with an overall luminosity constraint and a constraint on the *pp* to *pep* ratio. Here the best fit is found at an increase of 57%, with a $\Delta\chi^2$ of -4.6, although not changing the density and just removing the flux constraints already gives a $\Delta\chi^2$ of -3.5.

4.6 Discussion

The above results seem to show that the data allow a vacuum to matter transition in the survival probability at higher energies than the SNO data suggests. It is important to consider the fit to the day night asymmetry, shown in Fig. 4.21

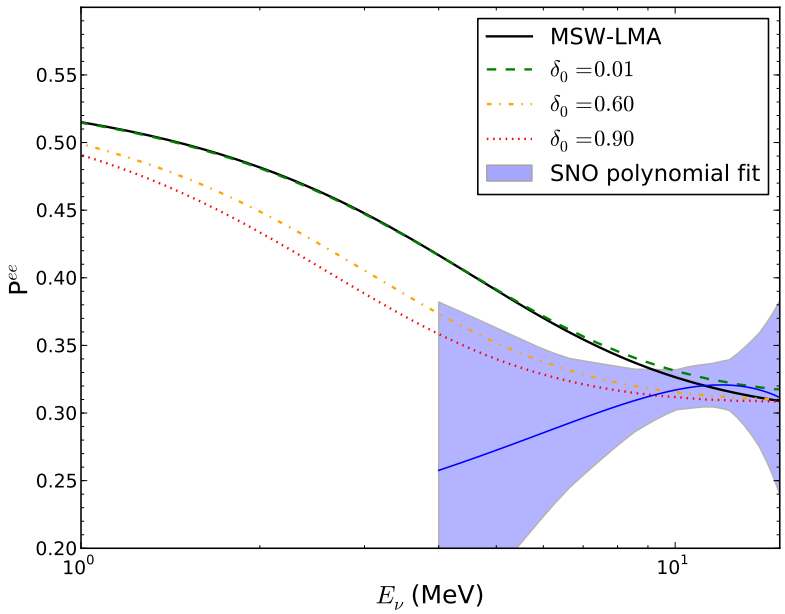

Figure 4.20: Survival probability for MSW-LMA with various fractional increases δ_0 of the solar core density compared to the SNO results.

for SNO. The non-standard models considered do not have a large effect on the asymmetry, and so for neither standard nor non-standard models does the best fit match the data well. The correlations between the asymmetry and the day survival probability translate this poor fit to an even broader allowed upturn, further limiting the significance of any flatness in the data. I show this effect by fitting the MSW-LMA predicted day-night asymmetry to Eq. 3.2 and then recalculating what the RMS spread in the day night survival probability would be after fixing a_0 and a_1 given the correlation matrix, as shown in 4.22.

In addition, since these plots scale the absolute rates to get survival probabilities, they hide the relationship between the survival probability and the absolute flux. Both of these effects can be seen more clearly in the correlation matrix for SNO's polynomial survival probability fit, Table VIII in Ref. [7]. The baseline level of the

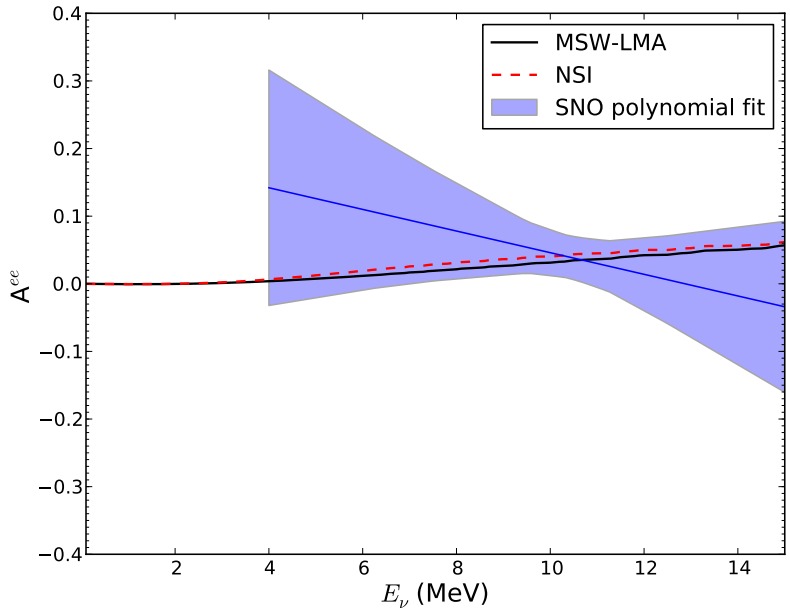

Figure 4.21: Day-Night asymmetry from SNO results compared to best fit MSW-LMA and NSI with real ϵ_1 and $\epsilon_2 = 0$. The band represents the RMS spread at any given energy, i.e., not including energy correlations.

survival probability c_0 is strongly anticorrelated with the absolute flux Φ_B, and the slope of the survival probability c_1 is anticorrelated with the slope of the day night asymmetry a_1.

To better visualize why the full fit does not have a better constraint, I apply the polynomial survival probability fit as used for the SNO data to the combination of the SNO, S-K, Borexino, and Homestake results. This represents a fit to the survival probability independent of any physics model, where the polynomial forms in Eqs. 3.1 and 3.2 are used to impose an energy correlation under the model independent assumption that there is no small scale structure to the survival probability. Since the Homestake results could contain a significant fraction of non-^{8}B events, one additional term for the average non-^{8}B survival probability is added to the fit,

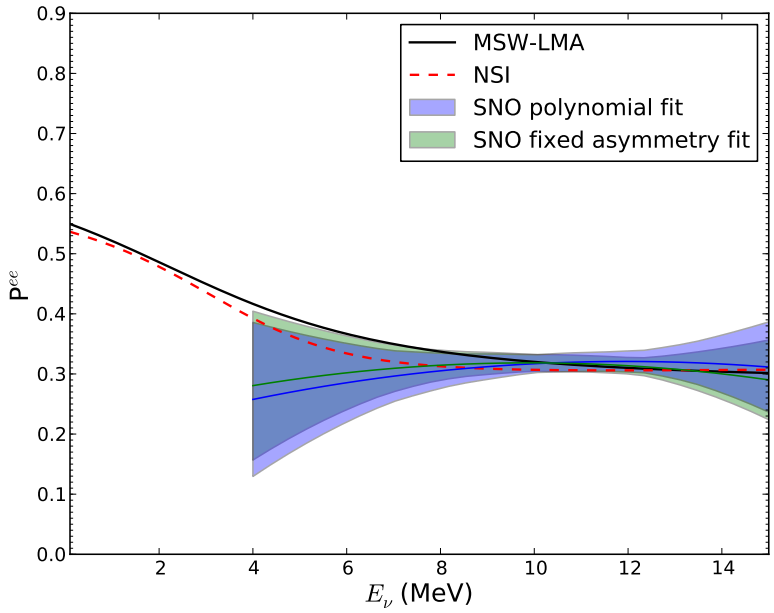

Figure 4.22: Day survival probability for SNO. The blue band shows the RMS spread from the best fit, and the green band shows the spread after the Day-Night asymmetry is fixed to the MSW-LMA prediction.

where non-^{8}B fluxes were fixed at SSM values. The results of the fit are given in Tables 4.1 and 4.2, and the best fit and RMS spread is shown in Fig. 4.23. The majority of the change from the SNO-only band is driven by the S-K results, where the high-energy end and the ^8B flux is pulled upward. Although their data looks flat in detected energy, when projected back into incident neutrino energy it becomes consistent with an LMA-like transition, as suggested in Figs. 4.3, 4.4, and 4.5. The band of the RMS spread shows the significance to which we can say anything about the shape of the survival probability at low energies, and we can see that the band covers the MSW-LMA prediction but at the same time allows for a perfectly flat or even downward bending survival probability. Note that this combined polynomial fit does not impact any of the results in this analysis since we are only using it to

	Best Fit	Fit Error
Φ_B	5.403	0.195
c_0	0.309	0.015
c_1	-0.0014	0.0055
c_2	0.008	0.0022
a_0	0.047	0.020
a_1	0.000	0.018
$P_{\text{non-}^8B}$	0.393	0.148

Table 4.1: Results for polynomial fit for the survival probability and day-night asymmetry fit to the data of SNO, S-K, Borexino, and Homestake.

	Φ_B	c_0	c_1	c_2	a_0	a_1	$P_{\text{non-}^8B}$
Φ_B	1.000	-0.793	0.215	-0.152	-0.027	0.016	0.045
c_0	-0.793	1.000	-0.289	-0.279	-0.204	-0.009	-0.074
c_1	0.215	-0.289	1.000	-0.010	0.042	-0.587	0.023
c_2	-0.152	-0.279	-0.010	1.000	-0.032	-0.004	-0.073
a_0	-0.027	-0.204	0.042	-0.032	1.000	-0.073	0.014
a_1	0.016	-0.009	-0587	-0.004	-0.073	1.000	0.005
$P_{\text{non-}^8B}$	0.045	-0.074	0.023	-0.073	0.014	0.005	1.000

Table 4.2: Correlation matrix from the polynomial fit for the survival probability and day-night asymmetry fit to the data of SNO, S-K, Borexino, and Homestake.

visualize the survival probability and it is not used in the likelihood fits.

4.7 Conclusions

I have compared the predictions of survival probabilities for several models of neutrino non-standard interactions compared to standard MSW-LMA oscillations using results from solar experiments constrained by terrestrial measurements of the mixing parameters. The results of the fits are summarized in Table 4.3.

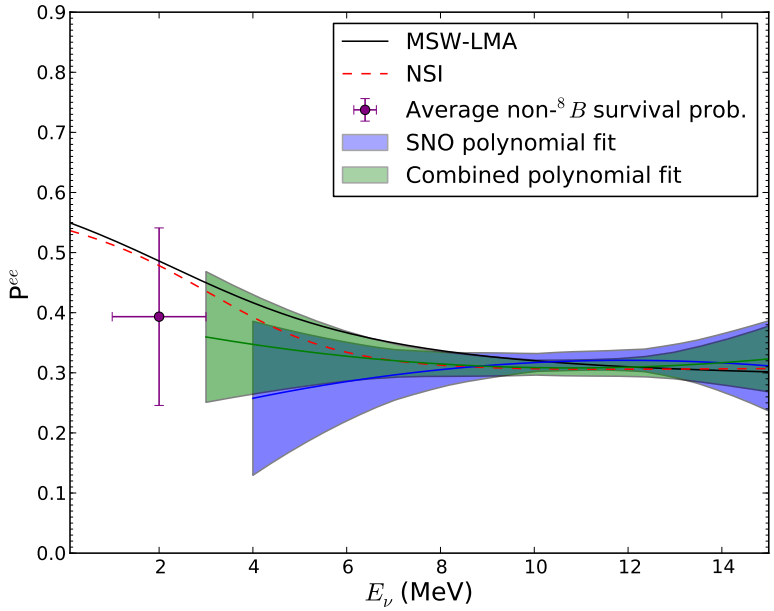

Figure 4.23: Polynomial fit to SNO, Super-Kamiokande, Borexino ^{8}B data and Homestake's results. The band represents the RMS spread at any given energy, i.e., not including energy correlations.

Model	Best Fit	$\Delta\chi^2$	Additional D.o.F.	C.L.
MSW-LMA	$\Delta m^2_{21} = 7.462 \times 10^{-5}$ eV^2, $\sin^2\theta_{12} = 0.301$, $\sin^2\theta_{13} = 0.0242$	0	—	—
MSW-LMA (AGSS09SF2)	$\Delta m^2_{21} = 7.469 \times 10^{-5}$ eV^2, $\sin^2\theta_{12} = 0.304$, $\sin^2\theta_{13} = 0.0240$	2.8	—	—
NSI (ϵ_1 real, $\epsilon_2 = 0$)	$\epsilon_1 = -0.145$	-1.5	1	0.78
NSI ($\epsilon_2 = 0$)	$\epsilon_1 = -0.146 + 0.031i$	-1.5	2	0.53
NSI (ϵ_1 real)	$\epsilon_1 = 0.014$,$\epsilon_2 = 0.683$	-1.9	2	0.60
MaVaN neutrino density dependence	$m_{1,0} < 0.033$ eV	0	1	0.0
MaVaN fermi density dependence	$\alpha_2 = 6.30 \times 10^{-5}, \alpha_3 = i2.00 \times 10^{-5}$	-3.3	2	0.81
Long range scalar leptonic force	$k_S = 6.73 \times 10^{-45}, \lambda = 1.56 R_\odot, m_{1,0} = 0$eV	-2.9	3	0.58
Long range vector leptonic force	$k_V = 3.26 \times 10^{-54}, \lambda = 16.97 R_\odot$	-1.8	2	0.59
Long range tensor leptonic force	$k_T < 1.3 \times 10^{-61}$eV^{-1}	0	2	0.0
Non-standard solar model without flux constraint	$\delta_0 = 0.57$	-4.6	1	—

Table 4.3: Comparison of survival probability fits to standard MSW-LMA. If the best fit remains at the MSW-LMA value for a model, a 90% confidence level upper limit (1 d.o.f.) on the model's parameters is given instead. $\Delta\chi^2$ is the difference between the model's best fit point and the MSW-LMA best fit. The final column gives the largest confidence level at which MSW-LMA is excluded.

Although several of these models allow for a better fit to the data and suggest an explanation for the flatness of the ^{8}B survival probability, I have shown that with the current available data on solar neutrino interactions, there is no model that has demonstrated to be better than MSW-LMA with greater than 2σ significance. I have found that the low significance is in part due to the known, large value of θ_{13}, but also because of the as-yet large systematic uncertainties and covariances in the experimental data sets. The critical transition region thus remains largely unexplored.

I have also examined whether small changes to the solar density profile could lead to a change in the transition region that could mimic the effects of new physics. The results of our simple model show that in fact this is not the case. The matter/vacuum transition region is therefore a good place to look for small effects of non-standard models.

My best fit survival probabilities show that because most of our non-standard model effects have a solar radial or density dependence, the effect is lessened in the *pep* or *pp* production regions and so it would be difficult to test these models merely by improving the measurement of either of those signals. It would require either a better measurement of lower energy ^{8}B, especially one with a charged-current interaction that preserves more of the spectral information, or a new model that can more closely match the data in order for this discrepancy to become more than a hint of something non-standard.

To fully probe this interesting region, in which the interferometry provided by neutrino oscillations lets us look for even tiny effects of new physics, will require new experiments or more precisely constrained systematic uncertainties. Both the Super-Kamiokande and Borexino experiments will continue to take data and hope-

fully their uncertainties will continue to improve. The SNO+ experiment will begin taking data in the near future and it, too, will be able to probe this region. It is possible, however, that a measurement using a charged-current reaction, which preserves more of the spectral information, may be necessary to provide the needed precision to see any new physics that may lie in this region.

Part II

Neutron Multiplicity in Atmospheric Neutrino Events at the Sudbury Neutrino Observatory

Chapter 5

Introduction

Neutron production from high energy neutrino interactions is not well understood. A measurement of neutron "multiplicity"—the number of free neutrons produced—can impact a broad range of physics analyses including searches for nucleon decay, measurements of the neutrino mass hierarchy, and precision measurements of neutrino-nuclear cross sections. The SNO experiment provides a unique opportunity to measure the neutron multiplicity of neutrino interactions in D_2O, and atmospheric neutrinos provide a source of high energy events.

In this chapter, I first describe the physics behind atmospheric neutrino production and detection as well as the interactions they can undergo in the SNO detector. I also summarize the various processes behind neutron production in heavy water. Next, I give an overview of the search for nucleon decay and the determination of the neutrino mass hierarchy and how a measurement of the neutron multiplicity factors in to each. Finally, I outline the analysis procedure.

5.1 Atmospheric Neutrinos

Although the neutron production from Solar neutrinos has been measured precisely by SNO, the production from higher energy interactions is not well understood. The average energy of atmospheric neutrinos that interact in the SNO detector is about 1.4 GeV, well above the understood energy range. Atmospheric neutrinos are produced by interactions that result from cosmic rays striking nuclei in the air. These collisions create a shower of hadrons, mostly consisting of pions and kaons, which further decay into neutrinos. At low energies the main neutrino producing process is the decay of pions to muons.

$$\pi^+ \rightarrow \quad \mu^+ \quad + \nu_\mu \tag{5.1}$$

$$\mu^+ \quad \rightarrow e^+ + \overline{\nu}_\mu + \nu_e \tag{5.2}$$

As the pions travel through the atmosphere they either decay or interact with the air on their way to the Earth's surface. The more dense the material they travel through, the higher the interaction rate. Therefore, they are unlikely to decay first, which results in fewer neutrinos produced. For this reason cosmic rays which travel more parallel to the Earth's surface and travel farther through the less dense upper atmosphere will produce neutrinos more frequently. Thus, the maximal atmospheric neutrino flux is at $\cos\theta_z = 0$.

As shown in the equation above, one expects muon neutrinos and antineutrinos to be produced at roughly twice the rate of electron neutrinos and antineutrinos. Early atmospheric experiments attempted to measure the ratio $R = \frac{\nu_\mu + \overline{\nu}_\mu}{\nu_e + \overline{\nu_e}}$. The Kamiokande experiment first measured this ratio to be significantly smaller than predicted [62]. Like the Solar neutrino problem, this result could be explained by

the oscillation of the neutrino flavors.

The energy range of interest and the baseline of tens to thousands of kilometers makes atmospheric neutrinos mostly sensitive to the mixing angle θ_{23} and the oscillation of muon to tau flavors due to the smallness of θ_{13}. The survival probability is a function of the distance traveled, and for atmospheric neutrinos the distance traveled depends on the zenith angle. The change in the survival probability as a function of zenith angle and energy allows for a measurement of Δm^2_{23}, while the absolute scale of the survival probability allows for a measurement of θ_{23}.

For atmospheric neutrinos we can neglect the solar mass difference Δm^2_{12} and consider an effective single mass difference. Then in vacuum, from Eq. 1.11 we have

$$P_{\nu_e \to \nu_e}(L) = 1 - \sin^2 2\theta_{13} \sin^2 \frac{\Delta m^2_{32} L}{E} \tag{5.3}$$

$$P_{\nu_e \leftrightarrow \nu_\mu}(L) = \sin^2 \theta_{23} \sin^2 \theta_{13} \sin^2 \frac{\Delta m^2_{32} L}{E} \tag{5.4}$$

$$P_{\nu_\mu \to \nu_\mu}(L) = 1 - 4\cos^2 \theta_{13} \sin^2 \theta_{23} \left(1 - \cos^2 \theta_{13} \sin^2 \theta_{23}\right) \sin^2 \frac{\Delta m^2_{32} L}{E}. \tag{5.5}$$

At higher zenith angles, there is an additional complication to calculating the survival probability, as the height in the atmosphere where the neutrino is produced becomes a significant contribution to the total distance traveled and must be accounted for.

In 1996, the successor to the Kamiokande experiment, Super-Kamiokande, was built. With over fifteen times the target mass of the original, it had greatly increased sensitivity. As atmospheric neutrinos are much higher energy than solar neutrinos, they are detected through neutrino-nucleus interactions instead of through elastic scattering off of electrons. These interactions produce high energy charged leptons plus hadrons, with all charged particles over their Cherenkov threshold being visible.

As mentioned above, the distance traveled by atmospheric neutrinos is related to the zenith angle, so measuring the event rate as a function of angle in the detector allows for a measurement of atmospheric neutrino oscillations. The distortion seen by Super-Kamiokande in the measured L/E spectrum was the first direct evidence for atmospheric neutrino oscillations.

In the most recent phase of running, the Super-Kamiokande trigger has been modified so that all PMT hits are recorded for 500 μs following any high energy events. This makes it possible to look for neutrons produced by neutrino interactions by giving the detector sensitivity to the 2.2 MeV gammas from neutron capture on hydrogen. Preliminary studies of the neutron multiplicity have been performed and the multiplicity was shown to increase as a function of visible energy, but the simulation was found to systematically underpredict the measured multiplicity [63].

The SNO experiment was also sensitive to atmospheric neutrinos, although statistics were much lower. Studies were performed mostly on events from neutrino interactions in the rock surrounding the detector, and usually with the goal of eliminating these events and following spallation events as a background from the SNO solar analysis.

5.2 Neutrino-Nucleus Cross Sections

Atmospheric neutrinos span a large energy range up to tens of GeV. At these energies the primary interaction is no longer elastic scatter off electrons. Instead the majority of these neutrinos undergo complicated interactions with the nucleus. A precise understanding of neutrino-nucleus cross sections around 1 GeV is needed for precision neutrino oscillation measurements. In recent measurements by T2K for example, the largest systematic uncertainty comes from the neutrino interaction

model [64]. This is the energy regime with the most complicated cross sections as scattering transitions from mostly quasielastic to deep inelastic.

At high neutrino energies (>10 GeV), the inclusive scattering cross section becomes directly proportional to the energy, as expected for point-like scattering off quarks, called deep inelastic scattering (DIS). At energies around a GeV or less, the cross section is dominated by quasielastic scattering, meaning $\nu_l n \rightarrow l^- p$ or $\overline{\nu}_l p \rightarrow l^+ n$. The differential cross section for quasielastic scattering from free nucleons as formulated by Llewellyn-Smith is given by

$$\frac{d\sigma}{dQ^2} = \frac{M^2 G_F^2 \cos^2\theta_C}{8\pi E^2}\left[A(Q^2) \pm B(Q^2)\frac{s-u}{M^2} + C(Q^2)\frac{(s-u)^2}{M^4}\right] \tag{5.6}$$

where M is the nucleon mass, E is the neutrino energy. A,B, and C are functions of nuclear form factors given by

$$\begin{aligned} A(Q^2) &= \frac{m^2+Q^2}{M^2}\left[(1+\tau)F_A^2 - (1-\tau)F_1^2 + \tau(1-\tau)F_2^2 + 4\tau F_1 F_2\right. & (5.7)\\ &\quad \left. -\frac{m^2}{4M^2}\left((F_1+F_2)^2 + (F_A+2F_P)^2 - 4(1+\frac{Q^2}{4M^2})F_P^2\right)\right], & (5.8)\\ B(Q^2) &= \frac{Q^2}{M^2}F_A(F_1+F_2), & (5.9)\\ C(Q^2) &= \frac{1}{4}(F_A^2 + F_1^2 + \tau F_2^2), & (5.10) \end{aligned}$$

where $\tau = \frac{Q^2}{4M^2}$ [65].

In the impulse approximation, the scattering off of each nucleon in the nucleus is incoherently summed. One can model the nucleus as a relativistic Fermi gas to get the initial nucleon momentum and binding energy. To determine the cross section one must then determine the nuclear form factors in the equation above that parameterize the weak charge distributions in the nucleons. The vector form

factors F_1 and F_2 can be measured from electron scattering experiments, and $F_A(0)$ is well known from measurements of neutron decay, so the only unknown is the Q^2 dependence of the axial form factor. If if the axial form factor is assumed to have a dipole form, then

$$F_A(Q^2) = \frac{F_A(0)}{(1 + Q^2/m_A^2)^2}, \tag{5.11}$$

and the quasielastic cross section can be parameterized by only one unknown, the axial mass m_A.

Data from bubble chamber experiments using hydrogen and deuterium targets provided a consistent picture of quasielastic scattering with the axial mass $m_A = 1.03$ GeV [66]. These experiments measured all outgoing particles so that the final state was known exactly. Recent measurements by MiniBooNE of cross sections on Carbon give a value of $M_A = 1.35$ GeV, suggesting that nuclear effects become important in larger nuclei [67]. However, MiniBooNE is insensitive to protons and neutrons produced in the interaction, and must make assumptions about the purity of quasielastic interactions in their selected events. To explain the axial mass discrepancy in the MiniBooNE results, multinucleon interaction processes have been proposed [68, 69].

These processes are though to be dominated by the meson exchange current (MEC), which is known to be important in electron scattering. It involves the exchange of a weak boson by a pair of nucleons, making the final state differ from quasi elastic interactions in that two nucleons are emitted. This difference would not detectable by MiniBooNE. Although statistics are limited, the SNO experiment's ability to detect neutron captures allow it to compare the predictions of the standard cross sections to a model including contributions from multinucleon emissions.

5.3 Neutron Production in Heavy Water

Atmospheric neutrinos can produce free neutrons in several different ways after interacting in D_2O. The most straightforward way is by directly converting a proton through an antineutrino quasielastic charged-current interaction, also known as inverse beta decay. Both neutrinos and antineutrinos can produce free neutrons through a neutral-current interaction with a neutron that knocks it free of the nucleus or in the case of deuterium, splits off the proton. In an oxygen atom, any struck nucleon or hadrons produced in resonant or deep inelastic scatters can undergo final state interactions (FSI) and rescatter off other nucleons in the nucleus. Negative hadrons can undergo charge exchange reactions and convert a proton to a neutron.

After all final state interactions, additional neutrons can be produced by interactions of the daughter particles with other nuclei in the heavy water. These neutrons can be created by photonuclear interactions with the nucleus, where either real or virtual photons are exchanged causing the ejection of nucleons. They can also be created by inelastic scatters with the nucleus, and by further scattering of any other particles produced. Current simulation packages like Geant4 make predictions for neutron production based on intranuclear cascade models that are verified using measurements from thin targets of various materials. In addition, neutron production from muon spallation has been measured using cosmic ray muons at various depths [70, 71] and muons from accelerators [72], although usually with scintillator or heavy element targets. Empirical studies of production in light water and heavy water from cosmic muons have been performed by Super-Kamiokande and SNO [9, 73] and found it to be consistent with predictions extrapolated to these materials and energies.

5.4 Nucleon Decay

Although the standard model has been a very successful theory, we know that it is incomplete. It does not contain gravity, and has an unsatisfyingly large number of free parameters. Glashow, Weinberg, and Salam developed the electroweak theory that showed how the electromagnetic and weak forces could be combined. In this theory the previously unrelated interactions could be described as different facets of a single force that only become distinguishable through spontaneous symmetry breaking. Grand Unified Theories (GUTs) attempt to extend the standard model in a similar manner, by unifying the electroweak and strong forces. These theories unify baryons and leptons at high energies, thus at low energies they often manifest as new rare processes that violate baryon and lepton number, like proton decay [74, 75]. The rates of these processes are related to the energy scale of the new physics, therefore they often predict proton lifetimes of 10^{30} years or greater.

The simplest group that contains the standard model gauge group $SU(3) \times SU(2) \times U(1)$ is $SU(5)$. The minimal $SU(5)$ GUT theory predicts baryon number violation, since leptons and quarks become part of the same multiplet. This in turn implies that the lowest mass baryon—the proton—is unstable and should decay [75]. It decays into the lightest possible particles via the interaction

$$p \rightarrow e^{+}\pi^{0} \tag{5.12}$$

with a lifetime on the order of 10^{31} years. In super symmetric GUT theories, additional decay modes with strange quarks in the final state are predicted. The lightest possible version is

$$p \rightarrow K^{+}\overline{\nu}. \tag{5.13}$$

The first experimental search for nucleon decay was performed in 1954, again by Cowan and Reines using the same detector as for the neutrino search, setting a limit on the lifetime of 10^{22} years. Since then, limits have been set on many decay modes, using either tracking calorimeters or water Cherenkov detectors. As proton decay is predicted to be a very rare process, a large target mass is needed to have sufficient statistics. The tracking calorimeter detectors consisted of iron plates, which provided a high density of neutrons surrounded by tracking chambers. The advantage of these detectors was that tracking allows the daughter particles to be easily identified. On the other hand, the cost of the materials and instrumentation was high limiting the ability to scale to larger experiments.

Water Cherenkov detectors do not have the same tracking capabilities, but can use Cherenkov ring shapes and light intensity for particle identification. In addition, the target material is very cheap allowing these experiments to be built at much larger scales. New experiments at these larger scales are needed as no evidence of nucleon decay has been seen yet.

Super Kamiokande looked for proton decay via the modes given above, among others. They currently have the best limit on lifetimes of these two modes at 8.2 x 10^{33} years and 2 x 10^{32} years respectively [76, 77]. In an idealized case, a $p \to e^+\pi^0$ event has a positron and a π^0 coming out back to back with the π^0 decaying into two gammas, making a total of three Cherenkov rings. The total momentum should equal zero since the initial proton was at rest, and the invariant mass should be the mass of the proton. In reality though, the situation can be more complicated—if the proton is in an oxygen atom it has Fermi momentum, and the π^0 can interact in the nucleus. The $p \to K^+\overline{\nu}$ decay is harder to identify since the neutrino is invisible. Instead one would see the K^+ decay into μ^+. In this case, the total momentum is

nonzero and there are many more background events.

One of the main backgrounds to measurements of nucleon decay in water Cherenkov experiments is atmospheric neutrinos. Atmospheric neutrino events occur throughout the detector and their rate scales with the detector size. These neutrinos can be energetic enough to produce events with an energy equal to the proton rest mass, and can produce multi-ring events. Super-Kamiokande rejects these events by cutting on the invariant mass and total momentum. They predict less than one background event from atmospheric neutrinos in their signal. On the other hand, a much larger next generation nucleon decay experiment would be limited by this background. Super-Kamiokande predicts 2.1 ± 0.9 events per Mton-year. In order for a much larger experiment to remain in the zero background limit, a different method for rejecting atmospheric events is needed.

It is possible to reduce this background using the high neutron multiplicity of atmospheric neutrino events. For proton decay events in water one expects to produce a neutron only a small fraction of the time. If one of the Hydrogen atoms decay by the simplest decay mode, no neutron can be created in the interaction and the π^0 produced will decay before it has a chance to produce any secondary neutrons. Since ^{16}O is a 'doubly-magic' light nucleus, decays of protons in the outer two shells will either produce final state bound nuclei or the emission of a gamma. Therefore, no primary neutrons are created.

On the other hand, atmospheric neutrino events can produce up to tens of neutrons through nuclear effects of pions or secondary scattering. For a $p \to e^+ + \pi^0$ search, for example, atmospheric neutrino events can create backgrounds through events like $\nu_e + n \to e^- + p + \pi^0$ or $\nu_e + n \to e^- + n + \pi^+$. In cases where there is only a proton in the final state, nuclear interactions can cause the proton to

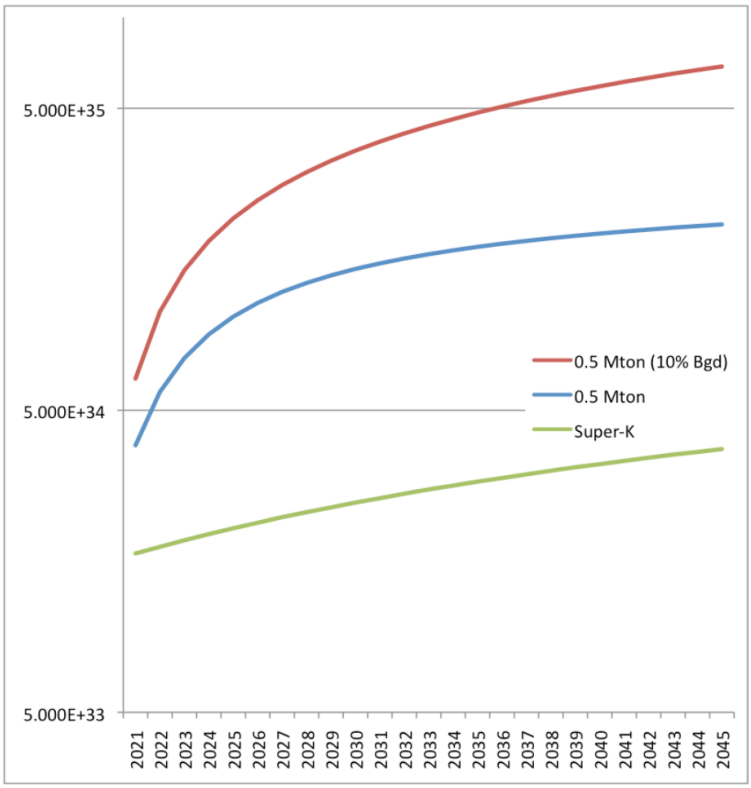

Figure 5.1: Proton decay sensitivity of Super-K and a 0.5 Mton detector assuming Super-K background levels (blue) or backgrounds reduced to 10% of Super-K levels (red). Figure from [6].

free a secondary neutron and allow it to be tagged some fraction of the time as a background.

In water Cherenkov detectors neutron captures create 2.2 MeV gammas and often have a low detection efficiency. For this reason it is important to understand fully the multiplicity distribution of atmospheric neutrino backgrounds so one can accurately determine the likelihoods of seeing no neutrons at all.

5.5 Neutrino Mass Hierarchy

Although measurements have been made of the neutrino mass differences, there remain many unknowns about the structure of these masses. Currently there are only weak limits on the absolute mass scale. In addition, only the magnitude of Δm^2_{23} is known. There are two possible scenarios for the "neutrino mass hierarchy." In the normal hierarchy, Δm^2_{23} is positive and ν_3 is the heaviest mass state. This scenario is called "normal" as the mass ordering is the same as the ordering by flavor content, with the lightest mass state being mostly ν_e. In the inverted hierarchy, Δm^2_{23} is negative, making ν_3 the lightest state. The mass hierarchy impacts oscillations, measurements of absolute neutrino mass, and the possibility of measuring neutrinoless double beta decay and the CP-violating phase.

It is difficult to determine the mass hierarchy, as the sign of the mass differences does not affect vacuum oscillations. We know the sign of the solar mass difference due to the MSW effect in the Sun, as it determines the sign of this effect. Thus one way to measure the mass hierarchy is to look for the matter effect on neutrinos where L/E makes us sensitive to Δm^2_{23}. Depending on the sign of the mass difference, the matter effect will either enhance or dampen the oscillation. This measurement is possible using a neutrino beam if the baseline is long enough. Experiments like NOvA and T2K will attempt to make this measurement, although their sensitivity depends on the value of δ_{CP}.

It is also possible to use atmospheric neutrinos. One difficulty is that the matter effect has the opposite sign for neutrinos and antineutrinos, making it difficult to see. Being able to distinguish atmospheric neutrinos and antineutrinos would solve this problem, and make it easier to measure the mass hierarchy. The ratio of atmospheric muon neutrino to antineutrino events has been

measured by the MINOS experiment. The MINOS far detector is a 5.4 kiloton steel-scintillator calorimeter. The presence of a magnetic field allows the determination of particle charge and thus the neutrino type. MINOS measured the double ratio $R^{data}_{\overline{\nu}/\nu}/R^{MC}_{\overline{\nu}/\nu} = 1.03 \pm 0.08(\text{stat.}) \pm 0.08(\text{syst.})$ [78]. Although this experiment is effective at separating neutrino and antineutrino events, it is not large enough to make a statistically significant measurement of the mass hierarchy using atmospheric neutrinos.

As argued in the previous section, water Cherenkov detectors make a good alternative to tracking calorimeters as they can have a much larger target mass. The difficulty with water Cherenkov detectors is in determining the neutrino type without a magnetic field to identify the charge of the leptons produced. Super-Kamiokande has attempted to produce antineutrino and neutrino enriched samples of events using the number of decay electrons following the interaction [79]. Antineutrino events more often produce π^-s which can be absorbed by other nuclei before decaying to a muon and then an electron, so they will have fewer decay electrons on average.

An independent method of separating neutrinos and antineutrinos is to use the number of neutron captures. This method has been proposed as being feasible in future gadolinium-loaded water Cherenkov detectors, but has never been used by an existing experiment. For simple quasielastic scatters, one extra neutron is expected to be produced by antineutrinos. In reality, inelastic contributions as well as nuclear effects and secondary production obscure this effect. Simulations of atmospheric neutrino and antineutrino events predict that on average neutrino events will produce 0.96 primary neutrons and antineutrino events will produce 1.56 (Here by primary neutron I mean any neutrons produced by the initial neutrino

interaction and any final state interactions of the daughter particles in the target nucleus. This does not include any secondary production of neutrons by interactions of these particles on other nuclei in the detector). For quasielastic interactions only the average is 0.64 for neutrinos and 1.6 for antineutrinos, with almost exactly one extra on average. Although it won't be possible to determine event by event the neutrino type, I can use the different expected neutrino and antineutrino event neutron multiplicity distributions, fitting for the contribution of each to the overall distribution to try to determine the total number of each kind of event.

5.6 Proposed Future Experiments

Currently the best measurement of atmospheric neutrino neutron multiplicity in water come from an unpublished Super-Kamiokande analysis [63], and no measurement exists in heavy water. As Super-Kamiokande has a light water target, this analysis suffers due to the difficulty in detecting the 2.2 MeV gamma from the capture of any produced neutrons on hydrogen, with each neutron capture expected to produce only 7 PMT hits. They were able to detect neutron captures with a 19.3% efficiency, with a 1% chance of a coincident background in any 500 μs time window. Although their simulation systematically underpredicted the measured multiplicity, they showed that the multiplicity increased as a function of the visible energy of the interaction.

One possibility for increasing the neutron detection efficiency in a light water detector is the addition of an isotope with a large neutron cross section. A proposals has been made to load a large water Cherenkov detector with gadolinium [80]. A 0.2% loading in Super-Kamiokande would lead to 90% of captures occurring on gadolinium, with a capture time of about 20 μs. Capture on gadolinium produces

an 8 MeV gamma cascade, which is well above the typical energy thresholds of water Cherenkov experiments.

In addition, a dedicated experiment designed to measure the neutron multiplicity of high energy neutrino interactions has been proposed [6]. This experiment would use the FNAL booster beam as a source of neutrinos and would use a gadolinium doped water Cherenkov detector instrumented with LAPPDs for precision timing. With a well understood neutrino source and large statistics, this experiment would be able to greatly reduce uncertainties in neutron production.

5.7 Outline of Analysis

The goal of this analysis is to measure the neutron multiplicity of high energy neutrino interactions in a heavy water Cherenkov detector. To that end I will identify a set of "contained" atmospheric neutrino events in SNO. Here "contained" means that the interaction occurs within the instrumented volume of the detector and that produced particles deposit all of their energy without leaving it. This is as opposed to "through-going" events where the neutrino interaction occurs in the rock surrounding the detector and produces a charged lepton energetic enough to make it all the way to —and usually straight through—the detector. It is necessary to select contained events in order to be able to detect the neutrons produced in the interaction. In the case of the SNO detector, we specifically want the interaction to occur in the heavy water inner volume so that any produced neutrons capture on deuterium. Furthermore, we want to understand the neutron multiplicity as a function of the event kinematics. Although we cannot directly measure the momentum transfer of the neutrino interaction, as a proxy we can use the visible energy of the event in the detector. We thus want any charged particles to release all of

their energy within the detector so we can accurately measure the visible energy.

For the first step of the analysis, a set of criteria for selecting only contained atmospheric neutrino interactions is developed. Next, in order to understand the event kinematics, we would like to identify as much as possible about the produced particles. For the separation of neutrino and antineutrino events, we saw that quasielastic events had the most significant difference in neutron production. We can try to identify quasielastic interactions by determining the number of particles produced in the event. An algorithm is developed to count visible Cherenkov rings, and classify events as either single-ring or multi-ring. In addition, in order to accurately determine the energy of the produced particles, and to separate out effects due to differences in the secondary production of different kinds of particles, it is necessary to identify the particle type. For this analysis I limit this to the classification of events with one identified particle as either electron-like or muon-like, where muon-like particles are those well below their critical energy and include charged pions, and electron-like events include any showering particles like gammas. Examples of the three classes of events are shown in Figs. 5.2 and 5.3.

Once contained atmospheric neutrino events have been found and have been categorized as either being a single electron-like ring, single muon-like ring, or multi-ring event, a time window following the event is searched for possible neutron capture events, and the multiplicity of these neutron followers is measured. For each category of atmospheric neutrino event, the average multiplicity as a function of the visible energy is calculated. For the single ring events, the energy of the single detected particle can be calculated under the hypothesis that it is an electron or a muon.

From Monte Carlo simulation the expected contribution to the multiplicity dis-

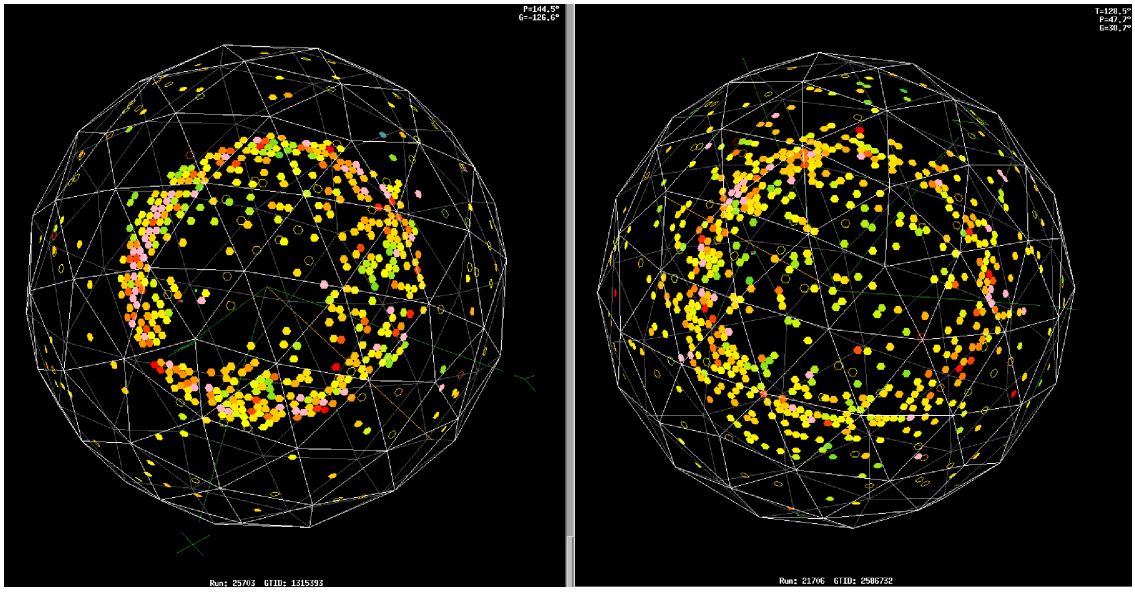

Figure 5.2: Example single ring events in SNO where each dot represents a hit PMT and the color shows the charge measured. The left shows a muon-like ring with a clear outer edge, while the right shows an electron-like ring with more visible showering.

tributions from neutrino and antineutrino interactions can be calculated. These distributions are used as PDFs and the fraction of each in the measured multiplicity distributions are fit for. This gives a measurement of the double ratio $R^{data}_{\overline{\nu}/\nu}/R^{MC}_{\overline{\nu}/\nu}$ and will demonstrate the ability to separate these two event types. Finally, the expected neutron multiplicities in the presence of multinucleon emission contributions to the neutrino-nuclear cross section can be simulated. The change from the nominal expected distribution is used to fit for the strength of this contribution.

There are unique challenges involved in analyzing these atmospheric neutrino events. The highest energy calibration sources deployed in SNO were only a few MeV, and so it is difficult to ensure that the detector behavior is modeled correctly and that analysis tools function as expected at higher energies. Michel electrons from muon decays provide a natural source of high energy events with a known

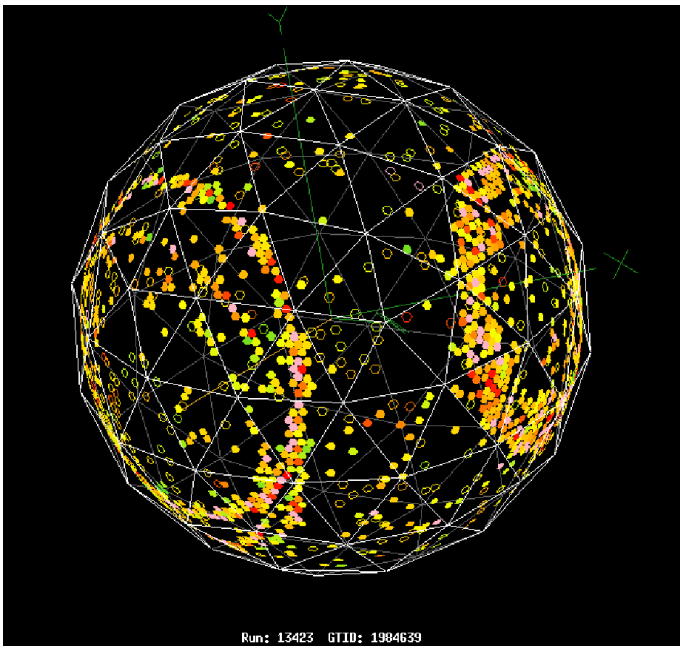

Figure 5.3: An example multi-ring event in SNO. Each dot represents a hit PMT and the color shows the charge measured.

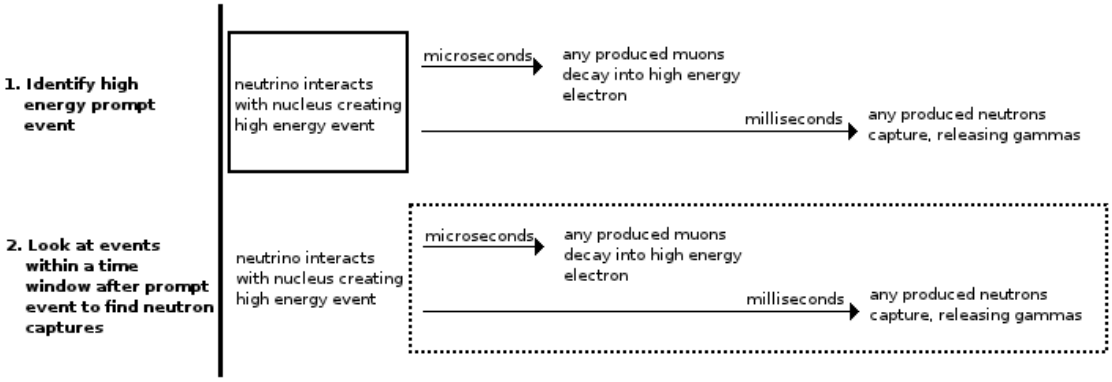

Figure 5.4: Process for finding atmospheric event neutron followers.

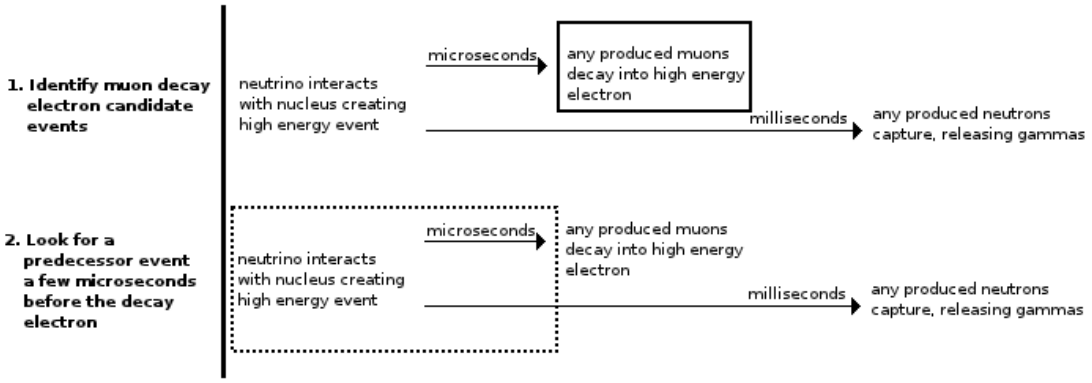

Figure 5.5: Process for identifying sample of atmospheric neutrino events without relying on prompt event selection.

energy distribution that can be used for calibration. These electrons come from the decay of any atmospheric muons or muons produced in neutrino interactions both inside and outside the detector that stop inside the detector. These decay electrons also allow for the identification of a sample of known neutrino interaction events independent of any selection criteria on the interaction event itself, as we know the event immediately preceding a real decay electron must be from a decaying muon, as shown in Fig. 5.5. It is then possible to compare the results of applying the criteria we have developed for selecting neutrino interactions (eventually including those that do not produce muons or decay electrons) on this sample with the prediction from simulation.

Chapter 7 describes how these neutrino interactions are simulated to create a prediction for multiplicity distributions. Chapter 8 describes how a potential interaction event is reconstructed and categorized by number of particles and lepton flavor, and Chapter 9 describes how a sample of contained atmospheric events and neutron followers of those events is then selected. Chapter 10 explains how decay electrons are used to calibrate the analysis and how sources of systematic error are

constrained. Finally Chapter 11 presents the measured multiplicity distributions for each category of event and their dependence on energy, and the result of using these distributions to fit for the ratio of antineutrino to neutrino interactions and for the contribution to the cross section from multinucleon emission.

Chapter 6

The Sudbury Neutrino Observatory

The Sudbury Neutrino Observatory (SNO) was a one kiloton water Cherenkov detector. It used a heavy water target, giving it a unique ability to detect solar neutrino flavors. It was designed to resolve the solar neutrino problem and provide direct proof of neutrino oscillations.

6.1 Physics

Neutrinos were detected in SNO through three different interactions. They can elastic scatter off electrons like in Super-Kamiokande, but can also undergo charged-current and neutral-current interactions off the deuterium in the heavy water. In the charged-current interaction,

$$\nu_e + d \rightarrow p + p + e^-, \tag{6.1}$$

the exchange of a W-boson converts a neutron in the deuterium to a proton. The energy threshold for this interaction is 1.44 MeV. This only occurs for the electron flavor of solar neutrinos as these neutrinos' energy is not sufficient to create the heavier leptons. In the neutral-current interaction,

$$\nu_x + d \rightarrow p + n + \nu_x, \tag{6.2}$$

the deuterium is broken up into a neutron and a proton through the exchange of a Z-boson. Here the energy threshold is the binding energy of the deuterium of 2.2 MeV. This interaction can occur for all flavors, and unlike for elastic scattering off electrons, is equally sensitive to all of them.

The elastic scattering and charged-current interactions create a scattered electron, with an energy and direction related to that of the incident neutrino. In particular, the proton in the charged-current interaction carries away very little of the energy making the electron energy closely related to the neutrino energy. The scattered electron is detected through the Cherenkov radiation it produces.

Cherenkov radiation is produced when a charged particle travels faster than the speed of light in the material. The number of photons produced is given by

$$\frac{d^2N}{dEdx} = \frac{2\pi\alpha}{\lambda^2}\left(1 - \frac{1}{\beta^2 n(\lambda)^2}\right) \tag{6.3}$$

where $n(\lambda)$ is the wavelength dependent index of refraction of the material. For a given wavelength, the number of photons produced scales linearly with the energy of the charged particle. The radiation comes out in a cone pointed in the direction

of the particles motion, with an opening angle

$$\cos\theta_c = \frac{1}{\beta n(\lambda)}. \tag{6.4}$$

In heavy water, the index of refraction is approximately 1.33, which gives a Cherenkov angle of 42° for relativistic particles and an energy threshold of 767 keV for electrons.

In addition to producing Cherenkov radiation, electrons and muons can interact with the material they're traveling through and produce bremsstrahlung photons. At higher energies the bremsstrahlung process dominates over ionization. The energy at which the two are equal is called the critical energy. As the amount of energy released by bremsstrahlung radiation is proportional to $1/m^2$, the critical energy for muons is much higher than for electrons, and muons contained within the SNO detector will lose almost all of their energy through ionization. Thus it is possible to distinguish muons and electrons by looking at the pattern of PMT hits in an event — muon events will produce much sharper rings at the Cherenkov angle, while electron events will be much more diffuse due to multiple scattering and bremsstrahlung.

On the other hand, the neutral-current interaction produces no charged particles above Cherenkov threshold, and so the SNO detector must be able to see the neutron by detecting the gamma rays produced when it captures on a nucleus. In a normal water Cherenkov experiment, neutrons capture on hydrogen creating a 2.2 MeV gamma, which is very difficult to see due to the broad energy resolution of a Cherenkov detector and the presence of radioactive backgrounds of very similar energies. SNO ran in three phases with different neutron detection capabilities. In the first phase ("D_2O phase") the target was pure D_2O, and neutrons were detected by the 6.25 MeV gamma produced by their capture on deuterium. Although this

was energetic enough to see, the capture cross section on deuterium is low, allowing many of the neutrons to escape the target volume. The second phase ("salt phase") involved the addition of 0.2% by mass of sodium chloride salt to the heavy water target. Chlorine has a much higher neutron capture cross section, and produces a gamma cascade with a total energy of 8.6 MeV. In the third phase ("NCD phase"), 40 ^{3}He proportional counters were installed in the heavy water which could directly measure the capture of neutrons on helium. This thesis will use data from the first two phases.

6.2 Detector

The SNO detector was located in the Creighton mine in Sudbury, Ontario. It was 6800 feet underground in the mine, giving it an effective 6000 mwe overburden, which reduced the muon flux to approximately three per hour in the detector. The target volume was 1 kiloton of D_2O contained within a 6 meter radius acrylic vessel (AV). The AV was surrounded by 7.4 kilotons of ultrapure water to shield it from background radiation from the rock, and the target volume is viewed by 9438 PMTs held within a 8.9 meter radius spherical PMT support structure (PSUP). In addition, 91 outward looking PMTs (OWLs) look out into the lightwater region, allowing the rejection of through going muon events. The PMTs are surrounded by 27 cm diameter light concentrators, which gives a total effective coverage of 54%. A diagram of the detector is shown in Fig. 6.1.

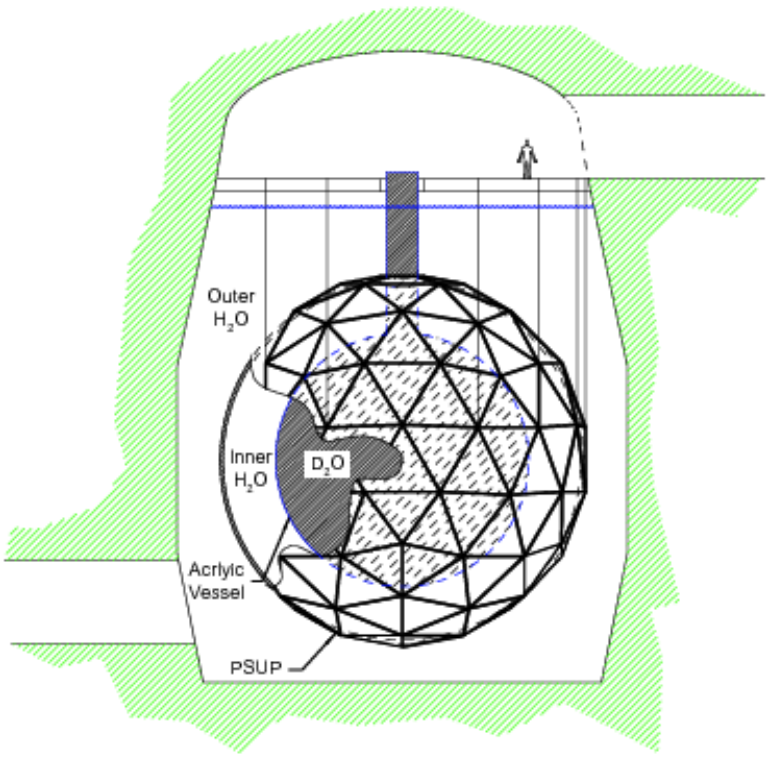

Figure 6.1: Diagram of the SNO detector. Figure from [7].

6.3 Electronics

Photons produced by the Cherenkov radiation of charged particles were detected by the 9456 Hamamatsu R1408 20 cm PMTs surrounding the AV. Single photoelectrons are amplified through the dynode stages creating a measurable charge pulse. The goal of the electronics was to read out the charge and time of the pulse each time a PMT fires.

The front end electronics were contained within 19 crates sitting on a deck above the detector. Each crate instrumented 512 PMT channels. The PMT Interface Card (PMTIC) provided the high voltage and receives the signal from 32 PMTs. They were then processed in the Front End Cards (FECs). Each FEC contained

four daughterboards (DB), which each handle eight channels. The DB contained three kinds of custom application specific integrated circuits (ASICs) that applied a threshold to the PMT signal, integrated the charge of the pulse, and measured the relative time of the hits. The charge was measured with two different gains over two different length time windows, approximately 60 ns and 390 ns long.

In addition to channel by channel thresholds, there was a detector wide trigger threshold in order to limit the amount of data read out. Each time a PMT signal crossed its threshold, four different pulses were sent to the trigger system to be summed: a 20 ns and a 100 ns square pulse, and a low and high gain shaped PMT pulse. The trigger pulses from all channels were summed on the analog trigger boards (MTCAs), and then those that cross a set threshold were sent on to the digital trigger board (MTCD). The MTCD checked the fired triggers against a mask to determine whether to send a detector wide "global trigger" that would tell all the front end electronics to save and read out all PMT pulses recorded for a time window around it. For physics analyses, the trigger signal used was the sum of the 100 ns square pulses, called NHIT100.

When the front end received the global trigger signal, the integrated charges and time measurement were stored in each channel's 16 cell analog memory. The FEC then iterated through the hit channels and digitized the signals using four 12 bit ADCs. The digitized charges were then stored in 4 MB of RAM located on the FEC, along with a trigger id that could be matched to information read out from the MTCD about the trigger type and time. The data was read out through a central computer, which was connected to a VME crate through a Motorola 68040 processor (eCPU). The VME crate was connected to the 19 front end crates through pairs of translator boards called XL1s and XL2s, which extended the VME address

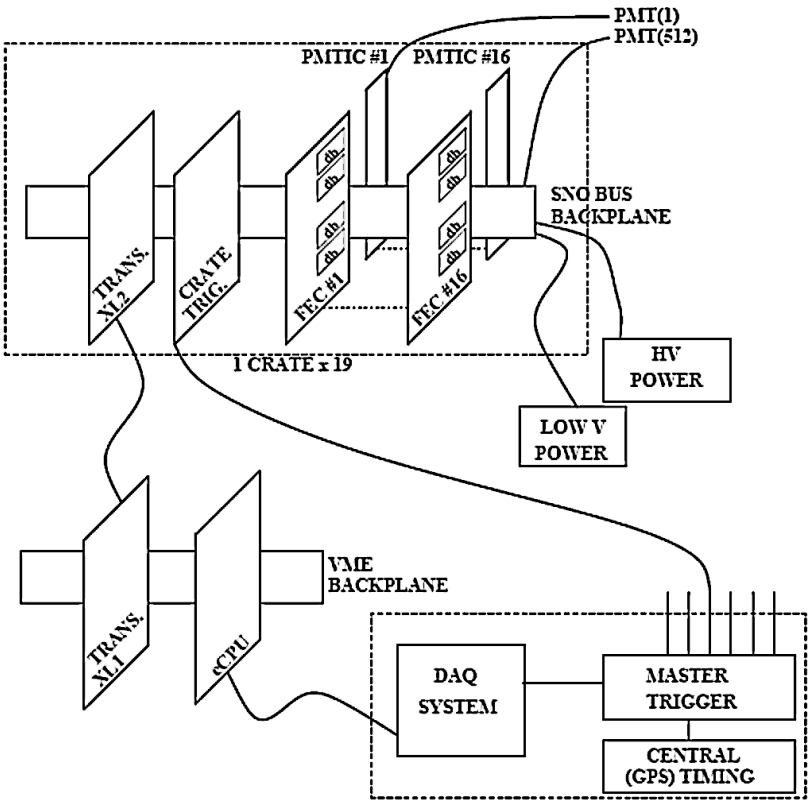

Figure 6.2: The SNO front end electronics.

space so that the whole front end was memory mapped and could be read out directly from the DAQ computer. An overview of the DAQ is shown in Fig. 6.2.

6.3.1 SNO+ Upgrade

The SNO experiment was designed for a heavy water target with a high energy threshold. The expected detector trigger rate was tens of Hz, and the electronics could handle a max data rate of 2 Mb/s. A new experiment, SNO+, is being developed that will use the same detector but with a scintillator target. This allows SNO+ to have a much lower energy threshold than SNO, low enough to see even the lowest energy pp solar neutrinos. In addition, by adding tellurium to the target

it is possible to investigate whether neutrinos are Majorana or Dirac particles by looking for neutrinoless double beta decay.

Scintillation produces significantly more light than Cherenkov radiation, and SNO+ expects to get around 500 pe per MeV with a pure scintillator target, compared to about 8 for SNO. In addition, the energy threshold creates a much higher event rate. For this reason, the data acquisition electronics needed to be upgraded in order to handle the increased data rate.

The upgrade plan is shown in Fig. 6.3. The VME extending XL1 and XL2 translator boards are replaced with a new board called the XL3 that sits in each front end crate. Each XL3 reads out its own crate, then autonomously pushes the data over ethernet to the DAQ computer. We use a Virtex 4 FPGA with an embedded PowerPC to do most of the processing on the XL3. The FPGA holds a VHDL state machine that implements the front end crate's custom SNOBUS protocol with very precise timing. The data is then passed over to the embedded processor, where we can use C code to easily control the ethernet output and any extra functionality. We implement a full TCP-IP stack using the light weight IP library (LWIP). In addition, the flexibility offered by programming in C allowed us to run most of the electronics testing and calibration software locally on each XL3. Each XL3 has a max data rate of around 14 MB/s, for a detector total of about 250 MB/s, which is equivalent to about 2 million PMT hits per second.

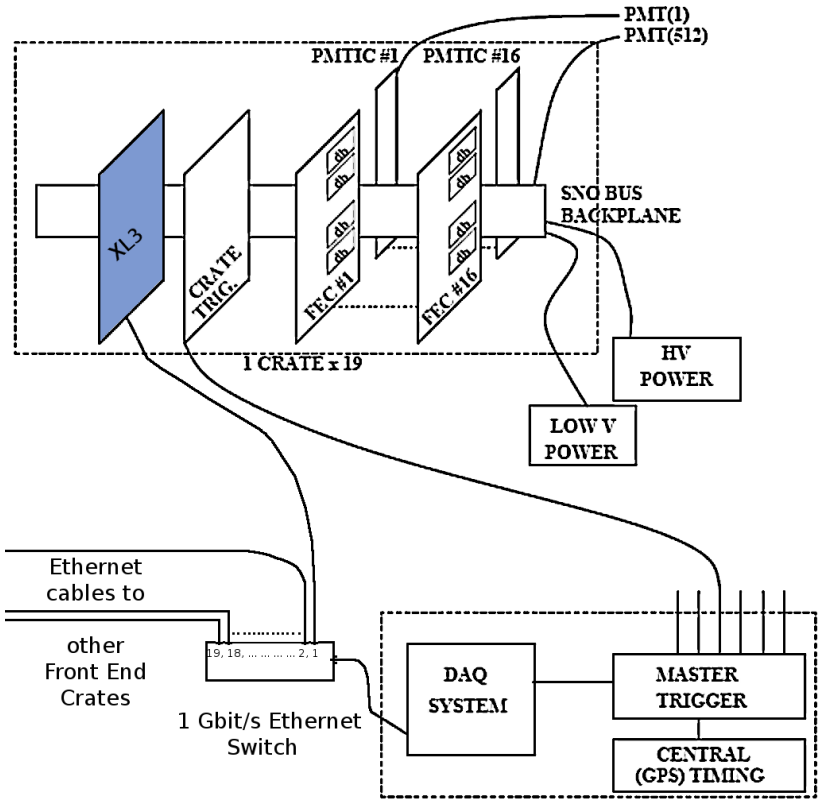

Figure 6.3: The SNO+ front end electronics.

Chapter 7

Simulation of Atmospheric Neutrino Events in SNO

7.1 Atmospheric Neutrino Flux

In this thesis I use the Bartol04 calculation of the atmospheric neutrino flux [11]. There are many complications in exactly calculating the expected flux. Lower energy cosmic rays are affected by the solar wind, and the Earth's geomagnetic field introduces position dependent changes in the flux. The Bartol04 flux is the result of a 3D Monte Carlo simulation and provides a Sudbury specific prediction for the neutrino flux as a function of energy and zenith angle for various flavors of neutrinos and anti-neutrinos [11]. The calculations are made specifically for Sudbury, Canada, and the predicted flux at SNO is given in Table 7.1.

The main uncertainties in the flux calculation come from the hadron production. In the energy range of interest, the uncertainty on the absolute flux is around 15%. A much more precise prediction can be made for ratios of fluxes as parts of these

	Flux ($m^{-2}s^{-2}$)
ν_e	10973.1
$\overline{\nu}_e$	9452.8
ν_μ	21304.5
$\overline{\nu}_\mu$	21283.6

Table 7.1: Flux predicted by Bartol04 [11] integrated over energy and solid angle, from 0.1 GeV to 10 GeV. Given in units of $m^{-2}s^{-1}$

uncertainties cancel. The $\nu/\overline{\nu}$ and ν_e/ν_μ ratios are known to within 1% for energies under a few GeV [81].

Three flavor neutrino oscillation was simulated using the equations given in Section 5.1. The production height is modeled as a single Gaussian distribution using low energy predictions from Ref. [82]. The neutrino mixing parameters used, from Ref. [83], are

$$|\Delta m^2| = 2.43 \pm 0.06 \times 10^{-3}\ \text{eV}^2 \tag{7.1}$$

$$\sin^2\theta_{12} = 0.308 \pm 0.017 \tag{7.2}$$

$$\sin^2\theta_{23} = 0.437^{+0.033}_{-0.023} \tag{7.3}$$

$$\sin^2\theta_{13} = 0.0234^{+0.0020}_{-0.0019} \tag{7.4}$$

with $\Delta m^2 = m_3^2 - (m_2^2 + m_1^2)/2$.

7.2 Event Simulation

7.2.1 GENIE

To simulate the interactions of neutrinos with various nuclei in the detector I use the GENIE software package [84]. GENIE is a ROOT based neutrino event generator being developed as the canonical generator for events from neutrinos of all flavors on any target over a wide energy range. It is currently being used by T2K, NOvA, MINERvA, MicroBooNE, ArgoNEUT, LAGUNA-LBNO, LBNE, INO, IceCUBE, NESSiE and others. The main design principles are similar to older generators like NUANCE and NEUT.

The nucleus is modeled using the Bodek-Ritchie version of the relativistic Fermi gas model [85]. Elastic, inelastic, resonant, and coherent interactions are all simulated separately, and for all but coherent interactions, the impulse approximation is used so it is assumed that the scatter can be considered to be off a single nucleon. Quasi-elastic scattering is modeled using the standard Llewellyn-Smith model as described above, with the BBBA2005 model of the electromagnetic form factors and the axial form factor assumed to have a dipole form [86, 87]. Single pion production is assumed to be through resonant interactions using the Rein-Sehgal model [88], and inelastic scattering using the Bodek-Yang model [89]. Hadronization for neutrino interactions on nucleons is modeled using the AGKY model at low invariant mass and PYTHIA at higher invariant mass [90]. Particles produced in the primary interaction are propagated through the nuclear medium using the INTRANUKE simulation of intranuclear hadron transport.

Meson exchange current contributions can be added using the Dytman model for the leptonic kinematics. This model is made to be tunable to electron scattering

	ν_e	$\overline{\nu}_e$	ν_μ	$\overline{\nu}_\mu$	ν_τ	$\overline{\nu}_\tau$
Total	71.7	20.6	88.2	31.0	12.2	5.8
CC	46.3	11.5	55.5	16.9	0.2	0.1
NC	17.7	6.7	23.4	10.7	10.6	5.0

Table 7.2: Interactions per year expected within heavy water volume of SNO from atmospheric neutrinos of 0.1 to 10 GeV.

inclusive cross section data, where the MEC contribution is added as a Gaussian distribution between the quasielastic and resonant peaks. It attempts to treat electron and neutrino scattering similarly. In GENIE the strength of the MEC contribution is tuned to agree with MiniBooNE results, and is made to linearly decrease from 1 to 5 GeV in order to agree with NOMAD data [91].

We provide GENIE with a simplified ROOT geometry including everything inside the PSUP. We assume the acrylic takes the simple form $C_4H_6O_2$. The total event rate within the D_2O volume for the first phase of SNO is given in Table X. Over the 306.4 live days of the D_2O phase we expect a total of 192.4 events within the acrylic vessel and 504.5 events within the PSUP.

We can use GENIE to propagate uncertainties in the neutrino cross section and nuclear medium effects. GENIE has the ability to reweight generated events based on possible retunings of its parameters. The parameters adjusted in this thesis are given in Table 7.3, along with their fractional uncertainty. For quasielastic charged-current (QECC) and resonant charged and neutral-current scattering we adjust the axial and vector form factors, which affect both the cross section normalization as well as the shape as a function of Q^2. For deep inelastic scattering we adjust the parameters of the Bodek-Yang model. For the intranuclear effects we adjust the mean free path of nucleons and pions, as well as the probability of charge exchange and absorption. For simplicity, the reweighting factor is found for each parameter

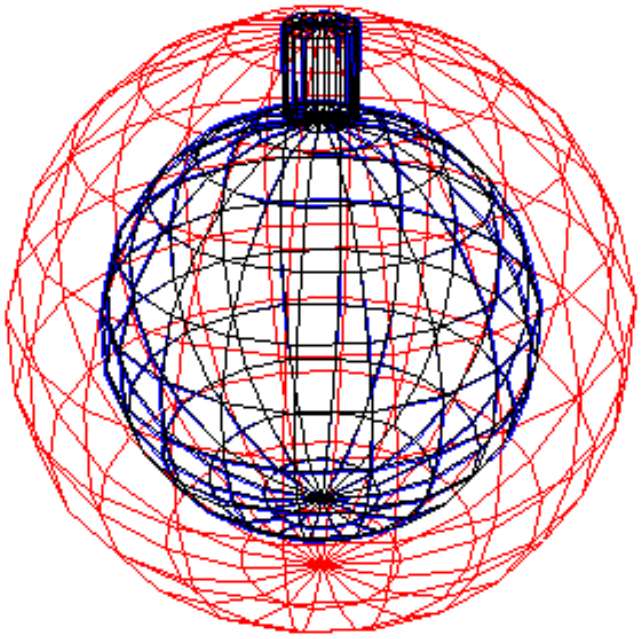

Figure 7.1: ROOT geometry for SNO detector. PSUP is modeled as sphere at 8.5 m, the acrylic vessel as a 5 cm thick sphere at 6.05 m with a 1.22 m tall chimney.

in Table 7.3 individually adjusted to plus or minus one sigma from its standard value.

7.2.2 RAT is an Analysis Toolkit

The SNO experiment used a Fortran package called SNOMAN for their simulation and analysis. SNO+ is using a newer C++ based package called RAT, which was originally developed for the Braidwood collaboration. RAT is built on Geant4 and ROOT, and like SNOMAN is designed to model physics processes on a very detailed

Parameter	Fractional Uncertainty
QECC axial mass	-15% +20%
CC/NC resonance axial mass	±20%
CC/NC resonance vector mass	±10%
QECC Pauli suppression	±35%
DIS nuclear modification	-
A_{HT} parameter in BY model	±25%
B_{HT} parameter in BY model	±25%
C_{V1u} parameter in BY model	±30%
C_{V2u} parameter in BY model	±40%
Nucleon / pion mean free path	±20%
Nucleon / pion charge exchange probability	±50%
Nucleon / pion absorption probability	±20%

Table 7.3: Parameters adjusted in GENIE to model cross section uncertainty, along with fraction uncertainties.

level, with every photon produced being individually tracked through the detector. The SNO+ version of RAT has been verified against SNOMAN, which itself has been shown to reproduce SNO calibration data. In this thesis all simulation and analysis of the SNO detector is done using a SNO detector model within RAT.

One issue with the version of RAT used in this thesis was the difficulty in using run-by-run channel status. Throughout the D_2O and salt phase, various electronics channels and PMTs were flagged as malfunctioning, disabled, or repaired. This analysis uses the detector status in salt run 20674, with 450 channels marked as offline. If the average number of offline channels during the running period was different than this, it will cause an energy scale bias. I can estimate this effect by comparing the PMT hit count spectrum of neutron capture events in simulation and data.

An issue was also found with neutron capture simulation in Geant4. The high precision neutron capture modules are mostly used for medical simulation where

averages are much more important than event by event accuracy. For captures where the nucleus de-excites via the emission of multiple gammas, the final state simulation is designed to reproduce the right average gamma multiplicities, but for any individual event the gammas are selected randomly. Thus not only are individual events not representative, they do not even conserve energy. It is possible to instead force Geant to use a photon evaporation model, but this often ends up creating a single gamma which further produces too few electrons leaving them with too much kinetic energy. Instead I added a new final state process for captures on ^{16}O and ^{35}Cl based on the implementation used in SNOMAN. For captures on Oxygen, it selects from two possible decay chains. For Chlorine, branching ratios for 75 energy levels from Ref. [92] are used to simulate the cascade down to the ground state. After this modification, RAT and SNOMAN agree on the detection efficiency of neutrons to within 1%.

Chapter 8

Event Reconstruction

8.1 Low Energy Event Reconstruction

I reconstruct neutron capture candidate events using the standard "water fitter" implemented in RAT. This fitter was designed for use in the water fill phase of the SNO+ experiment, but is equally effective on SNO data. It fits for event positions using a 1-dimensional PDF for hit time residuals assuming a straight path from the event vertex to each PMT, so

$$t_{res} = t_{PMT} - t_{path} - t_{event}, \tag{8.1}$$

$$t_{path} = d_{target} \times v_{target} + d_{AV} \times v_{AV} + d_{H_2O} \times v_{H_2O}. \tag{8.2}$$

The group velocity of 400 nm photons is used as the speed in the target, AV, and outer H_2O volumes. A time residual PDF is generated by simulating 6 MeV electrons throughout the detector.

In order to reduce the effect of noise hits and scattered light, only the hit times

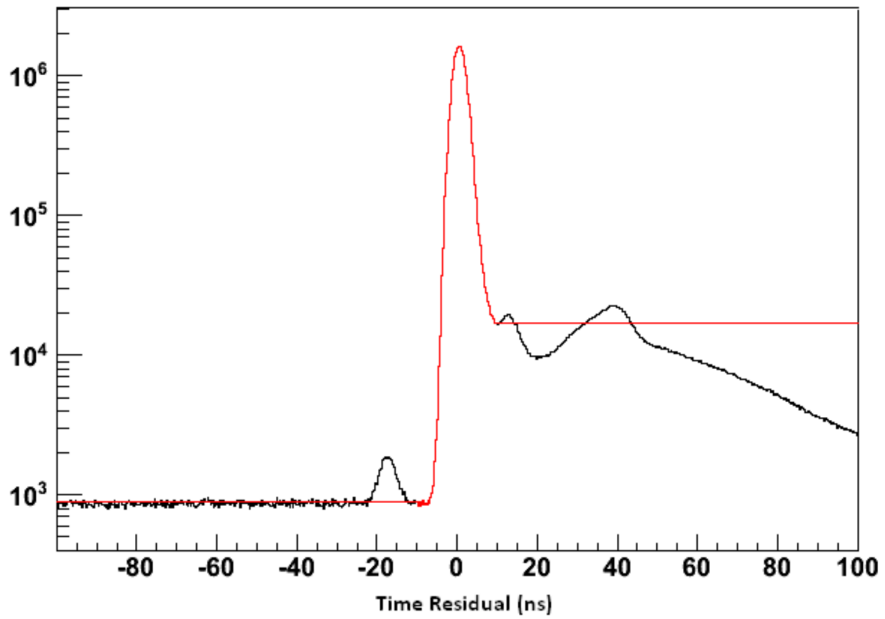

Figure 8.1: PDF of time residuals for simulated 6 MeV electrons. In black is the raw time distribution from simulation, while red shows the model used for the PDF in the reconstruction, which simplifies early and late hit contributions.

from PMTs within 50 ns of the median hit time are considered.

The position resolution for 6 MeV electrons is found to be about 25 cm. The performance of the position reconstruction has been compared to the standard SNO position fitter, and was found to have equivalent resolution, bias, and failure rate [93]. In turn, the SNO position fitter has been extensively studied with calibration source data. The water fitter next reconstructs event energies using a radial dependent PMT hit count lookup table.

8.2 High Energy Event Reconstruction

I want to determine as much about the prompt neutrino event as possible in order to make the best guess as to what kind of interaction the neutrino underwent and exactly what neutron distribution we expect. Compared to the events of interest for SNO's solar analysis, our prompt events are much higher energy and often involve multiple particles. For the simplest quasielastic interactions we expect only a high energy lepton plus a proton or a neutron to be produced. Neither the proton nor neutron will create Cherenkov radiation, and so identifying when there is only a single particle in the prompt event will allow us to select for quasielastic events and reject other types of interactions.

Although the SNO+ water fitter is sufficient for simple low energy events, it is not as helpful with atmospheric neutrino events. It cannot deal with events with multiple particles, and has very poor resolution at high energies. In addition, it gives us no information about the number of particles in the event, nor can it distinguish electrons from muons. For SNO, most high energy fitters were designed to look for through-going muon events and use the characteristic entrance and exit points to direct the fit. These will not exist for a contained event, and so a new reconstruction method is needed.

In order to determine the number of particles in an event, we will use the characteristic shape of Cherenkov radiation. Each charged particle over threshold will produce a cone of Cherenkov light, and the intersection of this cone with our sphere of PMTs produces a ring. Determining the number of particles then just becomes counting the number of rings in an event. I find rings using the Hough transform technique [94]. The circular Hough transform maps circles of a specific radius to peaks at each circles' center. Given a radius R to search for, each point in the origi-

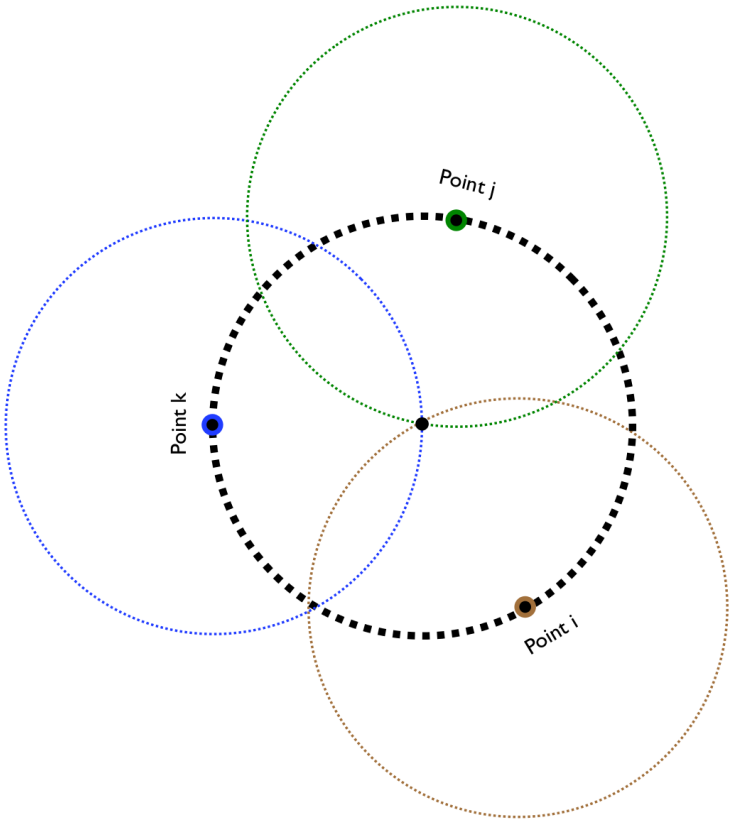

Figure 8.2: The Hough transform maps circular patterns to peaks. A circle is drawn around each point, overlapping at the center of the circle of points. Figure from [8].

nal space is mapped to a circle of radius R centered at that point. Points originally arranged in a circle will have their mapped circles overlap at the center, creating a peak, as shown in Fig. 8.2.

As I will be using the results of the Hough transform as a seed for further fitting, I can coarsely grid the possible ring centers to be checked. This makes it possible to invert the implementation of the transform — for each possible ring center I will count the number of hits within a certain radial bin. This implementation is much faster when dealing with events with a high number of hits.

As the Hough transform is made to work for continuous circles on a plane, it

is important to ensure its accuracy when working with scattered points around a circle projected onto a sphere. The discontinuity of our circles are mitigated by using wide radial bins. I transform the positions of the PMTs to spherical coordinates to make a two dimensional map in ϕ and $\cos\theta$. Instead of circles, I am fitting for the intersection of the Cherenkov cone with the sphere of PMTs on the PSUP. This intersection only makes a circle for Cherenkov cones directed exactly radially out from the center of the sphere. For this Hough transform fit, I will assume that every event is directed radially outward.

I bin the Hough transform space in ϕ, $\cos\theta$, and radius r, and for each bin sum the amount of charge from PMT hits within the radial bin of that position on the PSUP. The highest point in the Hough space is found, and then it is determined whether the point represents a ring or if it is false positive using three parameters. First, I calculate the solid angle covered by this radial bin, and the density of charge in the ring. If the density of charge is too low, the ring is thrown out. Next, I calculate the total charge from the whole event and the average charge density. If the density in the ring is not significantly higher than the average density, the ring is thrown out. Finally, I find the ϕ distribution of charge around the ring, and compare using a KS test to a flat distribution. The Hough transform often fails by adjusting the ring so that a single spot of high charge hits happens to fall inside one side of it, especially when looking for a secondary ring in a multi-ring event. This test helps to reject these rings, although the cut must be made fairly loose since non radial events will produce non circular intersections on the PSUP. For secondary rings, I also check that the charge and charge density outside 60 degrees of the first ring is above a threshold.

Once the first ring has been found, I do a full position, energy, and particle

identification fit before testing for a second. I fit simultaneously for the event position, time, energy, and ϕ and $\cos\theta$ for the intersection point on the PSUP (center of the Cherenkov ring). The design is based on the FTI fitter developed by Chris Kyba [95]. It uses a similar likelihood function and a modified version of the FTI time PDF, while having a completely new hit probability PDF. I do a maximum likelihood fit where the likelihood is given by

$$L(\vec{x}) = \prod_{i}^{\text{unhit pmts}} [P(\text{unhit}|\vec{x})] \prod_{i}^{\text{hit pmts}} [P(Q_i, T_i(\vec{x})|\vec{x})], \tag{8.3}$$

where $\vec{x}$ are the fitted parameters listed above, Q_i is the QHS charge of the ith PMT, and $T_i(\vec{x})$ is the time residual of the ith PMT. Given a value for $\vec{x}$, an expected number of photoelectrons (pe) is calculated for each tube, $\lambda_i(\vec{x})$. Then we can write

$$L(\vec{x}) = \prod_{i}^{\text{unhit pmts}} \left[\sum_n P(\text{unhit}|n)P(n|\lambda_i(\vec{x})\right] \tag{8.4}$$

$$\times \prod_{i}^{\text{hit pmts}} \left[\sum_n P(Q_i|n)P(T_i(\vec{x})|n)P(n|\lambda_i(\vec{x}))\right], \tag{8.5}$$

where the actual number of pe is assumed to have a Poisson distribution, so $P(n|\lambda_i(\vec{x})) = \frac{e^{-\lambda}\lambda^n}{n!}$.

The time residual PDF, $P(T_i(\vec{x})|n)$, is a variation on the one developed in Ref. [95]. The single pe PDF is parameterized as a prompt and prepulse peak, plus a uniform noise contribution throughout the PDF and a flat scattering contribution for $t > 0$. The relative contributions of each of these and the position and width of the two peaks is determined from Monte Carlo. Multi-pe hits are expected to be earlier, as the PMT will fire on the first photon that hits it and thus record the earliest time. To model this, each contribution is scaled based on the number of

pe. The probability of a scattered late hit time for a PMT with n pe is given by p_l^n, where p_l is the probability of a late hit. The probability of a prompt peak time is then

$$p_p(n) = (p_p + p_l)^n(1 - p_l^n) = (p_p + p_l)^n * p_l(n), \tag{8.6}$$

where p_p is the probability of a prompt time hit, and similarly the probability of a prepulse peak time is

$$p_r(n) = (p_r + p_p + p_l)^n(1 - p_p(n) - p_l(n)). \tag{8.7}$$

In addition to changing the proportions of late / prompt / prepulse hit times, I modify the time pdf by having multiple pe also changes the shape of the prompt and prepulse peaks from a simple Gaussian curve. These peaks are expected to become skewed to earlier times as well. I model this effect on the prompt pulse by randomly drawing n times from the standard Gaussian shape and picking the earliest time to fill a new shape, which is then scaled appropriately to make the new prompt peak. The charge PDF $P(Q|n)$ is easily generated from Monte Carlo, and for pe greater than 5 is fit to two half-Gaussian distributions centered on the mode charge.

The remaining piece is the calculation of the expected mean pe λ_i given a position, direction, and energy. As mentioned earlier, the events of interest in this analysis don't have the simplicity of a through-going muon, which allowed all possible events to be parameterized by only the impact parameter. It is thus impractical to create a look up table, and so a new method has been developed for this analysis. I create an angular PDF that will allow the calculation of the expected λ for a PMT given any event parameters. At higher energies muon events are complicated by

the fact that the track length can be as long as the detector, and this length is dependent on the energy. This makes even the angular distribution of hits dependent on the position, direction, and energy of the event. Thankfully, the situation can be simplified by noting two properties of muon events.

First, since at these energies muons are well below their critical energy, tracks for muons of a given energy are similar. Fig. 8.3 shows the displacement of muons from their creation point as a function of their current energy for simulated muons generated at 1 GeV. The energy loss is very consistent, as is the photon creation rate. Second, most of the light produced in the event is generated near the muon track. Fig. 8.4 shows the perpendicular distance from the muon track for the creation position of all photons that created a PMT photoelectron. Thus I can create a 2-D PDF of pe's as a function of position along the muon track where the photon originated, and the angle between the muon track direction and the hit PMT, shown in Fig. 8.5. The x-axis gives the distance from the end point of the track. We can see the Cherenkov angle decreasing near the end of the track where the muon slows down. Then given a muon energy it is possible to predict the length of the track. Given the position and direction of the track we can calculate for each step along it the expected contribution to the total pe at each PMT.

This process does not work well for electrons. Radiative processes makes the rate of energy loss differ drastically from event to event, and photons can be generated very far from the track by secondaries. On the other hand, the average track length for electrons is much smaller, so these events can be approximated as points. I instead create a 2-D PDF of pe's as a function of both the angle between the interaction position and the hit PMT as well as the electron energy.

Once a ring has been identified, I fit it for both an electron and a muon hypoth-

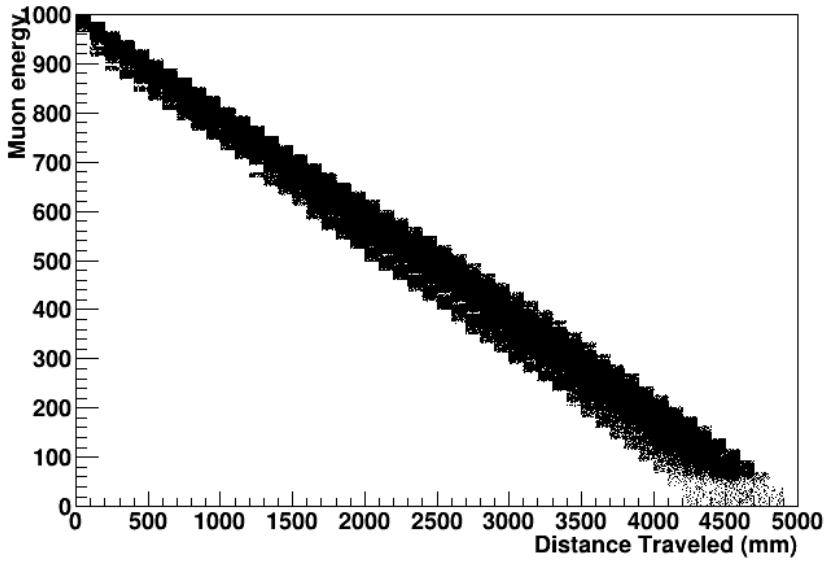

Figure 8.3: Muon energy after traveling the given distance for muons generated at 1 GeV.

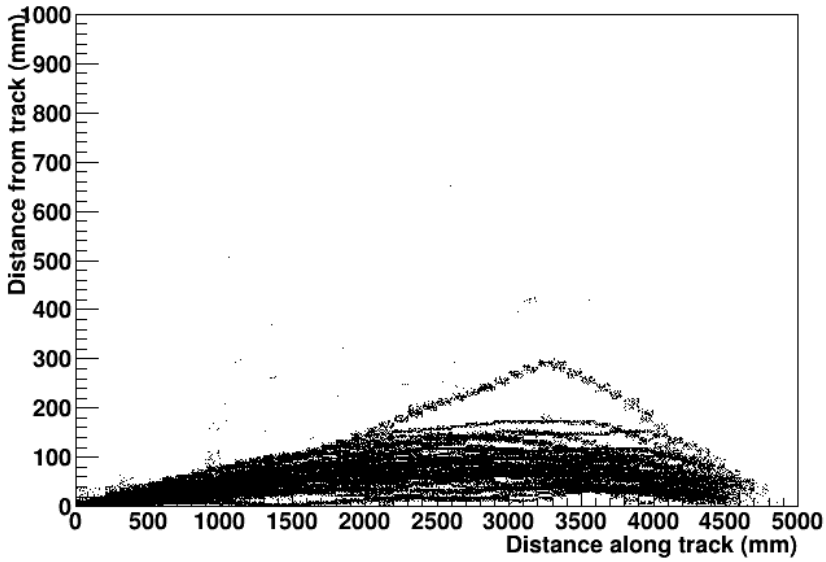

Figure 8.4: Perpendicular distance from muon track for photons generated by 1 GeV muons.

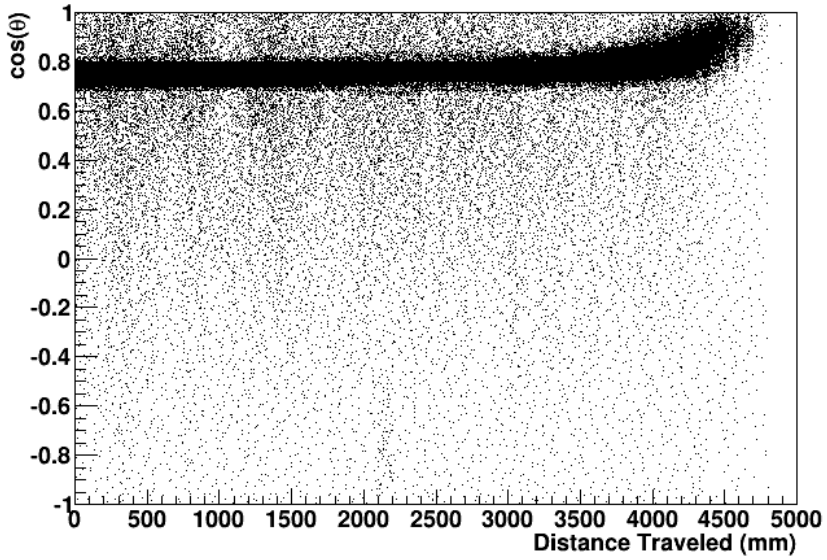

Figure 8.5: Photon production PDF for muons.

esis and find the likelihood for each fit. If the total likelihood difference is greater than 50, the fit with the better likelihood determines the predicted particle type. Otherwise, I calculate a charge-only likelihood and use that to determine particle type.

Although it would be preferable to allow the energy to freely float in our fit, I found that the non-Poissonian nature of multi-pe hits cause inaccuracies in the PMT charge predictions that lead to significant biases in the fitted energy. I instead use a radial and particle-type dependent charge lookup table to fix the energy at any given fit position.

Once the ring has been identified as either electron- or muon-like, I can subtract its charge from the event and look for a second ring. I calculate the mean predicted charge in each PMT and subtract it from the actual charge, and then repeat the Hough transform procedure. Here the KS test will help reject false rings where a

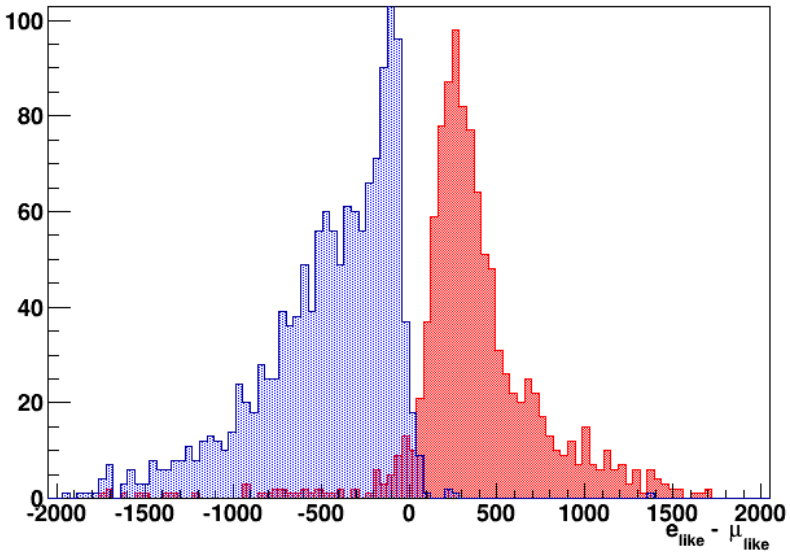

Figure 8.6: PID likelihood parameter for simulated muons (red) and electrons (blue).

high charge area of the old ring remains.

The ring fitter has been run on simulated electrons and muons with energies ranging from 20 to 1000 MeV (100 to 1000 MeV for muons) to determine its performance on single ring events. The results are shown in Fig. 8.7. The ring counting works very well for events under 100 MeV, and becomes slightly less accurate at higher energies, especially for electrons. The particle identification is the opposite, increasing from less than 84% accurate at 50 MeV to better than 98%. The position resolution starts at around 15 cm and gets worse with increasing energy, up to 35 cm at 1 GeV. The angular resolution is found to increase drastically with energy, with an average fit-true angle of 16 degrees for 20 MeV electrons down to 2.8 degrees for 1 GeV electrons. For muons, the average angular difference is 10.8 degrees for 100 MeV muons down to 2.3 degrees for 1 GeV muons.

I next looked at the performance of the fitter on atmospheric neutrino Monte

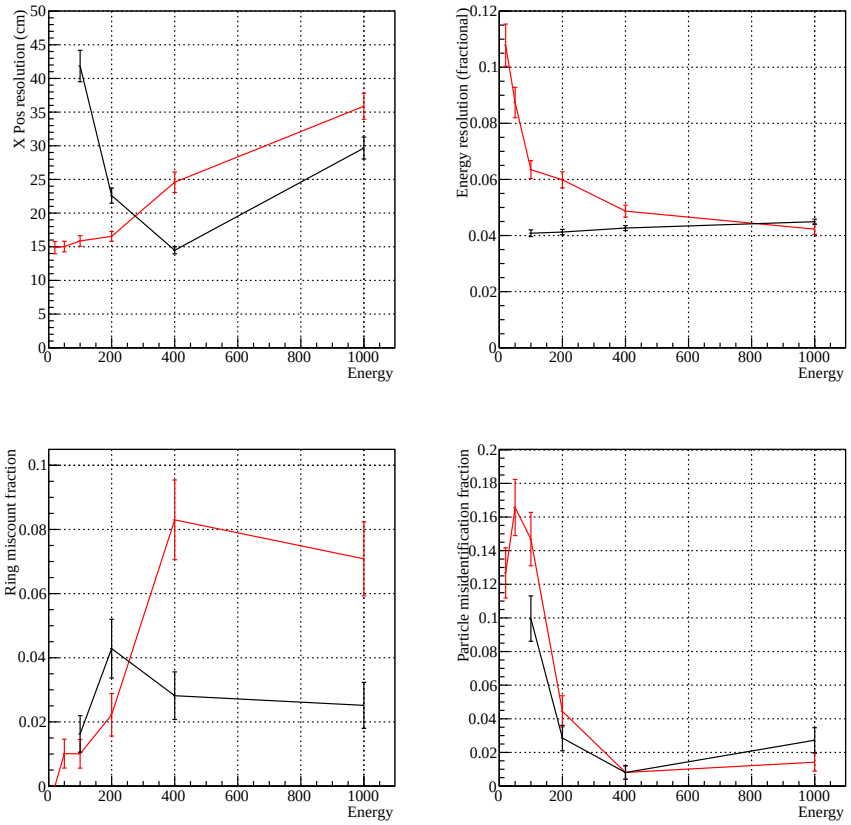

Figure 8.7: Position resolution (top left), energy resolution (top right), ring counting mistag fraction (bottom left), and particle identification mistag fraction (bottom right) for simulated electrons (red) and muons (black) inside the AV at various energies.

Carlo. The position resolution for all atmospheric events and for only those with a true position within the AV is given in Table 8.1. I find that for events with a fitted radius less than 5.5 m, 97% have a true position within the AV and 76% of events with a true position inside the AV (and 98% of those inside 5.5 m) are accepted.

Eventually we want the ring counting and particle identification to tell us something about the neutrino interaction. For quasielastic charged-current events we know most precisely what the interaction products should be, and so for example

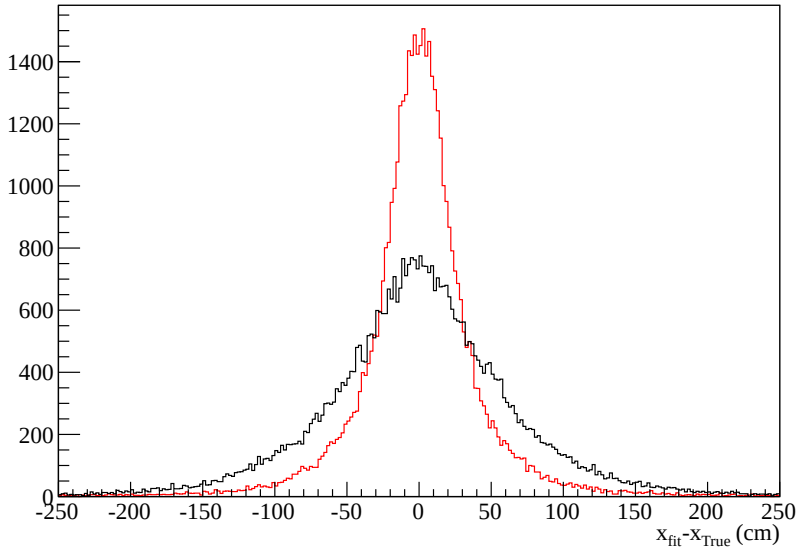

Figure 8.8: Fit minus true x position for the ring fitter developed for this thesis (red) compared to the SNO+ water fitter (black) for simulated atmospheric neutrino events throughout the PSUP.

	Full volume		Inside AV	
	Ring Fitter	Water Fitter	Ring Fitter	Water Fitter
σ_x	50.5	73.0	44.7	70.7
σ_y	49.9	72.8	44.5	70.4
σ_z	47.8	68.5	42.2	65.8
σ_r	48.1	72.5	40.8	65.8
$< \Delta r >$	-8.3	-0.1	0.8	21.4

Table 8.1: Position resolution in cm for the ring fitter developed for this thesis compared to the SNO+ water fitter for simulated atmospheric neutrino events throughout the PSUP or within the AV. Here σ is the standard deviation to the residual distribution, and not the width of a Gaussian fit, as the distributions have large tails. The last rows give the average radial bias.

we expect to get the most neutrino / antineutrino separation from their multiplicity distributions. I have looked at how well the fitter results compare with the simulated muon type and interaction to see if we can use the ring identification to improve our understanding of these events. I find that 93% of QECC events are tagged as single ring, with 89% of ν_e QECC tagged as a single electron ring and 82% of ν_μ QECC tagged as a single muon ring. I find 50% of non quasielastic are marked as multi-ring, leaving the single ring sample 67% pure quasielastic (starting from 51% of all events being quasielastic), and the multi-ring sample 87% pure non quasielastic.

Chapter 9

Data Selection

9.1 Run Selection

I use the SNO Phase I and Phase II run list used in Ref. [31]. These runs were selected ensuring that fewer than a maximum number of channels were offline, the OWL tubes were online, they lasted at least a minimal time, and had an acceptable amount of deadtime. Various cuts to remove background events become effective reductions in detector livetime. For this analysis, the only relevant cut is the muon follower cut, which removes all events within 20 s of a tagged through-going muon. With SNO's muon rate this corresponds to a fractional livetime cut of 0.0184.

9.2 Prompt Event Selection

Previous studies of atmospheric neutrino events in SNO have looked at through-going muon events — where the produced muon is created outside the detector and travels all the way through it. This has the advantage of using a much larger target mass of the surrounding rock, and these events can be clearly distinguished by their

entry and exit points and the triggering of the outward looking tubes (OWLs). Since we want to be able to see the neutrons produced at the interaction point and measure the lepton energy, I look for only fully contained events. These are events where the neutrino interacts within the instrumented volume, and the produced lepton deposits all of its energy without leaving the detector. Although the OWL tubes can no longer be used to select the event, an event sample with very few backgrounds can still be selected using the high energy of the events of interest. The mean neutrino energy in atmospheric neutrino interactions is 1.4 GeV, making these events much more energetic on average than almost every other physics event. I select only events with at least 200 PMT hits, or "N_{hit}." It was found that 66.9% of atmospheric neutrino interactions within the PSUP result in a prompt event that passes this cut. The highest energy solar neutrinos are the hep neutrinos, with an endpoint of 18.8 MeV. Over the livetime of the SNO experiment, no hep or ^{8}B events with over 200 N_{hit} are expected.

The main high energy backgrounds are atmospheric muons, through-going and partially contained atmospheric neutrino events, and instrumental events. The atmospheric muon rate is much higher than the rate of atmospheric neutrino events, but they can be rejected using the OWL tubes. Fig. 9.1 shows the distribution of number of OWL tubes from hand scanned muon events.

The SNO detector has a pulsed global trigger that causes the electronics to trigger at 5 Hz regardless of the number of PMT hits. These "pulsegt" events can be used to measure the PMT noise rates. The distribution of number of OWL hits for pulsegt events from the D_2O phase is shown in Fig. 9.2. Only 0.27% of events have more than 1 OWL hit. To remove atmospheric muons and non-contained backgrounds, any event with 3 or more OWL tubes is rejected.

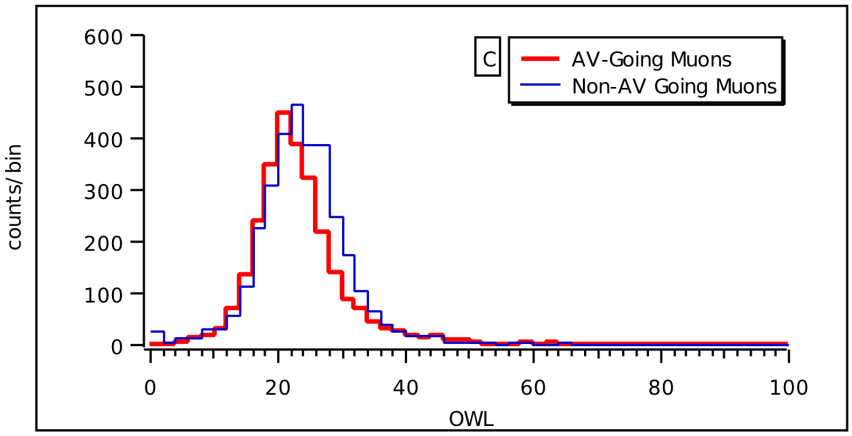

Figure 9.1: Number of OWL tubes in hand scanned muon events. The peak at 0 is from fully contained events. Figure from [9].

In addition to physical sources of backgrounds, instrumental effects can also cause high energy backgrounds. Electrical discharges within a PMT can cause very high N_{hit} events, called flashers. The N_{hit} distribution of flasher events is shown in Fig. 9.3. These events can be rejected using their time and charge distributions. Since the discharge occurs within a PMT, flasher events usually have one PMT with very high charge, often with cross talk into adjacent PMTs. In addition, the timing distribution of flasher events is generally much broader than the relatively short duration Cherenkov events.

Another type of instrumental background was "bubbler events." These were caused by light coming from the bubbler tubes inside the AV that were used to monitor the D_2O fill height. It was found that the gas-water interface would emit light on occasion, and so at the beginning of the D_2O phase the bubbler lines were flooded and an alternative method for measuring the D_2O height was developed. There can also be bursts of light from the acrylic/water boundary in the neck of the acrylic vessel. Several PMTs were installed in the neck in order to reject these

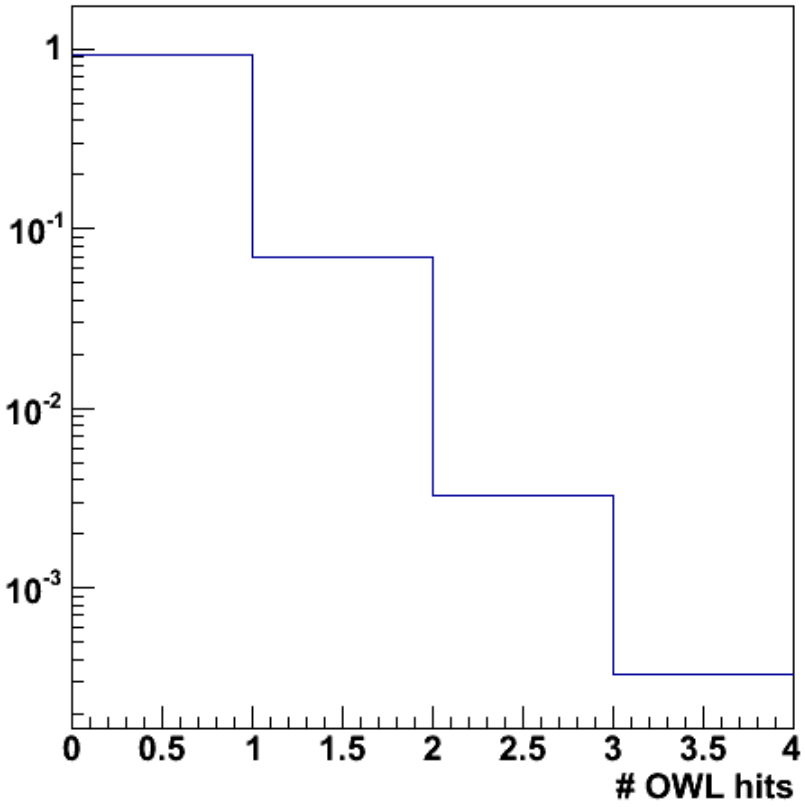

Figure 9.2: Number of OWL tubes in pulsegt events.

events. They can also be rejected by using the pattern of hits at the bottom of the detector. Many analysis cuts were developed for SNO's main solar neutrino analysis, although these were tuned for low energy events. As flashers are known to occur frequently after blasting in the mine, several samples of instrumental events were collected using a hydrophone to detect seismic events. The SNO cuts were tested on these samples to check their ability to tag these backgrounds at high energy. They were also applied to atmospheric Monte Carlo to test their "sacrifice"—the fraction of the physics events of interest removed by the cut—for high energy events.

A reduced set of the SNO low level instrumental background cuts that were

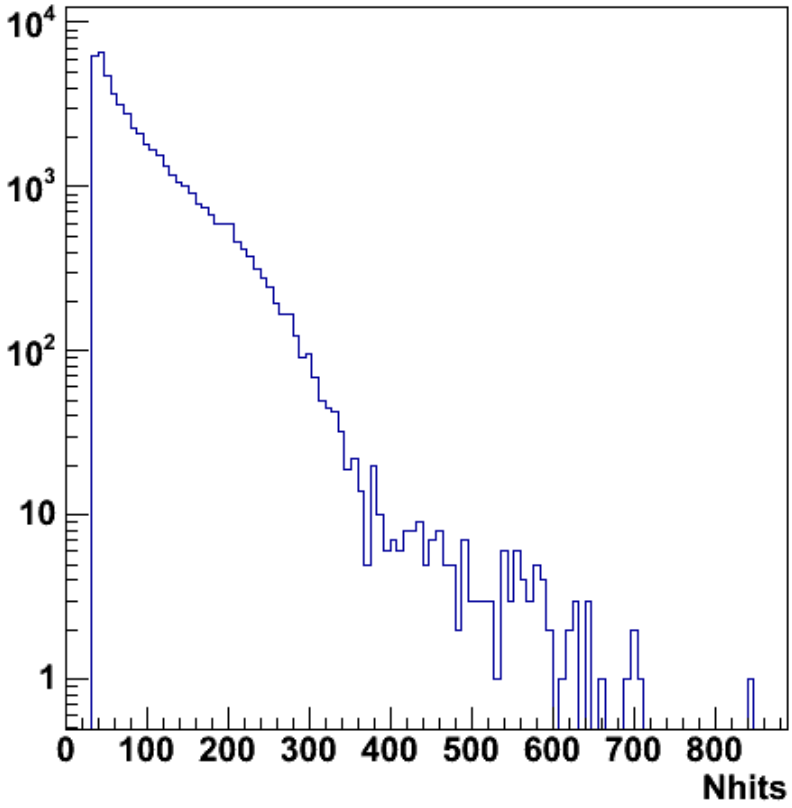

Figure 9.3: N_{hit} of flasher events from the golden flashers sample from run 10000 to 10655.

found to have a small sacrifice at atmospheric neutrino event energies were applied to the data. A description of the cuts is given in Appendix A.

In addition, two new cuts were developed to cut high N_{hit} flasher and noise events. Originally the crate isotropy cut was used to cut electronic cross talk events by looking for events where a large fraction of the hits are in a single board in a single front end crate. At higher energies, this is almost never true due to the sheer number of hits. The "empty crate cut" instead looks for the inverse, and cuts events where several adjacent crates have zero hits. Even highly directional events

will have some hits from scattered light across the detector so this selects for events from purely electronic effects. All events with more than six crates in a row with no hits are removed.

The "flasher wedge cut" flags flasher events that would normally be removed by the QCluster cut, which is not used. The QCluster cut looks for a high charge PMT surrounded by other hit PMTs, which are assumed to be electronic pickup. At the energies of interest, high charge hits occur naturally and so this cut has a high sacrifice. The new cut instead uses the characteristic wedge shape of flashers, as shown in Fig. 9.4. First the center of the wedge is found by finding the average PMT hit direction. Then the orientation of the wedge is found by finding the peak in the angular distribution of hits around the center. Once the potential orientation is found, it is required that a large fraction of hits fall within a semicircular wedge, and that there are many hits both at the center of the wedge and the ends. It is possible for Cherenkov ring events to look wedge-like if they are highly non-radially directed. To avoid flagging these events, the average hit time of the top half and bottom half of the wedge is calculated, and the difference is required to be less than 10 ns. It was found that this cut flagged the majority of events in the flasher event samples.

The low level cuts are applied to the Monte Carlo as well as the data to get a sense of the sacrifice. It was found that 0.65% of the simulated events are removed by the SNO cuts, and 0.87% are removed by the flasher wedge cut. The instrumental effects these cuts are designed to look for, like cross talk, are not simulated. As these effects are present to some degree in real physics events as well the above number should be taken as a lower limit on the true sacrifice, which will be measured by comparing data and Monte Carlo response to a known source of physics events.

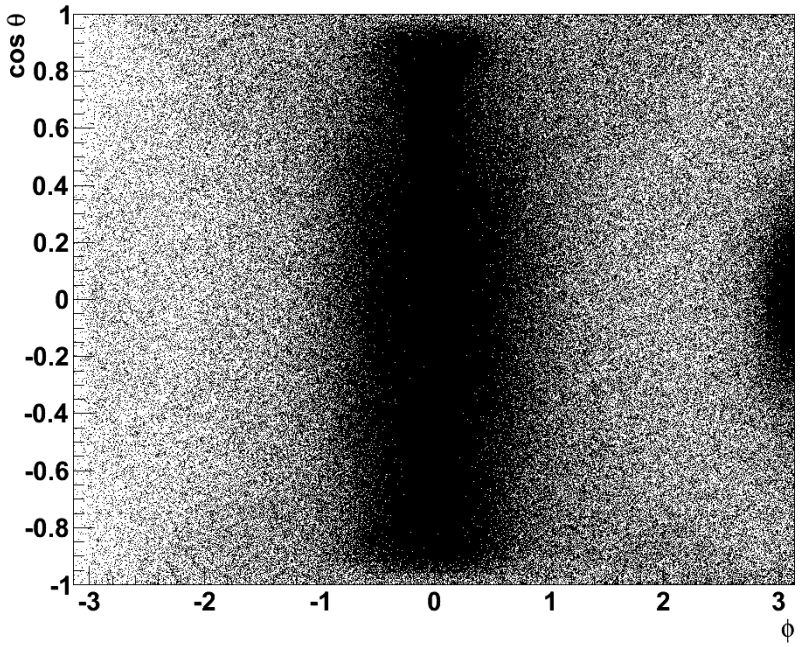

Figure 9.4: Distribution of hits from golden flashers sample after rotating to align the majority of the hits along $\phi = 0$. The flashing tubes are seen at $\phi = 3.14$ and $\cos\theta = 0$, with the majority of the hit PMTs being across the detector from them. It has been suggested that the wedge shape is caused by shadowing by the dynode inside the flashing PMT.

The prompt events are also required to pass several high level cuts. After applying the Hough transform, the charge density in the ring found is required to be above 1.5 counts per PMT and to be at least 50% higher than the charge density outside the ring. After fitting for the event position, time, and direction, events that fail to fit are cut, as well as events with a small in time ratio (ITR) — the ratio of prompt to total hits. This cuts non physics events as well as events that reconstruct poorly. Finally, the fitted position is required to be within 5.5 m.

An overview of the selection cuts on atmospheric neutrino events is given below:

1. N_{hit} >= 200

2. Low level cuts: crate isotropy, flasher geo, in time channel time spread, junk cut, QvNhit, QvT, OWL, OWL trigger, neck, retrigger, muon follower short
3. Flasher wedge cut
4. Empty crate cut
5. # of Neck PMT hits = 0
6. ITR ($\pm$10 ns) > 0.3
7. Hough transform charge density > 1.5
8. Hough transform charge density ratio > 1.5
9. $r_{water} < 8.5$ m
10. $r_{ring} < 5.5$ m

9.3 Neutron Follower Event Selection

Once a prompt event has been found, events within a short time window after it are searched for neutron captures. In D_2O the average capture time is about 50 ms, and all events outside of a 250 ms window are rejected. In the salt phase the much higher cross section on Cl leads to a capture time of about 5 ms, and so all events outside of a 50 ms window are rejected.

Background sources for neutron events were studied extensively for SNO. Possible sources include photodisintegration of deuteron by gammas from thorium or uranium chain decays or external gammas, cosmic ray spallation, spontaneous fission of uranium, and (α,n) reactions in the acrylic. For this analysis, these backgrounds

are dwarfed by the actual solar NC signal, for which we expect 870 events in the D_2O phase and 3257 in the salt phase [31]. We can use the time coincidence with the prompt atmospheric neutrino event to reject all of these sources. For a time window of 250 ms, a rate of less than ten thousand neutrons per year corresponds to less than 0.01% chance of a coincidence per prompt event.

Instrumental background events are removed using the standard SNO low level cuts, including those that could not be used for the prompt event. The full list of cuts is given in Appendix A. As the neutron follower events are identical to the events of interest for the SNO solar analyses, the effectiveness of these low level cuts in this energy regime have been extensively studied and verified [96]. For neutron followers the only cuts not used were the Nhit burst cut and the Missed Muon Follower cut, both which were designed specifically to remove the atmospheric neutrino events of interest.

These events are fit for their energy and position using the standard SNO+ water fitter, calibrated for heavy water optics. Events that fail to fit and those with an ITR$<$ 0.5 are removed. Cuts on the radius and energy can be very loose since the time coincidence greatly reduces the rate of backgrounds, and so neutron follower events are required only to have a fit radius of less than 6 m and an energy greater than 4 MeV.

Pulsegt events can again be used to check the number of background coincidences expected. Random pulsegt events spread throughout the D_2O and salt datasets are selected, and then the number of events within the 250 or 50 ms time window of those pulsegt events that pass the neutron follower cuts are counted. In the D_2O phase, 3 followers are found for 12000 pulsegt event, giving an expected coincidence background of 0.00025 events for each prompt atmospheric event. In the salt phase

no follower coincidences were found for 17000 pulsegt events.

Additional backgrounds are expected only in coincidence with atmospheric events. As muons and pions will be produced, Michel decay electrons are expected following some fraction of these events. The lifetime for a positively charged muon is 2.2μs so all events within 20μs of the atmospheric event are rejected. Decays from spallation products are also expected to follow atmospheric events. A list of the possible decays can be found in Table 6.1 of Ref. [9]. The longer-lived decays will again be cut by the short time coincidence with the prompt event. From simulation of atmospheric events I find that $1.3 \pm 0.2\%$ of atmospheric neutrino events in the D_2O phase and $1.6 \pm 0.1\%$ in the salt phase have a spallation product decay that passes the neutron follower event selection.

An overview of the selection cuts on neutron follower events is given below:

1. $\Delta t > 20$ μs and < 250 (50) ms for D_2O (salt)
2. Low level cuts: crate isotropy, flasher geo, in time channel time spread, junk cut, QvNhit, QvT, OWL, neck, retrigger, fitterless time spread, QCluster, AMB, OWL trigger, ESUM, muon follower short
3. $r_{water} < 6.0$ m
4. Energy > 4 MeV
5. ITR (-2.5 to 5 ns) > 0.5

I use the simulation to determine the efficiency for detecting neutrons after applying these cuts. The detection efficiency for a thermal neutron is highly dependent on the radius at which it's produced, as the majority of the neutrons that escape the AV will capture on hydrogen and be missed. In addition, the efficiency may

be dependent on the prompt event characteristics as higher energy primaries could create secondary neutrons distributed over a larger area. I calculate the efficiency by counting the number of followers that pass the cuts listed above and dividing by the number of true neutrons in the event, where the number of neutrons includes those produced by the initial neutrino interaction, those created by secondary production of the prompt particles, and includes neutrons that leave the AV without capturing.

In the D_2O phase, the dependence of the efficiency on the prompt event energy is found to be small, and so I use only a radially dependent efficiency, shown in Fig. 9.5. The PDF has an average statistical uncertainty of 2.2% per bin. The average efficiency for events that reconstruct within 5.5 m is 22.5%. In the salt phase, the efficiency decreases significantly as the prompt energy increases, from an average of 67.7% below 100 MeV to 55.6% above 3 GeV for events that reconstruct within 5.5 m. I construct a two dimensional efficiency PDF binned in prompt event energy and radius, shown in Fig. 9.6. The average bin uncertainty for the salt PDF is 2.9%.

9.4 Decay Electron Event Selection

Although decay electron events must be rejected as a background for neutron follower events, they are useful as a check of the analysis. These events are selected by looking at all events over 100 N_{hit} within the 20μs window following the prompt event. The main background in this window is from electronics induced events due to noise following large events. These events are cut very efficiently using the In Time Channel Time Spread low level cut. In addition, any event within 800 ns of the prompt event is rejected. An overview of the selection cuts for decay electrons

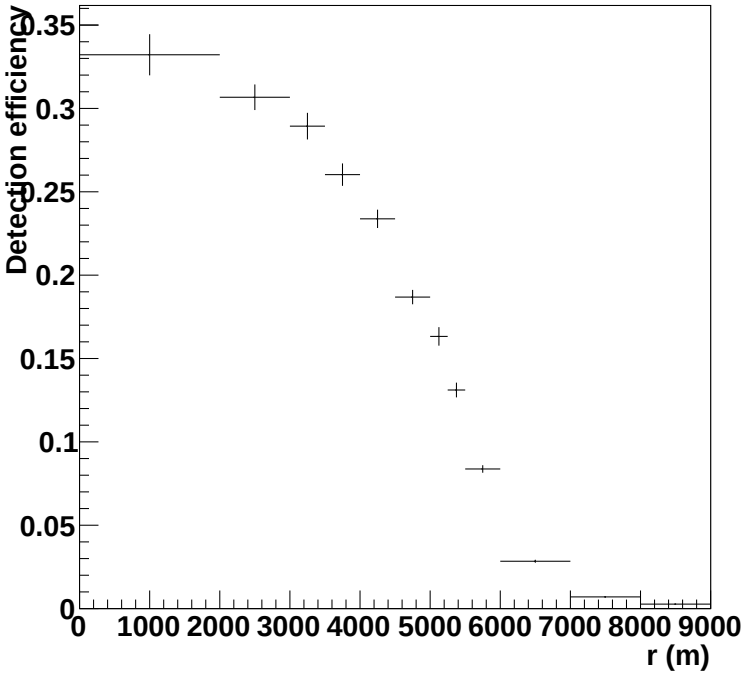

Figure 9.5: Neutron detection efficiency in the D_2O phase as a function of prompt event radius.

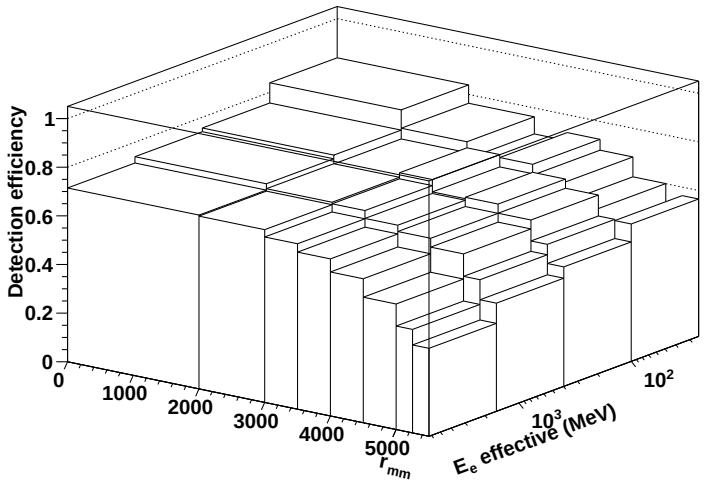

Figure 9.6: Neutron detection efficiency in the salt phase as a function of prompt event effective electron energy and radius.

is given below:

1. $\Delta t > 800$ ns and < 20 μs
2. $N_{hit} > 100$
3. In time channel time spread

Chapter 10

Systematic Uncertainties

There are many possible sources of systematic error in this analysis as it uses a new simulation package to study a not-well-understood and mostly-uncalibrated energy regime in the SNO detector. The effect of unmodeled electronic effects such as cross talk or afterpulsing is unknown, and there are few tests available for understanding the new reconstruction algorithms performance and biases. On the other hand, the main result of this analysis will be averaged neutron multiplicity distributions, and so it is mostly independent of uncertainties in absolute event normalizations. The flux itself already has a 15% normalization uncertainty, so additional unknowns here will not have as much of an impact. What is more important is to understand systematic effects on neutron acceptance, or effects that will bias the multiplicity or energy distribution.

The effect of cross section uncertainties listed in Table 7.3 on energy and multiplicity distributions are considered by calculating event reweighting fractions using GENIE. The bin by bin distortion for all distributions is calculated. Overall, they add an 11% uncertainty to the prompt event normalization. Uncertainties in the neutrino mixing parameters give a 1% uncertainty in the overall normalization. The

production height model is simplified, but fixing it to a constant value changes the event rate by less than one percent.

10.1 Neutron Follower Energy Scale

As run-by-run channel status is not simulated, it is necessary to check for a difference in the energy scale between data and simulation. Any such difference could impact the event selection efficiency. In particular, it is important to check at low energies where any difference would effect the neutron follower acceptance.

An independent high statistics source of neutron followers can be selected by looking for followers of through-going muons. These events are selected by using the normal neutron follower event cuts but only requiring that the prompt event pass the low level instrumental background cuts and that it has at least 3 OWL hits. A total of 2039 and 4727 followers are found in the D_2O and salt phases respectively. The fitted energy distributions are shown in Fig. 10.1. A Gaussian curve is fit to the peak of the N_{hit} and energy distributions for data and simulation. In both phases, the data is found to have a peak 4% higher in N_{hit} and 5% higher in energy than the simulation. This corresponds to a 3% uncertainty in the follower acceptance due to the energy cut.

10.2 Atmospheric Neutrino Event Energy Scale

Again it is necessary to check if there is an energy scale difference that could effect the efficiency of the cut on atmospheric event N_{hit}. In addition, as we want to measure the neutron follower multiplicity as a function of energy, we would like to check the performance of the energy fit at high energies. As the energy fit is

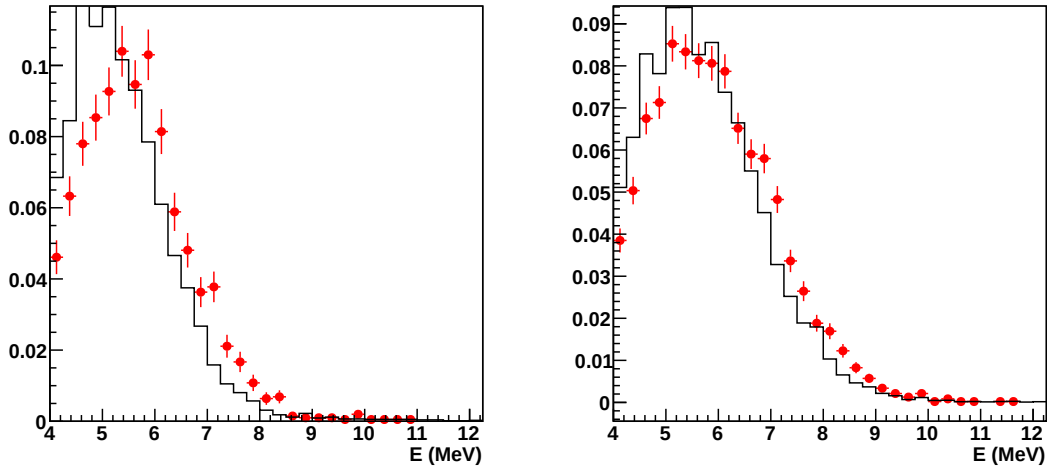

Figure 10.1: Reconstructed energy of muon neutron follower events (red) in the D_2O phase (left) and the salt phase (right) compared to simulation (black).

based on the charge in the event, any differences in the PMT charge response to multi-pe hits between data and Monte Carlo could cause a systematic error. The only high energy events with known energy distributions are the decay electrons and through-going muons. As discussed in Section 8, muons will produce a relatively constant amount of light per unit track length, up to a certain energy. It is possible to determine the track length of muons that travel completely through the detector by finding the entry and exit points, and thus possible to determine the energy deposited in the detector. As no tool to identify through-going muons or find their entry and exit points exists in RAT yet, I use decay electrons instead, which can be analyzed using the same ring fitter developed for the atmospheric neutrino events.

I want to identify a set of decay electron events independent of the rest of the analysis to use for data / Monte Carlo comparisons. Instead of identifying high energy prompt events and looking for decay electron followers, it is possible to use the very short 2.2 μs lifetime to do the inverse. I select possible decay electron

events, and then look for any predecessor event that triggered the detector within a 5 μs window before it. This coincidence is short enough that practically the only kinds of event that remain are decay electrons and instrumental backgrounds. To remove potential instrumental backgrounds, I require that the decay electron event successfully reconstruct and have an ITR > 0.5 in addition to the cuts described in the previous section. As instrumental retrigger events are not due to light, they will not reconstruct well and will be removed by these additional cuts. Note that this procedure is more restrictive than the one described in Section 9.4, which uses the prompt selection to improve the time coincidence.

In the D_2O dataset 337 decay electrons are found following 316 predecessor events, and in the salt dataset 474 decay electrons are found following 443 predecessor events. The time since the predecessor event is shown in Fig. 10.2. A exponential fit gives a lifetime of 1.8 ± 0.2 μs in the D_2O phase and 2.3 ± 0.2 μs in the salt phase, compared to the expected 1.8 μs. The agreement is good for the D_2O phase, suggesting that the sample is mostly decay electrons, while the lifetime in the salt phase is slightly long.

The Michel electron energy spectrum is not a Gaussian peak, but peaks and then drops sharply at a maximum energy of about 52 MeV. While these events will be much lower energy than many of the atmospheric neutrino events, they at least provide a sample well above the neutron capture events. Unfortunately, it is found that events this shortly after a high energy event will have a distorted charge, making an accurate measurement of the energy more difficult. Fig. 10.3 shows the average total charge of the decay electron events as a function of their predecessor's N_{hit}. After a very high N_{hit} event, these events have a much higher charge than expected for decay electrons. The cause of this distortion is unknown. As it appears

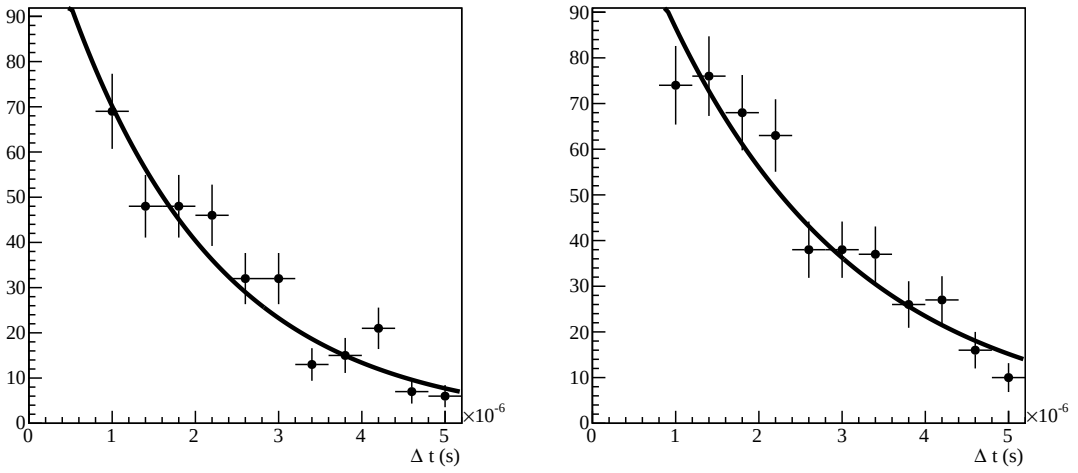

Figure 10.2: Time since predecessor event for decay electron events, with exponential fit to lifetime.

to be mostly independent of the time since the predecessor event, it is unlikely to be due to extra reflected light. Instead, it is hypothesized to be caused by PMT afterpulsing, which is not modeled in the simulation. Afterpulsing occurs in large PMTs due to ionized gas particles inside the tube which are accelerated toward the photocathode and can free electrons on impact. It can occur for many μs following a real pulse, and so it is a plausible explanation for the flat time distribution of the effect.

As the amount of afterpulsing is expected to be proportional to the number of real pulses, I model the effect with a linear fit to the distortion as a function of predecessor N_{hit}. The linear fit was found to describes the effect well, and the charge predicted at an N_{hit} of zero is close to what is expected for an average decay electron event. In D_2O decay electron events have their charge increased by 1.68 counts per N_{hit} of the predecessor event, and in salt by 1.35 counts per N_{hit}.

The fit energy distributions for decay electron events in the D_2O and salt phases

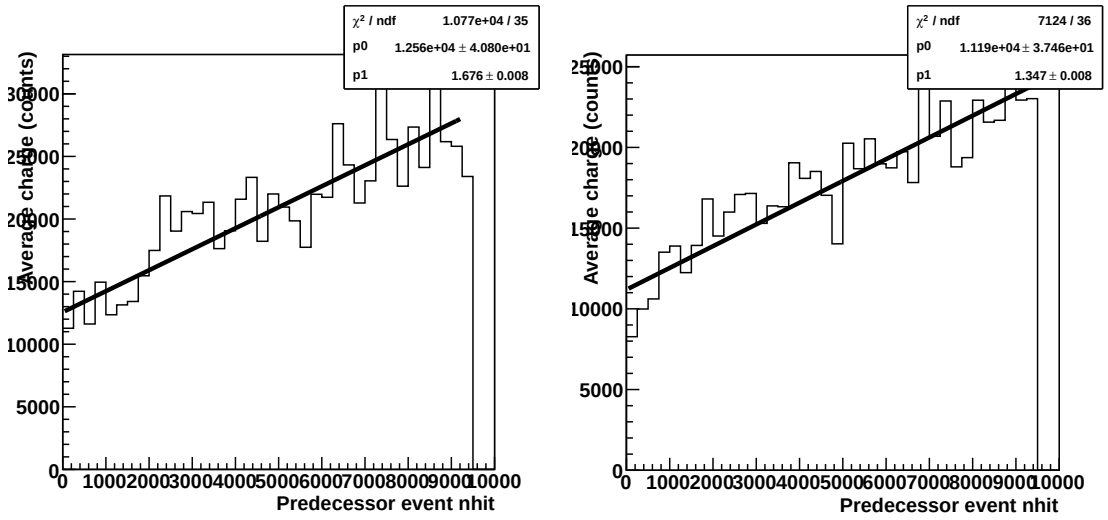

Figure 10.3: Average total event charge of decay electron events as a function of the N_{hit} of the predecessor event in the D_2O phase (left) and in the salt phase (right). It is assumed that the y-intercept is the true average charge and that the decay electron event's charge increases linearly with predecessor N_{hit}.

are shown in Figs. 10.4 and 10.5, before and after correcting for the effect of the predecessor. The mean energy in both phases is 3% lower than in the simulation. The agreement between the distributions is fair, with the data being wider than the simulation. This may be due to variation in the predecessor event effects. As a check, we fit for the energy of these events using a radius dependent lookup table for N_{hit} instead of charge, as the N_{hit} appears to be less effected by the predecessor event. The mean N_{hit} in the data is 8% higher than the simulation for D_2O and 5% higher for salt. Figs. 10.6 and 10.7 show the fit distributions, where the right plots have the data shifted so the mean matches the simulation. Here the shape of the distributions agree very well. The difference in N_{hit} leads to a 1.1% and 0.7% uncertainty on the efficiency of the N_{hit} cut on prompt atmospheric neutrino events.

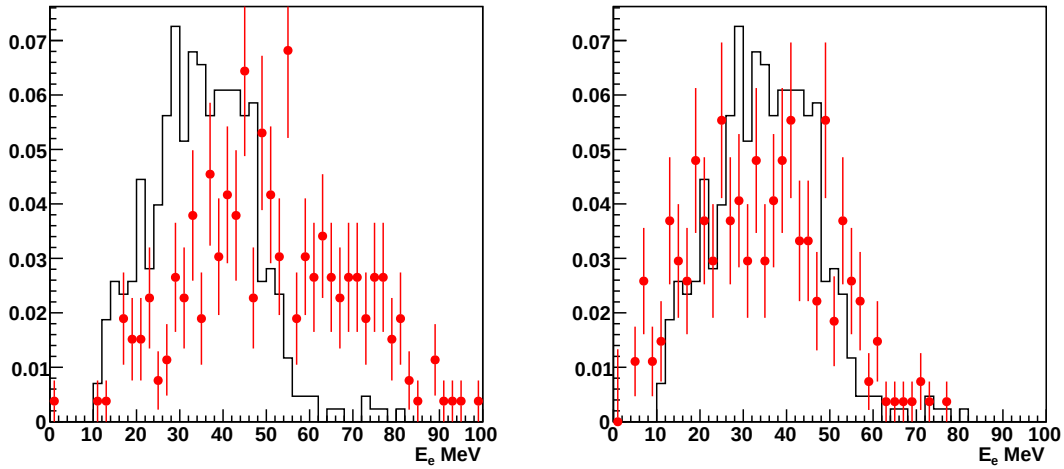

Figure 10.4: Fit energy of decay electron events (red) in the D_2O phase compared to simulation of decay electron followers of atmospheric neutrino events. The plot on the left is the default fit, while on the right the charge has first been corrected using the predecessor event's N_{hit}.

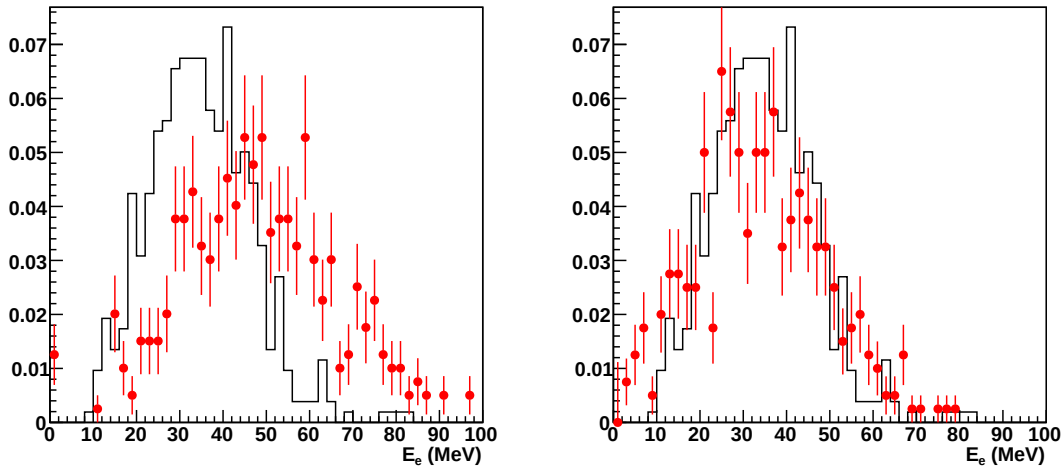

Figure 10.5: Fit energy of decay electron events (red) in the salt phase compared to simulation of decay electron followers of atmospheric neutrino events. The plot on the left is the default fit, while on the right the charge has first been corrected using the predecessor event's N_{hit}.

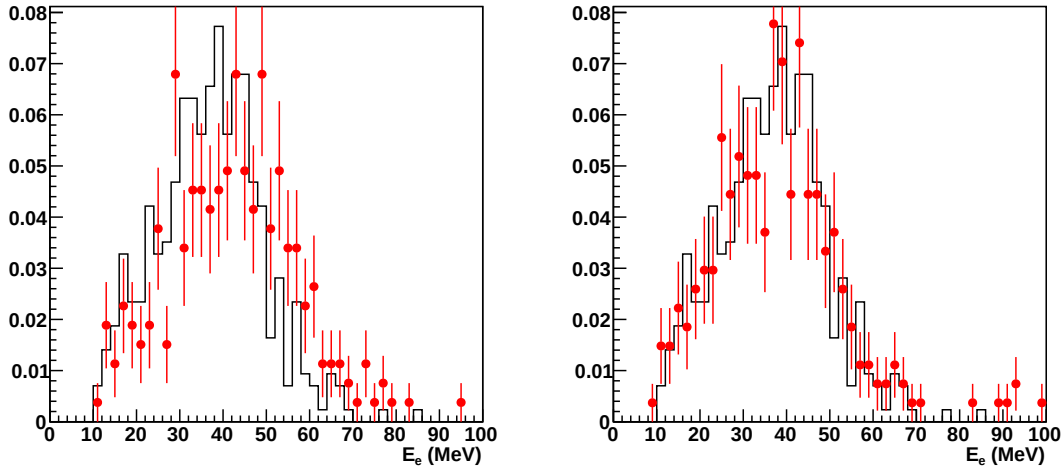

Figure 10.6: Fit energy of decay electron events (red) in the D_2O phase using N_{hit} instead of charge compared to simulation of decay electron followers of atmospheric neutrino events. The plot on the left is the default fit, while on the right the data has been shifted so that the means are equal.

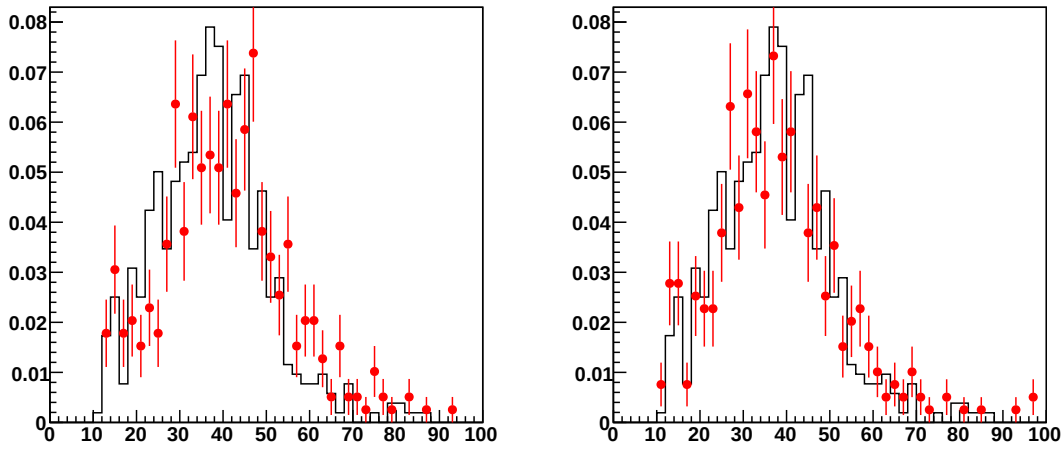

Figure 10.7: Fit energy of decay electron events (red) in the salt phase using N_{hit} instead of charge compared to simulation of decay electron followers of atmospheric neutrino events. The plot on the left is the default fit, while on the right the data has been shifted so that the means are equal.

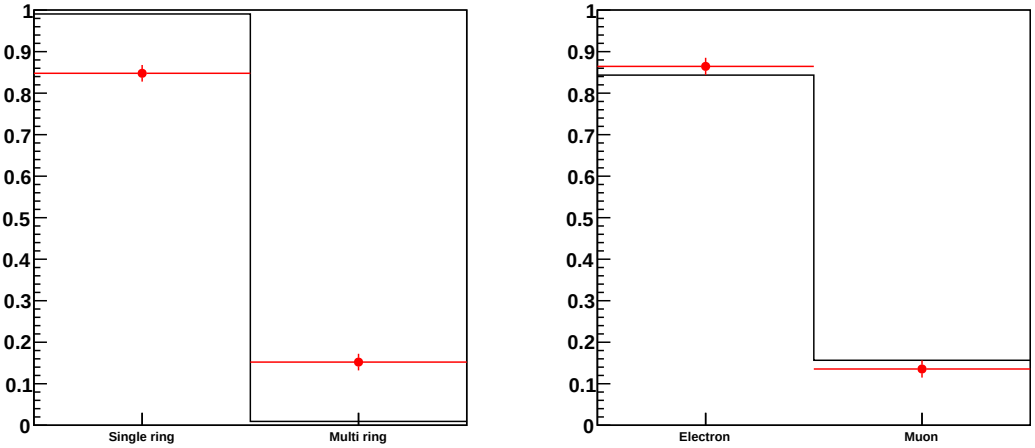

Figure 10.8: Number of rings tagged (left) and particle id of single ring events (right) for retrigger events in the D_2O phase (red) compared to simulation of decay electron followers of atmospheric neutrino events.

10.3 Fitter Ring Counting and Particle ID

We will use the ring counting and particle identification of the fitter described in Chapter 8 to measure separate multiplicity distributions for electron ring, muon ring, and multi-ring events. The decay electrons can also be used to check the performance of the fitter's ring identification. Fig. 10.8 shows the fit number of rings and particle type for decay electron events, compared to simulation. It is found that 15% of the events in the data are tagged as multi-ring events, compared to only 1% in the simulation. Hand scanning shows that there are a handful of true multi-ring events in the data, and the rest appear to be mistagged. On the other hand, the particle id of single ring events is similar, with 87% of these decay electron events being tagged as electron-like, compared to 85% in simulation.

It is believed that the additional charge from the high energy predecessor event is causing the ring counting to malfunction. If the afterpulsing occurs in the hardest

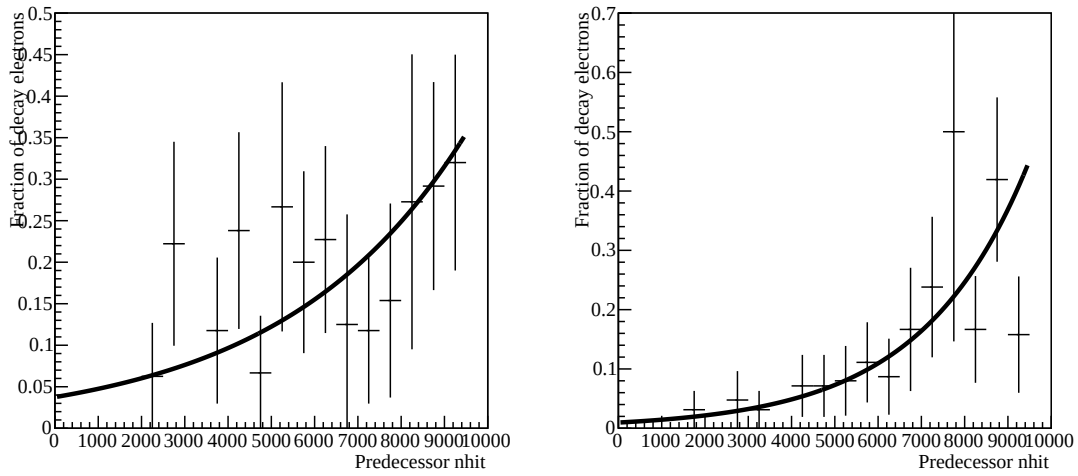

Figure 10.9: Number of decay electron events tagged as multi-ring in the D_2O phase (left) and salt phase (right) as a function of predecessor event N_{hit} fit to an exponential distribution.

hit tubes along the original predecessor event ring, it can easily be mistaken for a second ring in the decay electron event by the fitter. Fig. 10.9 shows the fraction of decay electron events that fit as multi-ring as a function of the predecessor event's N_{hit}. This distribution was found to fit well to an exponential. Extrapolating to a predecessor N_{hit} of zero, the fraction of events tagged as multi-ring is found to be $3.7 \pm 6.4\%$ in the D_2O phase and $1.9 \pm 1.1\%$ in the salt phase, in good agreement with the prediction from simulation.

To check that the fitter is not just tagging everything as electrons, a known source of high energy muon events is needed. Conveniently, the set of predecessor events for these decay electrons should have a significant fraction of muon rings. The ring identification of predecessor events with less than three OWL events is shown in Fig. 10.10 compared to simulation. The majority of the single ring events are identified as muon-like rings, and there is good agreement with the Monte Carlo

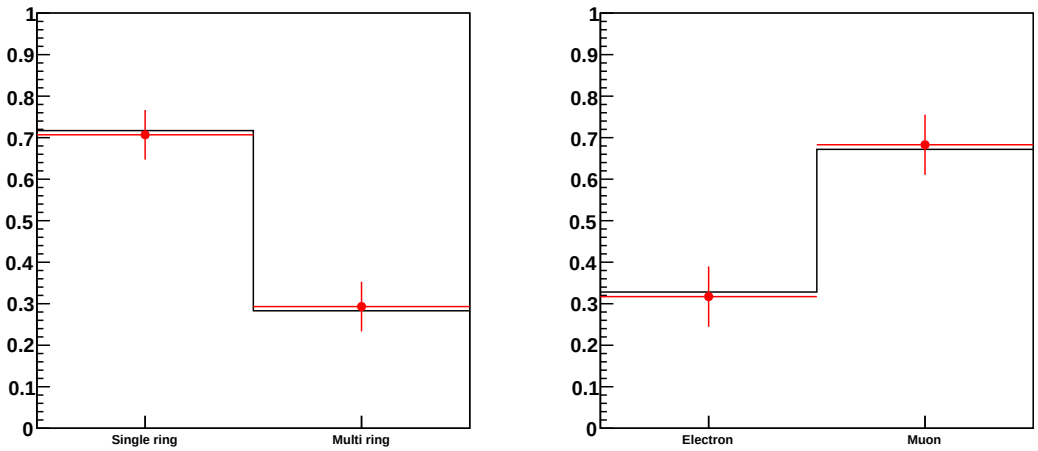

Figure 10.10: Number of rings tagged (left) and particle id of single ring events (right) for predecessor events in the D_2O phase (red) compared to simulation of atmospheric neutrino events with decay electron followers.

prediction, suggesting that the particle identification is working as expected.

10.4 Event Selection Efficiency

Although we are little affected by overall changes in efficiency, we would like to check that there are no serious differences that could bias our measured multiplicity distributions. The efficiency of the selection cuts on simulation is compared to data using the predecessors of our set of decay electron events. The distribution of number of OWLs of the predecessor event is shown in Fig. 10.11. Although there is a peak at zero, there is not an obvious cutoff between contained and non-contained events. The cut at less than 3 OWLs seems reasonable, but it is difficult to estimate the sacrifice of contained events or the leakage of external muons.

Assuming that the OWL cut perfectly selects contained events and rejects through-going muons, I now apply the prompt event selection criteria to the prede-

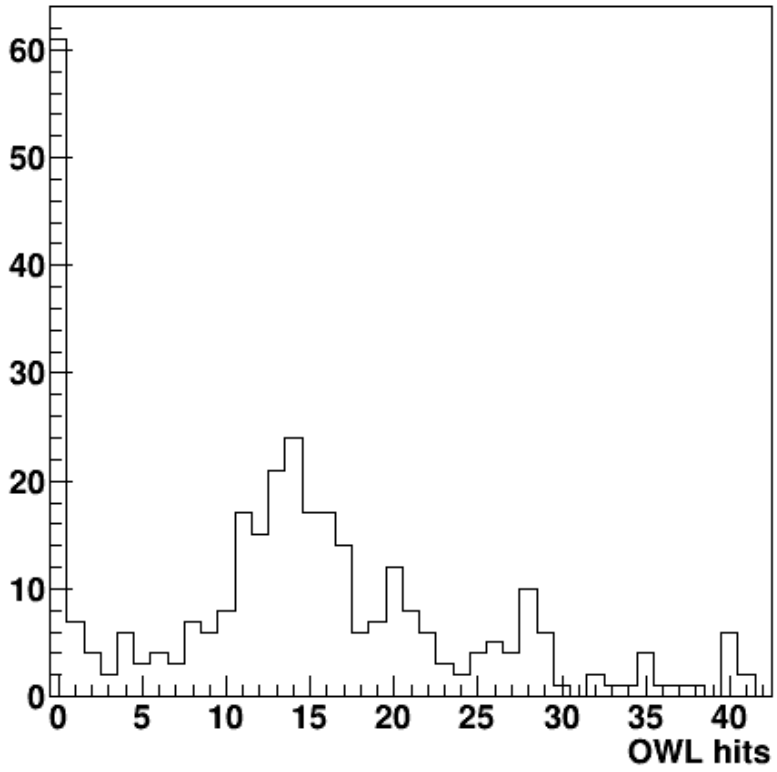

Figure 10.11: Number of OWL tubes hit for predecessor events of selected decay electron events.

cessor events with less than 3 OWLs. A comparison of the cut efficiency for these prompt events and simulated events with decay electrons is shown in Table 10.1 for D_2O and Table 10.2 for salt. The results from data and simulation agree to within statistical uncertainties. This suggests that there are no drastic differences between the data and simulation affecting these cuts.

The accuracy of the fitted position is important for determining any systematic error on the efficiency due to the fiducial volume. In addition, we are interested in constraining any possible radial bias as the neutron detection efficiency is heavily dependent on the radius. There are many ways by which the fitted position could

Cut	Data	Data fraction	MC fraction
All	67	100%	100%
$N_{hit} > 200$	59	88%	87%
Low level cuts	58	87%	85%
Flasher wedge cut	58	87%	86%
Empty crate cut	58	87%	86%
# Neck hits = 0	57	85%	86%
Hough cut	57	85%	86%
$r_{water} < 8.5$ m	56	84%	82%
ITR	56	84%	82%
$r_{ring} < 5.5$ m	27	40%	34%

Table 10.1: Cut efficiency for events with muon decay electron followers for D_2O phase data and Monte Carlo.

Cut	Data	Data fraction	MC fraction
All	106	100%	100%
$N_{hit} < 200$	92	87%	91%
Low level cuts	89	84%	90%
Flasher wedge cut	89	84%	89%
Empty crate cut	89	84%	89%
# Neck hits = 0	88	83%	89%
Hough cut	88	83%	89%
$r_{water} < 8500$	86	81%	85%
ITR	86	81%	85%
$r_{ring} < 5500$	42	40%	36%

Table 10.2: Cut efficiency for events with muon decay electron followers for salt phase data and Monte Carlo.

become biased. When fitting a Cherenkov ring, the hit distribution determines the size of the ring and thus the mean distance to the event position from the hit PMTs. Thus if there are more noise hits due to the lack of run-by-run channel status or due to cross talk, the fitted rings could be larger than expected, pushing the fitted position farther away from the PSUP. On the other hand, the hit distribution itself gives very little information about the incident angle on the PSUP, i.e. how non-radial an event is. The position fitter constrains this by looking at the PMT hit times, where a large time difference between one side of the ring and the other indicates that the light was coming from the direction of the early side. If the PMT multi-pe hit timing model overpredicts how early these hits are measured to be, it could rotate the fitted position away from the center of the detector to a larger radius.

As there are no sources with known positions in the energy range of interest, these decay electron predecessors are as close as we can get to a calibration of the fitted position. Our predecessor events were selected by only requiring a decay electron follower. The predecessor sample should be unbiased compared to Monte Carlo even if the simulated decay electron efficiency is incorrect, unless the magnitude of the efficiency difference depends on the predecessor event properties. We estimate the radial bias by comparing the total efficiency for the decay electron events between data and Monte Carlo, and assuming any difference is completely caused by a radial bias.

For the D_2O phase, we find 40% of events are accepted, compared to 34% in Monte Carlo. To be conservative we add the 6% difference to the 6% uncertainty in the ratio for data in quadrature to get a total systematic uncertainty of 8.5%. This is a 25% fractional uncertainty on the efficiency, which is equivalent to increasing

the fiducial volume by 42.5 cm. A flat inward radial bias of this magnitude leads to a 10.1% uncertainty on the total number of followers, a 12.6% uncertainty on the average number of followers per prompt event, and a 11.8% uncertainty on the neutron detection efficiency. In the salt phase, we find 40% of events are accepted compared to 36% in Monte Carlo. Adding the difference and the statistical uncertainty in quadrature gives a fractional uncertainty in the efficiency of 17.3%, or a 30.0 cm increase in the fiducial volume. A radial bias by this amount leads to a 10.5% uncertainty on the total number of followers, a 5.9% uncertainty on the average number of followers per prompt event, and a 6.5% uncertainty on the neutron detection efficiency. The analysis is rerun with these offsets applied in order to determine the bin by bin effect of this uncertainty on each distribution.

10.5 Cut Efficiency on One-Third Dataset

The reconstruction and event selection described in Chapters 8 and 9 was tuned on data from the first third of each phase. The rest of the data was only unblinded once this was fixed. Analyzing an unbiased prescaled selection of a dataset is a technique to allow for the identification of any unexpected backgrounds or problems with the analysis while avoiding unintentionally biasing the analysis [97]. With a one-third dataset I can test the new reconstruction algorithm on real data and check that my selection cuts are removing all instrumental events. It prevents the possibility of introducing a bias, for example by tweaking a cut to accept or remove events in order to force the results to better match predictions. After initially analyzing the first third of the data, several discrepancies were noted. The relative normalization of the number of prompt events between the D_2O and salt phases, with the salt phase only having 10% more events despite having over 40% longer livetime. Within the

AV there were actually more events found in the D_2O phase. The number of decay electron followers was also lower than expected, both as an absolute number and as a fraction of the number of prompt events. By inspecting events in the one third dataset by hand, I noticed that a significant amount of instrumental backgrounds had made it past the SNO low level cuts, mostly flashers and electronics bursts that would have been cut by the QCluster cut in a standard SNO analysis. To remove these events I added the flasher wedge cut and the empty crate cut described in Section 9.2.

I described above how I used retrigger events to compare the predicted and actual efficiency of my prompt event cuts, but I did not have any real calibration sources to compare to. As I saw a deficit of decay electrons in my one third dataset, I wanted to further check each cut to make sure I was not accidentally removing signal events. Table 10.3 shows the effect of removing or modifying each cut one at a time on the number of events in the one third dataset.

To check the impact of any energy scale uncertainty on the efficiency of the 200 N_{hit} cut on the prompt event, I increased the N_{hit} threshold. A 25% increase in the threshold removes only one prompt event in both D_2O and salt. To check for a fit radial bias in the data I compared the ratio of events within 5.5 and 6 m, which all agreed to within statistical uncertainties. To check if a bias in the particle identification could be causing a radial bias, I also compared the events that fit within 5.5 m when forced to use an electron ring fit and when forced to use a muon ring fit. There is only a small variation of a few events. To check that requiring the water fitter to successfully fit for the position to use as a seed was not causing me to throw out events, I also did the full analysis using the "quad fitter" to get a seed position for the ring fit. The quad fitter calculates an average position from sets

of four hit PMTs, and so will always successfully find a position within the PSUP. This method accepts 3 more prompt events in the D_2O phase and 1 less prompt event in the salt phase. Of the other cuts, the two with the largest effect were the flasher geo cut and the flasher wedge cut. Both cut a large number of prompt events but no followers, suggesting that they are successful at only cutting instrumentals. After performing this analysis, there was no clear problem explaining the deficit of decay electrons, so it was assumed to be a statistical fluctuation, and the decision was made to unblind the rest of the dataset.

	D_2O			salt		
	Prompt	Neutron	Michel	Prompt	Neutron	Michel
Normal cuts	37 (31.9)	38 (25)	8 (12.1)	32 (45.5)	108 (98.6)	10 (17.2)
$N_{hit} > 250$	36	38	8	31	108	10
- ITR	38	38	8	32	108	10
- Hough	37	38	8	32	108	10
OWL < 5	40	40	9	35	121	10
OWL < 10	58	47	9	49	192	13
- Neck hits $= 0$	37	38	8	34	114	10
$r < 6$ m	51 (48.9)	42 (42.7)	11 (10.6)	46 (41.6)	134 (123.8)	12 (12.9)
$r_e < 5.5$ m	39	38	9	31	108	10
$r_\mu < 5.5$ m	37	39	8	30	104	10
$r_{\text{quad seed}} < 5.5$ m	40	38	8	31	108	10
- crate isotropy cut	37	38	8	32	108	10
- Flasher Geo cut *	970	38	8	736	104	10
- ITC time spread cut	37	38	8	32	108	10
- Junk cut	37	38	8	32	108	10
- QvNhit cut	37	38	8	32	108	10
- QvT cut	37	38	8	32	108	10
- Flasher wedge cut	45	38	8	39	108	10
- empty crate cut	37	38	8	33	110	10
- retrigger cut	37	38	8	33	108	10
- neck cut	37	38	8	32	108	10

Table 10.3: Effect on number of prompt events, Michel decay electrons, and neutron followers of removing or modifying a single cut. In the top row, the numbers in parenthesis are the predictions from simulation. For $r < 6$ m, the number in parenthesis is the prediction from simulation after scaling the simulation to match the number in the first row. The full ring fit was only applied to events that passed the flasher geo cut, so when looking at events that failed that cut I use the seed fit position from the waterFitter instead of the full fit position.

Source of error	Affected parameter	D_2O	salt
Atmospheric neutrino flux	Prompt normalization	15%	15 %
Atmospheric neutrino flux	$\overline{\nu}/\nu$ ratio	1%	1%
Mixing parameters	Prompt normalization	1%	1%
Cross section	Prompt normalization	11%*	11%*
Cross section	Follower normalization	10%*	10%*
Radial bias	Prompt normalization	25%*	17.3%*
Radial bias	Follower normalization	10.1%*	10.5%*
Radial bias	Neutron detection efficiency	11.8%	6.5%
Energy scale	Prompt normalization	1.1%	0.7%
Energy scale	Follower normalization	3%	3%
SNO systematic	Follower normalization	2%	1.4%
MC stats	Follower normalization	1%	1%
MC stats	Neutron detection efficiency	2.2%	2.9%
Fitter performance	Particle id	2%	2%
Fitter performance	Ring counting	6.9%	1.4%

Table 10.4: Causes of systematic uncertainty and the parameters they effect, with uncertainties for the D_2O and salt phases. Percentages marked with * indicate that the number given is an average and that the bin by bin distortion of any distribution is modeled for that uncertainty.

10.6 Summary

Possible sources of systematic error have been identified and constrained. These include theoretical uncertainties in the neutrino flux, cross sections, and mixing, and uncertainties in the detector model. The source and impacted parameter for all considered systematics is given in Table 10.4, along with the constraint found through the analysis of the decay electron and predecessor event samples.

Chapter 11

Results

In this chapter I first describe the event sample selected by the prompt event cuts as well as the results of the ring reconstruction and particle identification. I next calculate the neutron multiplicity as a function of the visible energy and compare the results to simulation. I then fit for the neutrino-antineutrino ratio using the multiplicity distributions, and finally fit for the strength of the multinucleon emission contribution.

11.1 D_2O phase

After applying the prompt event selection cuts to the entirety of the D_2O data set, I find 111 prompt events total in the D_2O phase compared to 93.8 ± 17.4 predicted by simulation, where the uncertainty given here is the combined flux and cross section uncertainties. The breakdown of events by ring count and particle identification is given in Table 11.1 and shown in Fig. 11.1. The number of single ring events agrees well with the prediction, but there are more than twice as many multi-ring events as expected. Note that throughout where I refer to electron ring, muon ring, and

multi-ring events I mean events where the reconstruction algorithm has tagged the event as being electron-like, muon-like, or has detected multiple rings, regardless of the true physics behind the event. Similarly electron and muon energy refer to the fitted energy under the assumption that the light in the event came entirely from a single lepton of that type.

	Data	Simulation			
		Total	QECC ν_e	QECC ν_u	Other
single ring	56 (50.5%)	68.6 (72.8%)	20.7 (22.0%)	25.3 (26.9%)	22.5 (23.9%)
e ring	26 (23.4%)	37.4 (39.7%)	20.0 (21.3%)	2.9 (3.1%)	14.5 (15.4%)
μ ring	30 (27.0%)	31.1 (33.1%)	0.7 (0.7%)	22.4 (23.8%)	8.0 (8.6%)
multi-ring	55 (49.5%)	25.6 (27.2%)	1.7 (1.8%)	1.5 (1.6%)	22.4 (23.8%)
total	111	94.1	22.4	26.8	45.0

Table 11.1: Results of ring identification on prompt events in the D_2O phase compared to simulation. In parentheses is fraction of total prompt events.

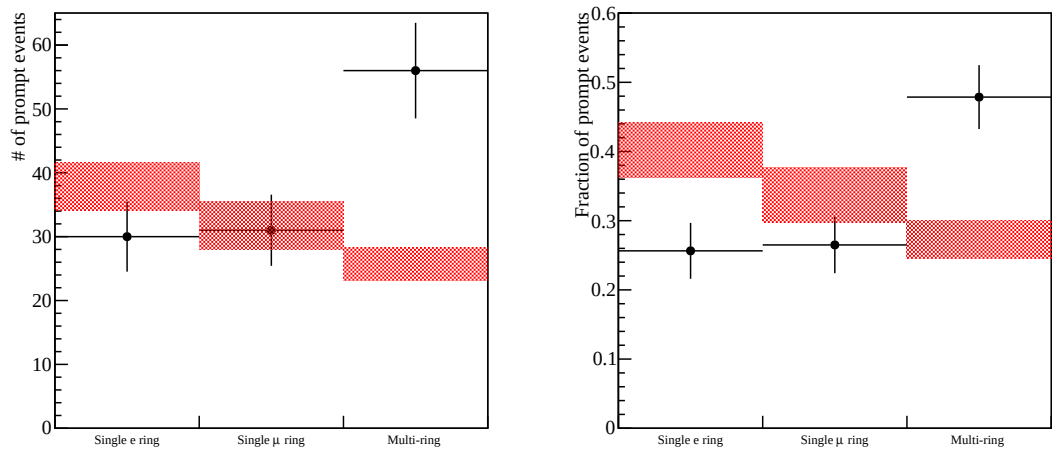

Figure 11.1: Absolute number (left) and fraction (right) of atmospheric neutrino events in data and simulation for D_2O phase. Simulation (red) includes only cross section uncertainties.

As an additional check of the cut efficiency, we can compare the distribution of cut parameters for data and simulation, shown in Fig. 11.2. I calculate the χ^2 for each distribution using only statistical uncertainties, combining adjacent bins so that the prediction in each bin is at least 10 counts. The statistics are low and the binning is somewhat arbitrary, so p-values aren't calculated, but the χ^2 can be used to get a sense of the agreement. I find a χ^2 of 7.8 for 4 degrees of freedom (dof) for the N_{hit} distribution, 9.7 for 7 dof for the radial distribution, 43.2 for 5 dof for the ITR distribution, and 25.7 for 7 dof for the Hough transform parameter distribution. The ITR distribution of the data is shifted lower than the simulation, which suggests that the simulation is underpredicting the amount of scattering or late pulsing. On the other hand, it is clear that shifting the simulated results down so that the average ITRs matched would not cause any additional simulated events to be cut. The Hough transform parameter agreement is poor due to the excess

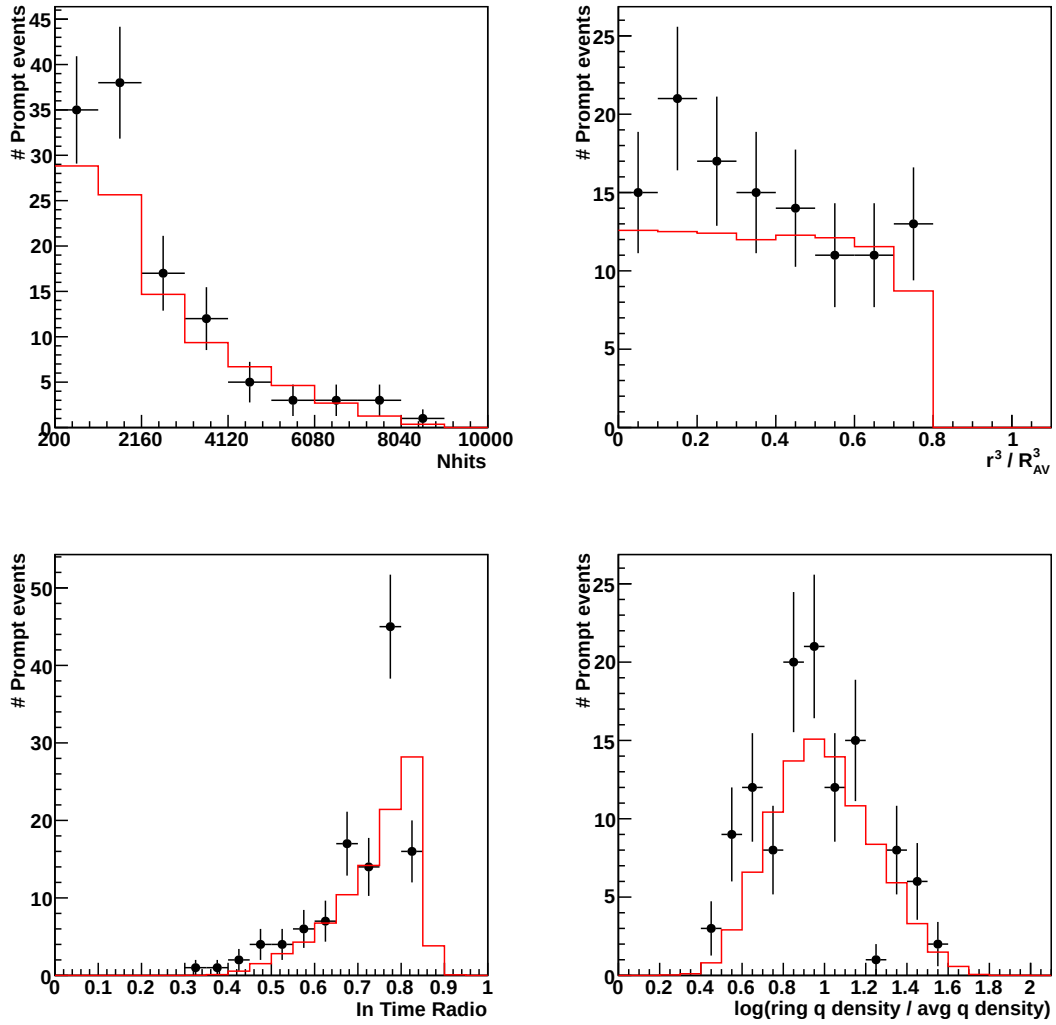

Figure 11.2: N_{hit} (top left), fitted radius (top right), in time ratio (bottom left), and Hough transform ring charge density (bottom right) of prompt events in D_2O phase after all cuts compared to simulation (red).

of multi-ring events, which are expected to have a distribution shifted lower than single-ring.

We also compare the fitted energy to the expected distribution. For single ring events, I fit for a particle type specific energy, while for the multi-ring events I find

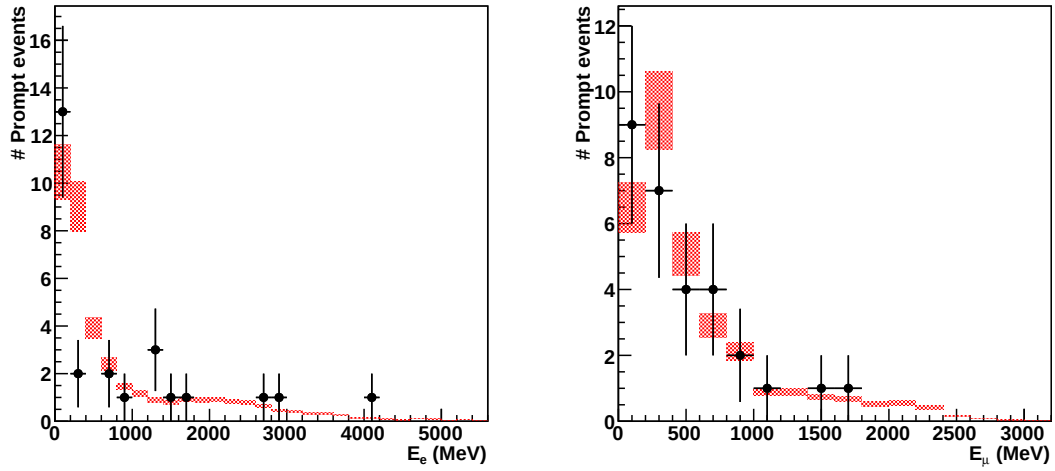

Figure 11.3: Reconstructed energy distribution of single electron-ring (left) and single muon-ring (right) events in D_2O phase. Simulation (red) includes cross section uncertainties. Reconstructed energy assumes that all visible light comes from a single charged lepton of the identified type.

an effective electron energy, or the energy of an electron that would produce an equivalent amount of light. Fig. 11.3 shows the fitted electron or muon energies for events fit as a single ring of that type, and Fig. 11.4 shows the fitted effective electron energy of multi-ring prompt events. The χ^2 for these distributions is 11.1 for 3 dof for single electron rings, 0.45 for 2 dof for single muon rings, and 39.3 for 2 dof for multi-ring events. The high χ^2 for multi-ring event energies is due to the large excess of events at low energy. We see that there is one event over 9 GeV, well above the energy range predicted by the simulation.

The N_{hit} distribution appears to have an excess under 2000 N_{hit}s. This corresponds to an electron energy of around 400 MeV. In Fig. 11.4 we see a similar excess under 800 MeV, especially in the 200 to 400 MeV bin. The single ring distributions have a slight deficit in this region which suggests that the excess may be partly due to mistagging single rings as multi-rings. If this excess is due to an instrumental

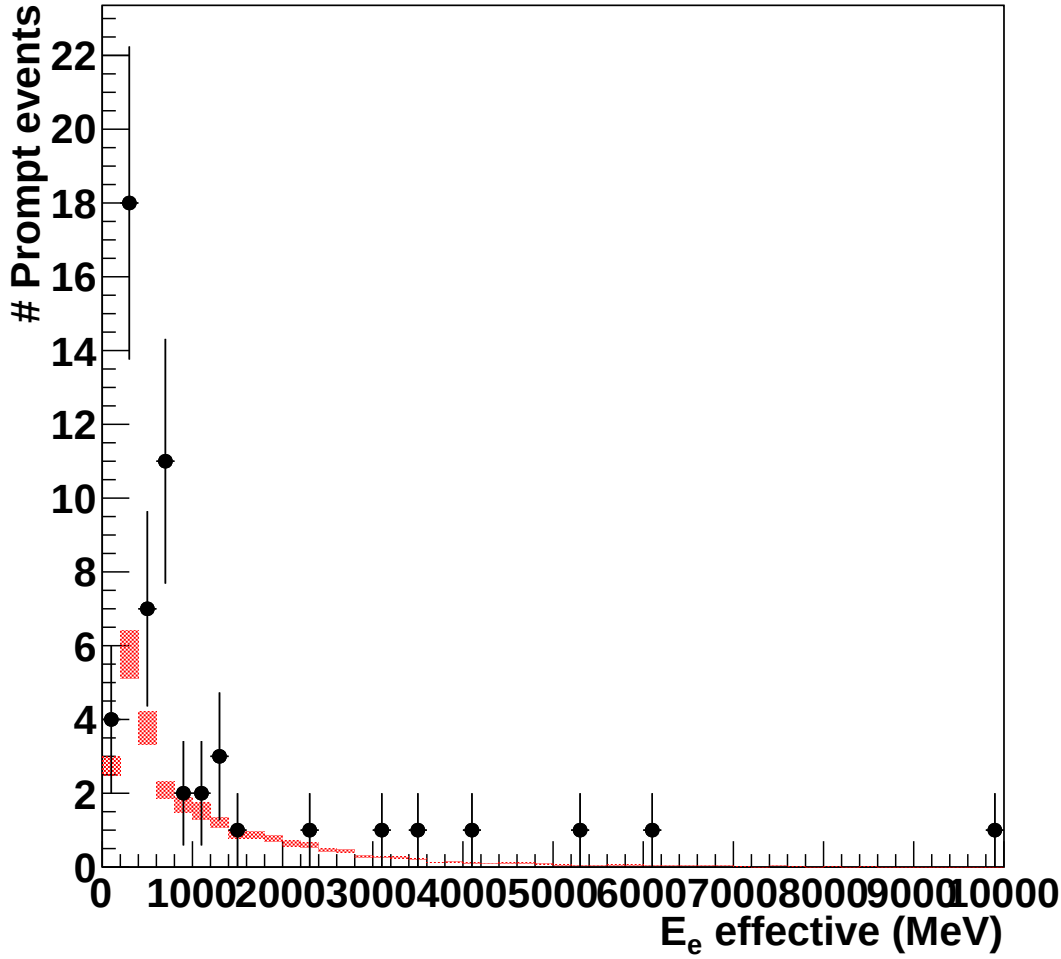

Figure 11.4: Effective electron energy for multi-ring prompt events in D_2O phase. Simulation (red) includes cross section uncertainties.

	Data	Simulation			
		Total	QECC ν_e	QECC ν_u	Other
single ring	21 (61.8%)	24.2 (66.5%)	0.1 (0.2%)	13.7 (37.5%)	10.5 (28.9%)
e ring	3 (8.8%)	5.9 (16.1%)	0.1 (0.2%)	0.4 (1.0%)	5.4 (14.9%)
μ ring	18 (52.9%)	18.4 (50.4%)	0.0 (0.0%)	13.3 (36.4%)	5.1 (14.0%)
multi-ring	13 (38.2%)	12.2 (33.5%)	0.0 (0.1%)	0.4 (1.2%)	11.7 (32.1%)
total	34	36.4	0.1	14.1	22.2

Table 11.2: Number of muon decay electrons predicted for various prompt event types versus D_2O phase data. In parentheses is fraction of total decay electrons.

background as opposed to being a statistical fluctuation, we expect to see that these events have few followers.

As a consistency check of the analysis I look for decay electron events following our prompt atmospheric neutrino interaction events. The number of decays following single and multi-ring events is given in Table 11.2, and the N_{hit} and Δt distributions are shown in Fig. 11.5. Here we see that despite the deficit seen in the one third dataset, now the absolute number of decays agrees well with the simulation for both single ring and multi-ring. On the other hand, the fraction of multi-ring prompt events with decay electrons in data is only 23% compared to 47% for simulation due to the excess of multi-ring prompt events. We see that as expected, there are many more decay electron followers of single ring muon events than single ring electron events, confirming that the particle identification is working.

Finally I look at the number of neutron capture followers of these atmospheric neutrino events, shown in Table 11.3. I find 94 followers, compared to 71.7 ± 12.7 predicted by the simulation. Here we see that the number of single muon ring followers agrees with the simulation, but there are fewer single-ring electron followers and many more multi-ring followers than expected. The distributions for cut parameters are shown in Fig. 11.6. The time and distance since the prompt

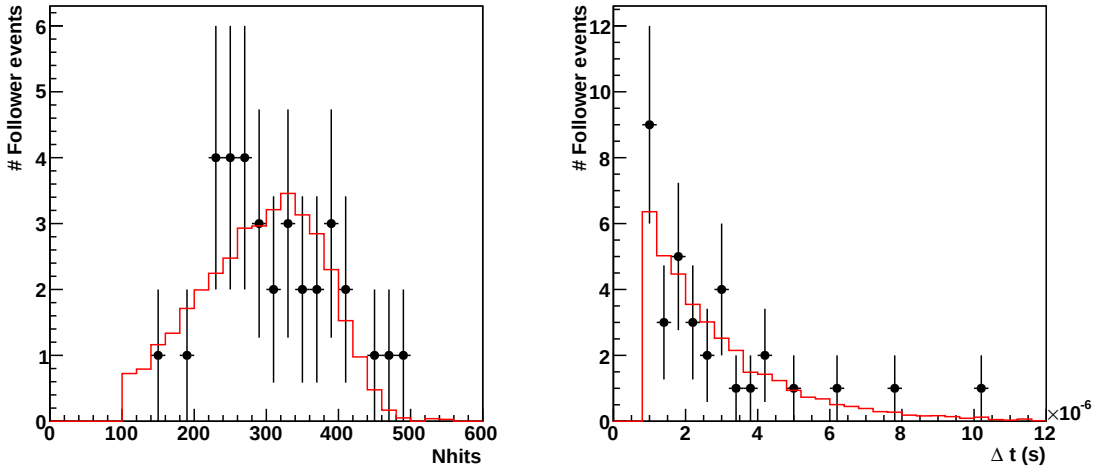

Figure 11.5: N_{hit} (left) and time since prompt event (right) for decay electron events in D_2O phase compared to simulation (red).

event are shown in Fig. 11.7. An exponential fit to the Δt distribution gives a capture time of 58 ± 11 ms, compared to 43 ms for the simulation. The χ^2 for these distributions is 6.5 for 5 dof for the energy distribution, 29.6 for 5 dof for the radial distribution, 1.4 for 4 dof for the time distribution, and 14.5 for 5 dof for the distance distribution. The reconstructed radius is seen to have a somewhat unexpected shape causing a large χ^2, the cause of which is unknown.

	Data	Simulation				
		Total	QECC ν_e	QECC ν_u	Other	Background
single ring	19 (20.2%)	40.4 (56.4%)	5.4 (7.5%)	7.8 (10.9%)	26.5 (37.0%)	0.7 (1.0%)
e ring	7 (7.4%)	24.7 (34.4%)	5.3 (7.4%)	0.7 (1.0%)	18.4 (25.7%)	0.3 (0.4%)
μ ring	12 (12.8%)	15.7 (21.9%)	0.1 (0.1%)	7.2 (10.0%)	8.1 (11.3%)	0.4 (0.6%)
multi-ring	75 (79.8%)	31.3 (43.7%)	0.8 (1.1%)	0.9 (1.3%)	29.0 (40.4%)	0.6 (0.8%)
total	94	71.7	6.1	8.8	55.5	1.3

Table 11.3: Number of neutron followers predicted for various prompt event types versus D_2O phase data. In parentheses is fraction of total neutron followers.

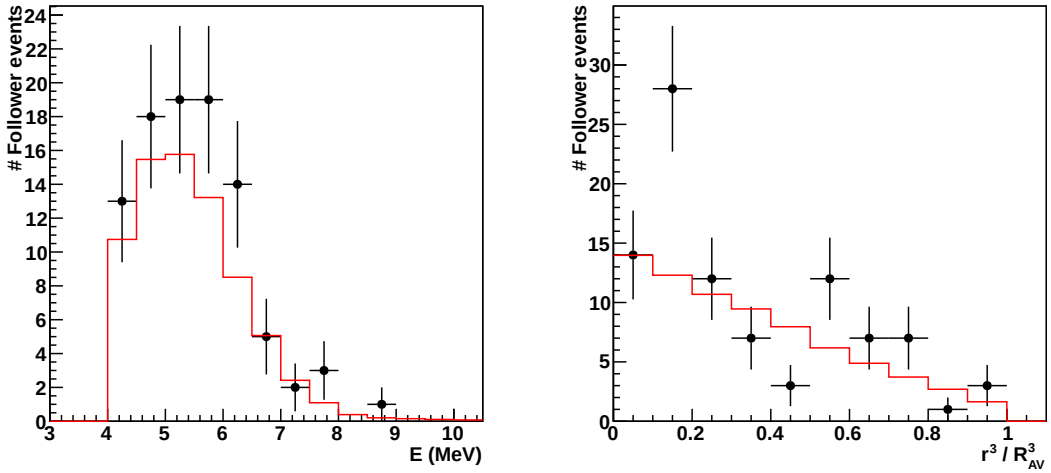

Figure 11.6: Neutron follower fitted energy (left) and radius (right) in D_2O phase compared to simulation (red).

The overall neutron follower multiplicity distribution is shown in Fig. 11.8, and the breakdown by number of rings in the prompt event is shown in Fig. 11.9.

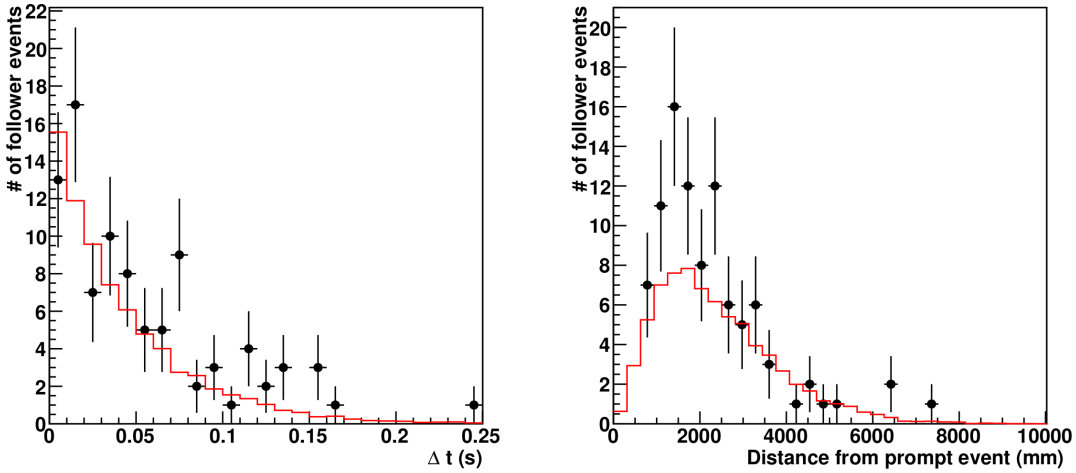

Figure 11.7: Time since prompt event (left) and distance from prompt event (right) for neutron follower events in D_2O phase compared to simulation (red).

There is an excess of multi-ring prompt events that have zero followers, as would be expected if the additional multi-ring events seen above were due to an instrumental background. We can confirm that this is in fact the same set of events as in the other excesses described above. The N_{hit} distribution for single ring and multi-ring events with no neutron or decay electron followers is shown in Fig. 11.10. In the 1000 to 2000 N_{hit} bin, I find that the simulation predicts 11.2 ± 2.1 single ring events (16.4% of all single ring events) and 3.0 ± 0.5 multi-ring events (11.6% of all multi-ring events). In comparison, in the data I have 9 single ring events (16.1%) and 15 multi-ring events (27.2%). Expanding to the entire N_{hit} range, I find 28 single ring events compared to 32.1 ± 5.8 predicted and 27 multi-ring events compared to 8.6 ± 1.4 predicted. Even including the 15% flux uncertainty and any cross section uncertainties (but not including any trials penalty for selecting this particular subset of events), this is a statistically significant difference. An excess of events with no followers suggests an instrumental background as opposed to a physical source. I have hand-scanned these 27 events to look for any obvious signal, but besides one obvious flasher nothing stands out. Possible instrumental backgrounds are bubbler or neck events, described in Section 9.2, which would be difficult to distinguish by eye. Shift reports for the runs for these events were checked to make sure the bubbler lines were flooded, and nothing out of the ordinary was noted.

From Fig. 11.8 we can also see that the majority of the excess of multi-ring event neutron followers can be attributed to 5 events with abnormally high multiplicity, including one event with 12 followers. The simulation predicts 1.5 events with a multiplicity greater than 5. In all of the Monte Carlo data, consisting of statistics equivalent to 100 times the D_2O livetime, I only find 7 events total with 12 or more followers. The simulation further predicts an average of 11.0 followers total coming

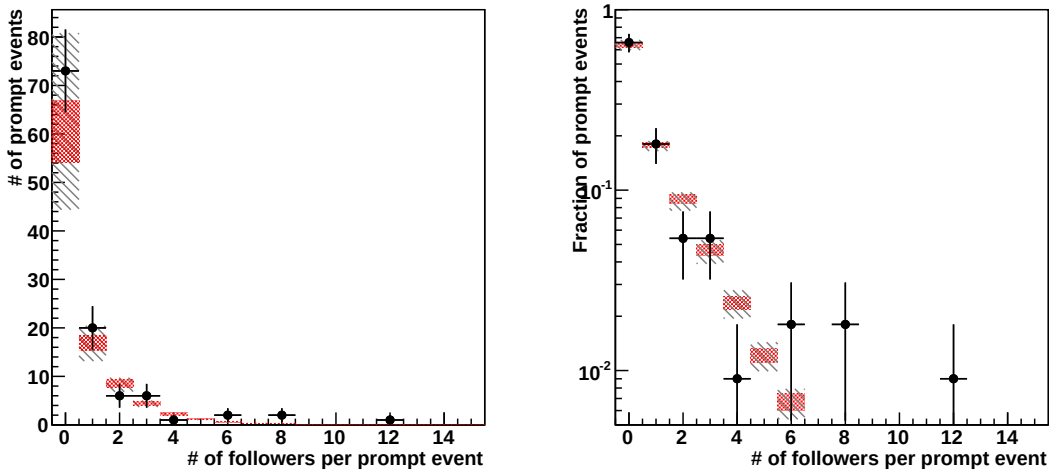

Figure 11.8: Absolute number (left) and fraction (right) of prompt events with given number of neutron followers in D_2O phase. Simulation is shown with cross section and Monte Carlo statistics uncertainty (solid red band) and with these combined with follower normalization systematic uncertainties (cross-hatched band).

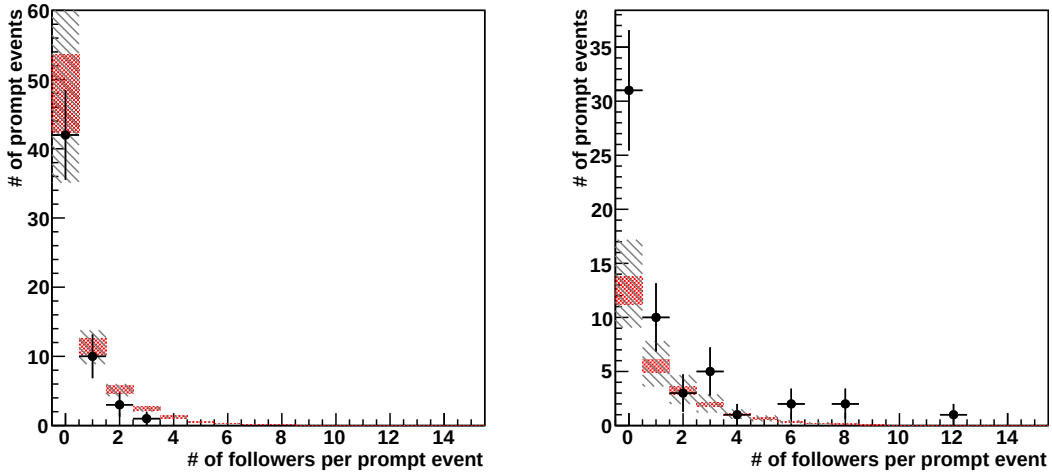

Figure 11.9: Number of single-ring (left) and multi-ring (right) prompt events with given number of neutron followers in D_2O phase. Simulation is shown with cross section and Monte Carlo statistics uncertainty (solid red band) and with these combined with follower normalization systematic uncertainties (cross-hatched band).

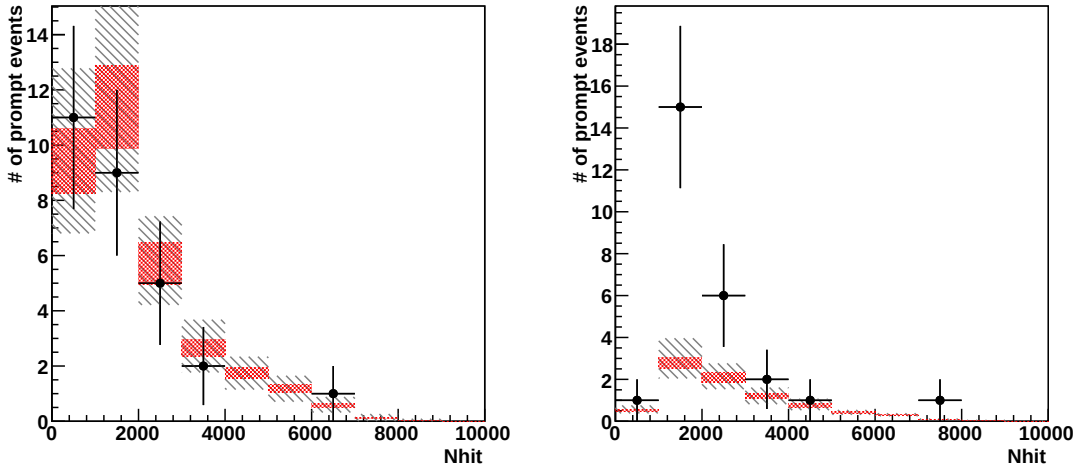

Figure 11.10: Number of prompt events with no decay electrons or neutron followers versus N_{hit} for single ring events (left) and multi-ring events (right) in the D_2O phase. Simulation is shown with cross section and Monte Carlo statistics uncertainty (solid red band) and with these combined with follower normalization systematic uncertainties (cross-hatched band).

from events with a multiplicity greater than 5. The 5 events in the data have a total of 40 followers. Randomly sampling from the simulated multiplicity distribution, I find that a total of 40 or more occurs 0.7% of the time (1.9% if we increase the flux by 15%).

For a nucleon decay analysis, we want to be able to predict the neutron multiplicity distribution for atmospheric events as accurately as possible using as much information about the event as we can, in order to quantify the likelihood that a given event is an atmospheric background. We expect the multiplicity distribution to be most directly affected by the neutrino interaction type and energy. The interaction type is related to the ring identification, for which we showed separate distributions above, and so we now look at the neutron follower multiplicity as a function of the visible energy of the prompt event. Fig. 11.11 shows the follower

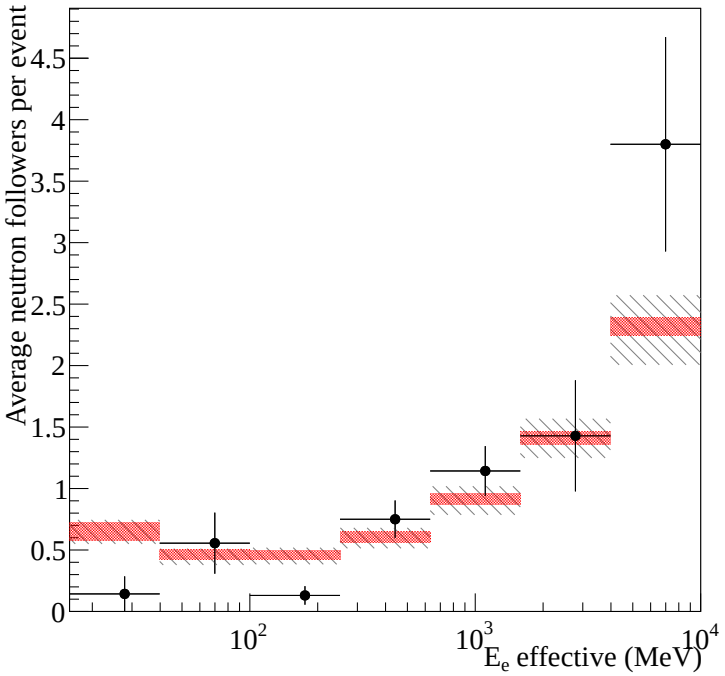

Figure 11.11: Prompt event effective electron energy versus average number of neutron follower events in D_2O phase. Simulation is shown with cross section and Monte Carlo statistics uncertainty (solid red band) and with these combined with follower normalization systematic uncertainties (cross-hatched band). Data bars represent statistical uncertainty assuming the number of followers for events in any bin is Poisson distributed.

multiplicity for all prompt events versus the fitted effective electron energy of the prompt event. We see that as expected, the average follower multiplicity increases with the energy of the event. The slight increase in the prediction below 50 MeV appears to be due to neutral-current resonant single pion production interactions where the only particle produced initially above Cherenkov threshold is a charged pion which then inelastically scatters. This gives a low visible energy for a possibly high energy interaction.

What we are truly interested in is the actual number of neutrons per atmo-

spheric neutrino event, and not just the number of followers detected. I apply the radial dependent neutron detection efficiency to convert from average number of followers to estimated average number of neutrons. I need to first determine how to calculate the average number of neutrons in each bin considering that the detection efficiency can vary significantly from event to event within the bin. Just averaging the efficiency corrected number of neutrons for each prompt event will lead to biases from low efficiency events. I use the fact that the combination of a Poisson distribution with mean λ and a binomial distribution with probability p is also a Poisson distribution with mean $p\lambda$; then assuming that the neutron detection efficiency ϵ is constant within any radial bin and that the number of neutrons per event in any energy bin is Poisson distributed with mean μ_N, given a radial bin and an energy bin, we expect the number of followers to be Poisson distributed with mean $\epsilon(R)\mu_N(E)$. We now want to find the μ_N that will maximize the likelihood of the data given n prompt events in an energy bin where the ith event has F_i followers and is in a radial bin with efficiency ϵ_i. Then

$$P(\vec{F}|\mu_N,\vec{\epsilon}) = \prod_{i=0}^{n} P_{poisson}(F_i|\epsilon_i\mu_N) \tag{11.1}$$

$$= \prod_{i=0}^{n} e^{-\epsilon_i\mu_N}(\epsilon_i\mu_N)^{F_i}\frac{1}{F_i!}, \tag{11.2}$$

$$\ln P(\vec{F}|\mu_N,\vec{\epsilon}) = -\sum(\epsilon_i\mu_N) + \sum(F_i \ln \epsilon_i\mu_N) - \sum(\ln F_i!) \tag{11.3}$$

and so we find the minimum

$$\frac{d\ln(P)}{d\mu_N} = -\sum \epsilon_i + \frac{\sum F_i}{\mu_N} = 0 \tag{11.4}$$

and thus

$$\hat{\mu_N} = \frac{\sum F_i}{\sum \epsilon_i}. \tag{11.5}$$

Fig. 11.12 show the average efficiency corrected number of neutrons as a function of effective electron energy for all prompt events. We see that the simulation overpredicts the neutron multiplicity at low energies and underpredicts above around 250 MeV. Some of the high energy excess comes from the five events with multiplicity greater than 5. Fig. 11.13 shows the average number of neutrons as a function of either electron or muon energy for single ring events, but we see that with only 7 and 12 neutron followers respectively, the statistics are too low to get a sense of the distribution as a function of energy. It does appear that the simulation systematically overpredicts the neutron multiplicity in both samples.

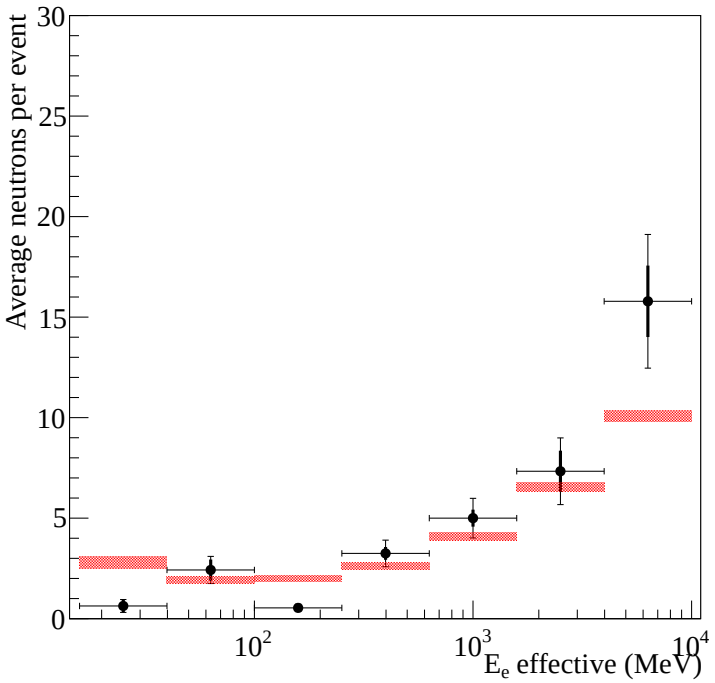

Figure 11.12: Prompt event effective electron energy versus efficiency corrected average number of neutrons in the D_2O phase. Data is shown with statistical uncertainty (thick bar) assuming the number of neutrons per event is Poisson distributed, and with statistical uncertainties added to neutron detection efficiency uncertainties (thin bar). Simulation (red) includes cross section and Monte Carlo statistical uncertainties.

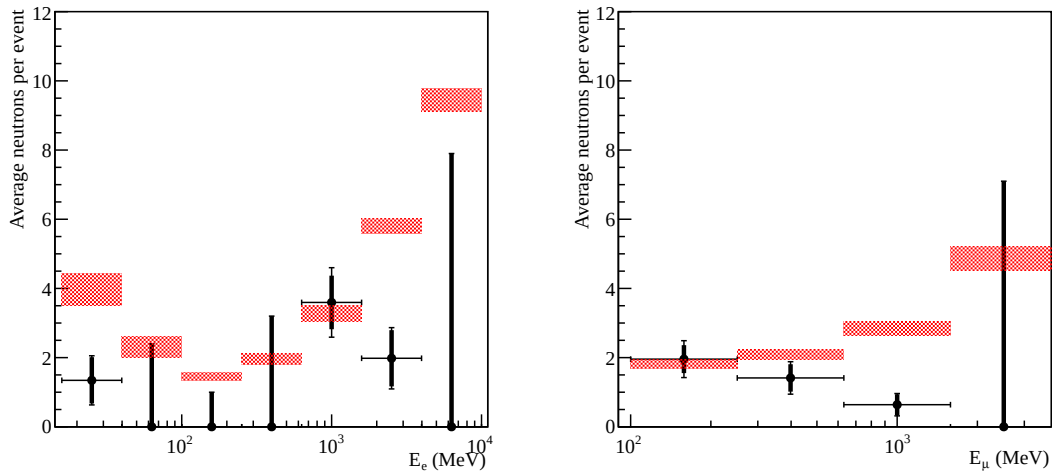

Figure 11.13: Prompt event energy versus efficiency corrected average number of neutrons for single electron ring (left) and single muon ring (right) events in D_2O phase. Data is shown with statistical uncertainty (thick bar) assuming the number of neutrons per event is Poisson distributed, and with statistical uncertainties added to neutron detection efficiency uncertainties (thin bar). For bins with zero followers an upper limit is calculated by $\frac{1.841/\epsilon_{avg}}{N}$ where N is the number of prompt events in the bin and ϵ_{avg} is the average expected efficiency for those events. Simulation (red) includes cross section and Monte Carlo statistical uncertainties.

11.2 Salt Phase

I find 135 prompt events total in the salt phase compared to 134.9 ± 22.5 predicted by simulation. The breakdown of events by ring count and particle identification is given in Table 11.4. The number of single ring events agrees with the simulation, while there are slightly more multi-ring events than expected. The distributions for various cut parameters are shown in Fig. 11.15. I find a χ^2 of 5.6 for 5 dof for the N_{hit} distribution, 5.4 for 8 dof for the radial distribution, 39.4 for 5 dof for the ITR distribution, and 10.4 for 6 dof for the Hough transform parameter distribution. As in the D_2O data, the ITR distribution of the salt data is shifted lower than the simulation. Although there are more multi-ring events than predicted, the difference is smaller than in the D_2O phase and there is no indication of an excess from 1000 to 2000 N_{hit}. Figs. 11.16 and 11.17 show the single ring electron or muon energies and multi-ring effective electron energies for prompt events. These distributions have a χ^2 of 5.2 for 4 dof, 1.45 for 3 dof, and 15.0 for 3 dof respectively.

	Data	Simulation			
		Total	QECC ν_e	QECC ν_u	Other
single ring	85 (63.0%)	98.7 (73.2%)	30.9 (22.9%)	36.5 (27.0%)	31.4 (23.3%)
e ring	45 (33.3%)	52.8 (39.1%)	29.7 (22.0%)	3.6 (2.7%)	19.5 (14.5%)
μ ring	40 (29.6%)	46.0 (34.1%)	1.2 (0.9%)	32.9 (24.4%)	11.9 (8.8%)
multi-ring	50 (37.0%)	36.2 (26.8%)	2.6 (2.0%)	2.0 (1.5%)	31.6 (23.4%)
total	135	134.9	33.5	38.4	62.9

Table 11.4: Results of ring identification on prompt events in the salt phase compared to simulation.

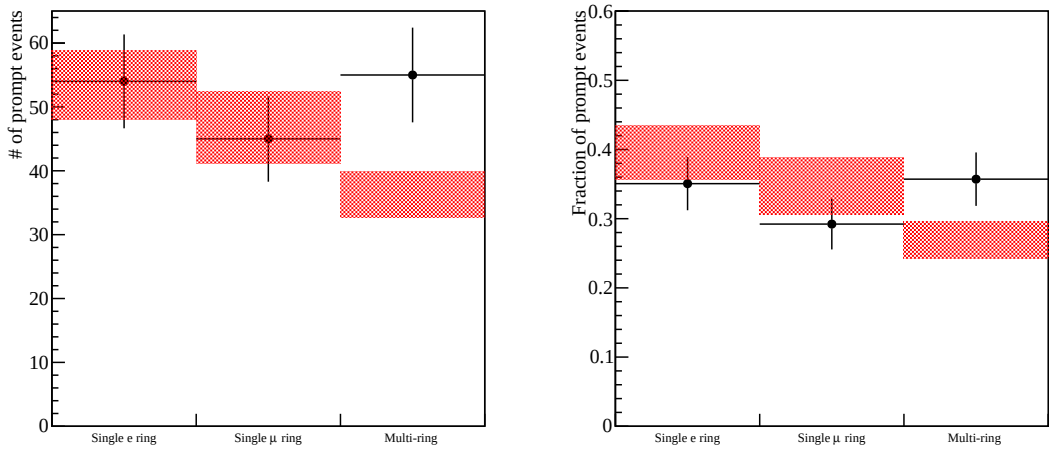

Figure 11.14: Absolute number (left) and fraction (right) of atmospheric neutrino events in data and simulation for the salt phase. Simulation (red) includes only cross section uncertainties.

I again look at the decay electron followers as a check of the analysis. The results are given in Table 11.5. Besides a slight deficit of single muon ring decay followers, it looks consistent with the simulation.

Finally I look at the number of neutron capture followers of these atmospheric neutrino events, shown in Table 11.6. I find 277 followers, compared to 288.0 ± 47.0 predicted by the simulation. Here we see the opposite scenario from the D_2O results;

	Data	Simulation			
		Total	QECC ν_e	QECC ν_u	Other
single ring	26 (55.4%)	34.4 (66.3%)	0.1 (0.1%)	18.8 (36.2%)	15.5 (29.9%)
e ring	8 (17.0%)	8.0 (15.4%)	0.1 (0.1%)	0.5 (1.0%)	7.4 (14.2%)
μ ring	18 (38.3%)	26.4 (50.9%)	0.0 (0.0%)	18.2 (35.2%)	8.2 (15.7%)
multi-ring	21 (44.7%)	17.5 (33.7%)	0.1 (0.1%)	0.5 (1.0%)	16.9 (32.6%)
total	47	51.9	0.1	19.3	32.5

Table 11.5: Number of muon decay electrons predicted for various prompt event types versus salt phase data.

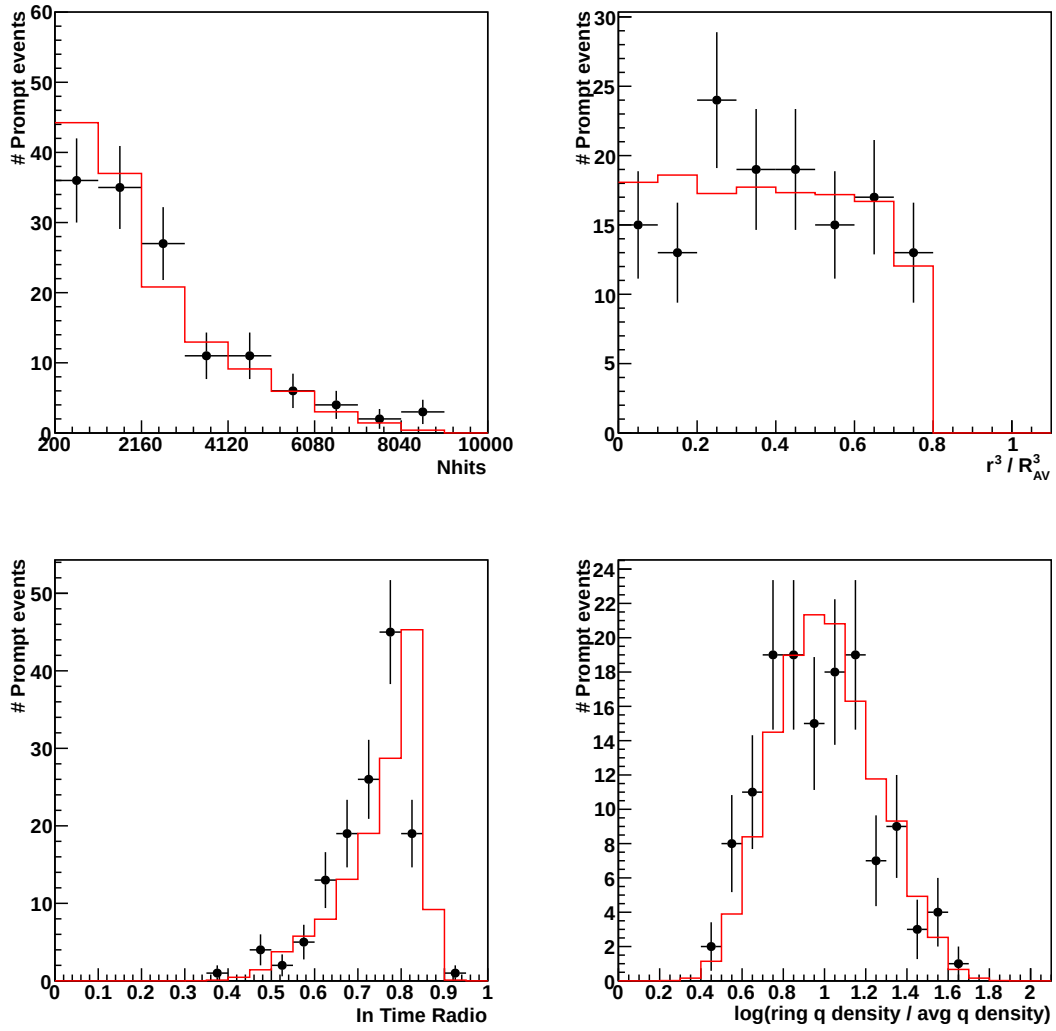

Figure 11.15: N_{hit} (top left), fitted radius (top right), in time ratio (bottom left), and hough transform ring charge density (bottom right) of prompt events in the salt phase after all cuts compared to simulation (red).

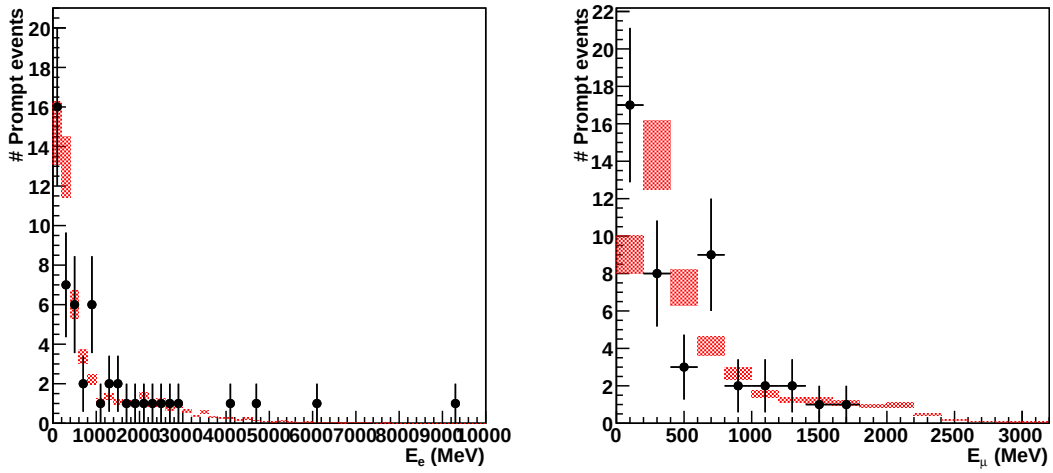

Figure 11.16: Reconstructed energy distribution of single electron ring (left) and single muon ring (right) events in the salt phase. Simulation (red) includes cross section uncertainties.

the number of single electron ring followers agrees with the simulation, but there are now fewer single muon ring followers and again more multi-ring followers than expected. It is again possible that there is a difference between data and Monte Carlo in the ring count mistagging fraction. As the average followers per prompt event is also significantly different, it is possible that non quasielastic events are more likely to be tagged as multi-ring in data. The simulation predicts that non quasielastic interactions make up a small fraction of the single muon ring prompt events but produce over half of the neutron followers for that event sample.

The distributions for neutron follower cut parameters are shown in Fig. 11.19. The time and distance since the prompt event are shown in Fig. 11.20. An exponential fit to the Δt distribution gives a capture time of 4.8 ± 0.3 ms, compared to 5.1 ms for the simulation. The χ^2 for these distributions is 11.1 for 8 dof for the energy distribution, 10.1 for 9 dof for the radial distribution, 5.8 for 13 dof for the

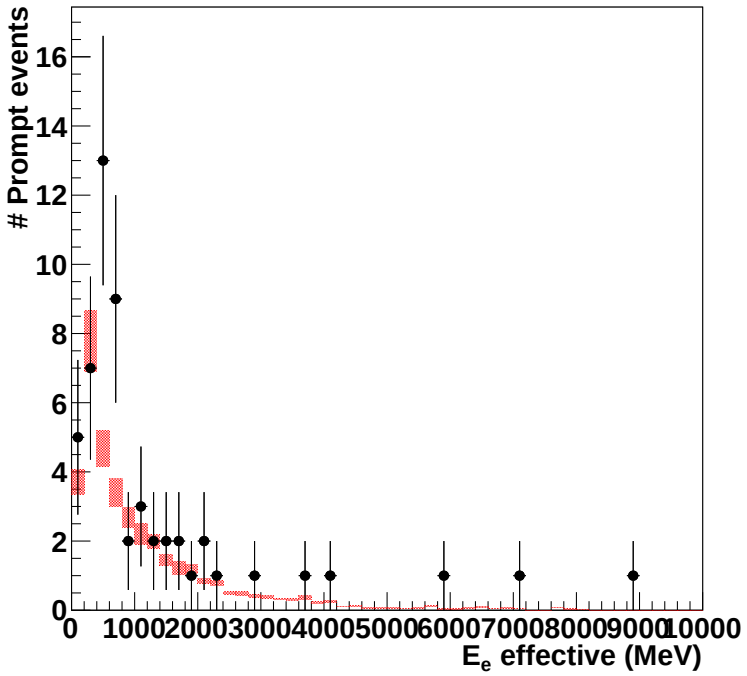

Figure 11.17: Effective electron energy for multi-ring prompt events in the salt phase. Simulation (red) includes cross section uncertainties.

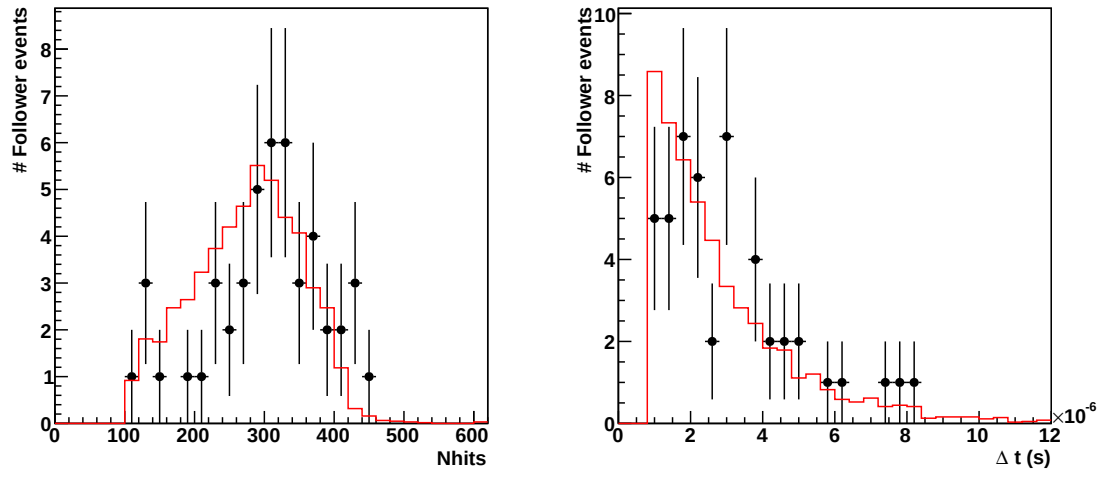

Figure 11.18: N_{hit} (left) and time since prompt event (right) for decay electron events in the salt phase compared to simulation (red).

time distribution, and 14.8 for 16 dof for the distance distribution.

	Data	Simulation				
		Total	QECC ν_e	QECC ν_u	Other	Background
single ring	123 (43.9%)	161.5 (56.2%)	24.2 (8.5%)	32.5 (11.4%)	103.8 (36.3%)	1.0 (0.3%)
e ring	91 (32.5%)	94.7 (33.0%)	23.6 (8.3%)	2.5 (0.9%)	68.1 (23.8%)	0.5 (0.2%)
μ ring	32 (11.4%)	66.8 (23.2%)	0.6 (0.2%)	30.0 (10.5%)	35.7 (12.5%)	0.5 (0.2%)
multi-ring	154 (55.0%)	126.5 (43.8%)	3.0 (1.0%)	2.1 (0.7%)	120.2 (42.1%)	1.2 (0.4%)
total	277	288.6	27.2	34.6	224.0	2.2

Table 11.6: Number of neutron followers predicted for various prompt event types versus salt phase data.

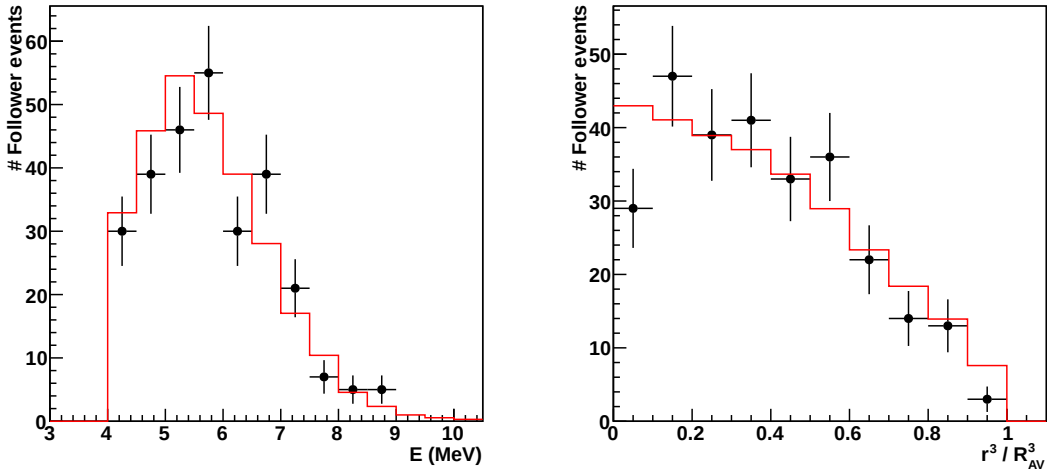

Figure 11.19: Neutron follower fitted energy (left) and radius (right) in salt phase compared to simulation (red).

The neutron follower multiplicity distributions are shown in Fig. 11.22, and the breakdown by number of rings in the prompt event is shown in Fig. 11.23. We see

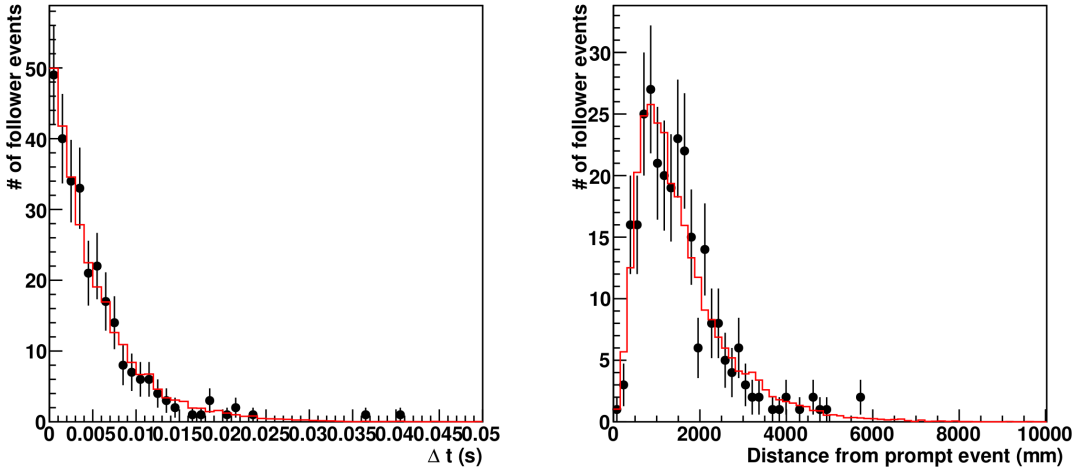

Figure 11.20: Time since prompt event (left) and distance from prompt event (right) for neutron follower events in salt phase compared to simulation (red).

that there is only a small excess of multi-ring events with no followers. The N_{hit} distribution of events with no followers is shown in Fig. 11.21 and we can see that it agrees with the prediction. If the excess in the D_2O phase was from an instrumental background, it was one that only impacted that one phase.

We again see a handful events with significantly more followers than any others. The simulation predicts 4.0 events with a multiplicity greater than 10, averaging 59.2 total followers. I find 5 events with multiplicity greater than 10 in the salt data with 104 followers between them. On the other hand, unlike in the D_2O phase we do not see more followers in total than predicted, so these outliers do not explain an excess. Again sampling from the simulated multiplicity distribution, I find that we expect 104 or more followers 8.2% of the time (14.9% if we shift the neutrino flux up by 15%), so these high multiplicity events are not as unlikely as those in the D_2O phase.

I now look at the neutron follower multiplicity as a function of the visible energy of the prompt event. Fig. 11.24 shows the follower multiplicity for all prompt events versus the prompt event effective electron energy. I then apply the energy and radius dependent neutron detection efficiency correction to get the average neutron multiplicity. Fig. 11.25 shows the efficiency corrected average number of neutrons as a function of effective electron energy for all prompt events. Compared to the result from D_2O, we see that the deficit below 40 MeV has gone away, but the deficit between 100 and 250 MeV remains. Both phases have the same excess above 4 GeV, which is partially driven by the handful of events with the abnormally high multiplicity. Fig. 11.26 shows the average number of neutrons as a function of either electron or muon energy for single ring events. This phase provides sufficient statistics to see the single ring distribution with energy. For single electron ring

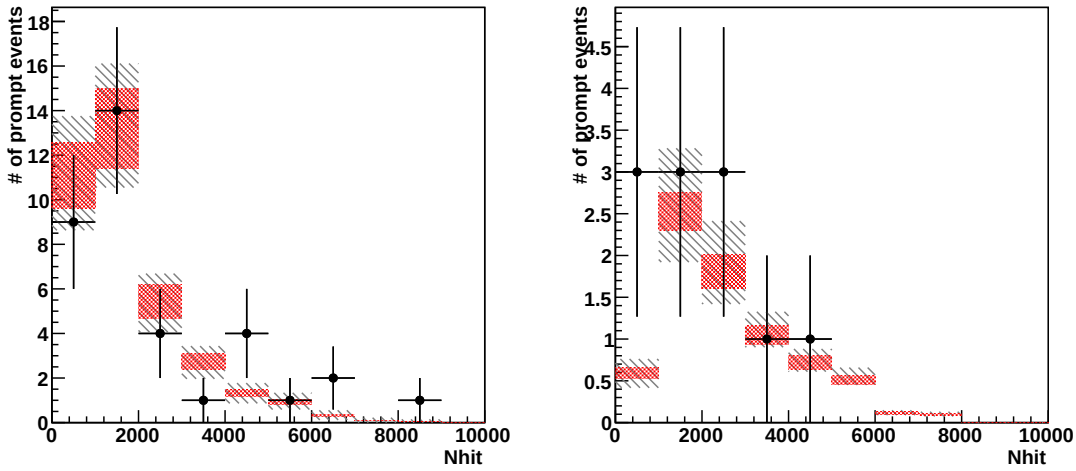

Figure 11.21: Number of prompt events with no decay electrons or neutron followers versus N_{hit} for single ring events (left) and multi-ring events (right) in the salt phase. Simulation is shown with cross section and Monte Carlo statistics uncertainty (solid red band) and with these combined with follower normalization systematic uncertainties (cross-hatched band).

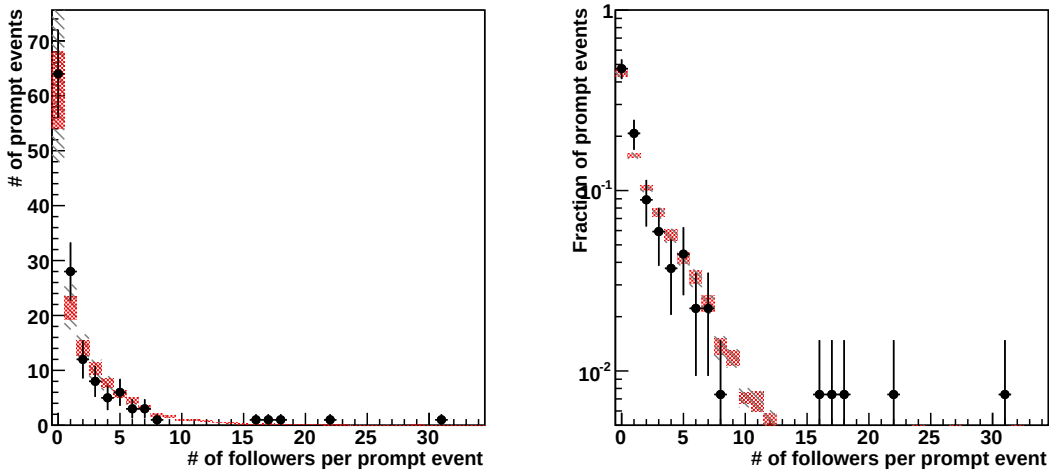

Figure 11.22: Absolute number (left) and fraction (right) of prompt events with given number of neutron followers in the salt phase. Simulation is shown with cross section and Monte Carlo statistics uncertainty (solid red band) and with these combined with follower normalization systematic uncertainties (cross-hatched band).

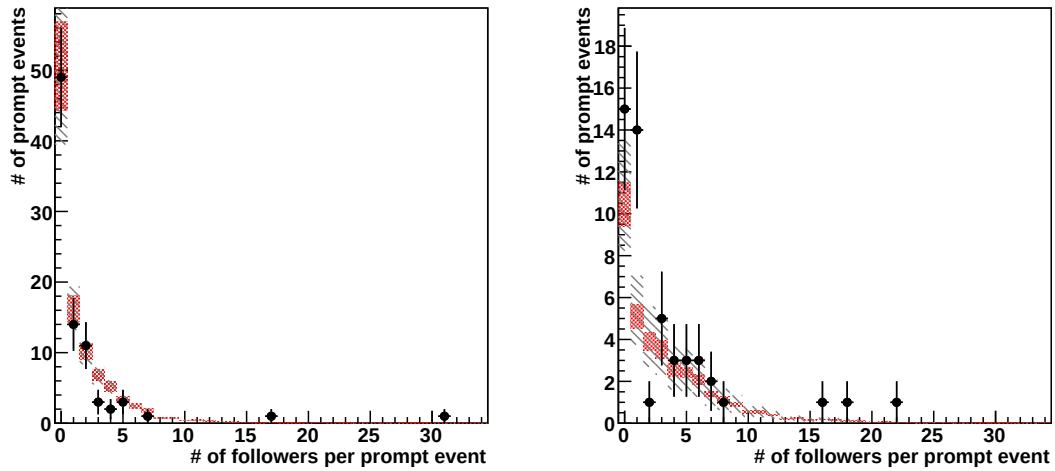

Figure 11.23: Number of single ring (left) and multi-ring (right) prompt events with given number of neutron followers in the salt phase. Simulation is shown with cross section and Monte Carlo statistics uncertainty (solid red band) and with these combined with follower normalization systematic uncertainties (cross-hatched band).

events, we see a similar trend as with the combined distribution — agreement at low energy, an average multiplicity lower than the prediction starting at 100 MeV, and an average higher than the prediction above 4 GeV. The single muon ring plot shows a deficit that increases with energy, as the measured average multiplicity actually decreases.

Now that we have corrected for any detector dependent efficiency, we can combine the results for the D_2O and salt phases. Fig. 11.27 shows the efficiency corrected average number of neutrons as a function of effective electron energy for all prompt events in both phases, and Figs. 11.28 and 11.29 show the average number of neutrons for the single-ring events as a function of either electron or muon energy. The end result is mostly driven by the salt measurements which had a much higher efficiency. The plot of all events and of single electron ring events show agreement

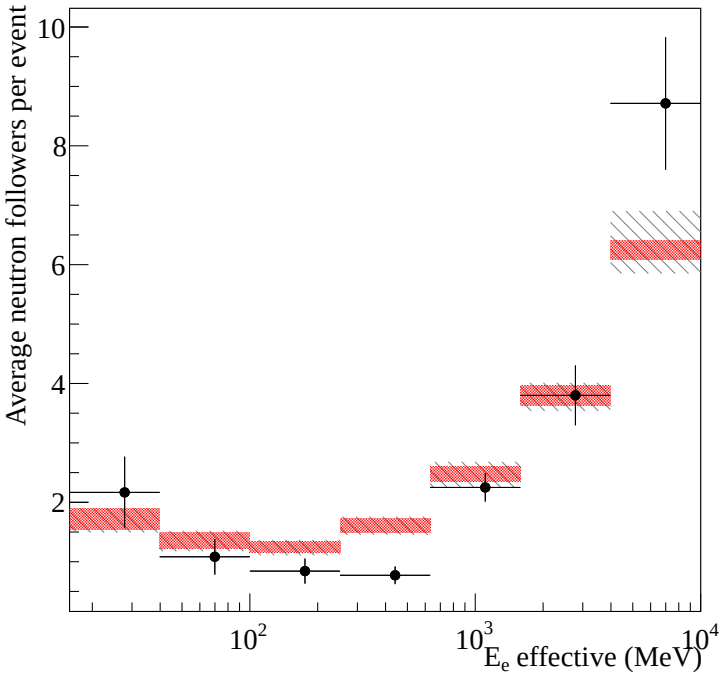

Figure 11.24: Prompt event effective electron energy versus average number of neutron follower events in salt phase. Simulation (red) includes cross section uncertainties.

below 100 MeV, the simulation overpredicting the multiplicity above 100 MeV and then underpredicting it above 4 GeV. In the single electron ring plot we see that there were no neutron followers of events between 100 and 250 MeV. The single muon ring distribution shows agreement from E_μ of 100 to 250 MeV, and then an increasing disagreement, with the simulation overpredicting the multiplicity up to $E_\mu = 4$ GeV.

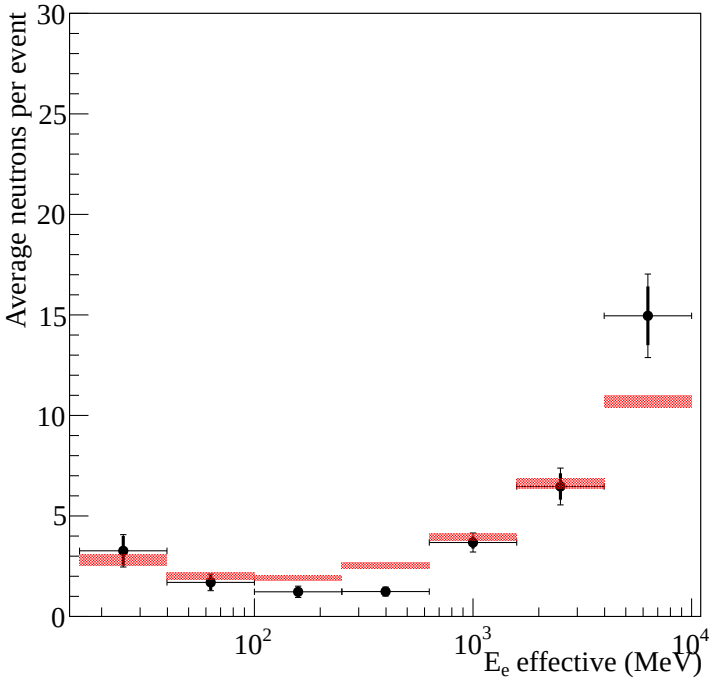

Figure 11.25: Prompt event effective electron energy versus efficiency corrected average number of neutrons in the salt phase. Data is shown with statistical uncertainty (thick bar) assuming the number of neutrons per event is Poisson distributed, and with statistical uncertainties added to neutron detection efficiency uncertainties (thin bar). Simulation (red) includes cross section and Monte Carlo statistical uncertainties.

11.3 Neutrino-Antineutrino Ratio

For measurements of the neutrino mass hierarchy, we would like to be able to separate neutrino and antineutrino events in water Cherenkov detectors. The neutron follower multiplicity does not let us identify the type on an event by event basis, but it should allow us to statistically separate the two. Within a larger fit it could increase the significance of any mixing measurement. The normalized predicted follower multiplicity distributions for neutrinos and antineutrinos in the salt phase is shown in Fig. 11.30. In order to determine how well we can separate the two

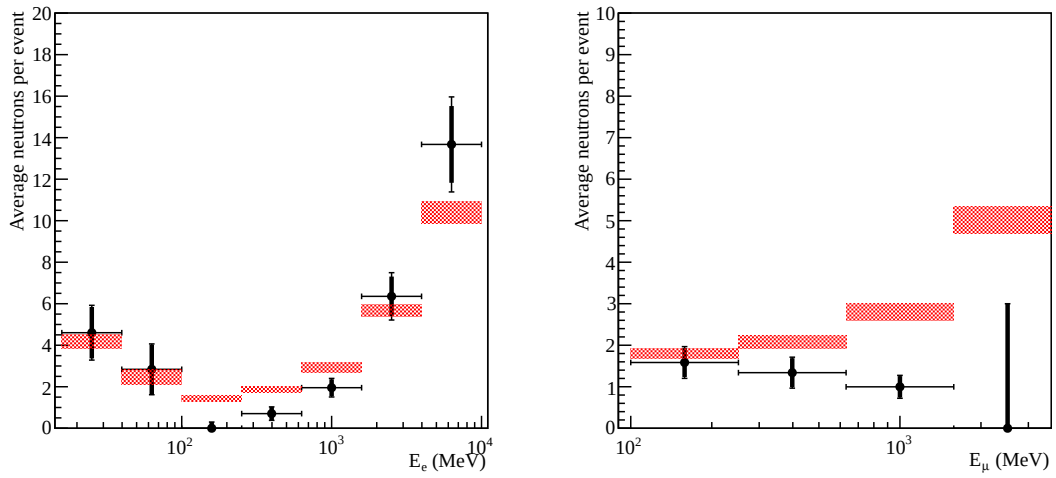

Figure 11.26: Prompt event energy versus efficiency corrected average number of neutrons for single electron ring (left) and single muon ring (right) events in the salt phase. Data is shown with statistical uncertainty (thick bar) assuming the number of neutrons per event is Poisson distributed, and with statistical uncertainties added to neutron detection efficiency uncertainties (thin bar). For bins with zero followers an upper limit is calculated by $\frac{1.841/\epsilon_{avg}}{N}$ where N is the number of prompt events in the bin and ϵ_{avg} is the average expected efficiency for those events. Simulation (red) includes cross section and Monte Carlo statistical uncertainties.

types of events, I use the multiplicity distributions to extract the fraction of our events that come from antineutrino interactions. The accuracy and significance to which I can determine this fraction will tell us the effectiveness of the separation.

In order to cancel out uncertainties in absolute normalization of fluxes and cross sections, I fit for the double ratio $R \equiv R^{data}_{\overline{\nu}/\nu}/R^{MC}_{\overline{\nu}/\nu}$, where $R_{\overline{\nu}/\nu}$ represents the ratio of the number of events from antineutrinos and neutrino interactions. I do a simultaneous fit for the D_2O and salt phases using only the multiplicity distributions shown in Figs. 11.8, 11.9, 11.22, and 11.23. From the Monte Carlo I can calculate separate neutrino and antineutrino contributions to these distributions allowing me to fit for R. I fit two different ways, first using just the total multiplicity distribution,

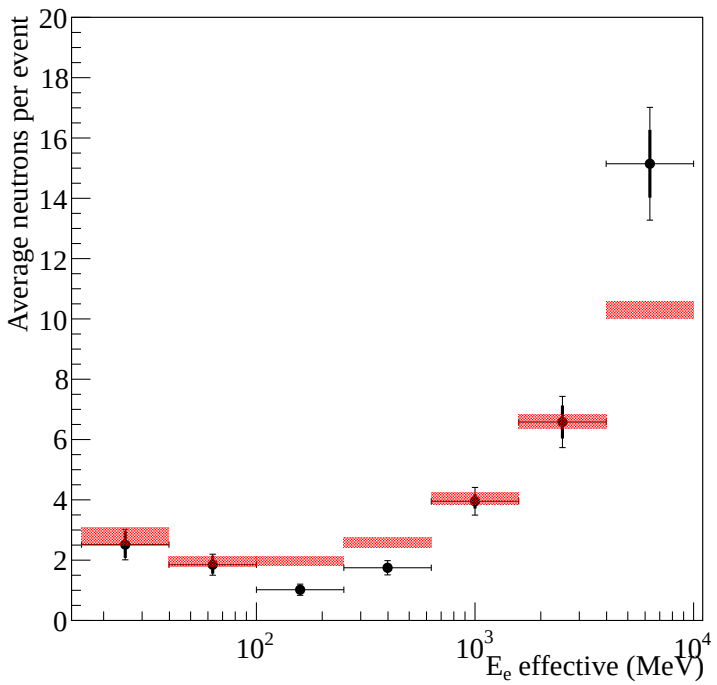

Figure 11.27: Prompt event effective electron energy versus efficiency corrected average number of neutrons in both phases combined. Data is shown with statistical uncertainty (thick bar) assuming the number of neutrons per event is Poisson distributed, and with statistical uncertainties added to neutron detection efficiency uncertainties (thin bar). Simulation (red) includes cross section and Monte Carlo statistical uncertainties.

and then simultaneously fitting separate distributions for single electron ring, single muon ring, and multi-ring events. I expect that separating the single ring events will give me a more precise fit by isolating the quasielastic charged-current events.

I perform a binned maximum likelihood fit to determine the best fit value and uncertainty on the ratio R. I assume the number of events in each multiplicity bin is a Poisson random variable, then the likelihood is given by

$$\mathcal{L}(\vec{x};\vec{\mu}(R)) = \prod_{i=1}^{N} \frac{\exp^{-\mu_i}\,\mu_i^{x_i}}{\mu_i!} \tag{11.6}$$

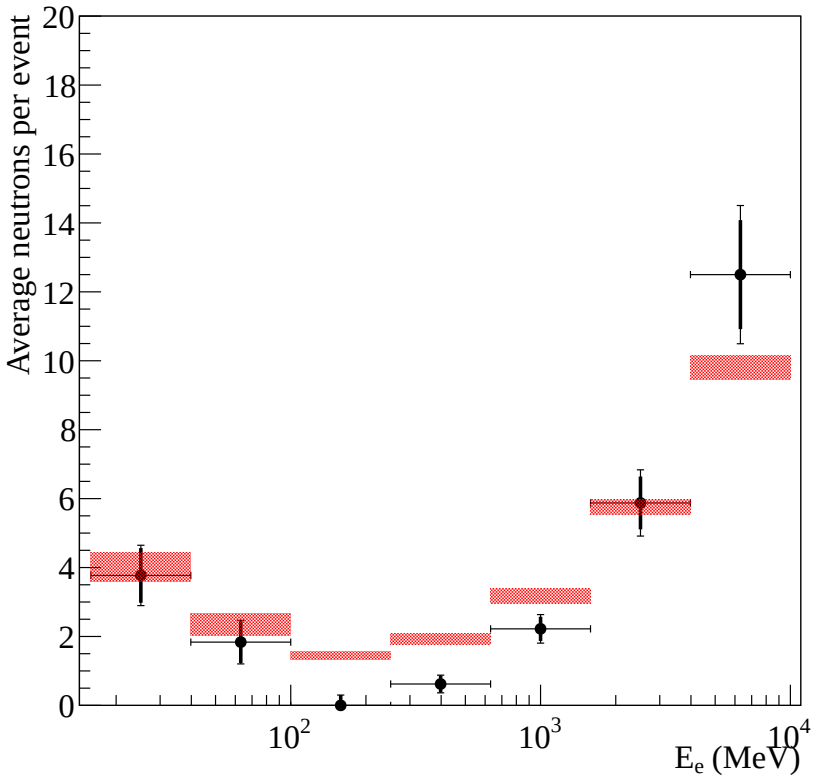

Figure 11.28: Prompt event energy versus efficiency corrected average number of neutrons for single electron ring events in both phases combined. Data is shown with statistical uncertainty (thick bar) assuming the number of neutrons per event is Poisson distributed, and with statistical uncertainties added to neutron detection efficiency uncertainties (thin bar). For bins with zero followers an upper limit is calculated by $\frac{1.841/\epsilon_{avg}}{N}$ where N is the number of prompt events in the bin and ϵ_{avg} is the average expected efficiency for those events. Simulation (red) includes cross section and Monte Carlo statistical uncertainties.

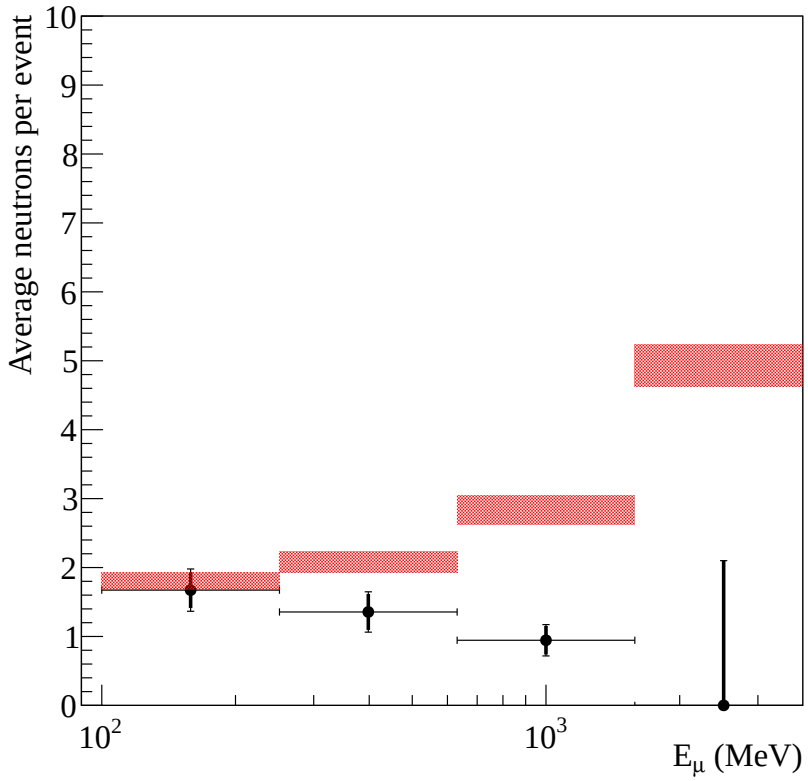

Figure 11.29: Prompt event energy versus efficiency corrected average number of neutrons for single muon ring events in both phases combined. Data is shown with statistical uncertainty (thick bar) assuming the number of neutrons per event is Poisson distributed, and with statistical uncertainties added to neutron detection efficiency uncertainties (thin bar). For bins with zero followers an upper limit is calculated by $\frac{1.841/\epsilon_{avg}}{N}$ where N is the number of prompt events in the bin and ϵ_{avg} is the average expected efficiency for those events. Simulation (red) includes cross section and Monte Carlo statistical uncertainties.

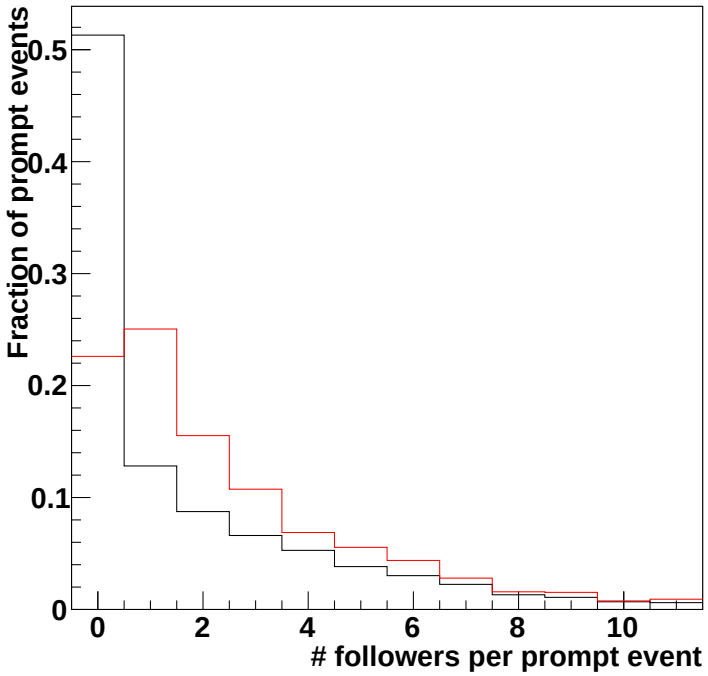

Figure 11.30: Fraction of prompt events with given number of neutron follower events in the salt phase for neutrinos (black) and antineutrinos (red).

where x_i is the observed counts in bin i and $\mu_i(R)$ is the predicted Poisson mean for that bin given some value of R. Systematic errors are also included in the fit by parameterizing their effect on $\vec{\mu}$. The uncertainty on each systematic parameter is included by adding a penalty term to the likelihood, assuming a Gaussian constraint. I then minimize

$$-2\ln\mathcal{L} = -2\sum_{i=1}^{N}(x_i \ln\mu_i - \mu_i - \ln x_i!) - 2\sum_{j=1}^{S}\frac{\epsilon_j^2}{\sigma_j^2}, \tag{11.7}$$

where ϵ_j is the change in the systematic parameter and σ_j is the one sigma constraint. The $\ln x_i!$ term is independent of $\vec{\mu}$ and can be ignored.

Although I fit for a double ratio in order to reduce the effect of normalization

uncertainties, the fit still involves number of counts instead of normalized distributions as even a weak constraint on the normalization will improve it. For any fixed value of the total number of events, we can vary R and calculate the expected number of neutrino and antineutrino events using

$$S_\nu = \frac{N_\nu + N_{\overline{\nu}}}{N_\nu + RN_{\overline{\nu}}}, \tag{11.8}$$

$$S_{\overline{\nu}} = \frac{R(N_\nu + N_{\overline{\nu}})}{N_\nu + RN_{\overline{\nu}}}, \tag{11.9}$$

where S_ν and $S_{\overline{\nu}}$ are the amount we scale the nominal number of events by and $R = S_{\overline{\nu}}/S_\nu$.

Systematic uncertainties included in the fit include the overall flux normalization, the follower acceptance, the ring misidentification fraction, the particle misidentification fraction, the radial bias (per phase), the cross section parameters, and the theoretical uncertainty on $R_{\overline{\nu}/\nu}$. In all the fit includes 25 free parameters. For each systematic parameter, I have estimated a one sigma upper and lower limits. I assume the constraint on each side takes the form of a half Gaussian, and that the change in each bin is linearly proportional to the value of the parameter. The one sigma upper and lower limits on R are found by finding the values of R where after minimizing over all systematic parameters the change from the global minimum in twice the log likelihood is ± 1.

For the fit to the combined multiplicity distribution, I find a best fit value of $R = 0.93^{+91}_{-63}$. Fitting separately to multiplicity distributions for single electron ring, single muon ring, and multi-ring events gives a best fit of 0.36 and a 68% upper limit of 1.0. The log likelihood distributions are shown in Fig. 11.31 and the best fits to the multiplicity distribution in Figs. 11.32 and 11.33. The two fits are consistent

with each other and are within their one sigma uncertainties of the expected value of $R = 1$. We expect the fit to be somewhat low due to the excess of multi-ring events with no followers in the D_2O phase. Since antineutrino interactions are expected to produce an additional neutron, this excess constrains the antineutrino contribution in the fit. The fit to separate distributions is supposed to increase the discriminating power as the single ring events will contain mostly quasielastic events where the difference between neutrino and antineutrino neutron multiplicities is greatest. We see the best fit value shifts to a lower value of R, which suggests that the single ring and multi-ring distributions were compensating for each other. Separated, the excess of no follower events becomes more pronounced in the multi-ring sample. It is also possible that statistical fluctuations that are averaged out in the combined sample are driving the difference. In the end, the fit to separated distributions does give a smaller uncertainty on R.

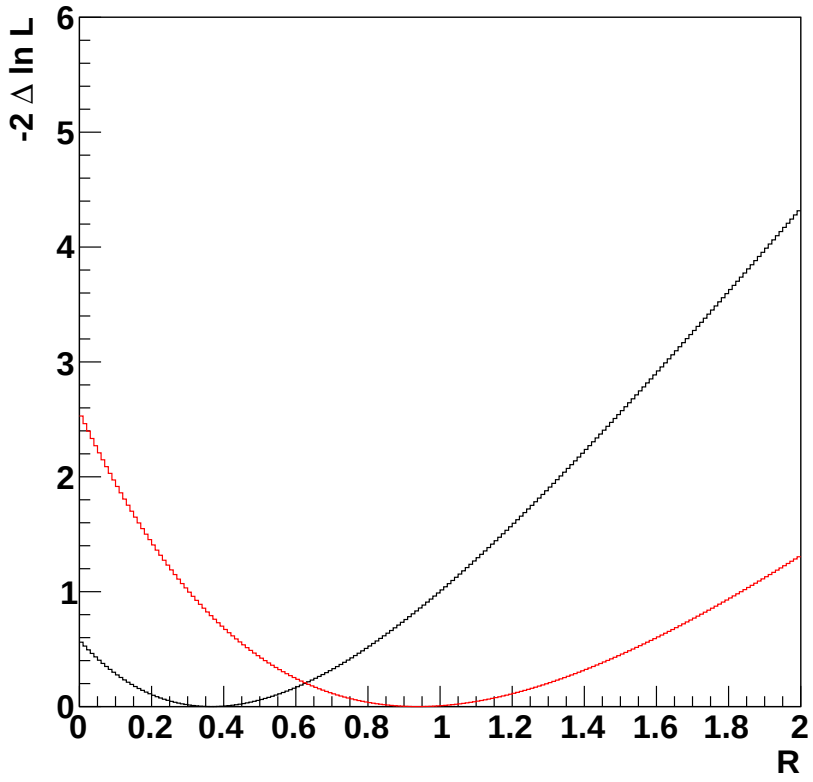

Figure 11.31: χ^2 distribution for fit to double ratio of $\overline{\nu}$ to ν using a single distribution (black) and separate distributions for single electron ring, single muon ring, and multi-ring events (red).

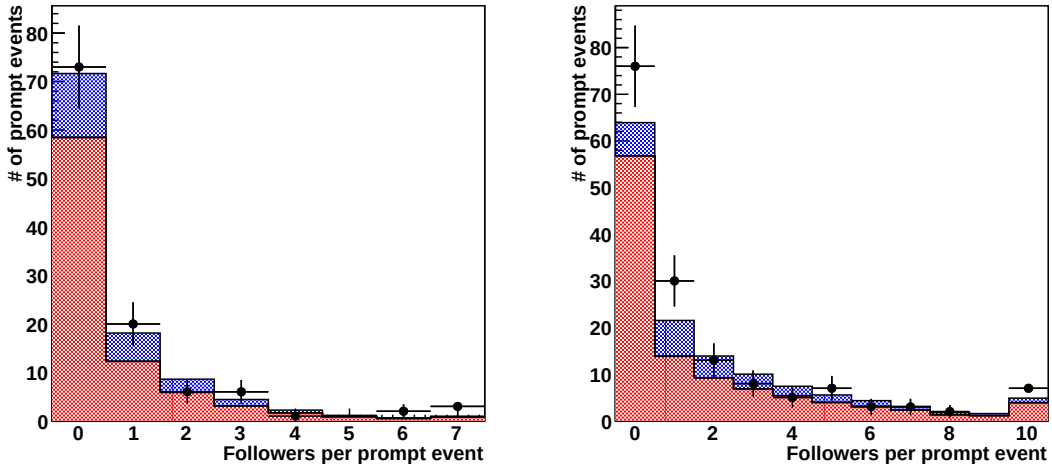

Figure 11.32: Best fit for ratio of ν to $\overline{\nu}$ from follower distribution using a single distribution for the D_2O phase (left) and salt phase (right). Fitted contribution from ν in red and $\overline{\nu}$ in blue.

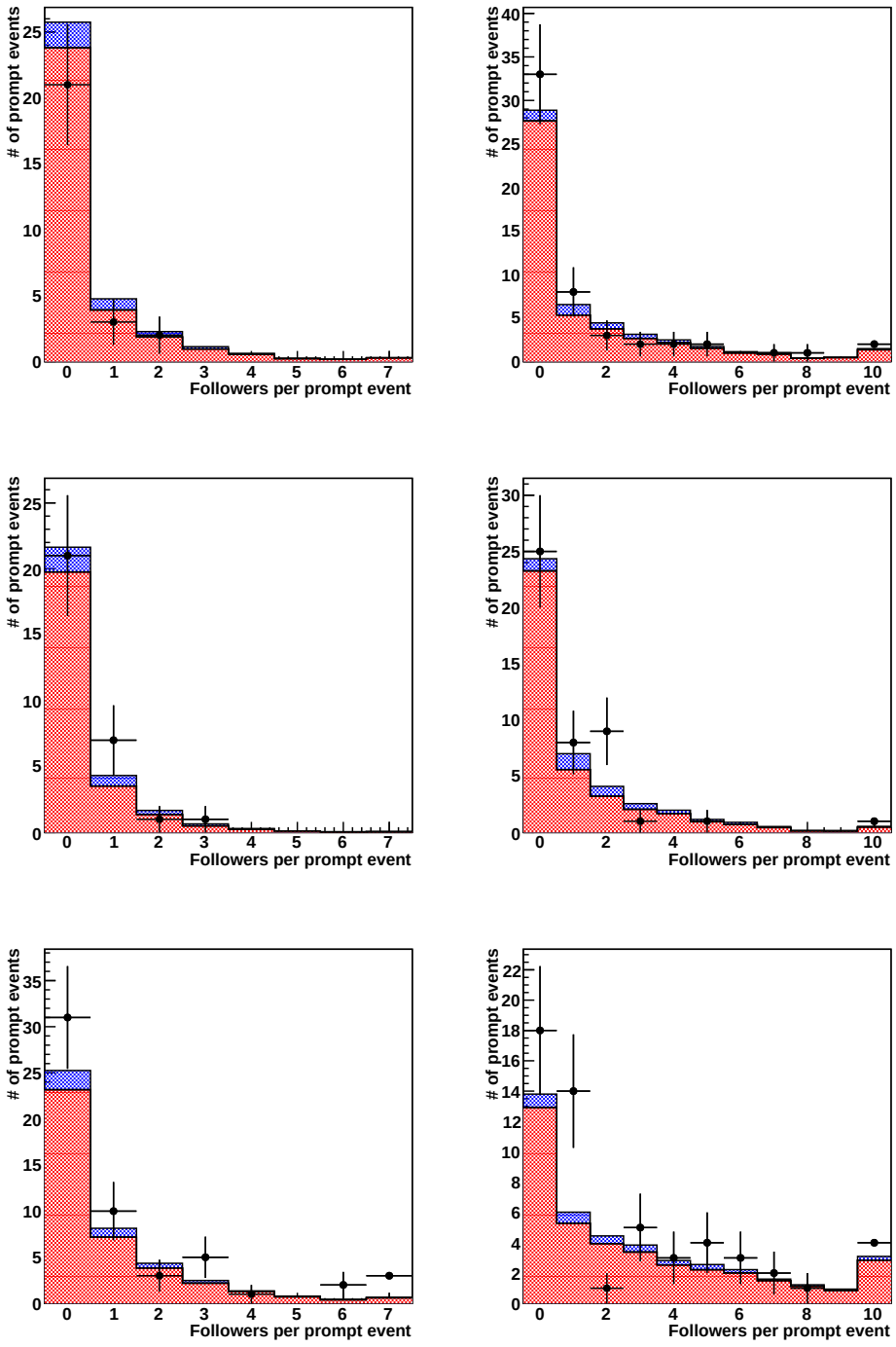

Figure 11.33: Best fit for ratio of ν to $\overline{\nu}$ from follower distribution using separate distributions for single electron ring (top), single muon ring (middle), and multi-ring (bottom) prompt events compared to D_2O phase (left) and salt phase (right) data. Fitted contribution from ν in red and $\overline{\nu}$ in blue.

11.4 Multinucleon Emission

I perform a similar likelihood fit to constrain the multinucleon emission fraction of the neutrino cross section. I again use the multiplicity distributions from data, but instead of finding predicted distributions for neutrinos and antineutrinos, I use the total distribution predicted from the standard simulation and from simulating atmospheric neutrino interactions with some contribution from multinucleon emissions. GENIE can add a contribution to the cross section from meson-exchange currents (MEC), which is the main contribution to multinucleon emission events. The integrated MEC cross section for a given neutrino energy and target nucleus is taken to be a fraction of the charged-current quasielastic cross section for those values. A dataset is simulated with the strength of the MEC cross section tuned to agree with MiniBooNE results. Any change in the multiplicity distributions will be proportional to this strength, so I fit for the value $M = \frac{\sigma_{MEC}}{\sigma_{QE}}$, where $M = 0$ is the standard case and $M = 0.45$ is the strength when tuned to the MiniBooNE results.

The difference in the number of neutrons produced in the initial neutrino interaction after running the simulation with $M = 0.45$ is shown in Fig. 11.34 and the impact on the measured follower multiplicity is shown in Fig. 11.35. The addition of MEC interactions causes a slight increase in the number of neutrons expected.

For any value of M the predicted mean for any bin in the multiplicity distributions is given by

$$\mu(M) = \mu_{M=0} + (\mu_{M=0.45} - \mu_{M=0})\frac{M}{0.45}. \tag{11.10}$$

I then calculate a likelihood again using Eq. 11.7, floating the same parameters and fitting both with a single multiplicity distribution for each phase and then with distributions separated by ring count and type.

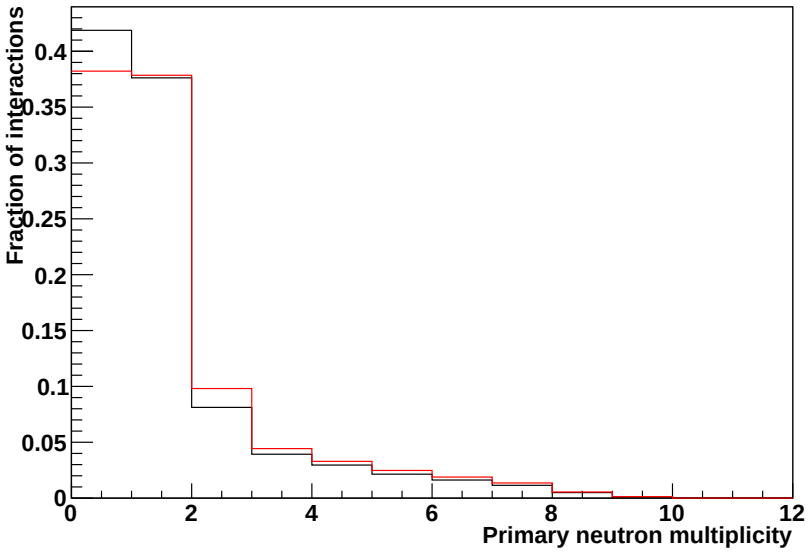

Figure 11.34: Number of neutrons produced in neutrino interaction by GENIE for standard cross sections (black) and with the addition of MEC (red). This does not include any secondary production of neutrons.

Here I find that the standard cross section model fits the data better than the MEC model. If I fit to a combined multiplicity distribution for each phase, I find a 68% upper limit on the MEC strength of $M < 0.17$. At a value of $M = 0.45$ where the prediction agrees with the MiniBooNE results, I find $-2\log(L_{M=0.45}/L_{M=0}) = 3.67$. For a fit to separate single electron-ring, single muon-ring, and multi-ring distributions I find an upper limit of $M < 0.04$, and at a value of 0.45 the likelihood ratio is $-2\log(L_{M=0.45}/L_{M=0}) = 16.66$. In the separated fit a large contribution to the likelihood ratio comes from the excess in the multi-ring events. As the MEC contribution effectively adds additional quasielastic single-ring events, a higher than expected multi-ring to single-ring event ratio causes it to be heavily disfavored.

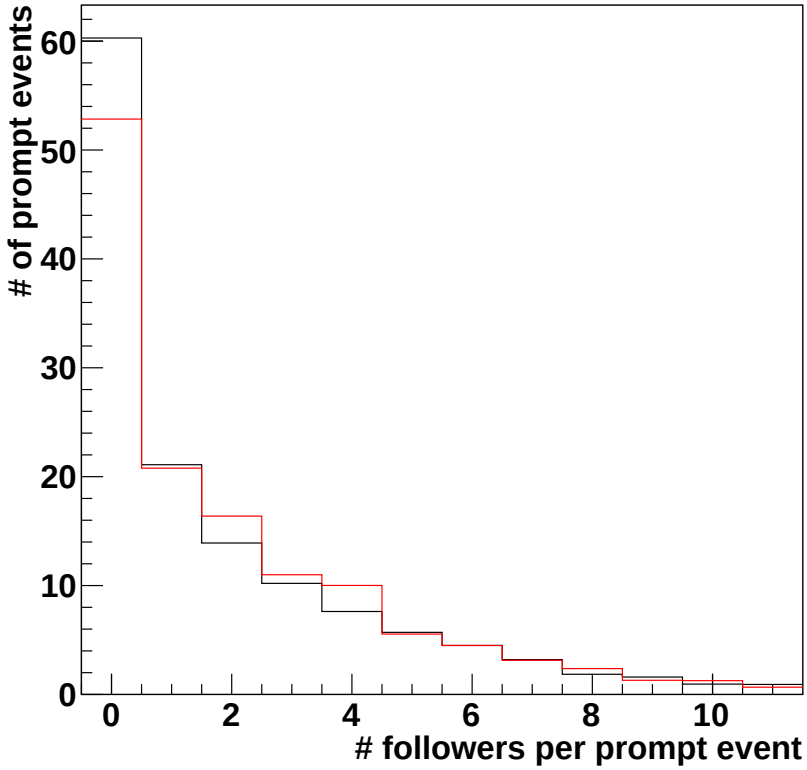

Figure 11.35: Follower multiplicity distribution prediction for standard cross sections (black) and with the addition of MEC (red). Band width includes cross section uncertainty.

Chapter 12

Conclusion

I have performed the first measurement of neutron follower multiplicities for atmospheric neutrino events in a heavy water target, as well as the first analysis of contained atmospheric events in SNO. The event reconstruction was calibrated using decay electron events. It was found that high energy events can have an impact on the charge seen in events for several μs, including all decay electrons. Future SNO+ analyses will require a more detailed understanding of afterpulsing and electronics noise in order to be able to effectively look at very short coincidence events. Systematic uncertainties are large due to low statistics in the decay electron sample. An analysis of through going and stopping muon events could provide an additional source to calibrate with and would allow a better understanding of the energy scale and resolution up to higher energies.

In the D_2O phase an excess of multi-ring events was seen. This excess was narrowed down to a set of events with an N_{hit} between 1000 and 2000 that had no decay electron or neutron capture followers. Although by eye the events look like they were caused by real physical interactions, it is possible that there is a contamination from some instrumental background like bubbler events, as we would

not expect followers for backgrounds. There were also somewhat fewer single ring events than expected, which combined with a multi-ring excess, suggests that the simulation may be underestimating how much single ring events are mistagged. It was already seen that this could happen with the decay electron events, where it is hypothesized afterpulsing from the predecessor event caused enough noise in the PMT charges to fool the ring counter. The salt phase saw almost exactly as many events total as expected, but again with slightly more multi-ring events and slightly fewer single ring events. There was no sign of an instrumental background-like set of events in the 1000 to 2000 N_{hit} range. An analysis of the NCD phase of SNO would be useful to see if a similar background returns.

I have measured the neutron multiplicity as a function of the event's visible energy, and measured separate distributions for electron- and muon-like single ring events as well as multi-ring events. The average multiplicity had the expected dependence on energy, and was seen to increase at high energies and at low energies where non-quasielastic contributions are expected. Compared to results from Super-Kamiokande, a higher average multiplicity is seen for events above a few hundred MeV, as expected due to differences in secondary production between light water and heavy water. On the other hand, at 100 MeV the multiplicity measured in SNO is about half the prediction, and actually agrees with the measurement in Super-K.

We also see a higher multiplicity than expected on average for high energy events, partially driven by a small number of events with much higher multiplicity. Fig. 12.1 shows that at these energies almost all of the neutrons are produced by secondary production. The very highest multiplicity events had more neutrons than there are nucleons in oxygen, so we expect these to almost all be from secondary production. Thus the simulation appears to be underpredicting secondary production at high

energy. The ability to identify all of the particles in multi-ring events would allow for a better understanding of where this excess comes from. The Super-Kamiokande analysis only gives the event multiplicity distribution up to 7 followers, so it is unknown whether they see anomalously high multiplicity events as well. It will be interesting to compare to a measurement in the water phase of SNO+ to see the difference between secondary production in heavy water and light water. SNO+ can use the XL3 electronics upgrade to set a low trigger threshold and look for the 2.2 MeV gammas as was done in Super-K.

Fig. 11.28 showed that for single electron ring events, there were no followers seen in either phase between 100 and 250 MeV. Fig. 12.2 shows the contribution to the neutron multiplicity from the initial neutrino interaction (including final state interactions within the nucleus) and from secondary production for single ring events. We see that in this energy range almost all of the neutrons come from the initial interaction. There is currently no explanation for the lack of neutrons followers seen. There could be less than expected electron antineutrinos of this energy. A breakdown of Super-Kamiokande's measured multiplicity as a function of their ring identification would be helpful in providing more statistics. A dedicated measurement by an experiment like ANNIE using a beam source of neutrinos would be able to make a much more precise measurement, and knowing the angle of the beam would be able to more directly measure the momentum transfer of the interaction instead of relying on visible energy.

I was able to use the measured neutron multiplicity to fit for the double ratio $R^{data}_{\overline{\nu}/\nu}/R^{MC}_{\overline{\nu}/\nu}$, with a result that was consistent with $R = 1$. The fit to separate distributions for single electron ring, single muon ring, and multi-ring events found a smaller value of R. Although MINOS measured R much more precisely, they used

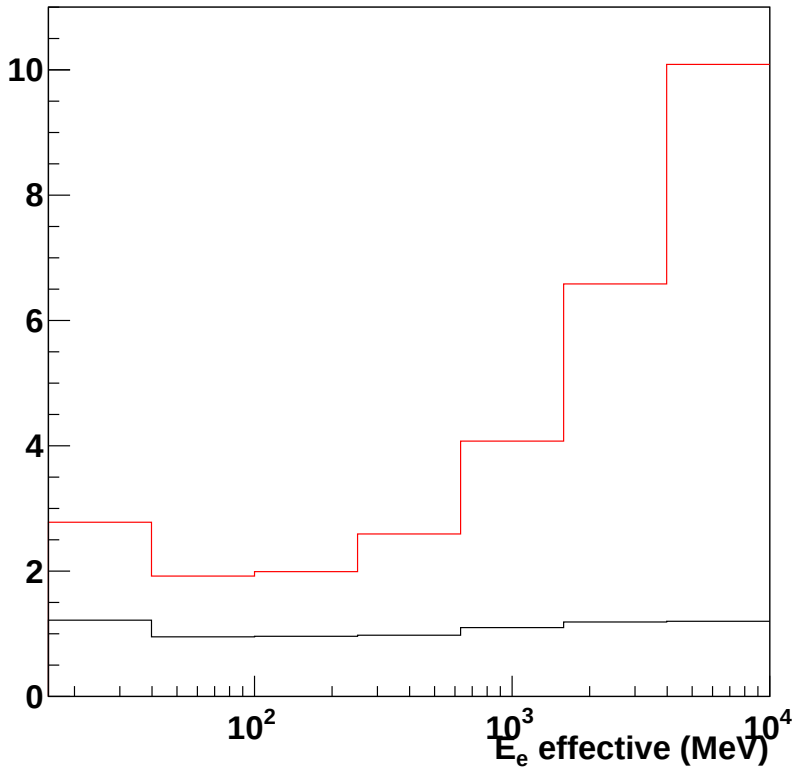

Figure 12.1: Average number of neutrons produced in initial interaction and final state interactions (black) compared to total number of neutrons produced by these effects and secondary production (red) from atmospheric neutrino simulation in the D_2O phase as a function of effective electron energy.

only muon neutrinos, so it is still possible that the atmospheric electron antineutrino flux is lower than expected. A better understanding is needed of the ring count and particle identification mistagging rate to determine why the fit result changed. In the end, the success of this fit proved that the neutron multiplicity can be used in water Cherenkov experiments to statistically separate neutrino and antineutrino events, and a future gadolinium loaded Super or Hyper Kamiokande will be able to use this technique to improve their sensitivity to the neutrino mass hierarchy.

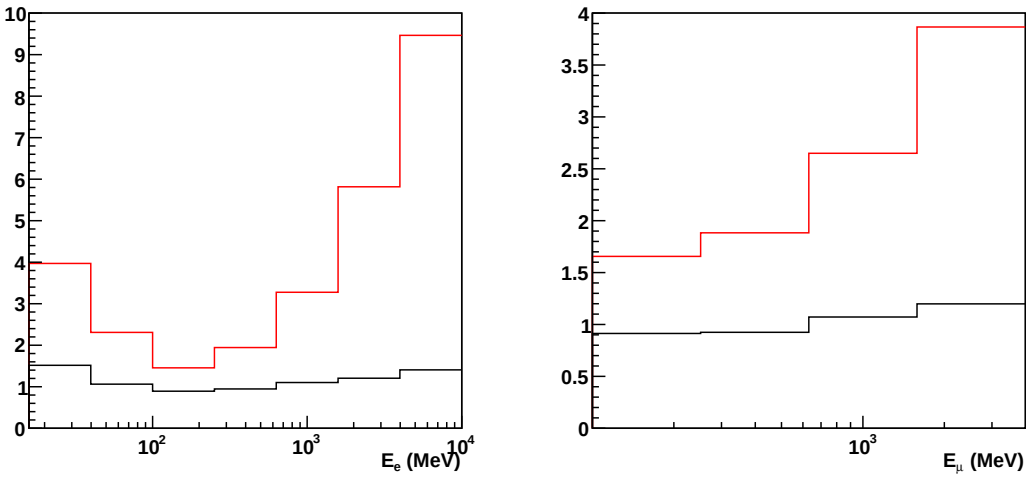

Figure 12.2: Average number of neutrons produced in initial interaction and final state interactions (black) compared to total number of neutrons produced by these effects and secondary production (red) for single electron ring (left) and single muon ring (right) events from atmospheric neutrino simulation in the D_2O phase as a function of reconstructed electron or muon energy.

Finally, I was able to set an upper limit on the strength of a multinucleon emmission interaction's contribution to the neutrino-nuclear cross section. A combined analysis including the MiniBooNE's results is needed in order to see if there is still any improvement using this sort of model to explain the measured large axial mass. On its own, the SNO data disfavors such a solution. A much smaller limit is found using separated distributions partially due to the deficit of single ring events compared to the simulation, so if the error on the ring count mistagging fraction is found to be large, this limit could be made weaker. A high statistics experiment like ANNIE with tracking to better select quasielastic events would be able to make a conclusive measurement.

Appendix A

Low Level Cuts

The following cuts were designed to reject instrumental background events in SNO while cutting a very small fraction of physics events. They were designed to be robust to problems with individual channels or calibrations, and do not require any reconstruction information but use only the PMT hit times, charges, and distributions.

The cuts used for the prompt event selection are:

- QvT: Cuts flashers by looking for events where the maximum charge hit is many counts away from the mean and occurs much earlier than the median time.
- QvNhit: Cuts electronic pickup events by comparing the charge in the event to the number of hits. Electronic noise is expected to integrate to zero, and so events with a low charge to nhit ratio are tagged. The 10% of hits with the highest charge are ignored, and then the average charge per hit of the bottom 90% is calculated, and the event is tagged if this ratio is less than 0.25 pe.
- Crate Isotropy: Electronic noise can cause pickup on the front end. This cut

looks for events where one crate has a large fraction of the hits, and a large fraction of the hits in that crate are in adjacent cards.

- Flasher Geometry Cut: Identifies flashers by looking for a cluster of hits either in electronics space or in PMT space and then calculating the average distance between the cluster and the rest of the hits in the event. If this distance is greater than 12 m the event is tagged.

- In Time Channel Time Spread: Cuts events by using the fact that most hits due to Cherenkov light occur within a time window equal to the amount of time it takes for light to cross the detector. It thus tags events where less than 60% of the hits occur within a 93 ns window.

- Retrigger: Flags all events that come within 5 μs of the previous event. The first event in the burst is not tagged as a retrigger event.

- Junk: Cuts nonsensical data including events where the same PMT is hit more than once and orphaned PMT hits with no associated event.

- Neck: Cuts events due to light in the neck. Looks for events where both of the PMTs in the neck fire or one of the PMT fires and it has a high charge hit and is early in time.

- OWL: Cuts atmospheric muons by tagging events where the sum of the number of OWL and BUTT PMTs hit is three or more.

- OWL Trigger: Tags evens where the OWLESUMHI trigger fires.

- Muon: Tags muons by looking for events with 5 or more OWL hits that occur more than 5 μs after the last OWL event. It also requires that the event have

at least 150 hits, have a time RMS less than 90 ns, and that the event is not tagged as a neck event

- Muon Follower short: Tags all events occurring within a time window of 20 s following a muon

The neutron follower event selection uses all of the above cuts plus the ones listed below:

- AMB: Cuts events using the Analog Measurement Board based on the ratio of the integral or the peak of the ESUM signal to the number of hits in the event. Events are tagged when these values are more than 3.7 σ away from the mean.

- Fitterless Time Spread: Cuts flashers including those where the flashing tube is missing from the event by looking at the time difference between pairs of nearby hits. It calculates the median time difference between pairs of hits on PMTs within 3 m of each other and tags the event if it is over 6.8 ns.

- ESUM: Cuts events that are triggered only by the ESUM trigger bits and not any of the NHIT, OWL, or pulsegt triggers.

- QCluster: Cuts flashers by looking for events where a high charge hit is found within a cluster of hits in electronics space that would be caused by pickup.

Bibliography

[1] M. F. Altmann, R. L. Mossbauer, and L. J. N. Oberauer, Rept. Prog. Phys. **64**, 97 (2001).

[2] N. F. F. de Barros, *Precision measurement of neutrino oscillation parameters: combined three-phase results of the Sudbury Neutrino Observatory*, PhD thesis, University of Lison, 2011.

[3] J. N. Bahcall, A. M. Serenelli, and S. Basu, The Astrophysical Journal Letters **621**, L85 (2005).

[4] Super-Kamiokande Collaboration, J. Hosaka *et al.*, Phys. Rev. D **73**, 112001 (2006).

[5] The KamLAND Collaboration, A. Gando *et al.*, Phys. Rev. D **83**, 052002 (2011).

[6] ANNIE Collaboration, I. Anghel *et al.*, (2014), 1402.6411.

[7] SNO Collaboration, B. Aharmim and Others, Phys. Rev. C **88**, 025501 (2013).

[8] M. Bergevin, *Search for Neutron Anti-neutron Oscillation at the Sudbury Neutrino Observatory*, PhD thesis, University of Guelph, 2010.

[9] Q. R. Ahmad, *Muon Correlated Background at The Sudbury Neutrino Observatory*, PhD thesis, Brown University, 2002.

[10] A. M. Serenelli, W. Haxton, and C. Peña-Garay, Astrophys.J. **743**, 24 (2011), 1104.1639.

[11] G. D. Barr, T. K. Gaisser, P. Lipari, S. Robbins, and T. Stanev, Phys. Rev. D **70**, 023006 (2004).

[12] W. Pauli, Letter to physicists at tubingen, 1930.

[13] C. L. Cowan, F. Reines, F. B. Harrison, H. W. Kruse, and A. D. McGuire, Science **125**, 103 (1956).

[14] L. Wolfenstein, Phys. Rev. D **17**, 2369 (1978).

[15] S. Mikheyev and A. Smirnov, Il Nuovo Cimento C **9**, 17 (1986).

[16] R. Davis, D. S. Harmer, and K. C. Hoffman, Phys. Rev. Lett. **20**, 1205 (1968).

[17] E. K. Akhmedov, M. Tortola, and J. Valle, JHEP **0405**, 057 (2004), hep-ph/0404083.

[18] B. T. Cleveland *et al.*, The Astrophysical Journal **496**, 505 (1998).

[19] SAGE Collaboration, J. N. Abdurashitov *et al.*, Phys. Rev. C **80**, 015807 (2009).

[20] The Super-Kamiokande Collaboration, J. P. Cravens *et al.*, Phys. Rev. D **78**, 032002 (2008).

[21] Super-Kamiokande Collaboration, K. Abe *et al.*, Phys. Rev. D **83**, 052010 (2011).

[22] Borexino Collaboration, G. Bellini *et al.*, Phys. Rev. Lett. **107**, 141302 (2011).

[23] Borexino Collaboration, G. Bellini *et al.*, Phys. Rev. Lett. **108**, 051302 (2012).

[24] Daya Bay Collaboration, F. P. An *et al.*, Chinese Physics C **37**, 011001 (2013).

[25] RENO Collaboration, J. K. Ahn *et al.*, (2012), 1204.0626.

[26] (LSND Collaboration), A. Aguilar *et al.*, Phys. Rev. D **64**, 112007 (2001).

[27] MiniBooNE Collaboration, A. A. Aguilar-Arevalo *et al.*, Phys. Rev. Lett. **105**, 181801 (2010).

[28] MINOS Collaboration, P. Adamson *et al.*, Phys. Rev. Lett. **107**, 011802 (2011).

[29] S. N. Gninenko, Phys. Rev. Lett. **103**, 241802 (2009).

[30] V. Barger *et al.*, Physics Letters B **462**, 109 (1999).

[31] SNO Collaboration, B. Aharmim *et al.*, Phys. Rev. C **81**, 055504 (2010).

[32] Double Chooz Collaboration, Y. Abe *et al.*, Phys. Rev. D **86**, 052008 (2012).

[33] LBNE Collaboration, T. Akiri *et al.*, (2011), 1110.6249.

[34] LAGUNA Collaboration, J. Kisiel *et al.*, PoS **EPS-HEP2009**, 283 (2009).

[35] K. Abe *et al.*, (2011), 1109.3262.

[36] J. N. Bahcall and C. Peña-Garay, New J.Phys. **6**, 63 (2004), hep-ph/0404061.

[37] A. Friedland, Nucl.Phys.Proc.Suppl. **221**, 79 (2011), hep-ph/0612266.

[38] A. Friedland, C. Lunardini, and C. Peña-Garay, Physics Letters B **594**, 347 (2004).

[39] M. Guzzo *et al.*, Nuclear Physics B **629**, 479 (2002).

[40] O. G. Miranda, M. A. Trtola, and J. W. F. Valle, Journal of High Energy Physics **2006**, 008 (2006).

[41] A. Palazzo, Phys. Rev. D **83**, 101701 (2011).

[42] V. Barger, P. Huber, and D. Marfatia, Phys. Rev. Lett. **95**, 211802 (2005).

[43] M. Cirelli, M. Gonzalez-Garcia, and C. Peña-Garay, Nuclear Physics B **719**, 219 (2005).

[44] M. C. Gonzalez-Garcia, P. C. de Holanda, and R. Zukanovich Funchal, Phys. Rev. D **73**, 033008 (2006).

[45] M. Gonzalez-Garcia and M. Maltoni, Physics Reports **460**, 1 (2008).

[46] M. C. Gonzalez-Garcia, P. C. de Holanda, E. Mass, and R. Z. Funchal, Journal of Cosmology and Astroparticle Physics **2007**, 005 (2007).

[47] R. Bonventre *et al.*, Phys. Rev. D **88**, 053010 (2013).

[48] L. Okun, Physics Letters B **382**, 389 (1996).

[49] I. Lopes and S. Turck-Chize, Astrophys.J. **765**, 14 (2013), 1302.2791.

[50] J. N. Bahcall, A. M. Serenelli, and S. Basu, The Astrophysical Journal Supplement Series **165**, 400 (2006).

[51] J. N. Bahcall, S. Basu, M. Pinsonneault, and A. M. Serenelli, The Astrophysical Journal **618**, 1049 (2005).

[52] Borexino Collaboration, G. Bellini *et al.*, Phys. Rev. D **82**, 033006 (2010).

[53] J. N. Bahcall *et al.*, Phys. Rev. C **54**, 411 (1996).

[54] J. N. Bahcall, Phys. Rev. C **56**, 3391 (1997).

[55] J. N. Bahcall, M. Kamionkowski, and A. Sirlin, Phys. Rev. D **51**, 6146 (1995).

[56] S. J. Parke, Phys. Rev. Lett. **57**, 1275 (1986).

[57] N. Grevesse and A. Sauval, Space Science Reviews **85**, 161 (1998).

[58] M. Asplund, N. Grevesse, A. J. Sauval, and P. Scott, Ann. Rev. Astron. Astrophys. **47**, 481 (2009).

[59] E. Lisi and D. Montanino, Phys. Rev. D **56**, 1792 (1997).

[60] J. N. Bahcall, Phys. Rev. C **65**, 025801 (2002).

[61] M. Gonzalez-Garcia, M. Maltoni, and J. Salvado, Journal of High Energy Physics **2010**, 1 (2010).

[62] K. Hirata and Others, Physics Letters B **205**, 416 (1988).

[63] H. Zhang, *Study of Low Energy Electron Antineutrinos at Super-Kamiokande IV*, PhD thesis, Tsinghua University, 2012.

[64] T2K Collaboration, K. Abe *et al.*, Phys. Rev. Lett. **112**, 061802 (2014).

[65] G. Zeller, (2003), hep-ex/0312061.

[66] V. Bernard, L. Elouadrhiri, and U.-G. Meiner, Journal of Physics G: Nuclear and Particle Physics **28**, R1 (2002).

[67] MiniBooNE Collaboration, A. A. Aguilar-Arevalo *et al.*, Phys. Rev. D **81**, 092005 (2010).

[68] M. Martini, M. Ericson, G. Chanfray, and J. Marteau, Phys. Rev. C **81**, 045502 (2010).

[69] M. Martini, M. Ericson, and G. Chanfray, Phys. Rev. C **84**, 055502 (2011).

[70] R. Hertenberger, M. Chen, and B. L. Dougherty, Phys. Rev. C **52**, 3449 (1995).

[71] H. Menghetti, M. Selvi, and L. collaboration, AIP Conference Proceedings **785**, 259 (2005).

[72] V. Chazal *et al.*, Nuclear Instruments and Methods in Physics Research Section A: Accelerators, Spectrometers, Detectors and Associated Equipment **490**, 334 (2002).

[73] Super-Kamiokande Collaboration, K. Bays and Others, Phys. Rev. D **85**, 052007 (2012).

[74] J. C. Pati and A. Salam, Phys. Rev. D **8**, 1240 (1973).

[75] H. Georgi and S. L. Glashow, Phys. Rev. Lett. **32**, 438 (1974).

[76] Super-Kamiokande Collaboration, H. Nishino and Others, Phys. Rev. Lett. **102**, 141801 (2009).

[77] (The Super-Kamiokande Collaboration), Y. Hayato and Others, Phys. Rev. Lett. **83**, 1529 (1999).

[78] The MINOS Collaboration, P. Adamson and Others, Phys. Rev. D **86**, 052007 (2012).

[79] Super-Kamiokande Collaboration, K. Abe *et al.*, Phys. Rev. Lett. **107**, 241801 (2011).

[80] J. F. Beacom and M. R. Vagins, Phys. Rev. Lett. **93**, 171101 (2004).

[81] G. Barr, S. Robbins, T. Gaisser, and T. Stanev.

[82] T. K. Gaisser and T. Stanev, Phys. Rev. D **57**, 1977 (1998).

[83] K. Olive and P. D. Group, Chinese Physics C **38**, 090001 (2014).

[84] C. Andreopoulos *et al.*, Nucl. Instrum. Meth. **A614**, 87 (2010), 0905.2517.

[85] A. Bodek and J. L. Ritchie, Phys. Rev. D **24**, 1400 (1981).

[86] C. L. Smith, Physics Reports **3**, 261 (1972).

[87] R. Bradford, A. Bodek, H. Budd, and J. Arrington, Nuclear Physics B - Proceedings Supplements **159**, 127 (2006), Proceedings of the 4th International Workshop on Neutrino-Nucleus Interactions in the Few-GeV Region Proceedings of the 4th International Workshop on Neutrino-Nucleus Interactions in the Few-GeV Region.

[88] D. Rein and L. M. Sehgal, Annals of Physics **133**, 79 (1981).

[89] A. Bodek and U. K. Yang, Journal of Physics G: Nuclear and Particle Physics **29**, 1899 (2003).

[90] T. Yang, C. Andreopoulos, H. Gallagher, K. Hofmann, and P. Kehayias, The European Physical Journal C **63**, 1 (2009).

[91] T. Katori, (2013), 1304.6014, 8th International Workshop on Neutrino-Nucleus Interactions in the Few-GeV Region (NuInt12), Rio de Janeiro, Brazil, 22-27 October 2012.

[92] B. Krusche *et al.*, Nuclear Physics A **386**, 245 (1982).

[93] P. Jones, Water fitter rat snoman comparison, SNO+ internal document SNO+-doc-2307, 2014.

[94] R. O. Duda and P. E. Hart, Commun. ACM **15**, 11 (1972).

[95] C. Kyba, *Measurement of the Atmospheric Neutrino Induced Muon Flux at the Sudbury Neutrino Observatory*, PhD thesis, University of Pennsylvania, 2014.

[96] N. McCauley, *Producing a Background Free Data Set for Measurement of the Charge Current Flux and Day-Night Asymmetry at the Sudbury Neutrino Observatory*, PhD thesis, Oxford University, 2001.

[97] J. R. Klein and A. Roodman, Annual Review of Nuclear and Particle Science **55**, 141 (2005), http://dx.doi.org/10.1146/annurev.nucl.55.090704.151521.